

A microscopic image of brain tissue showing a clear boundary between normal brain tissue (top right, pinkish-purple) and a tumor (bottom left, brownish-purple). The tumor tissue is more densely packed and has a different cellular structure compared to the surrounding normal brain tissue.

# Plugging the brain drain

exploring brain tumor dynamics  
and effective treatments

Rebeca Uceda Castro



**Plugging the brain drain:  
exploring brain tumor dynamics  
and effective treatments**

Rebeca Uceda Castro

About the cover:

The cover shows a close-up view of a mouse brain with a tumor. The cluster of pink-stained star-shaped cells are astrocytes stained against GFAP. These astrocytes, typically found in the brain, are shown as activated and moving towards the top, indicating the presence of a brain tumor. This dynamic illustration captures the ongoing battle within the brain as astrocytes respond to the cancer cells.

Cover design: Robin Weijland, [persoonlijkproefschrift.nl](http://persoonlijkproefschrift.nl)

Cover concept: Rebeca Uceda Castro

Layout and design: Tara Schollema, [persoonlijkproefschrift.nl](http://persoonlijkproefschrift.nl)

Printing: Ridderprint

©Copyright, Rebeca Uceda Castro, 2024

ISBN: 978-94-6483-946-3

All rights reserved. No part of this book may be produced in any form or by any means without permission of the author.

The research described in this thesis was performed at the Division of Molecular Pathology of the Netherlands Cancer Institute – Antoni van Leeuwenhoek Hospital (NKI-AVL) (Amsterdam, The Netherlands) and was financially supported by the KWF Dutch Cancer Society.

# **Plugging the brain drain: exploring brain tumor dynamics and effective treatments**

Het stoppen van de brain drain: onderzoek naar de dynamiek van hersentumoren en effectieve behandelingen  
(met een samenvatting in het Nederlands)

Detener la fuga de cerebros: explorar la dinámica de los tumores cerebrales y la efectividad de sus tratamientos  
(con un resumen en español)

## **Proefschrift**

ter verkrijging van de graad van doctor aan de  
Universiteit Utrecht  
op gezag van de  
rector magnificus, prof. dr. H.R.B.M. Kummeling,  
ingevolge het besluit van het college voor promoties  
in het openbaar te verdedigen op

maandag 6 mei 2024 des ochtends te 10.15 uur

door

**Rebeca Uceda Castro**

geboren op 4 oktober 1994  
te Madrid, Spanje

**Promotor:**

Prof. Dr. J.E. van Rheenen

**Copromotor:**

Dr. C. Vennin

**Beoordelingscommissie:**

Prof. Dr. M.L.D. Broekman

Prof. Dr. E.M. Hol (voorzitter)

Prof. Dr. J. Jonkers

Prof. Dr. M.M. Maurice

Dr. O. van Tellingen

"I have no special talent. I am only passionately curious."  
Albert Einstein





## TABLE OF CONTENTS

<b>Chapter 1</b>	General introduction and thesis outline.	9
<b>Chapter 2</b>	BCRP drives intrinsic chemoresistance in chemotherapy-naïve breast cancer brain metastasis.	37
<b>Chapter 3</b>	Re-purposing the pro-senescence properties of doxorubicin to introduce immunotherapy in breast cancer brain metastasis.	87
<b>Chapter 4</b>	GFAP splice variants fine-tune glioma cell invasion and tumour dynamics by modulating migration persistence.	141
<b>Chapter 5</b>	Epithelial-to-mesenchymal transition drives invasiveness of breast cancer brain metastases	177
<b>Chapter 6</b>	General Discussion	209
<b>Appendix</b>	Nederlandse samenvatting	231
	English summary	233
	Resumen en español	235
	<i>Curriculum vitae</i>	237
	List of publications	238
	Acknowledgments	240



# Chapter 1

General introduction and thesis outline.



Brain malignancies are categorized into two main types: primary tumors that originate within the brain tissue, such as gliomas, and secondary tumors (metastases) that originate outside the brain and subsequently spread to it [1]. The primary tumors most commonly associated with brain metastases are lung, melanoma, and breast cancers (BCs) [2]. Despite improvements in tumor detection, local treatment, and the introduction of new therapies, including molecular-targeted and immune-based approaches, the prognosis for individuals diagnosed with aggressive tumors in their brain remains poor. The 5-year overall survival rates are extremely low [3], highlighting the urgent need for a deeper understanding of this disease in order to develop effective treatment strategies.

## **PRIMARY BRAIN TUMORS: EXPLORING GLIOMA INVASION AND INTERMEDIATE FILAMENTS**

Gliomas, particularly malignant gliomas such as glioblastoma (GBM), are the most common primary brain tumors in adults [3]. These tumors possess a unique characteristic that sets them apart from other neoplasms: their remarkable ability to invade the surrounding healthy brain tissue. Glioma invasion poses significant challenges for effective treatment and contributes to high rates of tumor recurrence [4]. Understanding the mechanisms underlying glioma invasion is essential for developing targeted therapies and improving patient outcomes.

One aspect of glioma invasion that has gained considerable attention in recent research is the involvement of intermediate filaments (IFs). IFs are a component of the cellular cytoskeleton and play a critical role in maintaining cell structure, stability, and signaling. These filamentous proteins are expressed in various cell types, including astrocytes and neurons, which are the primary cell types involved in gliomas [5, 6].

The IFs present in gliomas, such as glial fibrillary acidic protein (GFAP), vimentin, and nestin, have been implicated in glioma invasion. Changes in the expression and organization of IFs within glioma cells are believed to contribute to their invasive behavior. These alterations may influence cell motility, adhesion, and interactions with the surrounding microenvironment [6].

In the last part of my thesis, I aim to explore the mechanisms of glioma invasion, with a specific focus on the role of IFs hoping to gain a deeper understanding of the invasive nature of gliomas and potentially identify novel targets for therapeutic intervention.

### ***GFAP and GFAP isoforms***

GFAP was classified as a type III IF protein along with vimentin, desmin and peripherin based on homology in sequence [7]. One unique characteristic of GFAP in comparison to other type III IFs is its regulatory mechanism involving alternative splicing of its pre-mRNA

transcript. This alternative splicing process gives rise to multiple isoforms being GFAP $\alpha$  and GFAP $\delta$  the two most highly expressed. These two isoforms differ in their last 41/42 amino-acid of their tail-region (Figure 1).

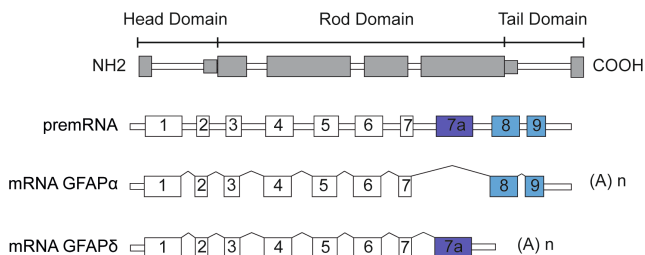


**Figure 1. GFAP isoforms.** White rectangles depict translated regions. The alternative exons for the GFAP tail-region are represented in blue and purple. Abbreviations: (A)<sub>n</sub> = poly-A-tail. Adapted from [6].

### **GFAP expression in glioma**

GFAP-positive cells are observed in tumors across all grades of malignancy, but there is a notable trend of decreasing GFAP levels as the astrocytoma grade increases. GFAP is expressed in astrocytoma cells, showing heterogeneity with two distinct phenotypes: a low malignant, well-differentiated, and noninvasive phenotype, as well as a high malignant, stem-cell-like phenotype characterized by increased invasiveness. GFAP exhibits distinct splicing patterns, and the isoforms GFAP $\alpha$  and GFAP $\delta$  represent the most abundantly expressed and extensively investigated variants. The emergence of the GFAP $\delta$  isoform results from an alternative splicing process involving a 3' polyadenylation occurrence. This process replaces the final two exons, namely exons 8 and 9 of GFAP $\alpha$ , with exon 7a. Consequently, this substitution results in a differing 42-amino acid C-terminal tail [8, 9]. Notably, these two isoforms exhibit contrasting characteristics in terms of their assembly properties [8, 9] and protein interactions [8]. Moreover, they exhibit different expression profiles: GFAP $\alpha$  is primarily prevalent among mature astrocytes, while GFAP $\delta$  in the neurogenic niches within the human brain [10, 11]. Higher levels of GFAP $\delta$  are specifically expressed in neurogenic stem-cell-like cells within the healthy brain [12] and in higher malignant astrocytomas [13]. Moreover, the GFAP $\delta/\alpha$  ratio is increased in grade IV astrocytoma [14]. Cells exhibiting a high GFAP $\delta/\alpha$  ratio are likely to represent the highly malignant, stem-cell-like, and invasive subpopulation within the GFAP cell population. These cells are less abundant in low-grade astrocytomas and may potentially drive the progression towards higher malignancy grades. The observed differences in malignant behavior between cells with high and low GFAP $\delta/\alpha$  ratios provide support for this hypothesis [14, 15]. Therefore, in this thesis I try to unravel the isoform specific function in glioma invasion.

## BREAST CANCER AND BRAIN METASTASES

### *Incidence and epidemiology of breast cancer*

Breast Cancer (BC) is the most common type of cancer worldwide among women and the fifth leading cause of cancer-associated deaths amongst females, with an estimated incidence of 2.3 million (11.7%) new cases and 684,996 (6.9%) deaths in 2020. BC is a very heterogeneous disease. In order to better predict prognosis and make treatment decisions, breast tumors are classified into different intrinsic subtypes based on the results of IHC testing for estrogen (ER), progesterone (PR), epidermal growth factor receptor 2 (HER2), and Ki67 status (Figure 2 A). The luminal A-like subtype is characterized by low grade, strong ER/PgR positivity, negative HER2, and low proliferation. Luminal B-like tumors, on the other hand, are ER-positive and may have lower levels of PR expression, a higher proliferative index, or positive HER2 expression. Other subtypes include HER2-positive with amplification of the HER2 gene and triple negative breast cancer (TNBC) which is characterized by the lack of expression of ER, PR and amplification of HER2 (Figure 2 B) [16-19].

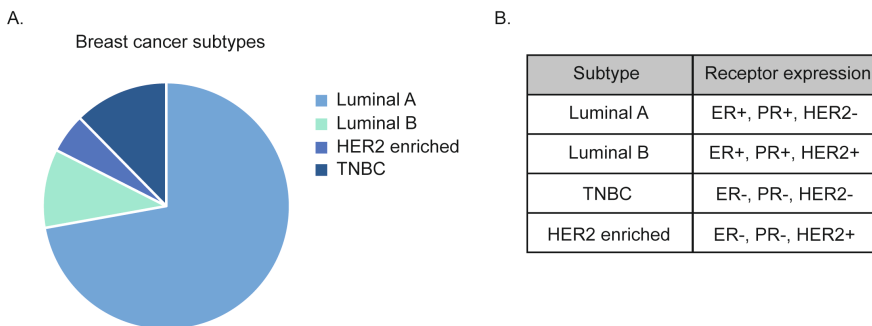


**Figure 2. Breast cancer subtypes.** A. Pie chart of breast cancer subtype distribution. B. Receptor expression in each subtype.

BC is influenced by various factors that can increase the risk of developing the disease. These factors can be categorized into three groups: genetic predisposition, reproductive and hormonal factors, and lifestyle. The reproductive and hormonal risk factors include early start of menstruation, late start of menopause, giving birth at an advanced age, having fewer children, not breastfeeding, and using menopausal hormone therapy or oral contraceptives. Lifestyle factors that can increase the risk of BC include excess body weight, physical inactivity, and alcohol consumption. Genetic predisposition to BC is also a significant risk factor, with certain germ line mutations in high-penetrance genes like BRCA1/2, PALB2, ATM, CHEK2, RAD51C, BARD1, TP53, and others increasing the probability of developing the disease [20].

### **Breast cancer diagnosis and treatment**

The diagnosis of breast cancer typically involves a combination of imaging tests, such as mammography, magnetic resonance imaging (MRI) and ultrasound, as well as a biopsy to confirm the presence of cancer cells and identify the subtype [17, 18, 21, 22].

Breast cancer treatment options depend on the type and stage of the cancer, the patient's age and overall health, and the presence of specific genetic mutations. Surgery is the most common treatment and involves removing the tumor from the breast, with a mastectomy being necessary in some cases. Radiation therapy kills any remaining cancer cells after surgery and alleviates symptoms of advanced breast cancer. Chemotherapy is used to kill cancer cells throughout the body and may be used in combination with surgery or radiation. Targeted therapy, which targets specific proteins on the surface of cancer cells, is used to treat specific types of breast cancer, such as HER2-positive breast cancer. Hormone therapy, which blocks the effects of estrogen or progesterone on cancer cells, is used to treat hormone receptor-positive breast cancer (Figure 3) [20].

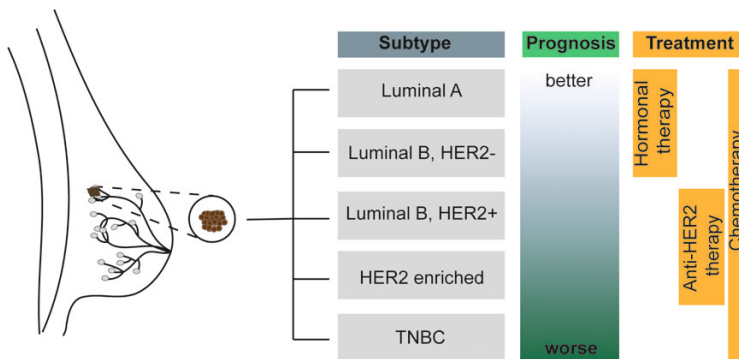


**Figure 3. Prognosis and treatment base on subtype.**

### **Breast Cancer Metastasis**

Metastasis is one of the main causes of cancer-related deaths [23]. When cancer cells spread from the primary tumor to other parts of the body, they can interfere with normal organ function and cause serious health problems. Metastatic cancer is often more difficult to treat than localized cancer because it has spread to other areas and is more likely to have developed resistance to treatment [24].

Breast cancer cell can metastasize to the bones, liver, lungs, or brain. In this thesis I focus on breast cancer brain metastasis (BCBM) that has unfortunately been increasing over the last years [25, 26]. This is due to several factors, including improvements in detection and treatment of breast cancer, which allow patients to live longer with the disease, giving more time for cancer cells to spread to other parts of the body. Additionally, brain metastases are becoming more common because they are being detected more frequently



with advanced imaging techniques. Importantly, patients with brain metastasis from breast cancer experience a 1-year survival rate in only 20% of cases [27].

### ***Brain metastasis***

Brain metastases develop in 10% to 30% of women with metastatic breast cancer [28]. Patients with HER2-positive breast cancer or TNBC have a higher risk of brain metastasis compared with those with the luminal subtype. The frequency of brain metastasis is thus as high as 20% to 30% in HER2-positive breast cancer and TNBC but is < 10% in luminal breast cancer [29].

Local therapeutic approaches such as surgery and radiotherapy have proved effective at the beginning of the disease for metastatic brain tumors, and systemic therapies that control extracranial disease are improving. However, specific therapies that target brain metastases in breast cancer patients have not been established, and the prognosis of such patients therefore remains poor.

Unlike gliomas, brain metastases often disseminate via hematogenous routes and tend to form multiple lesions within the brain parenchyma. The process of metastasis to the brain involves a complex interplay between cancer cells, the blood-brain barrier (BBB), and the unique microenvironment of the brain.

### ***The blood-brain barrier (BBB)***

The BBB is a highly specialized system that separates the blood circulating throughout the body from the central nervous system (CNS) in the brain. The BBB is made up of tightly packed cells that line the blood vessels in the brain and act as a protective barrier, preventing harmful substances from entering the brain while allowing essential nutrients and molecules to pass through (Figure 4) [30-32].

One of the mechanisms by which the BBB maintains its integrity is through the action of ATP-binding cassette (ABC) transporters [33, 34]. ABC transporters are a family of proteins that play a critical role in regulating the movement of molecules across cellular membranes. In the context of the BBB, these transporters work to actively remove potentially harmful substances from the brain, including drugs and toxins [35, 36]. ABC transporters work by using energy from ATP hydrolysis to pump molecules out of the brain and back into the bloodstream. This process, known as efflux, helps to protect the brain by preventing harmful substances from accumulating in the CNS. However, the efflux of drugs from the brain by ABC transporters can also limit the effectiveness of drugs used to treat CNS disorders, such as brain tumors or neurodegenerative diseases [32]. P-glycoprotein (P-gp, *ABCB1*, or *MDR1*) and breast cancer resistance protein (BCRP, *ABCG2*) are two prominent members of the ABC transporter superfamily (Figure 4).

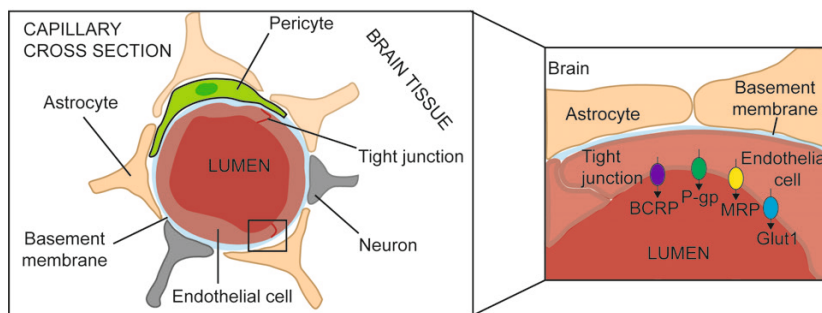


**Figure 4. Schematic representation of the BBB.**

While the significance of P-gp and BCRP in pharmacokinetics is widely accepted, its involvement in drug resistance within human tumors remains a topic of debate. Extensive studies conducted on cellular systems and mice have provided exciting evidence. Consequently, numerous clinical trials were undertaken to evaluate the potential of inhibitors in enhancing the delivery of chemotherapeutic drugs to tumors. Unfortunately, the outcomes of most of these trials were disappointing, as they did not succeed in improving therapeutic efficacy or enhancing patient survival [37].

Therefore, understanding the role of ABC transporters is essential for the development of new therapies for CNS disorders. Further research in this area is likely to yield insights into the mechanisms underlying the efflux of drugs from the brain and inform the development of new strategies to improve drug delivery to the CNS.

### ***The immune system in breast cancer and BCBM***

In the past, BC has been considered an immunologically cold cancer type with little immune cells infiltration [38, 39]. However, in the last years there has been an increase in the literature for studies on the immune effect in breast cancer. The breast cancer immune environment comprises numerous cells and cytokines, each playing distinct roles. While some contribute to suppressing tumor growth, others have protumorigenic effects or exhibit immunosuppressive functions. Chronic inflammation, facilitated by certain cells and cytokines, can additionally facilitate the progression of breast cancer [40].

Natural killer (NK) cells, as part of the innate immune system, actively target and attack the primary tumor. Similarly, cytotoxic T-cells, belonging to the adaptive immune system, also play a crucial role in attacking the primary tumor. However, certain adaptive immune cells like B-cells can exhibit dual roles within the breast tumor immune microenvironment, where they may either promote tumor progression or impede it [41].

The brain, once considered an immune-privileged site, was thought to be less susceptible to immune responses compared to other organs [42]. However, emerging evidence suggests that the immune system does play a role in brain metastasis [43].

Nonetheless, the brain microenvironment poses unique challenges for immune surveillance and response. The BBB restricts the entry of immune cells into the brain [44], limiting their ability to directly engage with metastatic cancer cells. Additionally, the brain microenvironment itself can be immunosuppressive, creating a niche that promotes tumor growth and inhibits effective immune responses [45-49].

Nevertheless, the significant involvement of the immune system throughout the process of brain metastasis formation has generated considerable interest in utilizing immune-based therapies to effectively treat BM.

### ***Treatment BM***

The treatment for BCBM is complex and requires a multidisciplinary approach. There are several treatment options available, including surgery, radiation therapy, chemotherapy, targeted therapy, stereotactic radiosurgery, and supportive care (figure 5). The choice of treatment depends on several factors, such as the size and location of the brain metastasis, the stage of the primary breast cancer, and the patient's overall health [50, 51]. Chemotherapy is a common treatment for BC, but its effectiveness in treating BCBM is limited by the BBB.

The disappointing results can be attributed, in part, to our limited understanding of the brain's structure and that molecular alterations that are specifically present in brain metastatic lesions are not in the primary tumors. Furthermore, because of the lack of proper models, we do not have a clear roadmap to create better therapies for treating brain metastases. The key to developing improved treatments lies in understanding the complexities of these metastases, but without models that mimic the real thing, we are in the dark. Our ability to develop effective strategies is limited when we cannot replicate the actual conditions. This gap in our knowledge highlights how urgently we need reliable models that can help us come up with smarter and more effective treatments for people dealing with brain metastases.

### ***Chemotherapy***

Chemotherapy treatment of BCBM has been proven to have very limited efficacy for several reasons. In contrast to gliomas, breast cancer cells form lesions with relative well-defined boundaries. Only when lesion progress and become large and require rapid neovascularization, the vasculature cannot mature and becomes leaky [52]. Therefore, smaller metastases have an intact BBB that will limit the penetration of the drugs. Different methods are being studied to overcome this challenge, including disruption of the BBB using light, radiation, focused ultrasound and biochemical agents [32]. Moreover, patients with CNS metastasis are usually excluded from clinical trials [53].

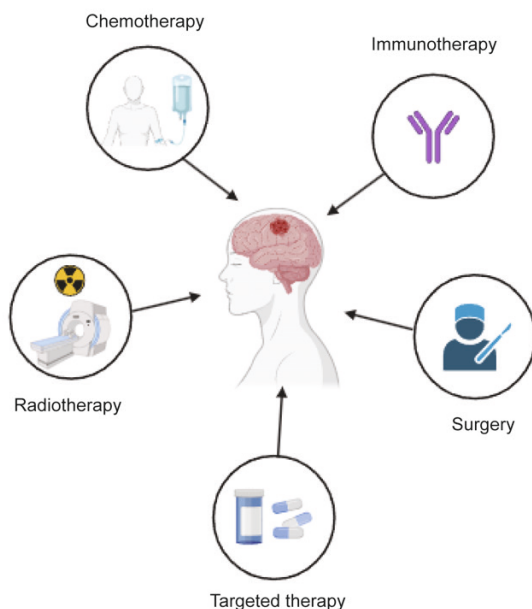


**Figure 5. Treatment options for BCBM include chemotherapy, radiotherapy, immunotherapy, targeted therapy and surgery.**

Furthermore, the presence of heterogeneity between the primary tumor and brain metastases is a significant obstacle to effective treatment. Various aspects of heterogeneity in BC, such as histological subtype, treatment sensitivity, and clinical outcomes, have been extensively studied. However, brain metastases in BC exhibit their own hormone receptor (HR) and HER2 expression statuses, which may not fully align with those of the primary tumor. Moreover, there are molecular subtype discordances and genetic heterogeneity between the primary BC and brain metastases, which can significantly impact treatment options and prognosis [54]. This situation limits the potential effectiveness of targeted therapies that primarily rely on the analysis of the primary tumor.

### ***Immunotherapy***

While traditional treatments, such as surgery, radiation therapy, and chemotherapy, may initially reduce the tumor size, they often have limited efficacy against brain metastases and the tumor will recur. In recent years, a promising new approach to treating BCBM has emerged: immunotherapy.

For a long time, the brain was believed to be an immune-privilege organ that kept circulating cells out of its parenchyma. However, this notion has recently changed. Recent findings have revealed and characterized functional lymphatic vessels within the meninges of the dorsal and basal skull. These structures have the capacity to carry cerebrospinal

fluid (CSF) and immune cells to deep cervical lymph nodes [55]. Additional research has confirmed their crucial role in the regulation of brain tumor immunity [56]. The identification of these brain lymphatic pathways prompted scientists to study the neuroimmunology hypothesis, marking a significant breakthrough in comprehending the mechanisms and creating treatment strategies for brain metastases. While the immune cell within the brain contrast with those found in peripheral organs, the brain is no longer considered as immune privilege organ. This new way of thinking makes it more possible to develop treatments that use the immune system to fight cancer that has spread to the brain.

Unlike traditional treatments such as chemotherapy and radiation, which directly target the tumor, immunotherapy focuses on enhancing the immune system's ability to recognize and kill cancer cells. One significant approach involves immune checkpoint inhibitors (ICIs), which are drugs designed to block specific proteins like PD-1, PD-L1, and CTLA-4 that diminish immune responses [57], thus releasing the immune system to effectively target cancer cells. Another notable type is CAR-T cell therapy, where a patient's T-cells are genetically engineered to express receptors (CARs) that enable them to identify and kill cancer cells upon reinfusion into the patient's body [58]. Tumor-infiltrating lymphocytes (TILs) constitute another form, involving the extraction of immune cells from the tumor, their selection and multiplication in a lab, and subsequent reintroduction into the patient to combat the tumor [59]. Last but not least, the development of cancer vaccines is an important breakthrough in treating solid tumors. These vaccines aim to cause both specific cellular immunity and humoral immune response to prevent tumor growth and ultimately eradicate tumor cells. Currently, most cancer vaccines are still in the stage of preclinical and clinical research [60] and although promising results have been observed [61-63], much work remains to be done on identifying neoantigens, developing combination therapy, and optimizing vaccine platforms before cancer vaccines become a powerful tool in fighting cancer through the immune system. These various approaches collectively represent the evolving landscape of immunotherapy, offering new avenues to combat cancer and potentially improve patient outcomes.

Having discussed broadly the different types of in cancer immunotherapy, I would like to now delve into a more detailed exploration of the mechanisms of ICIs and how they influence the immune response. I will focus on the role of PD-1 since it has been later used in chapter 3, however many other molecules such as CTLA4 or TIGIT are being used regularly in the clinic [64-66] or are part of clinical trials [67]. PD-1 also known as CD279, is found on the surface of T cells, NK cells, B lymphocytes, macrophages, dendritic cells (DCs) and monocytes upon activation [68]. Its role is to inhibit T cell activity and prevent excessive immune responses, acting like a "brake" to avoid immune overactivity that could harm healthy cells and tissues [69, 70]. However, cancer cells can exploit the PD-1 pathway by expressing PD-L1, effectively using it to evade immune detection and elimination [71]. PD-L1 binds to PD-1, sending a signal to T cells to suppress their function [72], in addition

to inhibition of tumor-infiltrating CD4+/CD8+ T cells (CD4+/CD8+ TILs) and decrease in cytokines including tumor necrosis factor (TNF), IFN- $\gamma$  and Interleucina-2 (IL-2) [70] thereby allowing the cancer cells to escape the immune system's surveillance.

By administering ICIs that block either PD-1 or PD-L1, or even both, this immune checkpoint pathway is disrupted. The inhibitor prevents the binding of PD-L1 to PD-1, essentially releasing the brake on the immune system. Consequently, the T cells are no longer suppressed, enabling them to recognize and attack cancer cells [73]. This unleashing of the immune response facilitates a more robust and effective assault on the tumor, often leading to significant tumor shrinkage and improved outcomes for cancer patients.

ICIs have demonstrated efficacy in brain metastases in patients with lung cancer [74] and melanoma [75] and represent a promising option for patients with triple-negative BCBM [76], a group with limited systemic therapy options. However, as previously mentioned, BM occurs in an environment with fewer immune cells than in primary BC tissues [77]; therefore, a high TIL content in the BCBM is associated with better outcomes. In chapter 3, we will explore deeper into how altering the brain immune microenvironment in combination with ICs may represent a novel and promising strategy for effectively treating BCBM.

### **Surgery**

Surgery is one of the most successful treatments for brain metastasis and it should be the starting point of treatment when possible. It can help alleviate symptoms, improve quality of life, and even extend survival in some cases. Nonetheless, curative surgery is often difficult to achieve due to the delicate equilibrium between tumor removal and preserving vital brain functions. In conventional surgical approaches, curative resection involves removing as much tumor mass as possible to impede further progression. However, due to the brain's delicate and indispensable functions, complete resection is often unfeasible without jeopardizing essential neural tissues.

One way to improve surgical outcomes is by using advanced imaging techniques, such as functional MRI [78], to precisely locate the tumor and identify any areas of infiltration. This can help the surgeon plan the optimal approach to the tumor and reduce the risk of leaving behind cancer cells. Another approach is to use newer surgical techniques, such as fluorescence-guided surgery (FGS) [79], that can help identify cancer cells that are difficult to see with the naked eye. In this technique, a fluorescent dye is injected into the bloodstream before surgery, and cancer cells absorb the dye, making them visible under special lighting during surgery. This technique has revolutionized many surgical procedures and has enabled surgeons to remove tumors with greater precision and accuracy. However, there are certain inconveniences associated with FGS, and one of the major ones is the inability to track infiltrative single cells in the brain. In the brain, tumors often infiltrate the surrounding healthy tissue, making it difficult to determine the extent of the disease. In such cases, FGS can be used to highlight the tumor tissue, but it may not be effective in detecting

infiltrative single cells that are not visible to the naked eye. This can make it challenging for surgeons to identify and remove all the tumor tissue, particularly in cases where the tumor is diffuse or has infiltrated the surrounding healthy tissue. Therefore, it is necessary to explore alternative strategies focusing on inhibiting tumor invasion, an approach vital for managing brain tumors effectively.

Consequently, to try to eliminate these infiltrative tumor cells we need to understand what triggers it, how cells transform, and what induces this invasive behavior. Specifically, the transition of cells from an epithelial state to a mesenchymal state is key in enabling invasive tendencies [80-82]. This change means a shift from a cohesive, stationary state to a more mobile, infiltrative one. Remarkably, substantial research has been made to understand invasion within the context of primary tumors, shedding light on the cellular and molecular intricacies. However, when it comes to brain metastases, this aspect of invasion, particularly the role of Epithelial-Mesenchymal Transition (EMT), remains relatively unexplored.

### ***EMT in brain metastases***

The migratory and infiltrative behaviors of BC cells that escape the primary tumor have been thoroughly examined [83-85]. It's widely acknowledged that for these cells to become invasive, they use a developmental process called EMT within the primary tumor [80-82, 86]. This process involves a sequence of events such as the reduction of epithelial markers (e.g., E-cadherin) and increase in mesenchymal markers (e.g., N-cadherin, vimentin) [87, 88]. Moreover, cells undergoing EMT acquire mesenchymal markers like Zeb1 and Twist, promoting stemness and invasiveness [80, 86, 89, 90]. This process was first described during development [91, 92] and later it was also shown that the EMT program is activated during tissue degeneration [93]. Shortly after the important discoveries regarding EMT in developmental and regenerative processes, a hypothesis emerged: cancer cells can hijack EMT programming to facilitate invasion into the adjacent tissue and dissemination from the primary tumor, ultimately forming distant metastases [94].

Since EMT enhances cellular mobility, it is no surprise that it has been connected to the dissemination of tumor cells. However, its role in cancer progression has been a hot topic over the last two decades, with researchers having differing opinions. Some strongly argue for its key role, establishing a connection between EMT and increased tumor invasiveness and dissemination. They point to the correlation of poor prognosis and increased tumor malignancy in tumors with lost or decreased expression of epithelial markers, such as E-cadherin [95, 96], and upregulation of mesenchymal markers such as vimentin (Vim) and Snai1 [97]. On the other hand, some have doubts, especially about whether EMT directly drives the spread of cancer. This skepticism primarily arises from the limitations of certain lineage-tracing experiments, which have failed to identify cells at the metastatic site that have undergone EMT and subsequently MET [98, 99]. Additionally, despite extensive

histopathological studies, convincing evidence of EMT in patient samples has remained elusive [100, 101].

Moreover, it should be noted that while the primary consequence of EMT is increased motility, the phenomenon is also associated with stemness [89, 102], therapy resistance [98, 103, 104], and immune evasion [105, 106]. For example, Slug and Snail expression is associated with radioresistance and chemoresistance by reducing apoptosis while increasing stemness [107]. Furthermore, standard chemotherapy methods used to target cancer, can promote EMT where methods of reversing EMT had presumed benefit [108, 109].

Up to now, research on EMT in BC has primarily focused on cancer cells disseminating from the primary tumor and during the formation of extracranial metastases. However, the presence and functions of EMT in BCBM have yet to be investigated. In chapter 5, we successfully identify mesenchymal cells in brain metastases of human samples. This finding is quite intriguing because the aggressive nature of brain metastases, along with the difficulty in removing a large area around the tumor, might be a potential reason why surgery for BCBM is not successful.

In summary, while surgery is currently one of the most successful treatments for brain metastasis, there is still room for improvement. Newer imaging and surgical techniques, as well as emerging therapies such as immunotherapy, offer hope for improved outcomes for patients with brain metastasis.

## **METHODS TO STUDY BRAIN TUMORS**

As mentioned before, brain tumors present big treatment challenges due to their distinct biological characteristics. These tumors infiltrate the brain, making them difficult to reach surgically. Additionally, they are positioned behind the protective BBB, limiting the effectiveness of systemic chemotherapy. Moreover, the brain's unique developmental, genetic, and microenvironmental characteristics frequently lead to resistance against both conventional and innovative therapies. To study these specific characteristics of tumors in the brain, researchers have developed a variety of methods, including *in vitro* and *in vivo* models. These experimental models provide valuable insights into tumor biology and help to develop therapeutic strategies to enhance patient outcomes.

### ***In vitro***

In the field of brain tumors research, 2D cell line models serve as indispensable tools for exploring various aspects of cancer cell behavior and response. These models enable controlled experiments in a simplified, two-dimensional environment. In 2D adherent cultures, cells grow in a single layer on plastic surfaces, lacking the complexity of natural



tissue or tumor structures. The advantages include the simplicity and cost-effectiveness of maintenance. Another benefit is the rapid cell multiplication, generating a considerable amount of material that can be used for multiple assays, including valuable migration assays like the scratch assay [110] and transwell migration assay [111] or biochemical assays such as western blot, PCR, or DNA or RNA sequencing. Moreover, drug response assays with 2D cell line models allow researchers to evaluate the efficacy and toxicity of potential treatments for tumors, assessing their impact on cell viability, proliferation, and apoptosis.

However, there are also several disadvantages that include altered cell morphology and limited representation of cellular interactions. These interactions play critical roles in cell differentiation, proliferation, gene and protein expression, drug metabolism, and other cellular functions [112]. Furthermore, adherently growing cells lose their polarity due to disruptions in interactions with the external environment [113], altering their response to various phenomena, including apoptosis [114]. Additionally, cells in the monolayer of 2D cultures have unrestricted access to oxygen, nutrients, metabolites, and signaling molecules. This contrasts with the changing availability of these components experienced by cancer cells in a living organism due to the natural structure of tumors [112].

In recent years, a particularly noteworthy breakthrough has been the arrival of organoids, a self-organizing cluster of cells that resembles the organ or tumor of origin. Unlike 2D cell cultures, organoids recapitulate the brain or tumor not only at the cellular level, but also in terms of general tissue structure. However, tumor organoids present both advantages and disadvantages. On the positive side, tumor organoids offer a more reliable representation of the original tumor's complexity, capturing its heterogeneity in terms of cell types and genetic traits. This 3D model closely mimics the actual tumor environment, allowing for a more accurate simulation of cell-cell interactions, nutrient gradients, and drug penetration. Consequently, these organoids have proven to be valuable in predicting responses to drugs, enabling a personalized approach to cancer treatment. Additionally, they provide a useful platform for disease modeling, helping in understanding early tumorigenesis and the impact of mutations on tumor behavior. Moreover, their utilization contributes to reducing reliance on animal models in preclinical studies, addressing ethical concerns and costs associated with animal research. On the negative side, establishing and maintaining tumor organoids can be resource-intensive and time-consuming. The absence of a functional vascular system within organoids restricts their growth and viability beyond a certain point, leading to the development of necrotic regions. Also, tumor organoids often lack an immune system component, missing critical interactions between tumors and the immune system, a vital aspect of cancer progression and treatment.

In conclusion, despite challenges, tumor organoids present significant promise in advancing cancer research, offering a deeper understanding of tumor biology, drug responses, and personalized treatment strategies.

***In vivo***

While *in vitro* systems are indispensable for initial screening, drug testing, and mechanistic studies, *in vivo* mouse models bridge the gap between bench research and clinical application. They allow to study the interaction between tumor cells and the immune system, essential for understanding cancer progression and treatment. Beyond this, they can be used to investigate drug pharmacokinetics and tumor vascularization.

In an ideal scenario, an experimental model of brain metastasis would require cancer cells to undergo all steps of the metastatic cascade, either from orthotopically injected tumor cells, such as the mammary fat pad for breast cancer or subdermal for melanoma. Alternatively, utilizing genetically engineered mouse models, where tumors spontaneously develop after manipulating oncogenes or tumor suppressors, is another effective approach. Unfortunately, only a small number of cancer cell lines spontaneously generate intracranial lesions following orthotopic injection [115-119]. Similar to brain metastasis in patients, their occurrence is rather late in the course of disease. Often, surgical removal of the primary tumor is necessary in mice to prevent them from reaching a humane endpoint prematurely due to advanced extracranial disease [115, 117].

Due to the notably low incidence of spontaneous tumor formation in the brain, and usually these models are in immunodeficient mice [115], innovative strategies have emerged to address this limitation. One commonly used approach to enhance brain tropism requires the careful selection of cell lines that exhibit an exceptional propensity for metastasizing to the CNS through *in vivo* techniques. Brain tropism refers to the specific tendency of these selected cells to target and migrate towards the brain. This affinity for the brain indicates these cells' capability to effectively infiltrate and colonize brain tissue, potentially leading to the development of secondary brain tumors. This approach has been described in [120-122] and usually requires additional rounds of enrichment and typically with some *in vitro* growth in between. Additionally, the inherent aggressiveness of the cell lines, arising from the selection process outlined earlier, further complicates matters, leaving a very small window to study the response to treatment. In response to these challenges, we have developed alternative models centered around the transplantation of organoids.

Regarding the different mouse models, xenograft models involve the transplantation of human tumor cells or tissues into immunocompromised animals. These models provide key advantages such as a nice recapitulation of human tumor behavior and evaluation of response to therapies. However, their lack of immune system limits their applicability in immunotherapy. On the other hand, syngeneic models allow to study of the interaction between tumor cells and the immune system and consequently to study the potential benefit of the use of immunotherapy to treat BM. While these existing models have contributed significantly to our understanding of brain tumors, they possess inherent limitations that restrict their ability to fully recapitulate the complexity and dynamics of the disease.

Therefore, there is a need for novel approaches that can bridge these gaps and provide more accurate representations of brain tumor biology.

When considering the different routes of BM cell inoculations, we can differentiate three types of inoculation (Figure 6): local (intracranial), systemic (intracardiac/intracarotid), and orthotopic (mammary fat pad). (A) Intracranial transplantation involves the injection of tumor cells or tissues directly into the brain. This method allows to study the interactions between tumor cells and surrounding normal brain tissue, as well as the assessment of local tumor progression. However, it may not recapitulate the metastatic cascade. (B) Carotid transplantation involves the injection of tumor cells or tissues into the carotid artery of experimental animals. This method allows for the systemic dissemination of tumor cells, mimicking metastasis. It enables the study of tumor invasion, angiogenesis, and the effects of therapies on metastatic spread. However, it can be technically challenging and requires invasive surgery. Intracardiac transplantation involves the injection of tumor cells directly into the heart. This method allows for the dissemination of tumor cells through the bloodstream and their subsequent colonization in distant organs, including the brain. Similar to carotid transplantation, it allows studying the first steps of metastatic colonization. However, there is a high risk of developing metastasis not only in the brain. (C) Injection of tumor cells in the mammary fat pad replicates the process of tumor colonization and also simulate the growth of the primary tumor and a more realistic systemic spread of cancer cells. However, there is a very variable and low rate of incidence of BM and the frequent need for removal of the breast tumor, which otherwise involves reaching humane endpoint before developing BM.

Each transplantation method has its own advantages and disadvantages, and the choice of approach depends on the specific research questions and objectives. Researchers must carefully consider these factors to select the most appropriate transplantation technique for their studies.

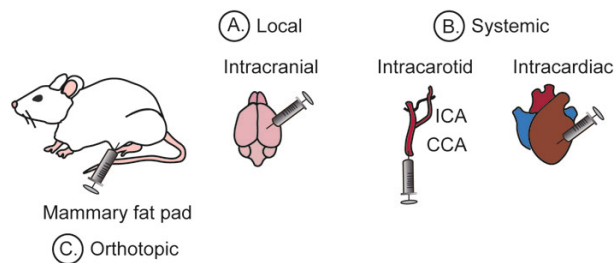


**Figure 6. Injections routes to develop BM models.**

### ***Intravital microscopy (IVM)***

Studying tumors within the brain needs a technique that not only provides high-resolution imaging but also captures the dynamic processes occurring within the tumor microenvironment. While histology and electron microscopy offer high-resolution and subcellular detail, they are limited to static snapshots and lack the ability to observe ongoing dynamic events within living tissues. IVM, on the other hand, specializes in studying real-time cellular behaviors, such as cell migration and interactions, essential for understanding tumor progression and response to treatments. This is very important for longitudinal phenomena like EMT that cannot be track in one-time histological experiments.

Most *in vivo* imaging methods, such as MRI, positron emission tomography–computed tomography (PET-CT), or ultrasound imaging, can only reach organ-scale resolution [123]. Two-photon fluorescence microscopy has become the gold standard for intravital imaging because of its multiple benefits over confocal fluorescence microscopy. It combines long-wavelength multi-photon fluorescence excitation with laser-scanning microscopy, facilitating high-resolution imaging at the single-cell level and deep within live tissues. This technique minimizes photo-bleaching and photo-damage while capturing detailed images. Additionally, the infrared light induces second harmonic generation (SHG) in collagen fibers and third harmonic generation (THG) at water-lipid and water-protein interfaces, enabling label-free detection of additional cell types and ECM components in tissues [124].

Surgical access to tissues is a standard procedure for IVM of internal organs. However, these terminal surgeries restrict imaging sessions to a single period lasting 6 to 24 hours, even with meticulous monitoring of animal vitals. In order to facilitate repetitive IVM in the brain, implantable imaging windows designed for extended imaging sessions suitable several weeks were innovated [125]. Implantation of a cranial imaging window involves performing a craniotomy on the parietal bone, removing the meninges to expose the brain cortex, and gluing a glass window along with an adaptor ring onto the microscope stage. These techniques now allow for extended observation of various stages of metastatic progression, cellular invasion, and alterations in the brain's tumor microenvironment (TME) [126-129].

However, even as IVM is a great tool to study tumors, it has some limitations. The invasive nature of the technique itself due to the necessity of surgeries to expose the organs or implantation of imaging windows, might have the potential to perturb the very biological processes it aims to elucidate. Furthermore, the scope of imaging depth remains confined, restricting observations primarily to superficial regions. Finally, the technique requires well trained surgeons and researchers with high knowledge in microscopy.

In summary, IVM provides a direct view into the dynamics of living tissues, offering valuable insights into the complicated landscape of brain tumors and helping in the understanding of the disease complexities, ultimately guiding the discovery of more efficacious treatments. In chapters 4 and 5 we make use of this powerful technique to dissect the role of GFAP and EMT in tumor in the brain.

## THESIS RATIONALE AND OUTLINE

The introduction illustrates the ongoing challenge in effectively treating tumors in the brain, emphasizing the need for comprehensive study, and improved therapeutic strategies. In this thesis I particularly focus on improving the treatments for BCBM. Additionally, the introduction discusses the limitations of current treatment options for brain metastasis and the development of resistance to therapies. It highlights the urgent need for innovative treatment approaches to improve patient outcomes.

The role of animal models to study brain metastasis is also addressed in the introduction. Animal models provide a valuable tool for understanding the underlying mechanisms of tumor growth, invasion, and response to treatments. They allow researchers to test new therapeutic strategies and evaluate their efficacy before clinical trials.

Together in this thesis, I aim to gain knowledge in the critical aspects of brain tumors, including primary brain tumors (such as GBM), and brain metastases. These aspects include cell migration and invasion, treatment resistance, and potential new clinical strategies.

In **Chapter 2**, we use the mouse BCBM models developed in our lab to study the mechanism of chemoresistance. We show how tumor cells can overexpress the breast cancer resistance protein (BCRP) to adapt to a new environment and consequently, they become resistant to therapy.

In **Chapter 3**, we propose a novel combination of treatments for the effective management of brain metastases through immune checkpoint inhibition. To modulate the brain microenvironment, we use doxorubicin treatments to induce senescence. The induction of tumor senescence leads to the recruitment of cytotoxic T cells that express PD1. Following the doxorubicin treatment, we apply immune checkpoint blockade, which results in a significant increase in the survival of mice. Our findings shed light on the potential of implementing immune checkpoint inhibitors specifically for brain metastases, providing valuable insights for the development of improved therapeutic strategies.

In **Chapter 4**, we demonstrate the importance of GFAP-isoforms in fine-tuning glioma invasion and tumor dynamics using intravital microscopy. Increasing the understanding of the mechanisms driving the invasive behaviors of different GFAP-positive populations that form glioma tumors will play an important role in developing more effective therapies to combat invasion.

In **Chapter 5**, we investigate the behavior of brain metastases in the absence of treatment using intravital microscopy. Our findings demonstrate that the process of epithelial-to-mesenchymal transition (EMT) plays a crucial role in driving the local invasion of brain metastases. By targeting the migration of these mesenchymal tumor cells through the knockdown of ARPC3, we observe a significant decrease in the likelihood of tumor recurrence in mice. Furthermore, our experiments reveal that these mesenchymal tumor cells exhibit plasticity and possess the ability to form new metastatic lesions when re-

injected into the brains of mice. Additionally, we analyze a small cohort of resected human breast cancer brain metastases to validate the relevance of our findings in a clinical context.

In **Chapter 6**, I provide a general discussion where I place my results in the context of the current literature.

## REFERENCE

1. Azzarelli, R., B.D. Simons, and A. Philpott, *The developmental origin of brain tumours: a cellular and molecular framework*. Development, 2018. 145(10).
2. Steindl, A., et al., *Changing characteristics, treatment approaches and survival of patients with brain metastasis: data from six thousand and thirty-one individuals over an observation period of 30 years*. Eur J Cancer, 2022. 162: p. 170-181.
3. Ostrom, Q.T., et al., *The epidemiology of glioma in adults: a "state of the science" review*. Neuro Oncol, 2014. 16(7): p. 896-913.
4. Vollmann-Zwerenz, A., et al., *Tumor Cell Invasion in Glioblastoma*. Int J Mol Sci, 2020. 21(6).
5. Hol, E.M. and M. Pekny, *Glial fibrillary acidic protein (GFAP) and the astrocyte intermediate filament system in diseases of the central nervous system*. Curr Opin Cell Biol, 2015. 32: p. 121-30.
6. van Asperen, J.V., P. Robe, and E.M. Hol, *GFAP Alternative Splicing and the Relevance for Disease - A Focus on Diffuse Gliomas*. ASN Neuro, 2022. 14: p. 17590914221102065.
7. Hol, E.M. and Y. Capetanaki, *Type III Intermediate Filaments Desmin, Glial Fibrillary Acidic Protein (GFAP), Vimentin, and Peripherin*. Cold Spring Harb Perspect Biol, 2017. 9(12).
8. Nielsen, A.L., et al., *A new splice variant of glial fibrillary acidic protein, GFAP epsilon, interacts with the presenilin proteins*. J Biol Chem, 2002. 277(33): p. 29983-91.
9. Blechingberg, J., et al., *Regulatory mechanisms for 3'-end alternative splicing and polyadenylation of the Glial Fibrillary Acidic Protein, GFAP, transcript*. Nucleic Acids Res, 2007. 35(22): p. 7636-50.
10. van den Berge, S.A., et al., *Longterm quiescent cells in the aged human subventricular neurogenic system specifically express GFAP-delta*. Aging Cell, 2010. 9(3): p. 313-26.
11. Roelofs, R.F., et al., *Adult human subventricular, subgranular, and subpial zones contain astrocytes with a specialized intermediate filament cytoskeleton*. Glia, 2005. 52(4): p. 289-300.
12. Middeldorp, J. and E.M. Hol, *GFAP in health and disease*. Prog Neurobiol, 2011. 93(3): p. 421-43.
13. Brehar, F.M., et al., *Immunohistochemical analysis of GFAP-delta and nestin in cerebral astrocytomas*. Brain Tumor Pathol, 2015. 32(2): p. 90-8.
14. Stassen, O., et al., *GFAPdelta/GFAPalpha ratio directs astrocytoma gene expression towards a more malignant profile*. Oncotarget, 2017. 8(50): p. 88104-88121.
15. Moeton, M., et al., *Silencing GFAP isoforms in astrocytoma cells disturbs laminin-dependent motility and cell adhesion*. FASEB J, 2014. 28(7): p. 2942-54.
16. Nolan, E., G.J. Lindeman, and J.E. Visvader, *Deciphering breast cancer: from biology to the clinic*. Cell, 2023. 186(8): p. 1708-1728.
17. Perou, C.M., et al., *Molecular portraits of human breast tumours*. Nature, 2000. 406(6797): p. 747-52.
18. Cancer Genome Atlas, N., *Comprehensive molecular portraits of human breast tumours*. Nature, 2012. 490(7418): p. 61-70.
19. Dai, X., et al., *Breast cancer intrinsic subtype classification, clinical use and future trends*. Am J Cancer Res, 2015. 5(10): p. 2929-43.
20. Hong, R. and B. Xu, *Breast cancer: an up-to-date review and future perspectives*. Cancer Commun (Lond), 2022. 42(10): p. 913-936.
21. Oeffinger, K.C., et al., *Breast Cancer Screening for Women at Average Risk: 2015 Guideline Update From the American Cancer Society*. JAMA, 2015. 314(15): p. 1599-614.
22. Coleman, C., *Early Detection and Screening for Breast Cancer*. Semin Oncol Nurs, 2017. 33(2): p. 141-155.
23. Fares, J., et al., *Molecular principles of metastasis: a hallmark of cancer revisited*. Signal Transduct Target Ther, 2020. 5(1): p. 28.
24. Ganesh, K. and J. Massague, *Targeting metastatic cancer*. Nat Med, 2021. 27(1): p. 34-44.

25. Kim, M.Y., *Breast Cancer Metastasis*. Adv Exp Med Biol, 2021. 1187: p. 183-204.
26. Weigelt, B., J.L. Peterse, and L.J. van 't Veer, *Breast cancer metastasis: markers and models*. Nat Rev Cancer, 2005. 5(8): p. 591-602.
27. Farahani, M.K., et al., *Breast cancer brain metastasis: from etiology to state-of-the-art modeling*. J Biol Eng, 2023. 17(1): p. 41.
28. Lin, N.U., J.R. Bellon, and E.P. Winer, *CNS metastases in breast cancer*. J Clin Oncol, 2004. 22(17): p. 3608-17.
29. Kennecke, H., et al., *Metastatic behavior of breast cancer subtypes*. J Clin Oncol, 2010. 28(20): p. 3271-7.
30. Daneman, R. and A. Prat, *The blood-brain barrier*. Cold Spring Harb Perspect Biol, 2015. 7(1): p. a020412.
31. Abbott, N.J., et al., *Structure and function of the blood-brain barrier*. Neurobiol Dis, 2010. 37(1): p. 13-25.
32. Wu, D., et al., *The blood-brain barrier: structure, regulation, and drug delivery*. Signal Transduct Target Ther, 2023. 8(1): p. 217.
33. Durmus, S., J.J. Hendriks, and A.H. Schinkel, *Apical ABC transporters and cancer chemotherapeutic drug disposition*. Adv Cancer Res, 2015. 125: p. 1-41.
34. Dean, M., Y. Hamon, and G. Chimini, *The human ATP-binding cassette (ABC) transporter superfamily*. J Lipid Res, 2001. 42(7): p. 1007-17.
35. Eichler, A.F., et al., *The biology of brain metastases-translation to new therapies*. Nat Rev Clin Oncol, 2011. 8(6): p. 344-56.
36. Saraiva, C., et al., *Nanoparticle-mediated brain drug delivery: Overcoming blood-brain barrier to treat neurodegenerative diseases*. J Control Release, 2016. 235: p. 34-47.
37. Tamaki, A., et al., *The controversial role of ABC transporters in clinical oncology*. Essays Biochem, 2011. 50(1): p. 209-32.
38. Gatti-Mays, M.E., et al., *If we build it they will come: targeting the immune response to breast cancer*. NPJ Breast Cancer, 2019. 5: p. 37.
39. Standish, L.J., et al., *Breast cancer and the immune system*. J Soc Integr Oncol, 2008. 6(4): p. 158-68.
40. Bunt, S.K., et al., *Inflammation induces myeloid-derived suppressor cells that facilitate tumor progression*. J Immunol, 2006. 176(1): p. 284-90.
41. Amens, J.N., G. Bahcecioglu, and P. Zorlutuna, *Immune System Effects on Breast Cancer*. Cell Mol Bioeng, 2021. 14(4): p. 279-292.
42. Louveau, A., T.H. Harris, and J. Kipnis, *Revisiting the Mechanisms of CNS Immune Privilege*. Trends Immunol, 2015. 36(10): p. 569-577.
43. Leibold, A.T., G.N. Monaco, and M. Dey, *The role of the immune system in brain metastasis*. Curr Neurobiol, 2019. 10(2): p. 33-48.
44. Rössler, K., et al., *Expression of leucocyte adhesion molecules at the human blood-brain barrier (BBB)*. J Neurosci Res, 1992. 31(2): p. 365-74.
45. Zhang, X., et al., *The immunosuppressive microenvironment and immunotherapy in human glioblastoma*. Front Immunol, 2022. 13: p. 1003651.
46. Xing, F., et al., *Reactive astrocytes promote the metastatic growth of breast cancer stem-like cells by activating Notch signalling in brain*. EMBO Mol Med, 2013. 5(3): p. 384-96.
47. Amit, M., et al., *Characterization of the melanoma brain metastatic niche in mice and humans*. Cancer Med, 2013. 2(2): p. 155-63.
48. Winkler, F., *The brain metastatic niche*. J Mol Med (Berl), 2015. 93(11): p. 1213-20.
49. Chen, Q., et al., *Carcinoma-astrocyte gap junctions promote brain metastasis by cGAMP transfer*. Nature, 2016. 533(7604): p. 493-498.
50. Kaleem, M., et al., *An Insight into Molecular Targets of Breast Cancer Brain Metastasis*. Int J Mol Sci, 2022. 23(19).
51. Bailleux, C., L. Eberst, and T. Bachelot, *Treatment strategies for breast cancer brain metastases*. Br J Cancer, 2021. 124(1): p. 142-155.
52. Fidler, I.J., et al., *The seed and soil hypothesis: vascularisation and brain metastases*. Lancet Oncol, 2002. 3(1): p. 53-7.
53. Patel, R.R., et al., *Exclusion of patients with brain metastases from cancer clinical trials*. Neuro Oncol, 2020. 22(4): p. 577-579.



54. Sperduto, P.W., et al., *Estrogen/progesterone receptor and HER2 discordance between primary tumor and brain metastases in breast cancer and its effect on treatment and survival*. *Neuro Oncol*, 2020. 22(9): p. 1359-1367.
55. Graham, M.S. and I.K. Mellingshoff, *Meningeal lymphatics prime tumor immunity in glioblastoma*. *Cancer Cell*, 2021. 39(3): p. 304-306.
56. Hu, X., et al., *Meningeal lymphatic vessels regulate brain tumor drainage and immunity*. *Cell Res*, 2020. 30(3): p. 229-243.
57. Alsaab, H.O., et al., *PD-1 and PD-L1 Checkpoint Signaling Inhibition for Cancer Immunotherapy: Mechanism, Combinations, and Clinical Outcome*. *Front Pharmacol*, 2017. 8: p. 561.
58. Sterner, R.C. and R.M. Sterner, *CAR-T cell therapy: current limitations and potential strategies*. *Blood Cancer J*, 2021. 11(4): p. 69.
59. Zhao, Y., et al., *Tumor Infiltrating Lymphocyte (TIL) Therapy for Solid Tumor Treatment: Progressions and Challenges*. *Cancers (Basel)*, 2022. 14(17).
60. Saxena, M., et al., *Therapeutic cancer vaccines*. *Nat Rev Cancer*, 2021. 21(6): p. 360-378.
61. Hammerich, L., et al., *Systemic clinical tumor regressions and potentiation of PD1 blockade with in situ vaccination*. *Nat Med*, 2019. 25(5): p. 814-824.
62. Brody, J.D., et al., *In situ vaccination with a TLR9 agonist induces systemic lymphoma regression: a phase I/II study*. *J Clin Oncol*, 2010. 28(28): p. 4324-32.
63. Kantoff, P.W., et al., *Sipuleucel-T immunotherapy for castration-resistant prostate cancer*. *N Engl J Med*, 2010. 363(5): p. 411-22.
64. Lipson, E.J. and C.G. Drake, *Ipilimumab: an anti-CTLA-4 antibody for metastatic melanoma*. *Clin Cancer Res*, 2011. 17(22): p. 6958-62.
65. Sondak, V.K., et al., *Ipilimumab*. *Nat Rev Drug Discov*, 2011. 10(6): p. 411-2.
66. Barbee, M.S., et al., *Current status and future directions of the immune checkpoint inhibitors ipilimumab, pembrolizumab, and nivolumab in oncology*. *Ann Pharmacother*, 2015. 49(8): p. 907-37.
67. Chu, X., et al., *Co-inhibition of TIGIT and PD-1/PD-L1 in Cancer Immunotherapy: Mechanisms and Clinical Trials*. *Mol Cancer*, 2023. 22(1): p. 93.
68. Ahmadzadeh, M., et al., *Tumor antigen-specific CD8 T cells infiltrating the tumor express high levels of PD-1 and are functionally impaired*. *Blood*, 2009. 114(8): p. 1537-44.
69. Han, Y., D. Liu, and L. Li, *PD-1/PD-L1 pathway: current researches in cancer*. *Am J Cancer Res*, 2020. 10(3): p. 727-742.
70. Francisco, L.M., P.T. Sage, and A.H. Sharpe, *The PD-1 pathway in tolerance and autoimmunity*. *Immunol Rev*, 2010. 236: p. 219-42.
71. Dong, P., et al., *Tumor-Intrinsic PD-L1 Signaling in Cancer Initiation, Development and Treatment: Beyond Immune Evasion*. *Front Oncol*, 2018. 8: p. 386.
72. Butte, M.J., et al., *Programmed death-1 ligand 1 interacts specifically with the B7-1 costimulatory molecule to inhibit T cell responses*. *Immunity*, 2007. 27(1): p. 111-22.
73. Kuzume, A., et al., *Immune-Checkpoint Blockade Therapy in Lymphoma*. *Int J Mol Sci*, 2020. 21(15).
74. Goldberg, S.B., et al., *Pembrolizumab for management of patients with NSCLC and brain metastases: long-term results and biomarker analysis from a non-randomised, open-label, phase 2 trial*. *Lancet Oncol*, 2020. 21(5): p. 655-663.
75. Tawbi, H.A., et al., *Combined Nivolumab and Ipilimumab in Melanoma Metastatic to the Brain*. *N Engl J Med*, 2018. 379(8): p. 722-730.
76. Schmid, P., et al., *Atezolizumab and Nab-Paclitaxel in Advanced Triple-Negative Breast Cancer*. *N Engl J Med*, 2018. 379(22): p. 2108-2121.
77. Ogiya, R., et al., *Comparison of immune microenvironments between primary tumors and brain metastases in patients with breast cancer*. *Oncotarget*, 2017. 8(61): p. 103671-103681.

78. Castellano, A., et al., *Advanced Imaging Techniques for Radiotherapy Planning of Gliomas*. Cancers (Basel), 2021. 13(5).
79. Mieog, J.S.D., et al., *Fundamentals and developments in fluorescence-guided cancer surgery*. Nat Rev Clin Oncol, 2022. 19(1): p. 9-22.
80. Bornes, L., G. Belthier, and J. van Rheenen, *Epithelial-to-Mesenchymal Transition in the Light of Plasticity and Hybrid E/M States*. J Clin Med, 2021. 10(11).
81. Luond, F., S. Tiede, and G. Christofori, *Breast cancer as an example of tumour heterogeneity and tumour cell plasticity during malignant progression*. Br J Cancer, 2021. 125(2): p. 164-175.
82. Bhatia, S., et al., *New Insights Into the Role of Phenotypic Plasticity and EMT in Driving Cancer Progression*. Front Mol Biosci, 2020. 7: p. 71.
83. van Rheenen, J. and C. Scheele, *Intravital microscopy to illuminate cell state plasticity during metastasis*. Curr Opin Cell Biol, 2021. 72: p. 28-35.
84. Margarido, A.S., et al., *Cellular Plasticity during Metastasis: New Insights Provided by Intravital Microscopy*. Cold Spring Harb Perspect Med, 2020. 10(11).
85. Condeelis, J. and J.E. Segall, *Intravital imaging of cell movement in tumours*. Nat Rev Cancer, 2003. 3(12): p. 921-30.
86. Dongre, A. and R.A. Weinberg, *New insights into the mechanisms of epithelial-mesenchymal transition and implications for cancer*. Nat Rev Mol Cell Biol, 2019. 20(2): p. 69-84.
87. Beerling, E., et al., *Plasticity between Epithelial and Mesenchymal States Unlinks EMT from Metastasis-Enhancing Stem Cell Capacity*. Cell Rep, 2016. 14(10): p. 2281-8.
88. Kalluri, R. and R.A. Weinberg, *The basics of epithelial-mesenchymal transition*. J Clin Invest, 2009. 119(6): p. 1420-8.
89. Mani, S.A., et al., *The epithelial-mesenchymal transition generates cells with properties of stem cells*. Cell, 2008. 133(4): p. 704-15.
90. Cano, A., et al., *The transcription factor snail controls epithelial-mesenchymal transitions by repressing E-cadherin expression*. Nat Cell Biol, 2000. 2(2): p. 76-83.
91. Nieto, M.A., et al., *Control of cell behavior during vertebrate development by Slug, a zinc finger gene*. Science, 1994. 264(5160): p. 835-9.
92. Newgreen, D.F. and J. Minichiello, *Control of epitheliomesenchymal transformation. I. Events in the onset of neural crest cell migration are separable and inducible by protein kinase inhibitors*. Dev Biol, 1995. 170(1): p. 91-101.
93. Thiery, J.P., et al., *Epithelial-mesenchymal transitions in development and disease*. Cell, 2009. 139(5): p. 871-90.
94. Thompson, E.W., D.F. Newgreen, and D. Tarin, *Carcinoma invasion and metastasis: a role for epithelial-mesenchymal transition?* Cancer Res, 2005. 65(14): p. 5991-5; discussion 5995.
95. Berx, G., et al., *E-cadherin is a tumour/invasion suppressor gene mutated in human lobular breast cancers*. EMBO J, 1995. 14(24): p. 6107-15.
96. Guilford, P., et al., *E-cadherin germline mutations in familial gastric cancer*. Nature, 1998. 392(6674): p. 402-5.
97. Sato, M., D.S. Shames, and Y. Hasegawa, *Emerging evidence of epithelial-to-mesenchymal transition in lung carcinogenesis*. Respirology, 2012. 17(7): p. 1048-59.
98. Fischer, K.R., et al., *Epithelial-to-mesenchymal transition is not required for lung metastasis but contributes to chemoresistance*. Nature, 2015. 527(7579): p. 472-6.
99. Zheng, X., et al., *Epithelial-to-mesenchymal transition is dispensable for metastasis but induces chemoresistance in pancreatic cancer*. Nature, 2015. 527(7579): p. 525-530.
100. Bukholm, I.K., J.M. Nesland, and A.L. Borresen-Dale, *Re-expression of E-cadherin, alpha-catenin and beta-catenin, but not of gamma-catenin, in metastatic tissue from breast cancer patients [seecomments]*. J Pathol, 2000. 190(1): p. 15-9.

101. Jeschke, U., et al., *Expression of E-cadherin in human ductal breast cancer carcinoma in situ, invasive carcinomas, their lymph node metastases, their distant metastases, carcinomas with recurrence and in recurrence*. *Anticancer Res*, 2007. 27(4A): p. 1969-74.
102. Kong, D., et al., *Epithelial to mesenchymal transition is mechanically linked with stem cell signatures in prostate cancer cells*. *PLoS One*, 2010. 5(8): p. e12445.
103. Shah, A.N., et al., *Development and characterization of gemcitabine-resistant pancreatic tumor cells*. *Ann Surg Oncol*, 2007. 14(12): p. 3629-37.
104. Yin, T., et al., *Expression of snail in pancreatic cancer promotes metastasis and chemoresistance*. *J Surg Res*, 2007. 141(2): p. 196-203.
105. Yaguchi, T., et al., *The mechanisms of cancer immunoescape and development of overcoming strategies*. *Int J Hematol*, 2011. 93(3): p. 294-300.
106. Dongre, A., et al., *Epithelial-to-Mesenchymal Transition Contributes to Immunosuppression in Breast Carcinomas*. *Cancer Res*, 2017. 77(15): p. 3982-3989.
107. Sahai, E. and C.J. Marshall, *Differing modes of tumour cell invasion have distinct requirements for Rho/ROCK signalling and extracellular proteolysis*. *Nat Cell Biol*, 2003. 5(8): p. 711-9.
108. Cheng, G.Z., et al., *Twist transcriptionally up-regulates AKT2 in breast cancer cells leading to increased migration, invasion, and resistance to paclitaxel*. *Cancer Res*, 2007. 67(5): p. 1979-87.
109. Baritaki, S., et al., *Pivotal roles of snail inhibition and RKIP induction by the proteasome inhibitor NPI-0052 in tumor cell chemosensitization*. *Cancer Res*, 2009. 69(21): p. 8376-85.
110. Kramer, N., et al., *In vitro cell migration and invasion assays*. *Mutat Res*, 2013. 752(1): p. 10-24.
111. Kenney, R.M., et al., *Paper-based Transwell assays: an inexpensive alternative to study cellular invasion*. *Analyst*, 2018. 144(1): p. 206-211.
112. Pampaloni, F., E.G. Reynaud, and E.H. Stelzer, *The third dimension bridges the gap between cell culture and live tissue*. *Nat Rev Mol Cell Biol*, 2007. 8(10): p. 839-45.
113. Mseka, T., J.R. Bamburg, and L.P. Cramer, *ADF/cofilin family proteins control formation of oriented actin-filament bundles in the cell body to trigger fibroblast polarization*. *J Cell Sci*, 2007. 120(Pt 24): p. 4332-44.
114. Weaver, V.M., et al., *beta4 integrin-dependent formation of polarized three-dimensional architecture confers resistance to apoptosis in normal and malignant mammary epithelium*. *Cancer Cell*, 2002. 2(3): p. 205-16.
115. Puchalapalli, M., et al., *NSG Mice Provide a Better Spontaneous Model of Breast Cancer Metastasis than Athymic (Nude) Mice*. *PLoS One*, 2016. 11(9): p. e0163521.
116. Nagpal, A., et al., *Neoadjuvant neratinib promotes ferroptosis and inhibits brain metastasis in a novel syngeneic model of spontaneous HER2(+ve) breast cancer metastasis*. *Breast Cancer Res*, 2019. 21(1): p. 94.
117. Schwartz, H., et al., *Incipient Melanoma Brain Metastases Instigate Astrogliosis and Neuroinflammation*. *Cancer Res*, 2016. 76(15): p. 4359-71.
118. Cho, J.H., et al., *AKT1 Activation Promotes Development of Melanoma Metastases*. *Cell Rep*, 2015. 13(5): p. 898-905.
119. Meuwissen, R., et al., *Induction of small cell lung cancer by somatic inactivation of both Trp53 and Rb1 in a conditional mouse model*. *Cancer Cell*, 2003. 4(3): p. 181-9.
120. Valiente, M., et al., *Brain Metastasis Cell Lines Panel: A Public Resource of Organotropic Cell Lines*. *Cancer Res*, 2020. 80(20): p. 4314-4323.
121. Bos, P.D., et al., *Genes that mediate breast cancer metastasis to the brain*. *Nature*, 2009. 459(7249): p. 1005-9.
122. Nguyen, D.X., et al., *WNT/TCF signaling through LEF1 and HOXB9 mediates lung adenocarcinoma metastasis*. *Cell*, 2009. 138(1): p. 51-62.
123. Wessels, J.T., et al., *In vivo imaging in experimental preclinical tumor research--a review*. *Cytometry A*, 2007. 71(8): p. 542-9.

124. Friedl, P., et al., *Biological second and third harmonic generation microscopy*. Curr Protoc Cell Biol, 2007. Chapter 4: p. Unit 4 15.
125. Alieva, M., et al., *Imaging windows for long-term intravital imaging: General overview and technical insights*. Intravital, 2014. 3(2): p. e29917.
126. Alieva, M., et al., *Preventing inflammation inhibits biopsy-mediated changes in tumor cell behavior*. Sci Rep, 2017. 7(1): p. 7529.
127. Alieva, M., et al., *Intravital imaging of glioma border morphology reveals distinctive cellular dynamics and contribution to tumor cell invasion*. Sci Rep, 2019. 9(1): p. 2054.
128. Margarido, A.S., et al., *Epithelial-to-Mesenchymal Transition Drives Invasiveness of Breast Cancer Brain Metastases*. Cancers (Basel), 2022. 14(13).
129. Kienast, Y., et al., *Real-time imaging reveals the single steps of brain metastasis formation*. Nat Med, 2010. 16(1): p. 116-22.





# Chapter 2

**BCRP drives intrinsic chemoresistance in chemotherapy-naïve breast cancer brain metastasis.**

**Rebeca Uceda-Castro**, Andreia S. Margarido, Ji-Ying Song, Mark C. de Gooijer, Hendrik A. Messal, Cecilia R. Chambers, Max Nobis, Ceren H. Çitirikkaya, Kerstin Hahn, Danielle Seinstra, David Herrmann<sup>5</sup>, Paul Timpson, Pieter Wesseling, Olaf van Tellingen, Claire Vennin<sup>#</sup> and Jacco van Rheenen<sup>#</sup>

<sup>#</sup>Correspondence

Published in *Science Advances* 2023





## **ABSTRACT**

Although initially successful, treatments with chemotherapy often fail due to the recurrence of chemo-resistant metastases. Since these tumors develop after treatment, resistance is generally thought to occur in response to chemotherapy. However, alternative mechanisms of intrinsic chemoresistance in the chemotherapy-naïve setting may exist but remain poorly understood. Here, we study drug-naïve murine breast cancer brain metastases (BCBM), to identify how cancer cells growing in a secondary site can acquire intrinsic chemoresistance without cytotoxic agent exposure. We demonstrate that drug-naïve murine breast cancer cells that form cancer lesions in the brain undergo vascular mimicry and concomitantly express the ABC transporter Breast Cancer Resistance Protein (BCRP), a common marker of brain endothelial cells. Importantly, we reveal that expression of BCRP by the BCBM tumor cells protects them against doxorubicin and topotecan. We conclude that BCRP overexpression can cause intrinsic chemo-resistance in cancer cells growing in metastatic sites without prior chemotherapy exposure.

## INTRODUCTION

While treatment of patients with breast cancer (BC) with chemotherapy is often initially effective, tumors regularly recur locally or systemically in a therapy-resistant form. In particular, breast cancer brain metastases (BCBM) are often chemoresistant, which hinders the successful development of therapies for this lethal disease [1]. The blood brain barrier (BBB) and the blood tumor barrier (BTB) are important contributors to extrinsic chemoresistance in BCBM, since they form highly impermeable fences that block drug delivery and diffusion to the brain [1-4]. The impermeability of the BBB and BTB is caused in part by brain endothelial cells that are closely connected by tight junctions, do not display fenestrations, and often express ATP-binding cassette (ABC) transporters which are responsible for active efflux of compounds [2-5]. In addition to this extrinsic resistance, earlier exposures to drugs for the treatment of previous lesions can render cancer cells intrinsically resistant by triggering the acquisition of mutations and/or epigenetic remodeling [6-8]. For example, in rodent cancer models, exposing cancer cells to cytotoxic agents can induce the upregulation of ABC transporters that export drugs in the extracellular space, thereby rendering tumor cells intrinsically resistant [6-8].

Although both experimental and clinical data demonstrate that tumors can acquire intrinsic resistance upon exposure to chemotherapies [7, 9], potential alternative mechanisms that are not triggered by drug treatment have not been characterized to the same extent. In part, this is because samples from untreated patients are scarce, in particular in BCBM patients, rendering the study of mechanisms driving intrinsic resistance in the drug-naïve setting challenging. To overcome this, we studied drug response in primary breast tumors and BCBM that have not been exposed to chemotherapy.

We reveal that creating BCBM-like tumors using serial transplantations of chemotherapy-naïve breast tumor cells in the brain leads to the acquisition of intrinsic chemoresistance. Mechanistically, we find that chemotherapy-naïve BCBM cells are capable of undergoing vascular mimicry (VM) and simultaneously express the ABC-transporter Breast Cancer Resistance Protein (BCRP), which is commonly expressed in endothelial cells of veins and capillaries in the brain [10]. We show that increased expression of BCRP in chemotherapy-naïve cancer cells renders BCBM cells intrinsically resistant to chemotherapies that are transported by BCRP, which can be reverted by reducing BCRP expression or activity. Together, our study identifies in the murine setting how cancer cells that grow in a foreign soil can acquire resistance to chemotherapeutics that they have never been exposed to.

## RESULTS

### ***Modeling BCBM to study chemoresistance.***

In order to identify potential mechanisms of chemoresistance in drug-naïve brain metastases, we worked with chemotherapy naïve organoids that form brain metastasis-like lesions in the PyMT [11] and the K14Cre, Brca1<sup>fl/fl</sup>, p53<sup>fl/fl</sup> (KB1P) [12] models. Tumor organoids retain critical characteristics of the tumors from which they are derived, including slow growth kinetics, cellular heterogeneity but also low metastatic potential, and therefore faithfully model the human disease [13]. In line with previous approaches to generate models of brain metastasis [14], we first injected PyMT primary organoids intracardially, however mice did not develop brain tumors. We instead performed six rounds of serial intracranial transplantations of organoids isolated from primary mammary tumors derived from the PyMT and the KB1P models [15]. From herein, breast cancer organoids enriched in the brain are referred to as BCBM. Characterization of the PyMT BCBM has previously been shown to mimic key features of the human disease in terms of pathology, immunohistochemical features, Magnetic Resonance Imaging (MRI) and Spectroscopy (MRS) profiles [15, 16]. The KB1P BCBM model shares key features with the PyMT BCBM models, including immunohistochemical and pathological characteristics (**Supplementary Figure 1 A-D**) [15]. Next, we intracranially injected tumor organoids derived from either primary tumors, tumors from the 3<sup>rd</sup> or 4<sup>th</sup> round of enrichment and the final BCBM tumors. When comparing the size of the brain tumors at 3 weeks after intracranial injection, we found that PyMT BCBM organoids had improved *in vivo* growth kinetics compared to organoids derived from primary tumors (**Supplementary Figure 1 E**). This difference in tumor growth correlated with increased proliferation in *in vitro* PyMT BCBM organoids compared to organoids derived from earlier rounds of enrichment (**Supplementary Figure 1 F**). In contrast, in the KB1P model we did not detect significant differences in tumor size between tumors derived from BCBM organoids and primary tumor organoids (**Supplementary Figure 1 G**), and there was also no significant difference in proliferation in *in vitro* organoids derived from the BCBM compared to the primary tumor organoids (**Supplementary Figure 1 H**). Lastly, we performed bulk RNA sequencing of PyMT primary and BCBM organoids, which demonstrated an enrichment in brain-related genes in organoids derived from the BCBM compared to organoids derived from primary donor tumors (**Supplementary Table 1**). These data confirm that transcriptional selection can occur during the rounds of enrichment in the brain and is maintained in *in vitro* BCBM. Moreover, we previously reported that the outgrowth of BCBM organoids from intracranial injection to humane endpoint takes several weeks, which is an adequate time window for therapeutic testing and study of mechanisms of therapy resistance [15]. Collectively, the generated BCBM models recapitulate key features of the human disease and can be used to study events occurring in established BCBM.

### ***The mouse BCBM is exposed to doxorubicin in vivo.***

Assessing BCBM tumor cell response to chemotherapy is challenging, partly due to the impaired penetration of drugs into the brain caused by the BBB and the BTB [17]. Indeed, chemotherapies commonly used to treat breast cancer patients such as carboplatin, are highly hydrophilic and polar and cannot permeate the lipid bilayers of the brain endothelial cells by passive diffusion [18]. Moreover, the distribution and efficacy for less hydrophilic cytotoxic compounds including doxorubicin and topotecan, are limited by the expression in the endothelial cells present in the brain of ABC efflux transporters, such as P-glycoprotein (P-gp) (also referred to as ABCB1) and BCRP.

We next assessed whether the ABC drug transporters expressed by endothelial cells [19-22] indeed have the potential to limit the distribution and efficacy of doxorubicin in the PyMT and KB1P BCBM models, by first comparing BCRP and P-gp expression in the endothelial cells of the primary tumors *versus* the paired BCBMs. While we observed that endothelial cells in both sites express BCRP and P-gp, we did not find significant differences in the expression of those two ABC transporters in the endothelial cells of the BCBM *versus* primary breast cancer tissue in neither the PyMT nor the KB1P BCBM model (**Figure 1 A-D**). To test whether the lack of enhanced expression of ABC transporters in endothelial cells correlates with diffusion of doxorubicin in the BCBM, we used chromatographic analysis to quantify the amount of doxorubicin present in the PyMT BCBM compared to the paired primary tumors. Mice bearing well established mammary PyMT tumors or PyMT BCBM received one treatment with doxorubicin and were sacrificed two hours after treatment. We isolated either the mammary tumor and the healthy gland, or the BCBM and the contralateral brain hemisphere and we measured doxorubicin concentrations in those tissues. In line with clinical data [23], doxorubicin concentration was higher in tumor tissues compared to healthy tissues, both in the mammary gland and in the brain (**Figure 1 E**). Moreover, the doxorubicin concentration is not significantly different in the primary tumor or BCBM (**Figure 1 E**).

Next, we used MRI with gadolinium [24] to confirm the leakiness of the BCBM vasculature in mice bearing PyMT BCBM (**Supplementary Figure 2 A**). In line with the detection of doxorubicin in the BCBM (**Figure 1 E**), we observed a stronger contrast enhancement at the BCBM periphery compared to the BCBM core, which suggests the presence of high interstitial fluid pressure (**Supplementary Figure 2 A**). Moreover, we injected mice bearing BCBM with Texas Red, a fluorescent dye with a molecular weight similar to doxorubicin (625.15 g/mol for Texas Red; 543 g/mol for doxorubicin). Using fluorescence microscopy, we observed Texas Red signal in the BCBM core and around the BCBM, indicating that the tumor vasculature is leaky [25] (**Supplementary Figure 2 B**). Collectively, these data demonstrate that doxorubicin penetrates our BCBM model, which warrants the study of the response to doxorubicin in chemotherapy-naïve BCBM in our model.

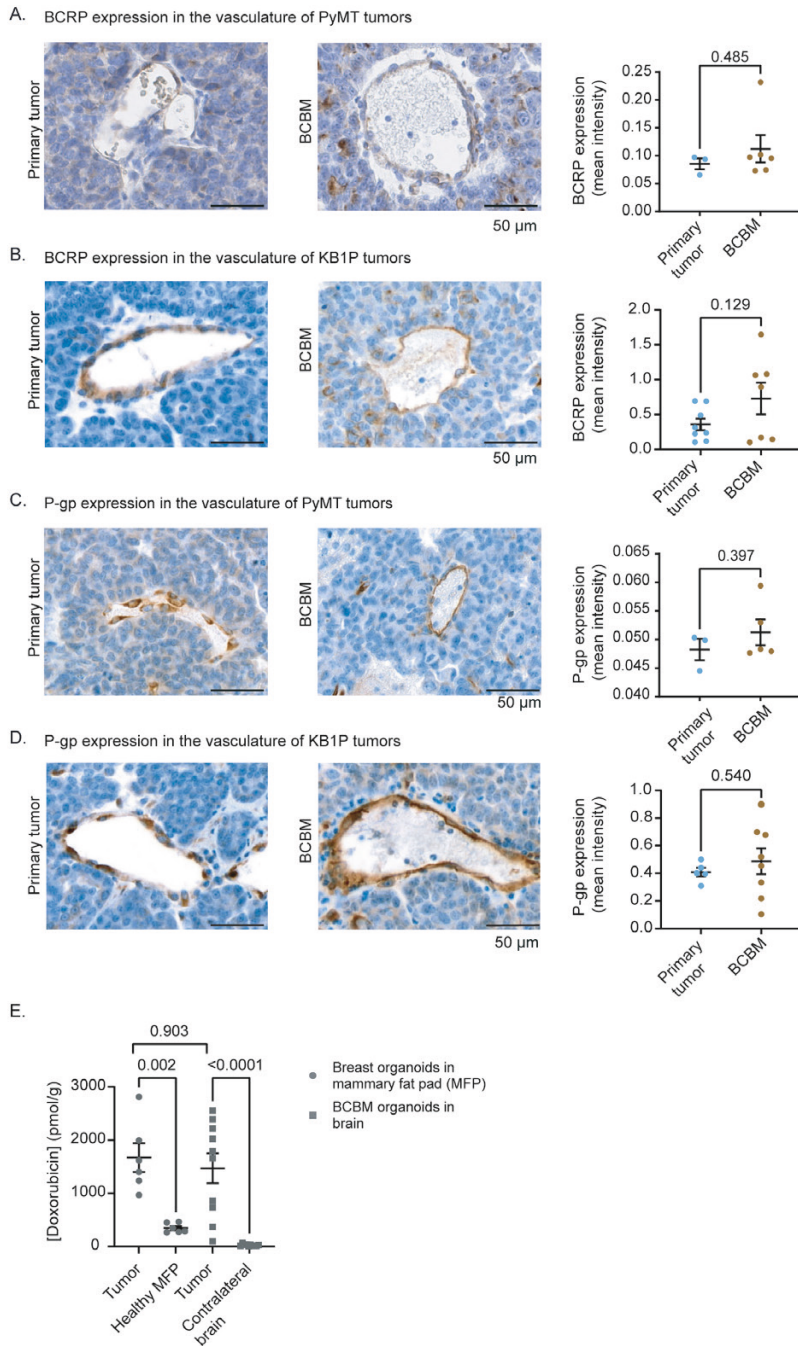


**Figure 1. The BCBM tumor vasculature does not prevent penetration of doxorubicin. A.** Representative images of immunohistochemistry of BCRP and quantification of DAB **optical density (OD)** in the endothelial cells forming the tumor vasculature in the PyMT model, in both primary tumors (n=3 mice) and BCBM (n=6 mice).

**Figure 1. Continued. B.** Representative images of immunohistochemistry of BCRP and quantification of DAB OD in the endothelial cells forming the tumor vasculature in the KB1P model, in both primary tumors (n=8 mice) and BCBM (n=7 mice). **C.** Representative images of immunohistochemistry of P-gp and quantification of DAB OD in the endothelial cells forming the tumor vasculature in the PyMT model, in both primary tumors (n=3 mice) and BCBM (n=5 mice). **D.** Representative images of immunohistochemistry of P-gp and quantification of DAB OD in the endothelial cells forming the tumor vasculature in the KB1P model, in both primary tumors (n=5 mice) and BCBM (n=8 mice). **E.** Doxorubicin concentration in breast tumors derived from PyMT primary organoids growing in the mammary gland compared to the healthy mammary fat pad and in brain tumors derived from PyMT BCBM organoids intracranially injected compared to the healthy contralateral brain hemisphere. Tissues were harvested 2 h after treatment with 5 mg/kg doxorubicin. Data are presented as mean  $\pm$  SEM (for breast tumors n=6 and for brain tumors F n=10).

### ***Breast cancer cells enriched in the brain overexpress BCRP.***

While studying the expression of ABC proteins in the vasculature of the PyMT and KB1P BCBMs, we unexpectedly observed changes in BCRP expression in the tumor cells rather than in the endothelial cells (**Figure 2 A, B**). Strikingly, BCBM cancer cells expressed significantly higher levels of BCRP compared to cancer cells of the paired primary tumors (**Figure 2 A, B**), while the expression of P-gp was not significantly different (**Figure 2 C, D**). Furthermore, the differential expression of BCRP was maintained in organoid cultures, suggesting that the increase in BCRP expression is stably inherited when BCBM cells are taken out of the brain environment (**Figure 2 E, F**). To confirm that the enhanced expression of BCRP is the result of the serial transplantations of breast cancer cells into the brain, we generated an additional PyMT BCBM line using a second breast tumor donor (referred to as PyMT BCBM#2). Similarly to the two other lines, BCRP expression was significantly enhanced in the PyMT BCBM#2 organoids compared to the paired primary tumor organoids (**Figure 2 G**), further demonstrating that BCRP expression is increased in breast cancer cells upon enrichment in the brain.

We next interrogated whether BCRP<sup>+</sup> cancer cells are also present in human BCBMs. We first analyzed BCRP expression in previously published RNA sequencing data obtained from human BCBM and patient-matched primary breast tumors tissues [26]. In Her2<sup>+</sup> patients, a number of ABC transporters were downregulated in BCBM compared to their matched primary tumors, however strikingly BCRP was upregulated in BCBM samples compared to matched primary tumors (**Figure 2 H**). Nonetheless, because the RNA sequencing data were obtained from whole tumor tissues, we cannot determine whether BCRP expression is increased specifically in the tumor cells, in the BTB and stroma of those BCBM samples or both. To further assess this, we performed IHC analysis of BCRP in samples, obtained from surgical resection in BCBM patients. This revealed indeed the presence of a small number of BCRP<sup>+</sup> tumor cells in human BCBMs (**Figure 2 I**).

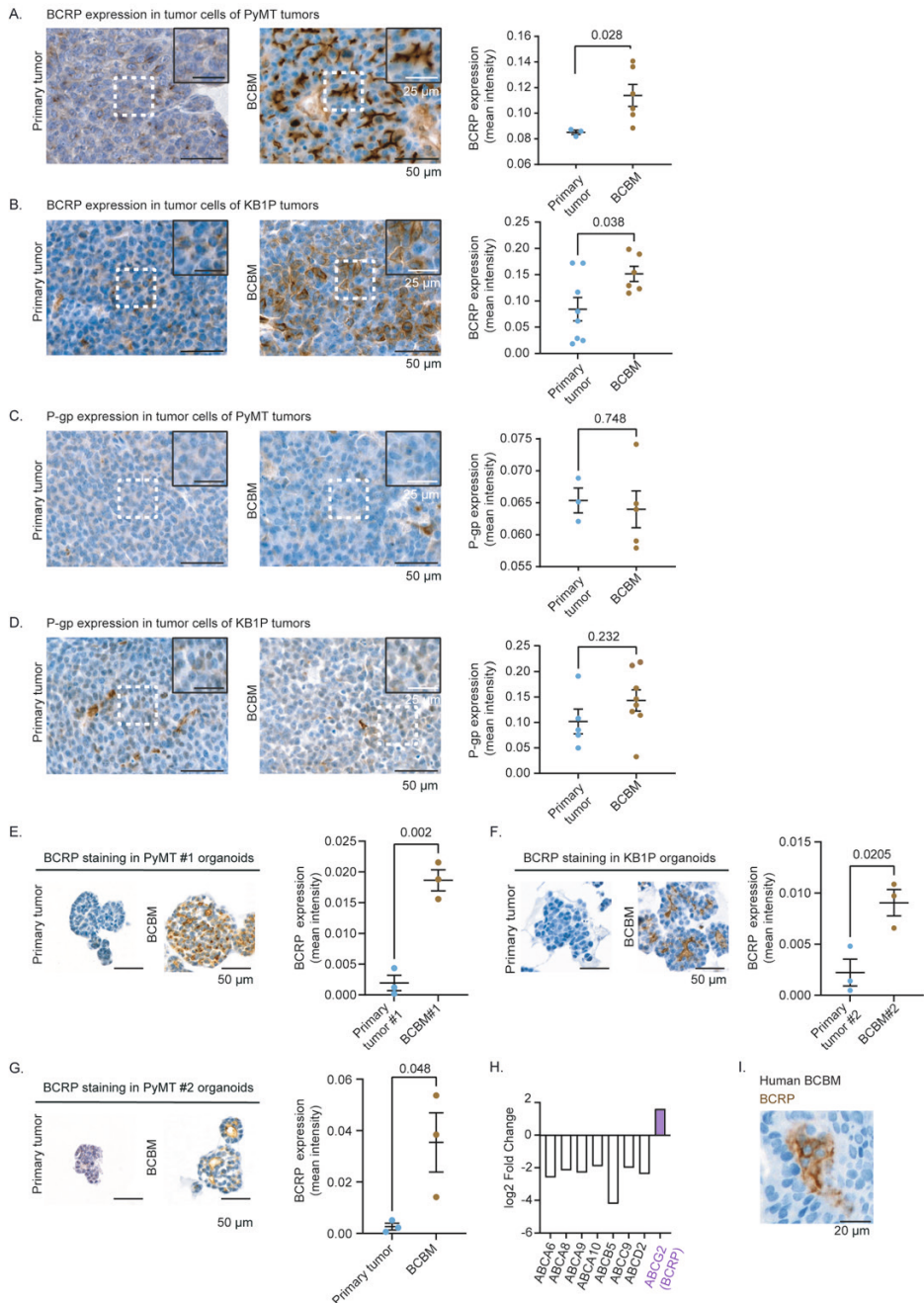


**Figure 2. BCRP is overexpressed in breast cancer cells enriched in the brain.** **A.** Representative images of BCRP immunohistochemistry staining and quantification of DAB OD in the tumor cells found in the PyMT#1 model in both primary tumors (n=3 mice) and BCBM (n=6 mice).

**Figure 2. Continued. B.** Representative images of BCRP immunohistochemistry staining and quantification of DAB OD in the tumor cells found in the KB1P model in both primary tumors (n=8 mice) and BCBM (n=6 mice). **C.** Representative images of P-gp immunohistochemistry staining and quantification of DAB OD in the tumor cells found in the PyMT model in both primary tumors (n=3 mice) and BCBM (n=5 mice). **D.** Representative images of BCRP immunohistochemistry staining and quantification of DAB OD in the tumor cells found in the KB1P model in both primary tumors (n=5 mice) and BCBM (n=8 mice). **E-G.** Representative images and quantification of DAB OD of immunohistochemistry staining of BCRP in organoids derived from primary mammary tumors (left hand panels) and BCBM (right hand panels) in (E) the PyMT#1 model; (F) the KB1P model and (G.) the PyMT#2 model. For E-G, n=3 biological repeats with one technical replicate *per* repeat. For A-G, data are presented as mean  $\pm$  SEM. **H.** Log2 fold change in mRNA expression of ABC transporters genes in BCBM compared to patient-matched primary tumors from the Cosgrove data set [26]. **I.** Representative images of immunohistochemistry staining of BCRP in cancer cells in human BCBM samples.

Lastly, we assessed whether the enhanced BCRP expression in metastatic cells was specific to BCBM by quantifying BCRP expression in extracranial, drug-naïve mouse metastatic tissues. We first studied primary pancreatic tumors and matched liver metastases in the mouse LSL-Kras<sup>G12D/+</sup>;LSL-Trp53<sup>R172H/+</sup>;Pdx1-Cre (KPC) model [27]. Here, we did not observe significant differences in BCRP expression in tumors generated spontaneously or by orthotopic injection (**Supplementary Figure 2 C, D**). Moreover, we did not find a significant difference in BCRP expression in lung metastases compared to matched primary breast tumor in the k14Cre;Cdh1<sup>fl/fl</sup>;Trp53<sup>fl/fl</sup> (KEP) model (**Supplementary Figure 2 E**). However, we detected a significant upregulation of BCRP in PyMT tumor cells that spontaneously metastasized to the lungs compared to matched primary breast tumors (**Supplementary Figure 2 F**). The latter finding suggest that BCRP can also be upregulated by tumor cells that have metastasized to other sites than the brain. However, whilst we consistently observe an increase in BCRP expression in multiple BCBM models, this increase does not consistently happen in extracranial metastases.

### ***BCRP positive BCBM cells can undergo vascular mimicry.***

Intriguingly, we also observed that BCRP<sup>+</sup> tumor cells formed canal-like structures in BCBM, with BCRP being polarized towards the lumen of those structures (**see cartoons Figure 3 A and images in Figure 2 A, E, F, G**). Considering that our BCBMs originate from epithelial breast tissues, we tested whether those canal-like structures may have secretory functions by performing immunohistochemistry (IHC) analysis of cytokeratin 8 (CK8) expression, a marker of secretory cells (**see cartoon in Figure 3 A (I)**) [28]. We indeed observed some canal-like structures positive for CK8 (**Figure 3 B, C (orange arrows) and Supplementary Figure 3 A**). However, a large proportion of the BCRP<sup>+</sup> cells lining the canal-like structures were negative for CK8 (**Figure 3 A (II), B and C and Supplementary Figure 3 B**), suggesting that most canal-like structures lined with BCRP<sup>+</sup> tumor cells do not have secretory functions. We therefore next interrogated whether the observed canal-like, non-secretory, structures displayed characteristics of a vascular mimicry (VM) phenotype.



VM is defined by the ability of tumor cells to transdifferentiate and to acquire features of endothelial cells (**see cartoon Figure 3 A (IV)**) [29, 30]. VM has been hypothesized to enable the generation of a tumor-derived vasculature that sustains cancer cell growth in non-permissive environments [31, 32]. In addition, VM has been reported to occur in human and mouse brain metastases and to drive tumor and metastasis formation in various sites including the brain [33, 34]. To characterize VM in the BCBMs, we next performed IHC analyses of CD31 (marker of endothelial cells) and histochemistry of periodic acid-Schiff (PAS). Structures that are lined with PAS and CD31<sup>+</sup> cells are considered to be VM-like structures [35]. While the vast majority of CD31<sup>+</sup> cells were also BCRP<sup>+</sup> (**see orange arrows at Figure 3 D and E and Supplementary Figure 3 C, D for the images of the separate channels**) a portion of canal-like structures lined with BCRP<sup>+</sup> cancer cells stained negative for CD31 (grey arrows) and positive for PAS (**Figure 3 F, G**). Additionally, IHC of TER-119, a marker of erythrocytes [36] was also applied in our BCBMs. We identified a small number of erythrocytes that were present inside the canal-like structures lined with cancer cells, which is compatible with blood cells circulating through some of those canal-like structures (**Figure 3 H**). Lastly, the observed canal-like structures were also maintained in *in vitro* organoids (**Figure 3 I, J**). These data suggest that breast cancer organoid cells that grow in the brain have the ability to form channels that are often described as VM and to concomitantly express BCRP.

### ***Breast cancer cells enriched in the brain are intrinsically resistant to doxorubicin.***

Because BCRP can actively export doxorubicin [37] we next hypothesized that the enhanced expression of BCRP in the drug-naïve BCBM cancer cells may influence their response to doxorubicin. To test this, we compared the response of primary tumors and paired BCBMs to doxorubicin. Organoids derived from donor breast tumors were transplanted into the fat pad of Friend leukemia Virus B (FVB) mice, and organoids derived from BCBM tumors were injected intracranially. Upon tumor formation, mice bearing tumors in the mammary fat pad were randomized based on tumor volume. Next, mice were subjected to weekly treatment with saline or doxorubicin (**Figure 4 A**). In line with previous studies [8, 38], doxorubicin treatment stalled primary breast tumor growth and resulted in a prolonged survival (PyMT primary tumor: median survival: 34 days for saline-treated mice *versus* 40.5 days for doxorubicin-treated mice (**Figure 4 B, C**); KB1P primary tumor: median survival: 8 days for saline-treated mice *versus* 35 days for doxorubicin-treated mice (**Figure 4 B, D**). For mice bearing BCBM, mice were assigned to treatment groups based on IVIS flux signal in order to treat tumors of similar size (**Supplementary Figure 4 A, B**). In contrast to the primary tumor setting, we did not observe a significant difference in survival upon doxorubicin treatment compared to saline control in mice bearing PyMT BCBM (median survival: 43 days for saline-treated mice *versus* 37 days for doxorubicin-treated mice,

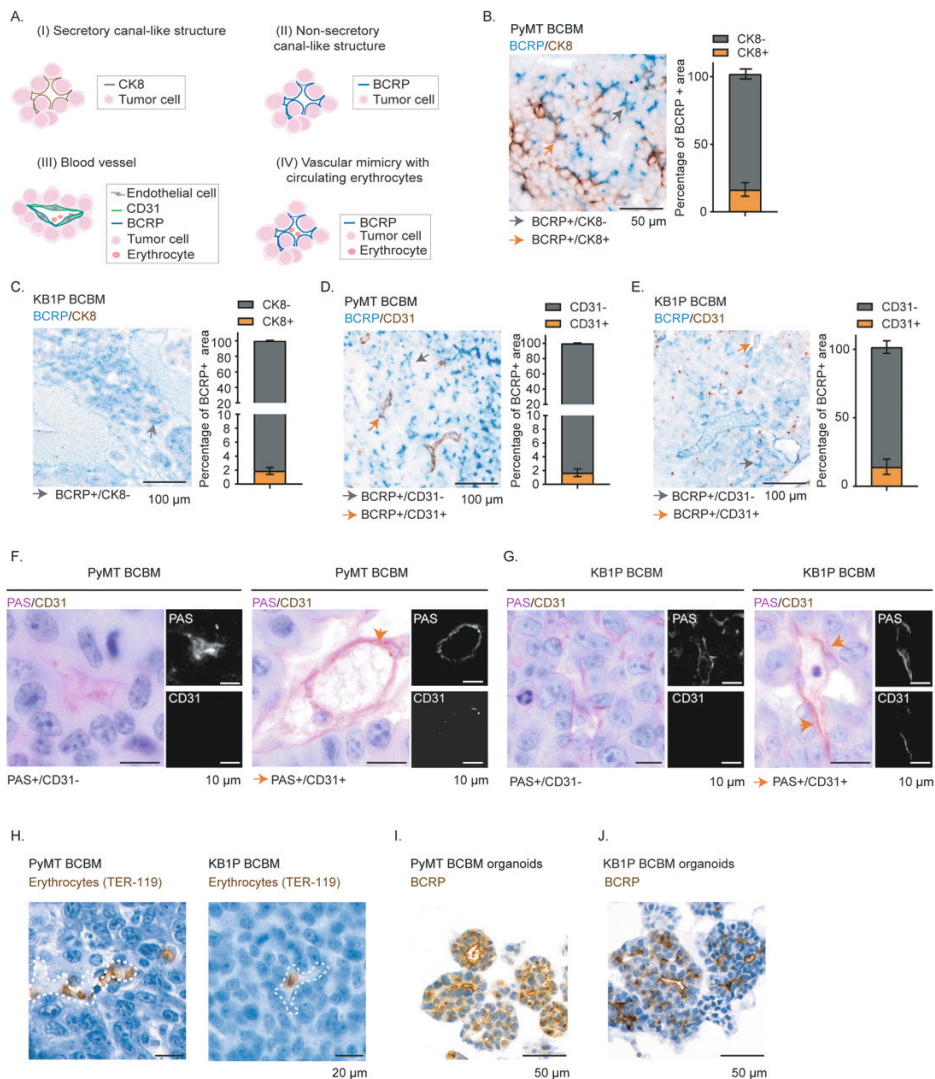


**Figure 3. BCRP<sup>+</sup> cancer cells can undergo vascular mimicry in BCBM.** **A.** Schematic representation of various canal-like structures found in BCBM and assessed in the rest of the figure *via* immunohistochemistry. **B and C.** Representative images and quantification of immunohistochemistry dual staining of BCRP (blue) and CK8 (brown) in the BCBM of the (B.) PyMT#1 model and the (C.) KB1P model. **D. and E.** Dual staining and quantification of BCRP (blue) and CD31 (brown) in the BCBM of the (D.) PyMT#1 model and the (E.) KB1P model. Grey arrows in B-E. indicate single positive staining and orange arrows indicate double positive staining. **F.** Representatives images of immunohistochemistry dual staining of PAS (pink) and CD31 (orange) in the BCBM of the PyMT#1 model and the **G.** KB1P model. **H.** Representative images of immunohistochemistry staining of TER-119 in the BCBM of the PyMT#1 model and of the KB1P model. Dotted lines in H. indicate the lumen of the canal-like structures. **I. and J.** Representative images of immunohistochemistry staining of BCRP in organoids derived from the BCBMs in the (I.) PyMT#1 model and (J.) the KB1P model. For figure 3, data were analyzed in three mice per group.

**Figure 4 E, F).** Moreover, doxorubicin-treatment only mildly increased the survival of mice bearing KB1P BCBMs compared to saline control (median survival: 16,5 days for saline-treated mice *versus* 24 days for doxorubicin-treated mice, **Figure 4 E, G**). This suggests that BCBM are less responsive to doxorubicin than their primary tumor counterparts.

To test whether the different response to doxorubicin was caused by the host tissue (mammary fat pad *versus* brain) or the type of organoid (primary tumor *versus* BCBM), we intracranially injected the doxorubicin-sensitive primary tumor organoids, and subjected mice to the same doxorubicin-treatment schedule (**Figure 4 A, K**). Mice were assigned to treatment groups based on IVIS flux signal in order to treat tumors of similar size (**Supplementary Figure 4 C**). In line with the data obtained at the orthotopic site (**Figure 4 C, D**), doxorubicin-treatment increased survival of mice bearing brain tumors generated by primary tumor organoids in both the PyMT and the KB1P tumors (**Figure 4 I, J**), albeit to a lesser extent than in the orthotopic setting (**Figure 4 C, D**). Next, we performed the reverse experiment and transplanted the BCBM organoids, into the fat pad of recipient mice (**Figure 4 K**). Upon tumor formation, mice were subjected to the same weekly treatment with saline or doxorubicin as before. In contrast to primary breast tumors (**Figure 4 C, D**), neither the tumor growth nor the mouse survival were altered upon doxorubicin treatment compared to the saline treatment in any of the two models (**Figure 4 L, M**). Importantly, doxorubicin intratumoral concentration was not significantly different in the tumors at the various transplantation settings (**Supplementary Figure 4 D**). Combined, these data suggest that BCBM organoids have acquired a resistance to doxorubicin that is maintained outside of the brain environment. To confirm this result, we subjected organoids derived from BCBMs and from their paired primary tumors to doxorubicin *in vitro*. In line with our *in vivo* data, doxorubicin treatment induced less apoptosis in organoids grown from BCBMs than in organoids grown from paired primary tumors (**Figure 5 A, B**). Together, this demonstrates that chemotherapy-naïve cancer cells that grow in the brain have acquired an intrinsic resistance to doxorubicin.

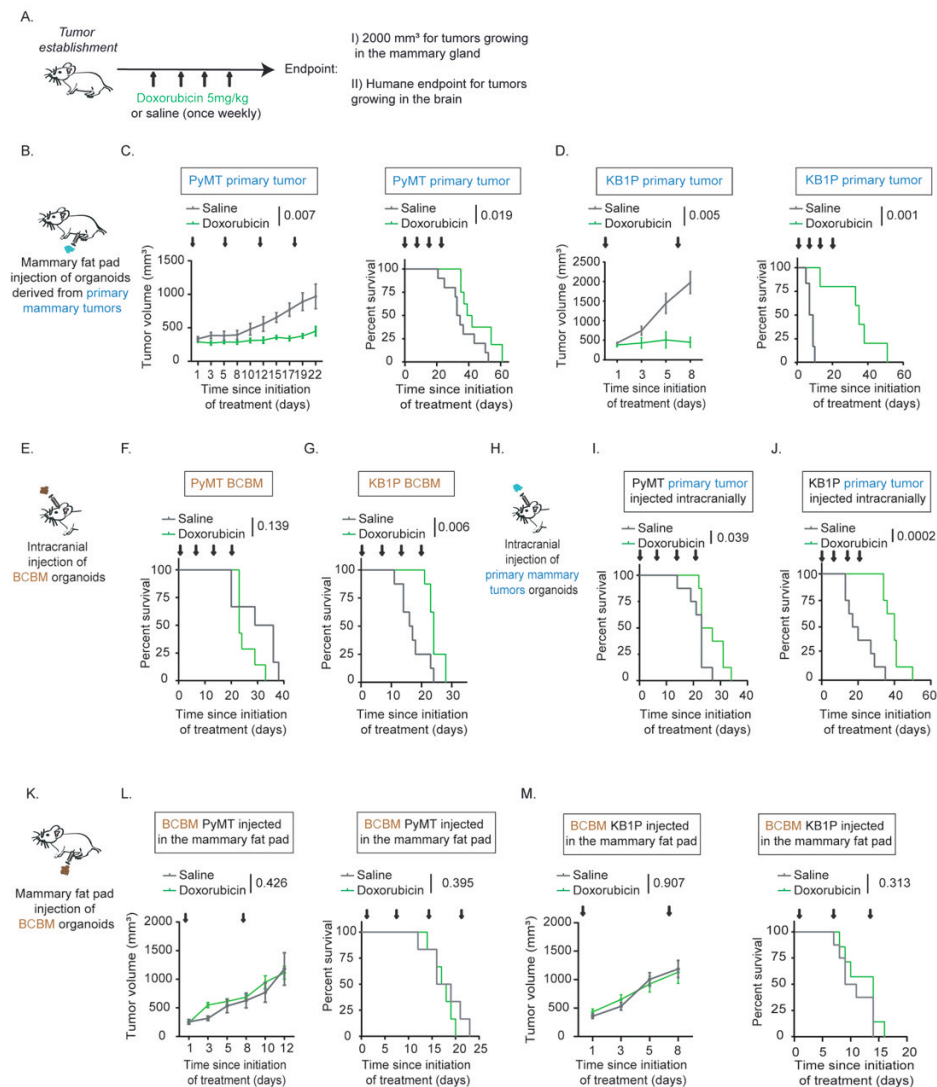


**Figure 4. Differential sensitivity of tumors grown upon injection of primary breast and BCBM organoids.** **A.** Schematic representation of treatment timeline and **B.** experimental setting in C-D. **C.** Tumor growth and Kaplan-Meier curves of mice bearing primary PyMT mammary tumors upon treatment with saline (n=10) or doxorubicin (n=7). **D.** Tumor growth and Kaplan-Meier curves of mice bearing primary KB1P mammary tumors upon treatment with saline (n=6) or with doxorubicin (n=5). **E.** Schematic representation of the experimental setting in F-G. **F.** and **G.** Kaplan-Meier curves of mice bearing (F.) PyMT or (G.) KB1P BCBM and treated with saline or with doxorubicin. For the PyMT BCBM model, n=6 mice treated with saline and n=7 mice treated with doxorubicin; for the KB1P BCBM model, n=8 mice *per* treatment group. **H.** Schematic representation of the experimental setting in I-J. **I.** and **J.** Kaplan-Meier curves of mice bearing tumors derived from PyMT (I.) and KB1P (J.) breast organoids injected intracranially and treated with saline (n=8 mice) or with doxorubicin (n=8 mice). **K.** Schematic representation of the experimental setting of L-M. **L.** Tumor growth and

Kaplan-Meier curves of mice bearing tumors generated by PyMT BCBM organoids implanted in the mammary fat pad and treated with saline (n=6 mice) or with doxorubicin (n=6 mice). **M.** Tumor growth and Kaplan-Meier curves of mice bearing tumors generated by KB1P BCBM organoids implanted in the fat pad and treated with saline (n=8 mice) or with doxorubicin (n=8 mice). Tumor volumes plotted until the first mouse of the cohort reached the maximum tumor volume. The p values were calculated using a mixed-effects model with the Geisser-Greenhouse correction for growth curves and Log-rank (mantel Cox) test for the Kaplan-Meier curves. Arrows indicate the time of intravenous administration of saline or doxorubicin.

### ***BCRP drives intrinsic chemoresistance in BCBM.***

We next asked whether the overexpression of BCRP in BCBM tumor cells drives the observed intrinsic resistance to doxorubicin. We first tested whether BCBM cancer cells specifically export BCRP substrates by subjecting organoids derived from BCBM and paired primary breast tumors to *in vitro* treatment with topotecan, another BCRP-specific substrate [39]. In both paired organoid lines, topotecan induced apoptosis to a significantly lower level in the BCBM organoids compared to the primary tumor organoids (**Figure 5 C, D**). Additionally, treatment with paclitaxel, a compound that is not a substrate of BCRP [40], triggered apoptosis to a similar level in the BCBM organoids and their paired primary tumor organoids for both lines (**Figure 5 E, F**). This demonstrates that chemotherapy-naïve BCBM tumor cells display a reduced response to chemotherapy drugs that are specific substrates of BCRP.

We subsequently interrogated whether reducing BCRP expression in BCBMs would improve their response to doxorubicin. We employed two shRNAs and confirmed their ability to downregulate the expression of BCRP in PyMT BCBM organoids (**Figure 6 A, B**). We treated those organoids with doxorubicin or topotecan, and observed a higher amount of apoptosis and a reduction in viability in BCBM organoids when BCRP expression is reduced compared to control upon treatment with doxorubicin and topotecan (**Figure 6 C** and **Supplementary Figure 5 A, B**). This data shows that knockdown of BCRP reduces the intrinsic resistance to doxorubicin. Next, we performed a rescue experiment by re-expressing BCRP in the PyMT BCBM organoids engineered with shRNA 1, and we confirmed that BCRP expression is enhanced in those organoids (**Supplementary Fig 6 A** and **Supplementary Table 2 for details on the vector**). We subjected those organoids to doxorubicin, and we found that survival after doxorubicin treatment in organoids engineered with the BCRP-shRNA1 was higher upon BCRP re-expression (**Supplementary Figure 6 B**), further confirming the specific role of BCRP in driving resistance to this compound in the BCBM organoids.

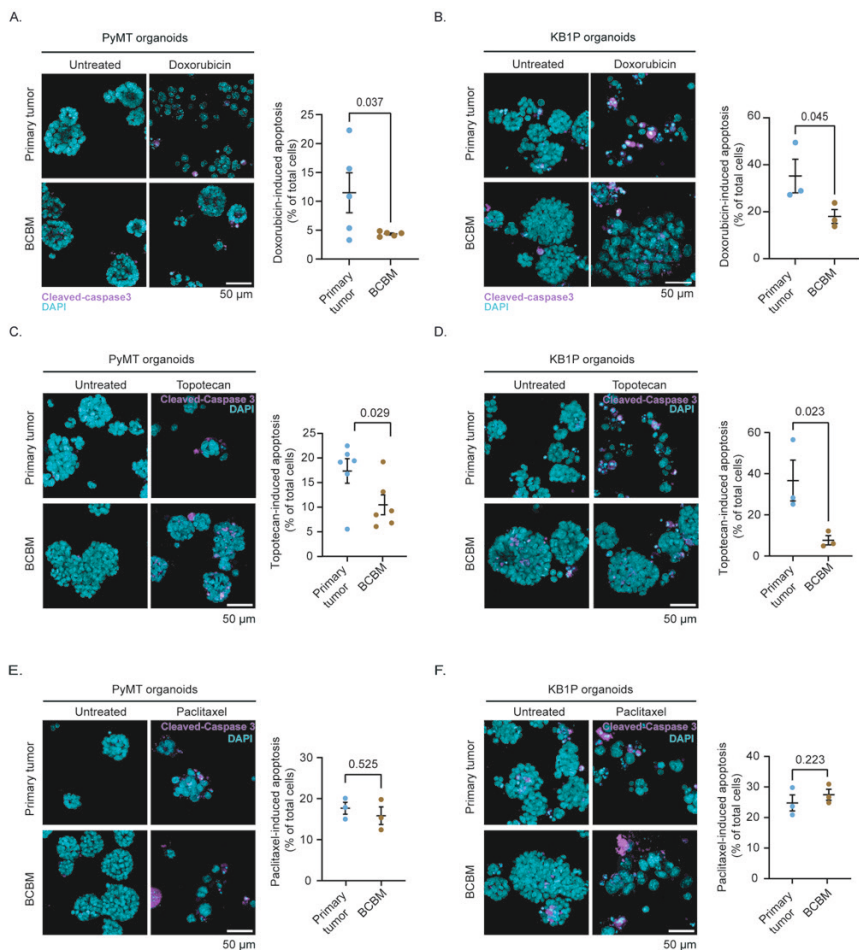


**Figure 5. Breast cancer tumor cells enriched in the brain are intrinsically resistant to doxorubicin.** **A.** Representative images and quantification of immunofluorescent staining of cleaved-caspase 3 in organoids derived from PyMT#1 primary tumors or BCBM, upon treatment with doxorubicin.  $n=3$  biological repeats with 1 technical replicate *per* repeat. **B.** Representative images and quantification of immunofluorescent staining of cleaved-caspase 3 in organoids derived from KB1P primary tumors or BCBM, upon treatment with doxorubicin.  $n=3$  biological repeats with 1 technical replicate *per* repeat. Data are presented as mean  $\pm$  SEM. **C.** Representative images and quantification of cleaved-caspase 3 immunofluorescent staining in PyMT#1 organoids derived from primary tumors and from BCBM, and upon treatment with topotecan. **D.** Representative images and quantification of cleaved-caspase 3 immunofluorescent staining in KB1P organoids derived from primary tumors and from BCBM, and upon treatment with topotecan. **E.** Representative images and quantification of cleaved-caspase 3 immunofluorescent staining in PyMT#1 organoids derived from primary tumors and from BCBM, and upon treatment with paclitaxel. **F.** Representative images and quantification of cleaved-caspase 3 immunofluorescent staining in KB1P organoids derived from primary tumors and from BCBM, and upon treatment with paclitaxel.  $n=3$  biological repeats with 1 technical replicate *per* repeat. Data are presented as mean  $\pm$  SEM.

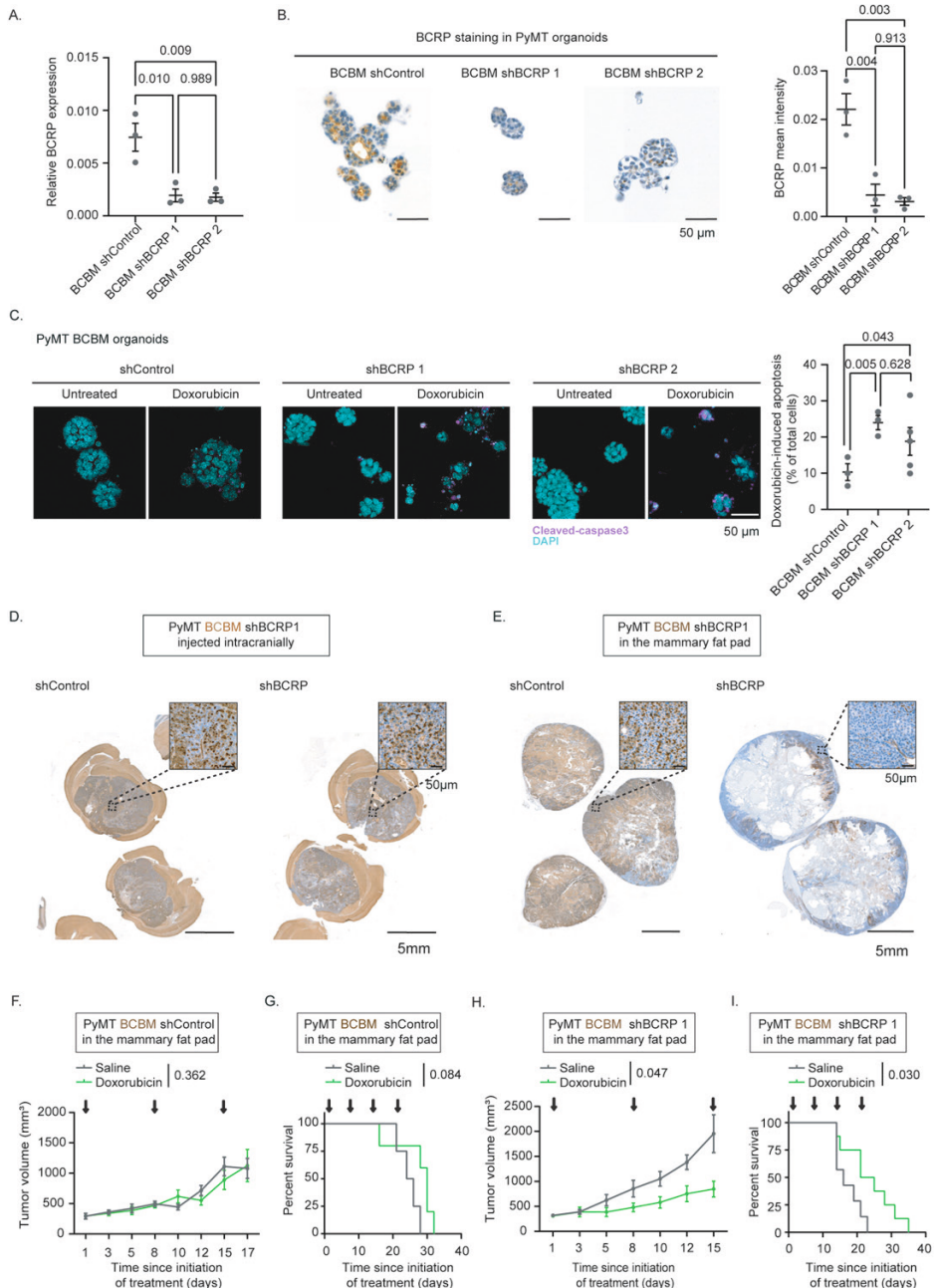


**Figure 6. Reducing BCRP expression and activity alleviates resistance to doxorubicin. A.** RT-qPCR of BCRP in PyMT organoids engineered with a shRNA control (shControl) or with shRNAs against BCRP (shBCRP 1 and shBCRP 2). n=3 biological repeats with 3 technical replicates *per* repeat.

**Figure 6. Continued. B.** Representative images and quantification of BCRP staining in organoids as indicated. **C.** Representative images and quantification of immunofluorescent staining of cleaved-caspase 3 in organoids and treatment conditions as indicated. n=3 biological repeats with 1 technical replicate *per* repeat. **D.** Representative images of BCRP immunohistochemistry staining in PyMT BCBM derived from shControl and shBCRP 1 BCBM organoids intracranially injected. **E.** Representative images of BCRP immunohistochemistry staining in PyMT breast tumors derived from shControl and shBCRP 1 BCBM organoids injected in the mammary fat pad. **F.** Tumor growth of mice bearing tumors generated by PyMT BCBM shControl organoids transplanted in the mammary fat pad treated with saline (n=4 mice) or with doxorubicin (n=5 mice). **G.** Kaplan-Meier curves of mice bearing tumors generated by PyMT BCBM shControl and transplanted in the mammary fat pad and treated with saline (n=4 mice) or with doxorubicin (n=5 mice). **H.** Tumor growth of mice bearing tumors generated by PyMT BCBM shBCRP1 organoids, implanted in the fat pad and treated with saline (n=7 mice) or with doxorubicin (n=8 mice). **I.** Kaplan-Meier curves of mice bearing tumors generated by PyMT BCBM shBCRP 1 organoids, transplanted in the fat pad and treated with saline (n=7 mice) or with doxorubicin (n=8 mice). The tumor volumes are plotted until the first mouse of the cohort reached the maximum tumor volume. The p values were calculated using a mixed-effects model with the Geisser-Greenhouse correction for growth curves and Log-rank (mantel Cox) test for the Kaplan-Meier curves.

We next tested whether reducing BCRP expression affects the response to doxorubicin in PyMT BCBM cancer cells *in vivo*. We first injected intracranially the PyMT BCBM organoids engineered with the control-shRNA or with the BCRP-shRNA 1. In this setting, the downregulation of BCRP expression was not maintained in tumors growing in the brain (**Figure 6 D**). While this observation again points to a model in which BCRP<sup>+</sup> tumor cells are positively selected in this organ (**Figure 6 D**), the re-expression of BCRP in BCRP-shRNA1 brain tumors technically prevents us from studying the response to doxorubicin in this setting. Instead, we injected the BCBM organoids engineered with the control-shRNA and the BCRP-shRNA 1 in the mammary fat pad. Here, BCRP downregulation was maintained in the BCRP-shRNA 1 breast tumors compared to the control-shRNA breast tumors (**Figure 6 E**). Upon tumor formation, mice were subjected to the same weekly treatment with doxorubicin as previously. Tumors derived from BCBM organoids engineered with the control-shRNA did not respond to doxorubicin (**Figure 6 F, G**). However, the growth of tumors derived from BCBM organoids engineered with BCRP-shRNA 1 was significantly reduced upon doxorubicin treatment (**Figure 6 H**), resulting in an increased mouse survival compared to control-treated mice (**Figure 6 I**). This data shows that BCRP knockdown sensitizes BCBMs to doxorubicin.

Lastly, to further confirm the role of BCRP in driving resistance to doxorubicin, we tested whether pharmacological inhibition of BCRP can also sensitize BCBM organoids to doxorubicin. We subjected KB1P BCBM and PyMT organoids to a non-lethal dose of elacridar, a pharmacological inhibitor of BCRP [41, 42], in combination with doxorubicin. In line with our findings using shRNA technology, inhibition of BCRP by elacridar increased the sensitivity of BCBM organoids to doxorubicin (**Figure 7 A and B**). Because elacridar is also a potent inhibitor of P-gp, we assessed whether Ko134, a more specific inhibitor of BCRP, also affects BCBM response to doxorubicin. Combining Ko134 with doxorubicin



indeed significantly increased apoptosis in the BCBM organoids (**Figure 7 C, D**). Together, these data demonstrate that targeting BCRP, either using shRNA technology or *via* pharmacological inhibition, alleviates intrinsic resistance in chemotherapy-naïve BCBM cancer cells.

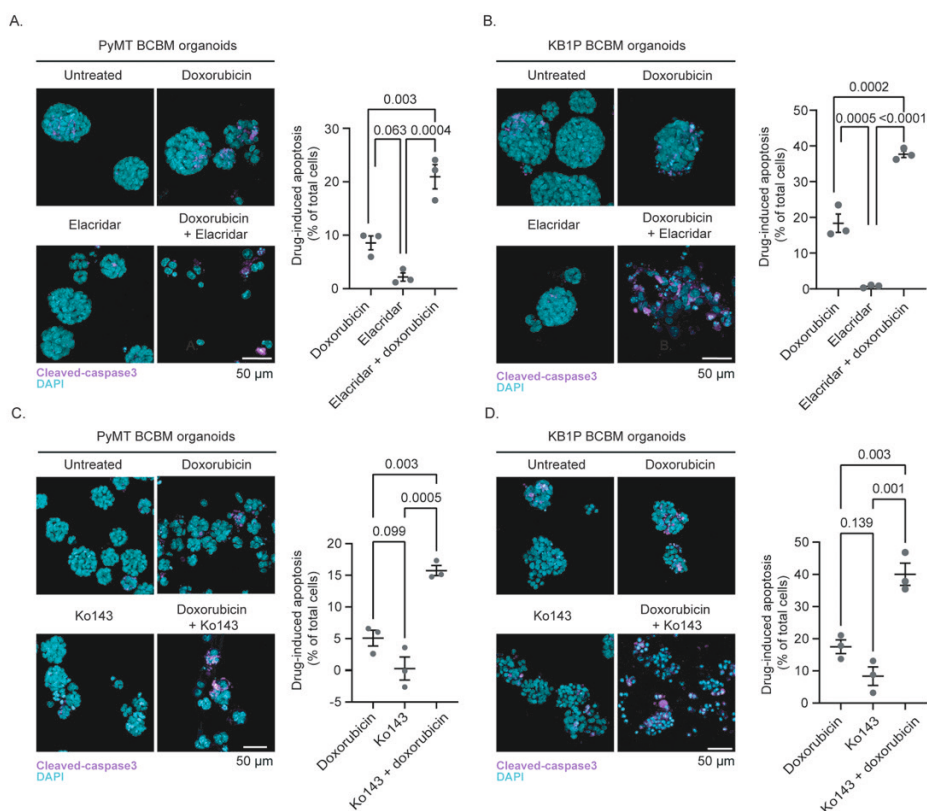


**Figure 7. Reducing BCRP activity alleviates resistance to doxorubicin.** Representative images and quantification of immunofluorescent staining of cleaved-caspase 3 in organoids derived from **A.** PyMT or **B.** KB1P BCBM, upon treatment with DMSO, elacridar, DMSO and doxorubicin or elacridar and doxorubicin.  $n=3$  biological repeats with 1 technical replicate *per* repeat. **C.** Representative images and quantification of immunofluorescent staining of cleaved-caspase 3 in organoids derived from PyMT or **D.** KB1P BCBM, upon treatment with DMSO, Ko143, DMSO and doxorubicin or Ko143 and doxorubicin.  $n=3$  biological repeats with 1 technical replicate *per* repeat. Data are presented as mean  $\pm$  SEM.

## DISCUSSION

Chemoresistance often correlates with increased expression of ABC drug transporters which can occur upon previous exposures to chemotherapy in a range of solid tumors [6-8, 37]. However, in our experimental settings, BCBM cancer cells have never been subjected to any chemotherapy, neither *in vitro* nor *in vivo*. Yet, we observed increased expression of BCRP by the BCBM cells and reduced response to BCRP-specific chemotherapy drugs both in *in vivo* BCBM and in *in vitro* BCBM-derived organoids. Our work therefore identifies in breast cancer mouse models a mechanism of chemoresistance, where chemotherapy-naïve cancer cells enriched in the brain can undergo VM and concomitantly overexpress BCRP, which protects them against chemotherapy. We also noted that doxorubicin concentrations in tumors derived from primary organoids were not significantly higher than in tumors grown from BCBM organoids. This observation may be explained by the fact that total tumor concentrations were measured, which does not distinguish intracellular *versus* extracellular concentrations. It is also possible that doxorubicin is sequestered in the BCBM tumors in non-functional VM-like channels, or inside intracellular compartments, which would explain why the drug is not clear but also does not induce tumor cell death.

The brain environment is an important source of selective pressure for tumor cells metastasizing in this unique site [1, 43]. Previous work has demonstrated that tumor cells growing in the brain can adapt by acquiring 'brain-like' properties in order to efficiently form metastatic masses in the brain [44]. In line with this, we demonstrate that breast cancer cells enriched in the brain form channel structures. Based on their morphology and on the expression of particular markers, these structures qualify as what has been described in the literature as VM. Moreover, cancer cells lining those VM-like channels express BCRP, an ABC transporter that is classically expressed by endothelial cells in capillaries and veins of most organs including the brain [39, 45, 46]. It is possible that transitioning towards a brain endothelial state enables tumor cells to survive and grow in the brain. Alternatively, the presence of BCRP expressing tumor cells may indicate differentiation towards lactating ductal cells [47], however the channel-like structures that we characterize do not resemble lactating ducts morphologically. Regardless of the differentiation route, transitioning towards channel-forming cells with high BCRP expression appears to enable tumor cells to grow in the brain. Indeed, although BCRP expression was much lower in cancer cells in the primary tumors compared to cancer cells in the BCBM, we could occasionally find some BCRP<sup>+</sup> cancer cells in the mouse mammary primary tumors. The inability to maintain low BCRP expression when BCBM organoids engineered with an shRNA against BCRP are injected in the brain also points to a model in which BCRP<sup>+</sup> cells are positively selected for colonizing the brain. However, further work is required to confirm causality. Yet, our study implies that by adapting to a secondary environment such as the brain, metastatic breast

tumor cells can become resistant to chemotherapy in a setting where they have never been subjected to these compounds.

Previous studies have suggested that while ABC transporters may mediate chemoresistance in murine tumors, this may be less relevant in the human setting [48]. However, the majority of those studies have focused on the role of P-gp, not BCRP, and were conducted without specific selection of patients whose tumors had high expression of ABC transporters [49]. In the murine setting, we find that the chemoresistance of chemotherapy-naïve murine BCBM is mediated by expression of the ABC transporter BCRP. Additionally, BCRP also appears to be upregulated in human BCBM (Figure 2 H). However, the vast majority of BCBM patients have been treated with multiple chemotherapies at diagnosis [50-53], consequently we cannot confirm in patient samples whether BCRP is also upregulated when chemotherapy-naïve human cancer cells colonize the brain. Yet, a handful of studies in clinical cohorts have linked the expression of a number of ABC transporters with increased metastatic potential. For instance, ABCB1 expression has been linked with increased metastasis in prostate cancer, uveal melanoma and breast cancer patient cohorts; while the expressions of ABCB5 and of ABCC1 were upregulated in metastases of patients and melanoma patients, respectively [54-57]. Although those studies may point to a broad role of ABC transporters in driving metastasis, the data emanating from those studies were not performed in the drug naïve setting, in contrast to our work.

Here, we have revealed in the murine setting how cancer cells that colonize a metastatic site can adopt traits that makes them chemoresistant without being exposed to therapies. Our data warrants further investigation of whether chemotherapy-naïve breast cancer cells may follow similar routes to chemoresistance in the human setting, potentially by upregulating non-ABC transporters that are also expressed by endothelial cells of the BBB, such as solute carrier transporters [58]. These efforts may provide a better understanding of drug resistance in BCBM to in turn help to develop a better cure for this disease in the future. In light of efforts to develop approaches to shuttle chemotherapeutics like doxorubicin over the BBB and BTB (for instance in clinical trials NCT01818713, NCT03387917 or NCT02536183), the intrinsic resistance to these compounds forms a second barrier that needs to be overcome for successful therapeutic outcomes. Encouragingly, a number of studies using PET tracers have assessed the potency of ABC transporter inhibitors to improve drug delivery to the brain [59, 60]. Our data suggest that targeting ABC transporters in the tumor cells in addition to targeting the BBB and BTB may be beneficial to improve responses to chemotherapy.

In conclusion, our work illustrates how murine cells that adapt to a new environment can acquire resistance to a therapy that they have never been exposed to. Future research will determine whether this or a similar mechanism may apply in the human setting.

## MATERIAL AND METHODS

### **Organoid culture**

Organoids were generated from end-stage, fully established mammary tumors derived from =PyMT [11] or K14-Cre; Brca1<sup>fl/fl</sup>; p53<sup>fl/fl</sup> (KB1P [12]) female mice. Organoids were cultured in 50  $\mu$ l drops of Cultrex PathClear Reduced Growth Factor Basement Membrane Extract Type 2 (BME, Amsbio, Cat. No. 3533-005-02), in either DMEM/F12 GlutaMAX (Gibco, Cat. No. 10565018) supplemented with 10 mmol/L HEPES (Gibco, Cat. No. 15630106), 100 g/ml streptomycin, 100 U/ml penicillin (Gibco, Cat. No. 15140122), 2% B27 (Thermo Fisher Scientific, Cat. No. 17504-044) and 12 ng/ml fibroblast growth factor (FGF, Invitrogen, Cat. No. PHG0261) for organoids derived from the PyMT model; or in Advanced Dulbecco's modified Eagle's medium (adDMEM/F12; Thermo Fisher Scientific, Cat. No. 12634-010) containing 10 mmol/L HEPES (Thermo Fisher Scientific, Cat. No. 15630-056), 10,000 U/ml penicillin/streptomycin (Thermo Fisher Scientific, Cat. No. 15140-122), 2% B27 (Thermo Fisher Scientific, Cat. No. 17504-044), 1.25 mmol/L N-acetylcysteine (Sigma-Aldrich, Cat. No. A9165) and 12 ng/ml fibroblast growth factor (FGF, Invitrogen, Cat. No. PHG0261) for organoids derived from the KB1P model. Organoids were cultured in 20% O<sub>2</sub>, 5% CO<sub>2</sub> and at 37°C. The absence of mycoplasma was routinely confirmed in organoids cultures using the MycoAlert PLUS kit (Lonza, Cat. No. LT07-118). Organoids were passaged using TrypLE Express (Gibco, Cat. No. 12605010) while shaking at 900 rpm for 10-15 min and at 37°C.

### **Mice**

Animal experiments described in this study were run in accordance with the Dutch national guidelines for animal experiments and the Australian code of practice for the care and use of animals for scientific purposes and were approved by the Animal Welfare Committee of the Netherlands Cancer Institute and the Garvan Institute/ St Vincent's Hospital Animal Ethics Committee, respectively. Animals were housed at the Netherlands Cancer Institute facility in Amsterdam, The Netherlands. Mice had access to chow and water *ad libitum* and were kept under specific-pathogen-free conditions in individually ventilated cage. All mice used in this study were FVB female mice, aged 8-20 weeks old at the time of intracranial or fat pad injections. Mice were purchased from Janvier and were allowed to acclimatize for 1 week upon arrival before initiating the experiments.

### **Transplantation of tumor organoids or tumor pieces in the mammary fat pad and monitoring of tumor growth**

Twenty-four hours before surgery, 0.067 mg/ml Rimadyl (Zoetis) in the drinking water was administered to mice and was maintained for 72h following surgery. Immediately before surgery, mice were sedated with 2% (v/v) isoflurane, which was maintained throughout the course of the surgery. The skin above the right fourth mammary gland was shaved and

disinfected using betadine. The fat pad was exposed by making a small incision below the nipple. 100,000 single cells derived from KB1P organoids or from PyMT organoids were resuspended in 30  $\mu$ l of BME (Amsbio, Cat. No. 3533-005-02) and injected into the fat pad using a 30G insulin syringe. The syringe was kept inside the fat pad for 30 seconds to avoid cells leaking out of the fat pad. Next, the skin was sutured, and mice were allowed to recover on a heating pad. Following transplantation of tumor organoids, mice were weighted, monitored and tumor volume was measured with calipers three times *per* week until reaching experimental endpoint. The researcher performing the tumor volume measurements was blinded to the treatment group. Experimental endpoint was reached when tumor volume reached 2000 mm<sup>3</sup>.

### ***Intracranial injection and monitoring of tumor progression***

Twenty-four hours before intracranial injection, mice were administered with 0.067 mg/ml Rimadyl (Zoetis) in the drinking water, which was maintained for three days following surgery. Mice were also treated with 0.1 mg/kg temgesic (Indivior Europe Limited) *via* subcutaneous injection 30 min before and 24h following surgery. Mice were sedated with 2% (v/v) isoflurane *via* inhalation and their eyes were covered with duratears (Alcon). The head of the mouse was shaved and disinfected with betadine, prior to being fixed on a stereotactic apparatus. The periosteum was revealed by making an incision in the skin and was subsequently dissected away to expose the bregma. 1 mg/mL Lidocaine (Fresenius Kabi) and 0.25 mg/mL Bupivacaine (Actavis, Aurobindo Pharma B.V.) diluted in NaCl was applied to the skull as a local anesthetic. The bregma was used as a 0 reference point to determine the position for intracranial injection: 1.5 mm to the right and 1.5 mm caudal of the bregma. At this coordinate, a sterile compact drill bit was used to drill a hole in the skull. Next, a 10  $\mu$ l glass Hamilton syringe with a 30G and point-4 style needle was used to inject the tumor cell suspension, at a depth of 1.5 mm. 40,000 single PyMT BCBM cells or 120,000 single KB1P BCBM cells were injected in 2  $\mu$ l of organoid medium. Before retracting the syringe, a 2-minute waiting time was given to avoid cells leaking out of the injection site. The skin around the injection site was sutured and mice were allowed to recover on a heating pad. Mice were closely monitored during the days following surgery. Mouse weight and behavior were monitored three times a week after intracranial injection and during treatment. To follow BCBM growth and for later analysis, BCBM organoids were engineered to express an H2B-Dendra2-luciferase construct. When mice demonstrated signs of sickness due to BCBM burden (weight loss, bump on the head, loss of reflexes, apathy), mice were monitored weekly. Experimental endpoint was reached when mice stopped eating or drinking, lost more than 15% of their body weight within 2 days; lost more than 20% of their body weight since the initiation of the experiment; had severe circulation or breathing problems or had severe aberrant behavior/movement. The researcher performing the monitoring of the mice and determining experimental endpoints was blinded to the treatment group.

### **Serial intracranial transplantation of breast cancer cells**

End-stage primary breast tumors isolated from PyMT or KB1P mice were harvested and frozen in recovery cell culture freezing medium (Gibco, Cat. No. 12648-010). For the PyMT model, before the first enrichment round in the brain, frozen PyMT tumor pieces from breast tumors were thawed and digested. For the KB1P model, organoids derived from primary KB1P tumors were made as single cells using TriplE. Single cells were resuspended in 3  $\mu$ l of PBS and intracranially injected in recipient mice (enrichment round n°1). Upon tumor formation in the brain of the recipient mice, the brain tumor was isolated, cut into smaller pieces and frozen in recovery cell culture freezing medium (Gibco, Cat. No. 12648-010), prior to being digested again and injected intracranially into a second batch of recipient mice (enrichment round n°2). A total of 6 serial rounds of intracranial transplantations were performed to enrich tumor cells in the brain. BCBM organoids described in this study were isolated from BCBMs after the 6<sup>th</sup> round of enrichment.

### **In vivo treatment**

For mice bearing primary tumors, mice were randomized based on tumor volume, with a tumor volume ranging from 200-400mm<sup>3</sup> and equal averaged volume *per* treatment group. For mice bearing BCBM, tumor growth was monitored *via* bioluminescence imaging on an IVIS twice *per* week. Mice were assigned to treatment groups based on IVIS total flux value. Both for primary tumors and BCBM, mice were treated as follows:

*Saline vehicle (control for doxorubicin):* mice were treated every 7 days, with a maximum of 4 treatments with saline (same volume as doxorubicin), administered *via* intravenous injection.

*Doxorubicin treatment:* mice were treated every 7 days, with a maximum of 4 treatments with doxorubicin (Actavis, 5mg/kg), administered *via* intravenous injection.

### **Magnetic Resonance Imaging (MRI)**

Mice bearing BCBM were imaged using MRI two weeks following intracranial injection of BCBM organoids. This corresponds to the initiation of the saline or doxorubicin treatment *in vivo*. Magnetic resonance imaging was performed with a 7 Tesla BioSpec 70/20 USR (Bruker; Billerica, MA USA). T1-weighted post-contrast sequence with a 3 ms echo-time, 235 ms repetition time and a flip angle of 30° was used. Gadoterate meglumine (Dotarem®; 0.025 mmol/ml; Guerbet; Villepinte, France) was used as a contrast agent and was injected intravenously through a cannula inserted into the tail vein. Mice were sedated with 2% (v/v) isoflurane before and during imaging, and their heart rate and frequency were monitored throughout the procedure. Image acquisition and processing were performed with Paravision software (v6.0.1; Bruker).

### **Texas Red analysis**

Following MRI, mice bearing BCBM were administered with Texas Red (6 mg/kg Sulforhodamine 101; Invitrogen, Cat. no. S359). 30 min later, mice were anesthetized with isoflurane and perfused with saline. The brain was next isolated and frozen on dry ice using Tissue-Tek (Sakura Finetek Europe BV; Alphen aan den Rijn, The Netherlands). Subsequently, the brains were sliced and imaged using an Axio Scan.Z1 (Carl Zeiss, Oberkochen, Germany). To distinguish the BCBM and the healthy brain tissue, BCBM were engineered to express H2B-Dendra2-luciferase. The intensity of Texas Red signal and the area covered by H2B-Dendra2<sup>+</sup> BCBM cells were measured in ZEISS ZEN (blue edition) software.

### **Measurements of doxorubicin concentration in tumor and healthy tissues**

Two hours after administration, animals were sacrificed and the breast tumor, contralateral mammary fat pad, brain tumor and contralateral hemisphere were collected and weighted. Brain, mammary fat pad and tumor samples were homogenized in 1% (w/v) bovine serum albumin using a FastPrep®-24 (MP-Biomedicals, NY). Next, 50 µl of homogenate was vortex-mixed with 5 µL daunorubicin (1 µM in DMSO; Internal Standard) and 300 µL of ice-cold acetonitrile:formic acid (100+1; v/v). Following 10 minutes at -20 degrees Celsius, the samples were centrifuged (20,000 g, 5 minutes 4 degrees) and 100 µl of supernatant was mixed with 400 µL of water. Next 10 µL was injected into an LC-MS/MS system that consisted of an UltiMate 3000 Autosampler and HPLC pump (Thermo Scientific, Waltham, MA, USA) and API3500 MS/MS (Sciex, Framingham, MA, USA). Separation was performed on a Zorbax Extend C18 column (2.1×100 mm, particle size 3.5 µM, Agilent, Santa Clara, USA) preceded by a Securityguard C18 pre-column (Phenomenex, Utrecht, The Netherlands). Mobile phase A (0.1% formic acid in water) and B (methanol) was used in a 5 minutes gradient from 20 to 95% B maintained for 3 minutes followed by re-equilibration at 20% B. MRMs for acquisition were 544.0/397.0 (doxorubicin) and 528.1/321.1 (daunorubicin).

### **Study of BCRP expression in extracranial metastases**

*KPC GEMM model:* Primary pancreatic tumors and liver metastases were isolated from Pdx1-Cre, LSL-Kras<sup>G12D/+</sup>, LSL-Trp53<sup>R172H/+</sup> (KPC) mice. KPC mice were bred at the Australian BioResources (ABR), and at the time of weaning, tail samples were obtained for genotyping by the Garvan Molecular Genetics (GMG) facility. Mice with the appropriate genotypes were ordered at ~6 weeks of age, and weighed, palpated, and monitored once weekly until detection of a palpable tumor, after which mice were weighed, palpated, and monitored 3x weekly. Mice were euthanized upon reaching study endpoint which included: weight loss ≥ 20% compared to the maximum body weight measured over the course of the study OR overnight weight loss of ≥ 10%; tumor interferes with mobility and affects access

to food and water; determination of a BCS  $\leq 2$ ; gross abdominal distension indicating development of ascites; prolonged diarrhoea for  $\geq 3$  days; signs of systemic illness. Mice were removed from the study if they had to be euthanized due to unspecific endpoints not related to pancreatic cancer, including: severe prolapse diameter  $\geq 7$ mm, protrusion  $\geq 4$ mm, ulcerations, dry tissue, dark red to black color; papilloma size  $\geq 10 \times 10$ mm, that cannot be removed surgically, signs of lymphomas in the neck or flank. Pancreatic tumors and liver metastases were isolated at humane endpoint.

*KPC orthotopic model:* This model was previously described here [61]. Briefly, 50 cancer cells and 150 cancer-associated fibroblasts isolated from end-stage KPC tumors were co-injected into the pancreas of NOD/SCID/IL2R $\gamma$  mice during open laparotomy. Mice were sacrificed at humane endpoint and pancreatic tumors and liver metastases were isolated.

*KEP model:* The KEP metastasis model has been applied as previously described [62]]. In short, mammary tumor pieces of 1 mm<sup>2</sup> size derived from spontaneously developed tumors in Keratin14(K14)-cre; Cdh1<sup>fl/fl</sup>;Trp53<sup>fl/fl</sup> (KEP) mice were orthotopically transplanted into the mammary fat pad of 9 week old wild type recipient FVB mice. Mammary tumors were surgically removed when they reached the size of 100 mm<sup>2</sup>. Mice were intraperitoneally injected twice weekly with 100  $\mu$ g rat IgG2a (clone 2A3, BioXCell) starting 14 days after mastectomy, when all mice have established metastases in the lung and/or lymph node, and treatments continued until the experimental endpoint. Mice were sacrificed when they developed signs of distress caused by metastatic disease (respiratory distress) or when lymph node metastasis reached the size of 225 mm<sup>2</sup>.

*PyMT lung metastasis model:*  $1 \times 10^6$  PyMT cells were injected in the mammary fat pad in NOD.Cg-Prkdcscid Il2rgtm1Wjl/SzJAusB female mice, aged 6 weeks. Mice were sacrificed 5 months after transplantation and mammary tumors and lung tissues were isolated and processed for immunohistochemistry.

## **Histochemistry and immunohistochemistry**

### ***In vivo samples***

Tumors grown in the mammary fat pad, brain and lungs, were collected and fixed in EAF (ethanol/acetic acid/ formaldehyde/saline at 40:5:10:45 v/v) and the tumors grown in the pancreas and liver were fixed in 10% buffered formalin before being embedded in paraffin. Sections were stained with hematoxylin and eosin (H&E) and Periodic Acid Schiff (PAS) according to standard procedures. For immunohistochemistry, 4  $\mu$ m-thick sections were stained with BCRP (Cell Signaling, Cat No. 42078S, 1:300), MDR-1 (P-gp) (Cell Signaling, Cat No. 13978, 1:200), CD31 (Abcam, Cat. No. 28364, 1:500), CK8 (DSHB University of Iowa, Troma I, 1:100), TER-119 (BD Bioscience, 1:1000, Cat. No. 550565), GFAP (BioTrend, 1:500, Cat No.BT46-5002-04) and E-Cadherin (Cell Signaling, 1:100, Cat No. 3195) antibodies. Slides were scanned with a Panoramic P1000 slide scanner (Leica Biosystems)



and reviewed with Slide Score (Slide Score B.V.). Staining intensity was quantified using QuPath 0.2.1 (Github). A classifier was built to detect cancer cells and endothelial cells in the entire sample section. Per section, and to account for the heterogeneity of BCRP and P-gp expression, more than 100,000 cells were analyzed. The averaged mean DAB optical density measured in the cell membrane and cytoplasm is depicted in the figures of this manuscript.

Quantification of the dual staining was performed in Fiji/ImageJ software. First, a mask was applied with a color deconvolution and the resulting images were converted to 8-bit files. Next, the areas stained only for BCRP and only for CD31/CK8 were quantified. We then created a mask based on BCRP expression and used it to quantify the area stained for both BCRP and CD31/CK8. Lastly, the percentage of BCRP<sup>+</sup> area stained for BCRP only and for both BCRP and CD31/CK8 was calculated.

### ***In vitro samples***

Organoids were collected, washed in medium and PBS to remove the BME. Next, organoids were fixed in 4% paraformaldehyde for 20 min. Organoids were washed in PBS twice prior to being embedded in 4% agarose. Once the agarose had solidified, organoids in agarose were moved to formalin and embedded in paraffin. 4 µm-thick sections were stained with BCRP (Cell Signaling, Cat. No. 42078S, 1:300) antibody. Slides were scanned with a Panoramic P1000 slide scanner (Leica Biosystems) and reviewed with Slide Score. The intensity of BCRP staining was quantified in Fiji as described before. Briefly, color deconvolution was applied on H DAB images and the same threshold was applied to all images to remove background signal. The mean grey values were quantified using the 'Analyze particle option', normalized to the number of cells per field of view and averaged for each biological repeat [63].

### ***Human samples***

All the human BCBM biospecimens are obtained at the Amsterdam UMC (location VuMC) and have been executed pursuant to the ethical rules and regulations of the Amsterdam UMC location VuMC. Hence, the procedures comply both with (inter-) national legislative and ethical standards. In the database of the Amsterdam UMC, location VUMC, eight samples of brain resections with a metastasis of mammary carcinoma were selected. These were all invasive ductal carcinomas, not otherwise specified, with a different receptor status: 2 ER-positive, 2 HER2-positive, 2 triple negative and 1 unknown receptor status. Immunohistochemistry of the FFPE tumor samples was performed on a BenchMark Ultra autostainer (Ventana Medical Systems). Briefly, paraffin sections were cut at 3 µm, heated at 75°C for 28 minutes and deparaffinized in the instrument with EZ prep solution (Ventana Medical Systems). Heat-induced antigen retrieval was carried out using Cell Conditioning 1 (CC1, Ventana Medical Systems) for 64 minutes at 95°C.

BCRP/ABCG2 was detected using clone D5V2K (1/100 dilution, 36 minutes at RT., Cell Signaling). Bound antibody was detected using the OptiView DAB Detection Kit (Ventana Medical Systems). Slides were counterstained with Hematoxylin and Bluing Reagent (Ventana Medical Systems). A PANNORAMIC® 1000 scanner from 3DHISTECH was used to scan the slides at a 40x magnification.

### ***In vitro* treatments**

Organoids were plated as small organoids (4-10 cells) and treated for 72h with chemotherapy. The PyMT breast tumor and BCBM tumor organoids were treated with either 30 nmol/L doxorubicin (Actavis), 50 nmol/L topotecan (Sandoz), 50 nmol/L paclitaxel (Fresenius Kabi), 200 nmol/L elacridar (MedChemExpress, Cat. No. 58407) or 1  $\mu$ mol/L Ko134 (Sigma-Aldrich, Cat. No. K2144-1MG). The KB1P breast tumor and BCBM tumor organoids were treated with either 10 nmol/L doxorubicin (Actavis), 20 nmol/L topotecan (Sandoz), 20 nmol/L paclitaxel (Fresenius Kabi) or 200 nmol/L elacridar (MedChemExpress, Cat. No. 58407).

### **Cytotoxicity assays**

8,000 cells were seeded in 5  $\mu$ l of BME in a 96-well plate and treated with 30 nmol/L doxorubicin (Actavis) for 120 hours. Next, cells were incubated with Cell-Titer Blue (Promega, cat, No G8080) for 4 h in the dark.

### **Cleaved-caspase 3 immunofluorescent staining, confocal imaging and analysis**

Following treatment, organoids were fixed in 4% paraformaldehyde in PBS for 20 min at room temperature. Organoids were next permeabilized with 0.2% TritonX-100 in PBS for 15 min at room temperature. A blocking step was next performed using 5% Bovine Serum Albumin diluted in PBS for 2h at room temperature, followed by staining overnight at 4°C with anti-Cleaved Caspase 3 (1:400, Asp175, Cell Signalling, Cat. No. 9661). Appropriate Alexa Fluor-labelled secondary antibody (Thermo Fisher Scientific) was combined with DAPI (1  $\mu$ g/ml) and incubated for 1 hour in the dark at room temperature. Stained organoids were imaged on an inverted Leica TCS SP8 confocal microscope (Mannheim, Germany), in 8 bit with a 25x water immersion objective (HCX PL APO CS 25.0x0.70 WATER UV). ImageJ was used to quantify the number of cleaved-caspase 3 positive cells. The percentage of cleaved-caspase 3 positive cells in untreated samples was subtracted to the treated group and plotted in the figures of this manuscript.

### **Organoids transduction**

Organoids were transduced with a construct containing either H2B-Dendra2-luciferase, luciferase, shRNA constructs or with the construct to rescue BCRP expression in the shRNA

1 for BCRP. shRNA constructs were provided by the RNAi Consortium mouse library. Resistance cassette from the shRNA BCRP vectors was changed from puromycin into blasticidin. Control shRNA pLKO.1 was purchased from Addgene (plasmid #26701). The rescue construct was produced by VectorBuilder where a Kozak and P2A sequence were included, as well as a hygromycin resistance cassette (Table 2). Lentivirus were generated by transient transfection of HEK293FT cells, as described before [64]. Lentiviral titers were determined using the qPCR Titration Kit (abm, Cat. No. LV900), following the manufacturer's instructions. For all experiments the amount of lentiviral supernatant used was calculated to achieve a MOI of 5 or 25. Organoids were trypsinized into smaller clusters of approximately 8 cells and incubated with the virus, 100 µg/ml polybrene (Sigma, Cat. No. TR-1003-G) and 10 µmol/L Y-27632 (Bio Connect, Cat. No. S1049) on a 48-well plate (Greiner, Cat. No. 677970). Spin infection was done at 32°C, 600 rcf for 1h and organoids were subsequently incubated at 37°C for 6h. Next, organoids were washed twice with DMEM/F12 GlutaMAX medium (Gibco, Cat. No. 10565018) and plated in BME. Complete DMEM/F12 GlutaMAX medium (Gibco, Cat. No. 10565018), supplemented with 10 mmol/L HEPES (Gibco, Cat. No. 15630106), 100 µg/ml streptomycin, 100 U/ml penicillin (Gibco, Cat. No. 15140122), 12 ng/mL FGF (Gibco, Cat. No. PHG0261), 2% B27 supplement (Gibco, Cat. No. 17504001) and 10 µmol/L Y-27632 (Bio Connect, Cat. No. S1049) was added to the organoids for 2 days. Virus titers were calculated with a qPCR lentivirus titration titer kit (abm, Cat. No. LV900) and a multiplicity of infection of 5 was used for transductions. Organoids transduced with shRNAs were selected with 10 µg/ml of blasticidin (Gibco, Cat. No. A1113903).

## RNA isolation, cDNA isolation and real-time quantitative PCR

For RNA extraction of cultured organoids,  $\sim 1 \times 10^6$  cells were harvested. Cells were lysed in TRIzol (Thermo Fisher Scientific, 15596018) and RNA was extracted using standard TRIzol-chloroform extraction methods. RNA concentration and purity were measured using DS-11/DS-11+ Spectrophotometer (DeNovix). 1000 ng of RNA were used to prepare cDNA using the Reverse Transcription Kit (Appliedbiosystems, Cat. No. 4368814) according to the manufacturer's protocol. The generated cDNA was used for real-time quantitative PCR using the SYBR Green Master mix in a QuantStudio Real-Time qPCR system, using the following primers:

**Table 1. Primers sequences.**

Gene name	Sequence forward	Sequence reverse
BCRP	5'-CAGTTCTCAGCAGCTCTTCGAC-3'	5'-TCCTCCAGAGATGCCACGGAT-3'
RPL38	5'-AGGATGCCAAGTCTGTCAAGA-3'	5'-TCCTTGTCGTGTGATAACCCAGGG-3'
ABCA6	5'-CTGAACCTGGAAGGAGAACCAAG - 3'	5'-TGGTGCTCACAGTCTCCTGAAC -3'
ABCA8	5'-GCTTTGCCAGAGTCTTGACAGC-3'	5'-TCCTTCTCCCACGATGTCAACC-3'

**Table 1. Continued.**

Gene name	Sequence forward	Sequence reverse
ABCB5	5'-TGACCACGCAAAGCGAAGAACG-3'	5'-CGCCATAATCCTCAATGCCTTGG-3'
ABCC9	5'-TGAAGCACTCGGTGATTGTGGC-3'	5'-AATGCCTGCTCCACAGAGGATG-5'
ABCD2	5'-CCATAGCAAGCGTGGAGGTAA C-3'	5'-CACTTCGCCCGCTGGTGTAAATT-3'
ABCA9	5'-TGACCACGCAAAGCGAAGAACG-3'	5'-CGCCATAATCCTCAATGCCTTGG-3'

Expression values were calculated by transforming Ct values ( $2^{-Ct}$ ) and were normalized to the mean value of the transformed Ct values of the reference gene *RPL38*.

### **Analysis of BCRP expression in the Cosgrove data set.**

We analyzed the differential expression of genes from the ABC transporter family in BCBM compared to patient-matched primary tumors published by Cosgrove et al [26]. In Figure 4, we represented the log<sub>2</sub> fold change of those genes that are significantly differentially expressed in BCBM compared to patient-matched primary tumors in the Her2<sup>+</sup> cohort.

### **Statistical analysis**

The normality of data was tested using the Shapiro-Wilk test. For all normally distributed measurements, one-way ANOVA (when >2 means were compared) followed by Tukey's multiple comparisons test or parametric t-test were used to determine significance, set to  $p < 0.05$ . Kaplan Meier survival curves were analyzed with a log-rank Mantel-Cox test. Tumor growth curves p-values were calculated using a mixed-effects model with the Geisser-Greenhouse correction. All statistical analyses were performed using GraphPad Prism software (version 9.1.2, GraphPad Software, USA).

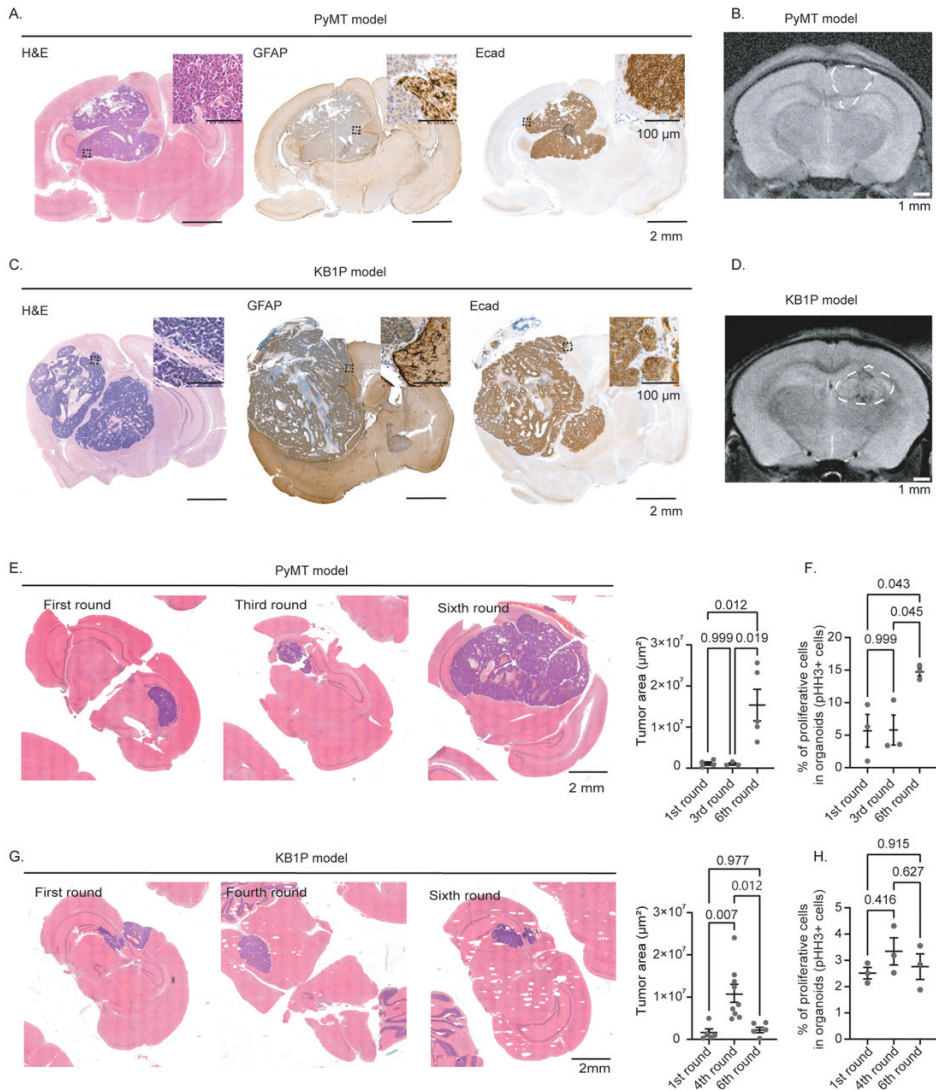
## REFERENCES

1. Boire, A., et al., *Brain metastasis*. Nature Review Cancer, 2019. 20: p. 4-11.
2. Abbott, N.J., et al., *Structure and function of the blood-brain barrier*. Neurobiol Dis, 2010. 37(1): p. 13-25.
3. Schinkel, A.H., et al., *Disruption of the mouse *mdr1a* P-glycoprotein gene leads to a deficiency in the blood-brain barrier and to increased sensitivity to drugs*. Cell, 1994. 77(4): p. 491-502.
4. Schinkel, A.H., *P-Glycoprotein, a gatekeeper in the blood-brain barrier*. Adv Drug Deliv Rev, 1999. 36(2-3): p. 179-194.
5. Agarwal, S., et al., *Breast cancer resistance protein and P-glycoprotein in brain cancer: two gatekeepers team up*. Curr Pharm Des, 2011. 17(26): p. 2793-802.
6. Zander, S.A., et al., *Sensitivity and acquired resistance of *BRCA1*;p53-deficient mouse mammary tumors to the topoisomerase I inhibitor topotecan*. Cancer Res, 2010. 70(4): p. 1700-10.
7. Rottenberg, S., et al., *Selective induction of chemotherapy resistance of mammary tumors in a conditional mouse model for hereditary breast cancer*. Proc Natl Acad Sci U S A, 2007. 104(29): p. 12117-22.
8. Pajic, M., et al., *Moderate increase in *Mdr1a/1b* expression causes in vivo resistance to doxorubicin in a mouse model for hereditary breast cancer*. Cancer Res, 2009. 69(16): p. 6396-404.
9. Holohan, C., et al., *Cancer drug resistance: an evolving paradigm*. Nat Rev Cancer, 2013. 13(10): p. 714-26.
10. Arvanitis, C.D., G.B. Ferraro, and R.K. Jain, *The blood-brain barrier and blood-tumour barrier in brain tumours and metastases*. Nat Rev Cancer, 2020. 20(1): p. 26-41.
11. Lin, E.Y., et al., *Progression to malignancy in the polyoma middle T oncoprotein mouse breast cancer model provides a reliable model for human diseases*. Am J Pathol., 2003. 163.
12. Duarte, A.A., et al., *BRCA-deficient mouse mammary tumor organoids to study cancer-drug resistance*. Nat Methods, 2018. 15(2): p. 134-140.
13. Foley, K.E., *Organoids: a better in vitro model*. Nat Methods, 2017. 14(6): p. 559-562.
14. Valiente, M., et al., *Brain Metastasis Cell Lines Panel: A Public Resource of Organotropic Cell Lines*. Cancer Res, 2020. 80(20): p. 4314-4323.
15. Uceda-Castro, R., et al., *Re-purposing the pro-senescence properties of doxorubicin to introduce immunotherapy in breast cancer brain metastasis*. Cell Rep Med, 2022. 3(11): p. 100821.
16. Margarido, A.S., et al., *Epithelial-to-Mesenchymal Transition Drives Invasiveness of Breast Cancer Brain Metastases*. Cancers (Basel), 2022. 14(13).
17. Mo, F., et al., *Blood-Brain Barrier in Brain Tumors: Biology and Clinical Relevance*. Int J Mol Sci, 2021. 22(23).
18. van Tellingen, O., et al., *Overcoming the blood-brain tumor barrier for effective glioblastoma treatment*. Drug Resist Updat, 2015. 19: p. 1-12.
19. Juliano, R.L. and V. Ling, *A surface glycoprotein modulating drug permeability in Chinese hamster ovary cell mutants*. Biochim Biophys Acta, 1976. 455(1): p. 152-62.
20. Gros, P., et al., *Isolation and characterization of DNA sequences amplified in multidrug-resistant hamster cells*. Proc Natl Acad Sci U S A, 1986. 83(2): p. 337-41.
21. Roninson, I.B., et al., *Isolation of human *mdr* DNA sequences amplified in multidrug-resistant KB carcinoma cells*. Proc Natl Acad Sci U S A, 1986. 83(12): p. 4538-42.
22. Riordan, J.R., et al., *Amplification of P-glycoprotein genes in multidrug-resistant mammalian cell lines*. Nature, 1985. 316(6031): p. 817-9.
23. Stallard, S., et al., *Distribution of doxorubicin to normal breast and tumour tissue in patients undergoing mastectomy*. Cancer Chemother Pharmacol, 1990. 25(4): p. 286-90.
24. de Gooijer, M.C., et al., *ATP-binding cassette transporters restrict drug delivery and efficacy against brain tumors even when blood-brain barrier integrity is lost*. Cell Reports Medicine, 2021. 2.

25. Lockman, P.R., et al., *Heterogeneous blood-tumor barrier permeability determines drug efficacy in experimental brain metastases of breast cancer*. Clin Cancer Res, 2010. 16(23): p. 5664-78.
26. Cosgrove, N., et al., *Mapping molecular subtype specific alterations in breast cancer brain metastases identifies clinically relevant vulnerabilities*. Nat Commun, 2022. 13(1): p. 514.
27. Hingorani, S.R., et al., *Trp53R172H and KrasG12D cooperate to promote chromosomal instability and widely metastatic pancreatic ductal adenocarcinoma in mice*. Cancer Cell, 2005. 7(5): p. 469-83.
28. Lehr, H.A., et al., *Cytokeratin 8 immunostaining pattern and E-cadherin expression distinguish lobular from ductal breast carcinoma*. Am J Clin Pathol, 2000. 114(2): p. 190-6.
29. Hendrix, M.J., et al., *Tumor cell vascular mimicry: Novel targeting opportunity in melanoma*. Pharmacol Ther, 2016. 159: p. 83-92.
30. Party, B.C.P.W., *Evidence for novel non-angiogenic pathway in breast-cancer metastasis*. The Lancet, 2000. 355(9217).
31. Hendrix, M.J., et al., *Vasculogenic mimicry and tumour-cell plasticity: lessons from melanoma*. Nat Rev Cancer, 2003. 3(6): p. 411-21.
32. Wechman, S.L., et al., *Vascular mimicry: Triggers, molecular interactions and in vivo models*. Adv Cancer Res, 2020. 148: p. 27-67.
33. El Hallani, S., et al., *A new alternative mechanism in glioblastoma vascularization: tubular vasculogenic mimicry*. Brain, 2010. 133(Pt 4): p. 973-82.
34. Wagenblast, E., et al., *A model of breast cancer heterogeneity reveals vascular mimicry as a driver of metastasis*. Nature, 2015. 520(7547): p. 358-62.
35. Seftor, R.E., et al., *Cooperative interactions of laminin 5 gamma2 chain, matrix metalloproteinase-2, and membrane type-1-matrix/metalloproteinase are required for mimicry of embryonic vasculogenesis by aggressive melanoma*. Cancer Res, 2001. 61(17): p. 6322-7.
36. Kina, T., et al., *The monoclonal antibody TER-119 recognizes a molecule associated with glycophorin A and specifically marks the late stages of murine erythroid lineage*. Br J Haematol, 2000. 109(2): p. 280-7.
37. Robey, R.W., et al., *ABCG2: a perspective*. Adv Drug Deliv Rev, 2009. 61(1): p. 3-13.
38. Hughes, R., et al., *Perivascular M2 Macrophages Stimulate Tumor Relapse after Chemotherapy*. Cancer Res, 2015. 75(17): p. 3479-91.
39. Maliepaard, M., et al., *Overexpression of the BCRP/MXR/ABCP gene in a topotecan-selected ovarian tumor cell line*. Cancer Res, 1999. 59(18): p. 4559-63.
40. Doyle, L. and D.D. Ross, *Multidrug resistance mediated by the breast cancer resistance protein BCRP (ABCG2)*. Oncogene, 2003. 22(47): p. 7340-58.
41. Bihorel, S., et al., *Modulation of the brain distribution of imatinib and its metabolites in mice by valsopodar, zosuquidar and elacridar*. Pharm Res, 2007. 24(9): p. 1720-8.
42. de Bruin, M., et al., *Reversal of resistance by GF120918 in cell lines expressing the ABC half-transporter, MXR*. Cancer Lett, 1999. 146(2): p. 117-26.
43. Chambers, A.F., A.C. Groom, and I.C. MacDonald, *Dissemination and growth of cancer cells in metastatic sites*. Nat Rev Cancer, 2002. 2(8): p. 563-72.
44. Valiente, M., et al., *Serpins promote cancer cell survival and vascular co-option in brain metastasis*. Cell, 2014. 156(5): p. 1002-16.
45. Begley, D.J., *ABC transporters and the blood-brain barrier*. Curr Pharm Des, 2004. 10(12): p. 1295-312.
46. Eisenblatter, T., S. Huwel, and H.J. Galla, *Characterisation of the brain multidrug resistance protein (BMDP/ABCG2/BCRP) expressed at the blood-brain barrier*. Brain Res, 2003. 971(2): p. 221-31.
47. Jonker, J.W., et al., *The breast cancer resistance protein BCRP (ABCG2) concentrates drugs and carcinogenic xenotoxins into milk*. Nat Med, 2005. 11(2): p. 127-9.
48. Borst, P., *Looking back at multidrug resistance (MDR) research and ten mistakes to be avoided*. FEBS, 2020.

49. Robey, R.W., et al., *Revisiting the role of ABC transporters in multidrug-resistant cancer*. Nat Rev Cancer, 2018. 18(7): p. 452-464.
50. Lin, N.U., J.R. Bellon, and E.P. Winer, *CNS metastases in breast cancer*. Journal of Clinical Oncology, 2004. 22: p. 3608-17.
51. Kadamkulam Syriac, A., N.S. Nandu, and J.P. Leone, *Central Nervous System Metastases from Triple-Negative Breast Cancer: Current Treatments and Future Prospective*. Breast Cancer (Dove Med Press), 2022. 14: p. 1-13.
52. Bowman, K.M. and P. Kumthekar, *Medical management of brain metastases and leptomeningeal disease in patients with breast carcinoma*. Future Oncol, 2018. 14(4): p. 391-407.
53. Garcia-Alvarez, A., A. Papakonstantinou, and M. Oliveira, *Brain Metastases in HER2-Positive Breast Cancer: Current and Novel Treatment Strategies*. Cancers (Basel), 2021. 13(12).
54. Landreville, S., et al., *ABCB1 identifies a subpopulation of uveal melanoma cells with high metastatic propensity*. Pigment Cell Melanoma Res, 2011. 24(3): p. 430-7.
55. Weinstein, R.S., et al., *Relationship of the expression of the multidrug resistance gene product (P-glycoprotein) in human colon carcinoma to local tumor aggressiveness and lymph node metastasis*. Cancer Res, 1991. 51(10): p. 2720-6.
56. Guo, Q., et al., *ATP-binding cassette member B5 (ABCB5) promotes tumor cell invasiveness in human colorectal cancer*. J Biol Chem, 2018. 293(28): p. 11166-11178.
57. Walsh, N., et al., *Membrane transport proteins in human melanoma: associations with tumour aggressiveness and metastasis*. Br J Cancer, 2010. 102(7): p. 1157-62.
58. Nigam, S.K., *What do drug transporters really do?* Nat Rev Drug Discov, 2014. 14: p. 29-44.
59. Bauer, M., et al., *Approaching complete inhibition of P-glycoprotein at the human blood-brain barrier: an (R)-[11C]verapamil PET study*. J Cereb Blood Flow Metab, 2015. 35(5): p. 743-6.
60. Verheijen, R.B., et al., *Molecular Imaging of ABCB1 and ABCG2 Inhibition at the Human Blood-Brain Barrier Using Elacridar and (11)C-Erlotinib PET*. J Nucl Med, 2018. 59(6): p. 973-979.
61. Vennin, C., et al., *CAF hierarchy driven by pancreatic cancer cell p53-status creates a pro-metastatic and chemoresistant environment via perlecan*. Nat Commun, 2019. 10(1): p. 3637.
62. Doornebal, C.W., et al., *A preclinical mouse model of invasive lobular breast cancer metastasis*. Cancer Res, 2013. 73(1): p. 353-63.
63. Crowe, R.A. and W. Yue, *Semi-quantitative Determination of Protein Expression Using Immunohistochemistry Staining and Analysis*. Bio Protocol, 2019. 9(24).
64. Follenzi, A., et al., *Gene transfer by lentiviral vectors is limited by nuclear translocation and rescued by HIV-1 pol sequences*. Nat Genet, 2000. 25(2): p. 217-22.

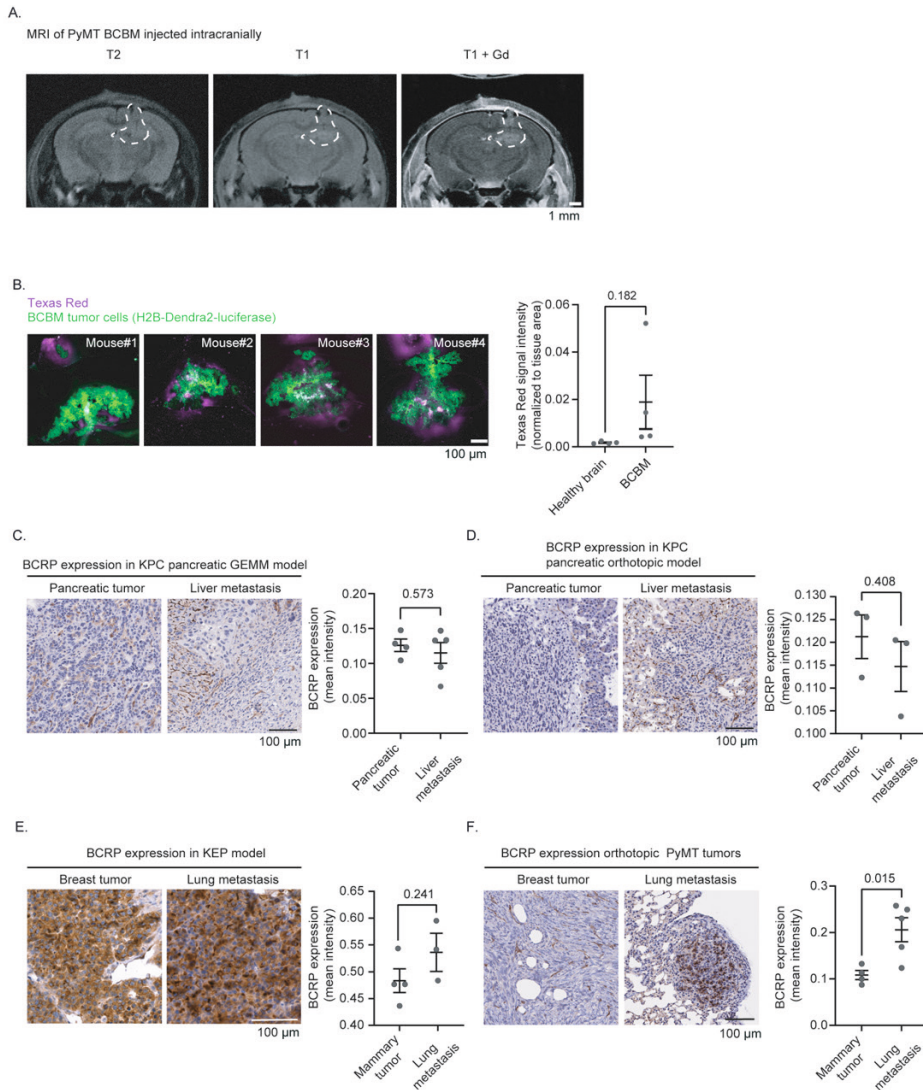
## SUPPLEMENTARY FILES



**Supplementary figure 1. Characterization of BCBM models** **A.** Representative images of H&E staining and immunohistochemistry staining for GFAP and E-Cadherin PyMT#1 BCBM. **B.** Representative example of Magnetic Resonance Imaging (MRI) of PyMT#1 BCBM in mice. The dotted line marks the BCBM edge. **C.** Representative images of H&E staining and immunohistochemistry staining for GFAP and E-Cadherin in KB1P BCBM. **D.** Representative example of Magnetic Resonance Imaging (MRI) of KB1P BCBM in mice. The dotted line marks the BCBM edge. For A-D, BCBM cells were injected intracranially, tumor formation and localization in the brain parenchyma at humane endpoint was confirmed by H&E. **E.** Representative images of H&E staining and quantification of tumor area

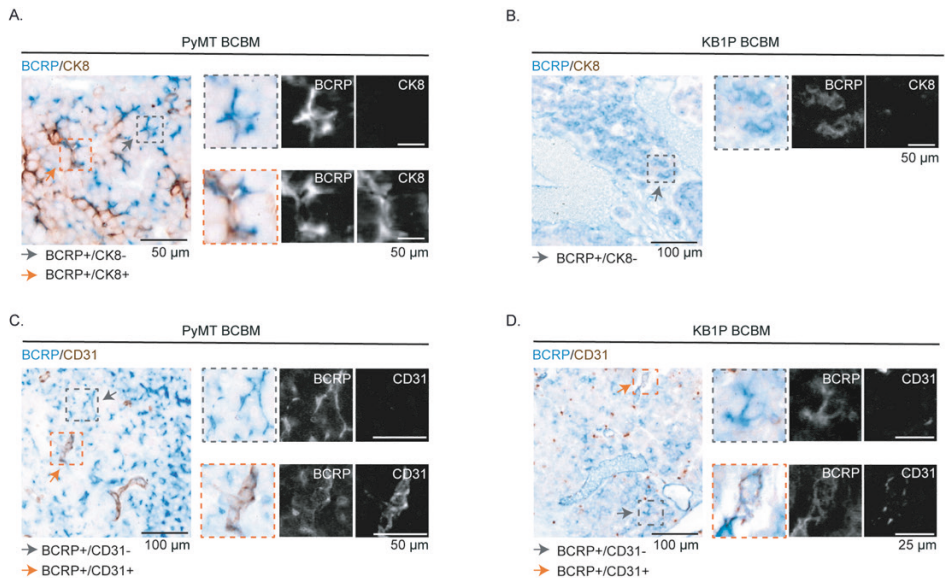


at endpoint in brain tumors generated upon intracranial injection of organoids derived from either the mammary tumors (first round), third round or sixth round of brain enrichment and quantification of the tumor area in the PyMT model (n= 5 mice *per* group). **F.** Quantification of cell proliferation using immunofluorescence staining for phospho histone H3 in organoids derived from either the mammary tumors (first round), third round or sixth round of brain enrichment and quantification of the tumor area in the PyMT model. **G.** Representative images of H&E staining and quantification of tumor area at endpoint in brain tumors generated upon intracranial injection of organoids derived from either the mammary tumors (first round), fourth round or sixth round of brain enrichment and quantification of the tumor area in the KB1P model (5 mice *per* group for the first and sixth round and 9 mice for the fourth round). **H.** Quantification of cell proliferation using immunofluorescence staining for phospho histone H3 in organoids derived from either the mammary tumors (first round), fourth round or sixth round of brain enrichment and quantification of the tumor area in the model.

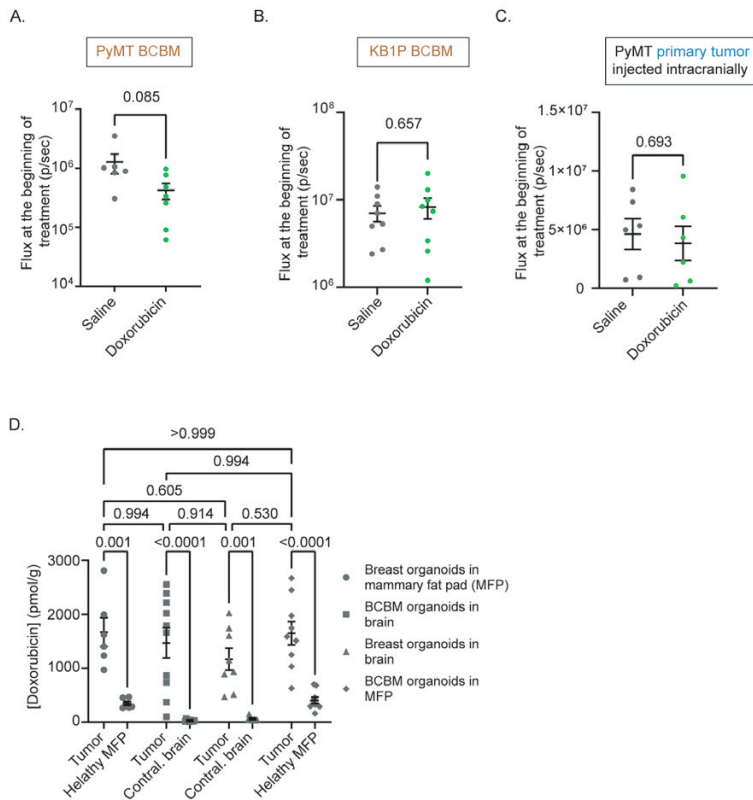


**Supplementary figure 2. Characterization of the vasculature of intracranial tumor and BCRP expression in other mouse models of extracranial metastases. A.** Representative example of T2-weighted, T1-weighted pre-contrast and T1-weighted post gadolinium (Gd) contrast Magnetic Resonance Imaging (MRI) of PyMT BCBM, two weeks after intracranial injection. **B.** Quantification of fluorescence microscopy of Texas Red (purple) detected in the healthy brain and the PyMT BCBM 2 weeks after intracranial injection of PyMT BCBM organoids (green, H2B-Dendra2-luciferase). **C.** Representative images and quantification of BCRP staining in pancreatic tumors and matched liver metastasis from the KPC GEMM model.  $n=4$  pancreatic tumors and 5 liver metastases **D.** Representative images and quantification of BCRP staining in pancreatic tumors and matched liver metastasis in mice orthotopically injected with tumor and CAFs cells derived from KPC tumors.  $n=3$  mice. **E.** Representative images and quantification of BCRP staining in breast tumors and matched lung metastases from  $k14Cre;Cdh1^{fl};Trp53^{fl}$  (KEP model).  $n=3$  mice. **F.** Representative images and quantification

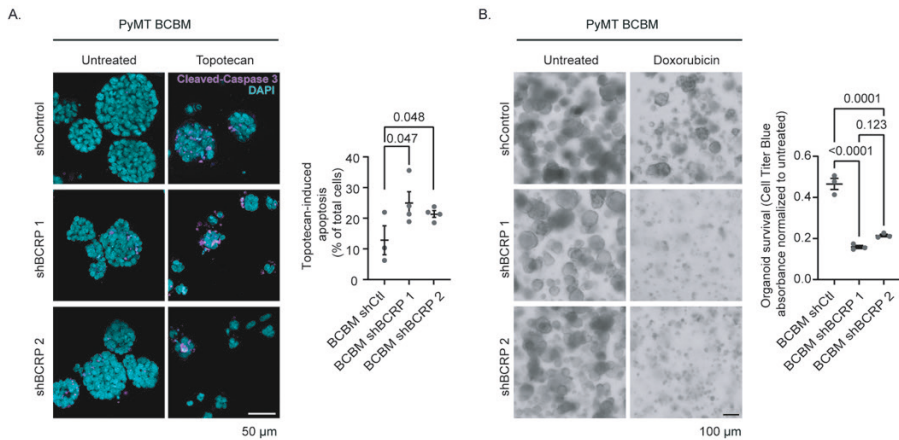
of BCRP staining in breast tumor and matched lung metastasis from PyMT orthotopic model, n=3 mice. Data are presented as mean +/- SEM.



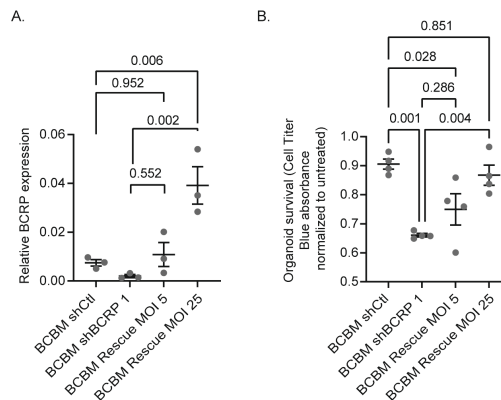
**Supplementary figure 3. Method for characterization of vascular mimicry by immunohistochemistry.** **A.** Representative images of immunohistochemistry dual staining of BCRP (blue) and CK8 (brown) in PyMT BCBM. **B.** Representative images of immunohistochemistry dual staining of BCRP (blue) and CK8 (brown) in KB1P BCBM. **C.** Representative images of immunohistochemistry dual staining of BCRP (blue) and CD31 (brown) in PyMT BCBM. **D.** Representative images of immunohistochemistry dual staining of BCRP (blue) and CD31 (brown) in KB1P BCBM. Grey arrows indicate single positive staining and orange arrows indicate double positive staining.



**Supplementary figure 4. Control experiment: equal distribution of mice in treatment groups based on IVIS signal and independency of doxorubicin penetration. A. to C.** Quantification of IVIS bioluminescent flux signal at the beginning of the treatment in mice bearing (A.) PyMT BCBM (saline treatment,  $n=6$ ; doxorubicin,  $n=7$ ), (B.) KB1P BCBM ( $n=8$  per group) and (C) PyMT primary tumor organoids injected intracranially ( $n=6$  mice per group). **D.** Quantification of doxorubicin concentration in tumors growing in the mammary fat pad compared to the healthy mammary fat pad ( $n=6$  mice), the BCBM organoids intracranially injected compared to the healthy contralateral hemisphere ( $n=10$  mice), upon injection of primary tumor organoids in the mammary fat pad ( $n=9$  mice) or BCBM organoids injected in the mammary fat pad ( $n=9$  mice). Please note that these data is compared to data also depicted in Figure 1 E. Data are presented as mean  $\pm$  SEM.



**Supplementary figure 5. Reducing BCRP expression sensitizes organoids to doxorubicin and topotecan.** **A.** Representative images and quantification of cleaved-caspase 3 immunohistochemical staining upon treatment with topotecan and **B.** representative images of organoids at endpoint and quantification of survival using Cell Titer Blue in PyMT BCBM organoids engineered with a shRNA control (shControl) or with shRNA against BCRP (shBCRP 1 and shBCRP 2), and upon treatment with doxorubicin.  $n=3$  biological repeats with 1 technical replicate *per* repeat for cleaved-caspase 3 data, and  $n=3$  biological repeats with 3 technical replicates *per* repeat for Cell Titer blue data. Data are presented as mean  $\pm$  SEM.



**S6. Rescue of BCRP expression reduces sensitivity in BCBM organoids to doxorubicin.** **A.** Relative BCRP expression in PyMT#1 organoids engineered with a shRNA control (shControl) or with shRNAs against BCRP (shBCRP 1) and shBCRP 1 transduced with BCRP cDNA, as assessed by RT-qPCR.  $n=3$  biological repeats with 3 technical replicates *per* repeat. **B.** Quantification of survival using Cell Titer Blue in PyMT BCBM organoids engineered with a shRNA control (shControl) or with shRNA against BCRP (shBCRP 1) or BCRP cDNA, and upon treatment with doxorubicin.  $n=3$  biological repeats with 1 technical replicate *per* repeat for cleaved-caspase 3 data, and  $n=4$  biological repeats with 2 technical replicates *per* repeat for Cell Titer blue data. Data are presented as mean  $\pm$  SEM.

**Table S1. RNA sequencing of BCBM organoids versus primary tumor organoids in the PyMT model.** Genes highlighted in purple are associated with a brain-like phenotype. Positive log2fold change reports genes overexpressed in the BCBM organoids.

ENSEMBLE ID and Gene name	log2FoldChange	pvalue	Comment
ENSMUSG00000030111_A2m	11.50743503	4.2873E-13	
ENSMUSG00000058354_Krt6a	10.44773019	2.19516E-10	
ENSMUSG00000036169_Sostdc1	9.884042336	2.21246E-09	High protein expression in the brain tissue (PMID: 23994639)
ENSMUSG00000116132_Gm49428	9.461504521	5.37298E-08	
ENSMUSG00000023966_Rsph9	8.469922779	1.80203E-07	
ENSMUSG00000098176_Ccdc166	8.465124837	1.31684E-06	
ENSMUSG00000020160_Meis1	8.206574831	2.58849E-10	
ENSMUSG00000055228_Zfp935	7.551062531	0.000149163	
ENSMUSG00000025089_Gfra1	7.50071735	6.37979E-06	glial cell derived neurotrophic factor
ENSMUSG00000036853_Mcoln3	7.470227563	4.41995E-05	
ENSMUSG00000047747_Rnf150	7.44402328	0.000317879	
ENSMUSG00000031253_Srxp2	7.287355698	0.000498116	expressed in neurons
ENSMUSG00000067924_Rtl8b	7.267531194	0.000371681	
ENSMUSG00000050930_Map10	7.241293822	0.000488875	
ENSMUSG00000020176_Grb10	6.946753034	1.20548E-07	
ENSMUSG00000020105_Lrig3	6.720736283	0.000129177	prognostic marker for improved survival in glioblastoma (PMID: 31245283)
ENSMUSG00000050936_Gm42743	6.655336924	0.000169298	
ENSMUSG00000078670_Fam174b	6.617448878	5.5585E-09	
ENSMUSG00000031503_Col4a2	6.458206395	7.60413E-07	
ENSMUSG00000023041_Krt6b	6.299030071	0.000133583	
ENSMUSG00000061144_Spink12	6.26284351	5.07959E-06	
ENSMUSG00000013418_B4galnt2	6.252051775	2.84139E-05	
ENSMUSG00000031502_Col4a1	6.247733898	2.05586E-08	
ENSMUSG00000027750_Postn	6.013640393	6.92602E-40	promotes neural stem cell proliferation
ENSMUSG00000073125_Xlrb3b	5.769653262	4.08071E-08	involved in synapse assemble
ENSMUSG00000025978_Rftn2	5.74483094	6.39212E-11	
ENSMUSG00000037287_Tbcel	5.624697575	7.87497E-05	

**Table S1. Continued.**

ENSEMBLE ID and Gene name	log2FoldChange	pvalue	Comment
ENSMUSG00000031841_Cdh13	5.509112571	2.90103E-17	involved in neuron disease
ENSMUSG00000060188_Cxcl17	5.402738947	0.000439942	
ENSMUSG00000031610_Scrg1	5.300342033	1.79051E-07	
ENSMUSG00000071064_Zfp827	5.289958644	3.12402E-05	
ENSMUSG00000025064_Col17a1	5.253654695	1.8349E-10	
ENSMUSG00000023885_Thbs2	5.219556409	4.02338E-05	
ENSMUSG00000100862_Gm10925	5.189981103	2.49955E-06	
ENSMUSG00000022602_Arc	5.083354713	4.83946E-18	involved in synaptic plasticity
ENSMUSG00000024697_Gna14	5.059505016	4.63829E-18	
ENSMUSG00000061527_Krt5	5.048317738	6.0389E-06	
ENSMUSG00000034612_Chst11	5.023380614	3.14122E-08	
ENSMUSG00000032595_Cdhr4	4.990573117	2.55859E-06	
ENSMUSG00000049493_Pls1	4.912750451	1.17644E-08	
ENSMUSG00000048387_Osr1	4.82607345	3.00533E-08	
ENSMUSG00000022949_Clic6	4.661371773	4.72185E-21	
ENSMUSG00000028464_Tpm2	4.6438842	1.73177E-06	
ENSMUSG00000020838_Slc6a4	4.565832176	8.98708E-07	
ENSMUSG00000021508_Cxcl14	4.463953427	1.12987E-05	
ENSMUSG00000040564_Apoc1	4.383268856	9.72209E-06	
ENSMUSG00000046768_Rhoj	4.307357166	4.15814E-15	
ENSMUSG00000023169_Slc38a1	4.276963261	5.15062E-08	
ENSMUSG00000057729_Prt3	4.236560969	2.59211E-06	
ENSMUSG00000021760_Gpx8	4.197353896	0.000183913	
ENSMUSG00000008999_Bmp7	4.194014606	0.000575485	
ENSMUSG00000017453_Pipox	4.174009268	3.00673E-07	
ENSMUSG00000048058_Ldlrad3	4.08515514	2.17958E-07	
ENSMUSG00000057880_Abat	4.07346617	0.000344605	metabolism of neurotransmitter
ENSMUSG00000104610_Gm567	4.067014142	0.000487478	
ENSMUSG00000021728_Emb	4.004385836	1.21867E-19	
ENSMUSG00000020000_Moxd1	3.988698202	4.057E-09	
ENSMUSG00000018593_Sparc	3.969244384	3.04945E-14	
ENSMUSG00000057315_Arhgap24	3.958070395	0.000399617	
ENSMUSG00000028475_Spaar	3.950008606	7.222E-05	
ENSMUSG00000021186_Fbln5	3.891197428	7.578E-08	

Table S1. Continued.

ENSEMBLE ID and Gene name	log2FoldChange	pvalue	Comment
ENSMUSG00000046688_Tifa	3.856610835	0.000411768	
ENSMUSG00000067818_Myl9	3.845766175	6.75724E-06	
ENSMUSG00000091423_Gm17509	3.83620368	8.51972E-11	
ENSMUSG00000049907_Rasl11b	3.772587559	6.01407E-05	
ENSMUSG00000079014_Serpina3i	3.767763634	3.81602E-05	
ENSMUSG00000044229_Nxpe4	3.761473855	0.000633936	
ENSMUSG00000021795_Sftpd	3.730801293	1.17944E-05	
ENSMUSG00000039316_Rftn1	3.726642002	0.000206614	
ENSMUSG00000010064_Slc38a3	3.704702799	0.000813906	
ENSMUSG00000041696_Rasl12	3.687365405	1.53013E-06	
ENSMUSG00000051879_Krt71	3.669431158	0.000620703	
ENSMUSG00000043496_Trl	3.632934873	7.14446E-06	
ENSMUSG00000015766_Eps8	3.578805909	1.68794E-08	
ENSMUSG00000020427_Igfbp3	3.516250234	9.52067E-05	
ENSMUSG00000041449_Serpina3h	3.440925258	0.000208023	
ENSMUSG00000053113_Socs3	3.418147567	3.78054E-07	
ENSMUSG00000021950_Anxa8	3.412029096	2.19388E-09	
ENSMUSG00000022043_Trim35	3.382752578	5.91354E-12	
ENSMUSG00000030088_Aldh1l1	3.302824391	0.000129323	
ENSMUSG00000000567_Sox9	3.286035673	4.42537E-12	
ENSMUSG00000034586_Hid1	3.271387086	3.80613E-09	Protein expression enhanced in brain tissue
ENSMUSG00000022510_Trp63	3.258267701	0.000393511	
ENSMUSG00000040653_Ppp1r14c	3.242886238	5.24033E-07	influences neuronal activity
ENSMUSG00000029001_Fbxo44	3.213500984	0.000130681	
ENSMUSG00000034127_Tspan8	3.186123811	0.00055074	
ENSMUSG00000026482_Rgl1	3.162661503	0.000478731	
ENSMUSG00000091971_Hspa1a	3.133752047	0.000147479	
ENSMUSG00000022885_St6gal1	3.112199135	1.2502E-06	
ENSMUSG00000020846_Rflnb	3.100001922	7.45691E-06	
ENSMUSG00000089945_Pakap	3.073781017	1.47043E-05	
ENSMUSG00000032373_Car12	3.067952199	1.17845E-09	
ENSMUSG00000089652_Gm16025	3.054505645	0.000553515	involved in response to neurotoxicity
ENSMUSG00000030077_Ch11	3.034200835	0.000549872	



**Table S1. Continued.**

ENSEMBLE ID and Gene name	log2FoldChange	pvalue	Comment
ENSMUSG00000067279_Ppp1r3c	3.030096583	1.4237E-05	
ENSMUSG000000022665_Ccdc80	2.915245267	0.000152395	
ENSMUSG00000024521_Pmaip1	2.896546215	0.000295438	
ENSMUSG00000103037_Pcdhgb1	2.876697333	5.71807E-06	
ENSMUSG000000029070_Mxra8	2.812173353	1.39695E-09	
ENSMUSG000000031342_Gpm6b	2.804474788	9.25957E-05	
ENSMUSG000000073415_Gm10501	2.796707606	0.000165253	
ENSMUSG000000027656_Ccn5	2.776564228	1.71228E-05	
ENSMUSG000000038059_Smim3	2.711123365	2.06975E-06	
ENSMUSG000000061048_Cdh3	2.684347733	0.000631009	
ENSMUSG000000022995_Enah	2.639616446	0.000596313	
ENSMUSG000000036256_Igfbp7	2.5964635	1.58634E-05	
ENSMUSG000000031133_Arhgef6	2.589549691	1.14797E-06	
ENSMUSG000000068335_Dok1	2.493198202	6.9839E-06	
ENSMUSG000000026473_Glul	2.472047934	3.65674E-06	
ENSMUSG000000006693_Loxl3	2.450032992	7.67937E-06	
ENSMUSG000000039646_Vasn	2.439038777	0.0005532	transmembrane protein involved in malignant progression and angiogenesis in glioma
ENSMUSG000000028641_P3h1	2.422059923	2.28086E-06	
ENSMUSG000000001911_Nfix	2.412345656	9.18818E-06	
ENSMUSG000000022146_Osmr	2.4082886	3.02059E-05	
ENSMUSG000000026421_Csrp1	2.349010377	6.30162E-06	
ENSMUSG000000025969_Nrp2	2.34691477	1.42052E-05	
ENSMUSG000000064105_Cnrm2	2.335261667	0.000280944	
ENSMUSG000000019055_Plod1	2.291547784	2.48876E-05	
ENSMUSG000000062609_Kcnj15	2.273898309	9.83466E-06	
ENSMUSG000000068735_Trp53i11	2.213300889	0.000806708	
ENSMUSG000000052837_Junb	2.212260273	9.85041E-06	
ENSMUSG000000017446_C1qtnf1	2.159894303	0.000395325	
ENSMUSG000000022952_Runx1	2.155320407	2.94288E-06	
ENSMUSG00000117975_Itprip	2.154340267	2.61636E-05	
ENSMUSG000000041895_Wipi1	2.086118758	0.000363696	
ENSMUSG000000034634_Ly6d	1.991963333	0.000718688	

Table S1. Continued.

ENSEMBLE ID and Gene name	log2FoldChange	pvalue	Comment
ENSMUSG00000041119_Pde9a	1.837415152	0.000249679	cGMP-specific phosphodiesterase expressed in neurons throughout the brain
ENSMUSG00000020733_Slc9a3r1	1.836524457	0.000331889	
ENSMUSG00000036181_Hist1h1c	1.824526665	2.92094E-05	
ENSMUSG00000018661_Cog1	1.656348	0.000350176	
ENSMUSG00000053560_Ier2	1.643701055	0.000464122	
ENSMUSG00000030605_Mfge8	1.630282951	0.000169617	
ENSMUSG00000064373_Selenop	1.627658788	0.000319217	
ENSMUSG00000027276_Jag1	1.624920139	0.000650661	Expressed in the vasculature of glioblastoma (PMID: 22296176)
ENSMUSG00000017057_Ii13ra1	1.56502907	0.000810366	
ENSMUSG00000039568_Ubald1	1.546112373	0.000701612	
ENSMUSG00000000253_Gmpr	1.538036939	0.00082183	
ENSMUSG00000117924_Tmem223	1.509613113	0.000782406	
ENSMUSG00000028364_Tnc	1.468981834	0.000598048	
ENSMUSG00000025666_Tmem47	-1.456576516	0.000545716	
ENSMUSG00000058135_Gstm1	-1.514235915	0.000349531	
ENSMUSG00000029621_Arpc1a	-1.551062303	0.000160469	
ENSMUSG00000016503_Gtf3a	-1.583829906	0.000502193	
ENSMUSG00000038859_Baiap2l1	-1.603474739	0.000326327	
ENSMUSG00000056076_Eif3b	-1.662685861	0.000480586	
ENSMUSG00000066551_Hmgb1	-1.731589989	0.000391657	
ENSMUSG00000068566_Myadm	-1.764689921	0.000817945	
ENSMUSG00000079111_Kdelr2	-1.776017585	0.000287331	
ENSMUSG00000047735_Samd9l	-1.933395644	0.000342483	
ENSMUSG00000029610_Aimp2	-2.033221068	0.000451143	
ENSMUSG00000036639_Nudt1	-2.05576457	2.21376E-05	
ENSMUSG00000063428_Ddo	-2.060160714	0.000692188	
ENSMUSG00000029635_Cdk8	-2.165866919	0.000112929	
ENSMUSG00000053553_3110082117Rik	-2.173128816	0.000673198	
ENSMUSG00000057963_Itpk1	-2.177876418	0.000569963	
ENSMUSG00000041313_Slc7a1	-2.205985166	4.48217E-05	
ENSMUSG00000058258_Idi1	-2.211004021	0.00016181	
ENSMUSG00000031575_Ash2l	-2.257163696	9.96087E-06	

**Table S1. Continued.**

ENSEMBLE ID and Gene name	log2FoldChange	pvalue	Comment
ENSMUSG00000044906_4930503L19Rik	-2.274388204	0.000385637	
ENSMUSG000000062949_Atp11c	-2.278260155	5.6967E-05	
ENSMUSG000000026779_Mastl	-2.358718847	0.000199161	
ENSMUSG000000024379_Tslp	-2.372809036	0.000384826	
ENSMUSG000000031803_B3gnt3	-2.461989516	3.43869E-05	
ENSMUSG000000031762_Mt2	-2.51628375	0.000544862	
ENSMUSG000000066861_Oas1g	-2.520224199	0.000249153	
ENSMUSG000000046718_Bst2	-2.54196184	0.000183921	
ENSMUSG000000029561_Oasl2	-2.57128959	0.000720785	
ENSMUSG000000075014_Gm10800	-2.574363565	0.000822355	
ENSMUSG000000040483_Xaf1	-2.607997366	0.000232783	
ENSMUSG000000096519_Gm10721	-2.623599118	0.000538049	
ENSMUSG000000095547_Gm10719	-2.651155774	0.000480605	
ENSMUSG000000075015_Gm10801	-2.656728073	0.000677484	
ENSMUSG000000056055_Sag	-2.656946828	0.000137235	
ENSMUSG000000021614_Vcan	-2.695146368	0.000248376	
ENSMUSG000000029762_Akr1b8	-2.705559747	1.38899E-08	
ENSMUSG000000041827_Oasl1	-2.722107527	7.70709E-05	
ENSMUSG000000029648_Flt1	-2.729767692	0.000696803	
ENSMUSG000000029298_Gbp9	-2.756804623	0.000152644	
ENSMUSG000000040345_Arhgap9	-2.772188222	4.05412E-08	
ENSMUSG000000047250_Ptgs1	-2.774215048	9.99206E-05	
ENSMUSG000000041147_Brca2	-2.79079542	8.05348E-07	
ENSMUSG000000044252_Osbp1a	-2.843926244	3.25499E-05	
ENSMUSG000000030041_M1ap	-2.9097778	0.000103696	
ENSMUSG000000074818_Pdzd7	-3.169427155	0.000808275	
ENSMUSG000000035692_lsg15	-3.1980649	0.000112605	
ENSMUSG000000043085_Tmem82	-3.238818662	0.000143663	
ENSMUSG000000100009_Gm7967	-3.590280897	4.04137E-05	
ENSMUSG000000031297_Slc7a3	-3.594781444	0.000135204	
ENSMUSG000000061654_Spry3	-3.636956409	2.15617E-07	
ENSMUSG000000044165_Bcl2l15	-3.636956409	0.000285261	
ENSMUSG000000028100_Nudt17	-3.637089322	2.84799E-08	
ENSMUSG000000037463_Fbxo27	-3.639691839	0.000100231	
ENSMUSG000000043613_Mmp3	-3.673909158	0.000821764	
ENSMUSG000000032496_Ltf	-3.729766443	0.000541426	
ENSMUSG00000018893_Mb	-3.875745082	0.000142036	

**Table S1. Continued.**

<b>ENSEMBLE ID and Gene name</b>	<b>log2FoldChange</b>	<b>pvalue</b>	<b>Comment</b>
ENSMUSG00000038067_Csf3	-3.886889901	1.73617E-07	
ENSMUSG00000078920_lfi47	-3.897284254	0.000718947	
ENSMUSG00000040838_Gm11639	-3.970546904	1.6033E-06	
ENSMUSG00000030107_Usp18	-4.401372817	1.97111E-09	
ENSMUSG00000030693_Klk10	-4.49166591	4.13979E-10	
ENSMUSG00000110298_Gm8189	-4.511143146	9.65621E-07	
ENSMUSG00000089728_Clec2f	-4.538109198	1.3546E-05	
ENSMUSG00000020728_Cep112	-4.583021393	1.87537E-11	
ENSMUSG00000034459_lfit1	-4.658735894	8.70814E-06	
ENSMUSG00000053522_Lgals7	-4.660359351	4.31064E-09	
ENSMUSG00000086321_Gm11413	-4.892516103	2.49097E-17	
ENSMUSG00000027669_Gnb4	-5.041239804	4.70269E-06	
ENSMUSG00000020774_Aspa	-5.159096842	3.05334E-10	
ENSMUSG00000095872_Gm15128	-5.164635273	3.56544E-05	
ENSMUSG00000033361_Prrg3	-5.252003267	0.000103985	
ENSMUSG00000052271_Bhlha15	-5.320072219	0.000623324	
ENSMUSG00000074607_Tox2	-5.370342652	0.00014437	
ENSMUSG00000100816_Gm28321	-5.514669457	1.43686E-09	
ENSMUSG00000046699_Slitrk4	-5.839593144	6.91468E-05	
ENSMUSG00000037010_Apln	-5.932135141	0.000120696	
ENSMUSG00000089929_Bcl2a1b	-7.201713205	0.000536753	
ENSMUSG00000096834_Gm15127	-7.919625765	3.31505E-05	
ENSMUSG00000082035_Rpl17-ps8	-7.933085328	2.48483E-05	
ENSMUSG00000034755_Pcdh11x	-7.981822922	1.88839E-05	
ENSMUSG00000079387_Luzp4	-8.022731775	3.85722E-05	
ENSMUSG00000025934_Gsta3	-8.045216132	3.8798E-09	
ENSMUSG00000113882_Gm48550	-8.221583234	1.50423E-06	
ENSMUSG00000099375_Gm28187	-8.291028406	0.00011842	
ENSMUSG00000103464_Gm38246	-8.565942167	3.33378E-08	
ENSMUSG00000022652_Morc1	-8.870766852	2.08115E-08	
ENSMUSG00000094941_Gm15093	-9.014290897	2.85562E-06	
ENSMUSG00000118575_BX908741.1	-9.345743264	1.3646E-07	
ENSMUSG00000091679_Vmn2r96	-9.722141332	1.36508E-08	
ENSMUSG00000103071_Gm38110	-10.09320408	1.30391E-09	

**Table Supplementary 2. Sequence of shRNA and rescue constructs used in the study.**

Name	Sequence
shRNA BCRP 1	GCCAGTCTATGTTACCTCTTT
shRNA BCRP 2	CCCTGGCTTGATGATTATTA
Rescue BCRP	GCCACCATGTCTCCAGTAATGACCACGTGTAGTACCAATGTGCGAGAGAAAC AACAACGGCCTTCCTAGGATGAACTCCAGAGCCGTTAGGACGCTCGCAGAAG GAGATGTGTTGAGTTTTTCATCACATCACCTATCGAGTGAAAGTAAAGAGTGGGT TTCTAGTCCGGAACAGTTGAGAAAAATACTATCAGATATCAATGGGATCATG AAACCTGGCCTTAATGCTATTCTGGGACCCACAGGCGGAGGCAAGTCTTCGTT GCTAGATGTCTTAGCAGCAAGGAAAGATCCAAAGGGATTATCTGGAGATGTTTT GATAATGGAGCACCTCAACCTGCCATTCAAATGCTGTTTCAGGTATGTGGT TCAAGATGACGTTGTGATGGGCACCCTGACAGTGAGAGAAAACCTTACAGTTCT CAGCAGCTCTTCGACTCCAACAACCTATGAAGAATCAGAAAAAATGAACGGA TTAACACAATCATTAAAGAGTTAGGTCTGGAAAAAGTAGCAGATTCTAAGGTCG GAACTCAGTTTACCGTGGCATCTCTGGAGGAGAAAAGAAAAGGACAAGCATAG GGATGGAGCTGATCACTGACCCTTCCATCCTCTTCTGGATGAGCCCACGACT GGTTTGGACTAAGCACAGCGAATGCTGTCCTTTTGCTCCTGAAAAGGATGTCT AAACAGGGTCGAACAATCATCTTCTCCATTCATCAGCCTCGGTATCCATCTTA AGTTGTTTGACAGCCTCACCTTACTGGCTTCCGGGAAAACCTCGTGTTCATGGG CCAGCACAGAAGGCCTTGGAGTACTTTGCATCAGCAGGTTACCACTGTGAGC CCTACAACAACCCTGCGGATTTTTCTTGTGATGTCATCAATGGAGATTCTTCTG CTGTGATGTTAAATAGAGAGGAACAAGACAATGAAGCAACAAGACTGAAGAG CCTTCCAAGGGAGAGAAGCCAGTAATAGAAAATTTATCTGAGTTTTATATCAACT CTGCCATCTATGGAGAAACAAAAGCTGAATTAGATCAACTTCCAGGAGCTCAG GAAAAGAAAGGAACATCGGCCTTCAAAGAGCGAGTCTTTGTTACCTTTACTGT CACCAGCTCCGATGGATTGCCAGGCGCTCATTAAAAACTTGCTCGGGAACC CTCAAGCTTCTGTTGCTCAGTTAATTGTTACAGTCATACTGGGGCTTATTATTGG TGCCATTTACTTTGATCTGAAATATGATGCCGCTGGAATGCAAAATAGAGCTGG AGTTTTGTTTTTCTGACTACCAACCAGTGTTTTTCCAGTGTGTCAGCTGTGGA GCTGTTGCTAGTGAGAAGAACTTTCATACATGAGTACATCAGTGGATATACA GAGTGTCTTCTACTTCTTTGGAAAGGTGATGCTGATTTACTCCCCATGAGGTT CTTGCCAAGTGTTATATTCACCTTGATATTATACTTCATGTTAGGACTGAAGAAGA CGGTGGATGCTTTTTTCATCATGATGTTTACCCTTATAATGGTGGCTTATACGGC CAGTTCATGGCACTGGCCATAGCCACAGGCCAAAGTGTGGTGTCTGTAGCAA CACTTCTCATGACAATCGCTTTTGATTTATGATGCTCTTTCTGGCCTCTGGT GAATCTCAGAACCATTGGGCCTTGGCTGTCCTGGCTTCAGTACTTTAGCATTCT CTCGATATGGCTTACAGCTTTGCAGTATAATGAATCTTGGGACAAGAGTTTTG TCCAGGATCAATGTAACGGACAACAGCACTTGTGTTAACAGCTATGCAATATG TACTGGTAACGAGTACTTGATAAATCAGGGCATCGAACTGTCACCTTGGGGAC TGTGGAAGAATCATGTGGCCCTGGCTTGATGATTATATCTTCCCTACAATTGC CTACCTGAAATTGTTGTTTCTTAAAAAGTATTCTGCCACCAACTTCTCCCTGCT GAAGCAGGCCGGCGACGTGGAGGAGAACCCCGGCCCAAGCTCCCGGGAG CTTGATATCCATTTCCGGATCTGATCAGCACGTGATGAAAAAGCCTGAACTCA CCGCGACGCTGTGCGAGAAGTTTCTGATCGAAAAGTTCCAGCAGCGTCTCCGA CCTGATGCACTCTCGGAGGGCGAAGAATCTCGTGTCTTTCAGCTTCGATGTAG GAGGGCGTGGATATGTCCTGCGGGTAAATAGCTGCGCCGATGGTTTCTACAAA GATCGTTATGTTTATCGGCACTTTGCATCGGCCGCGCTCCCGATTCCGGAAGT GCTTGACATTGGGGAATTCAGCGAGAGCCTGACCTATTGCATCTCCCGCCGT

**Table Supplementary 2. Continued.**

Name	Sequence
	GCACAGGGTGTACGTTGCAAGACCTGCCTGAAACCGAACTGCCCGCTGTTCTGCAGCCGGTCGCGGAGGCCATGGATGCGATCGCTGCGGCCGATCTTAGCCAGACGAGCGGGTTCGGCCCATTTCGGACCGCAAGGAATCGGTCAATACACTACATGGCGTGATTTTCATATGCGCGATTGCTGATCCCCATGTGTTCACTGGCAAACCTGTGATGGACGACACCGTCAGTGCCTCCGTCGCGCAGGCTCTCGATGAGCTGATGCTTTGGGCGGAGGACTGCCCCGAAGTCCGGCACCTCGTGCACGCGGATTCGGCTCCAACAATGTCCTGACGGACAATGGCCGCATAACAGCGGTCATTGACTGGAGCGAGGCGATGTTTCGGGGATTCCCAATACGAGGTCGCCAACATCTTCTTCTGGAGGCCGTGGTTGGCTTGATGGAGCAGCAGACGCGCTACTTCGAGCGGAGGCATCCGGAGCTTGCAGGATCGCCGCGGCTCCGGGCGTATATGCTCCGCA TTGGTCTTGACCAACTCTATCAGAGCTTGGTTGACGGCAATTCGATGATGCAGCTTGGGCGCAGGGTCGATGCGACGCAATCGTCCGATCCGGAGCCGGGACTGTCGGGCGTACACAAATCGCCCGCAGAAGCGCGGCCGTCTGGACCGATGGCTGTGTAGAAGTACTCGCCGATAGTGAAACCGACGCCCCAGCACTCGTCCGAGGGCAAAGGAATAG







# Chapter 3

Re-purposing the pro-senescence properties of doxorubicin to introduce immunotherapy in breast cancer brain metastasis.

**Rebeca Uceda-Castro**<sup>\*</sup>, Andreia S. Margarido<sup>\*</sup>, Lesley Cornet, Serena Vegna, Kerstin Hahn, Ji-Ying Song, Diana A. Putavet, Mariska van Geldorp, Ceren H. Çitirikkaya, Peter L.J. de Keizer, Leon C. ter Beek, Gerben R. Borst, Leila Akkari, Olaf van Tellingen, Marike L.D. Broekman, Claire Vennin<sup>#</sup> and Jacco van Rheenen<sup>#</sup>

<sup>#</sup> Correspondence

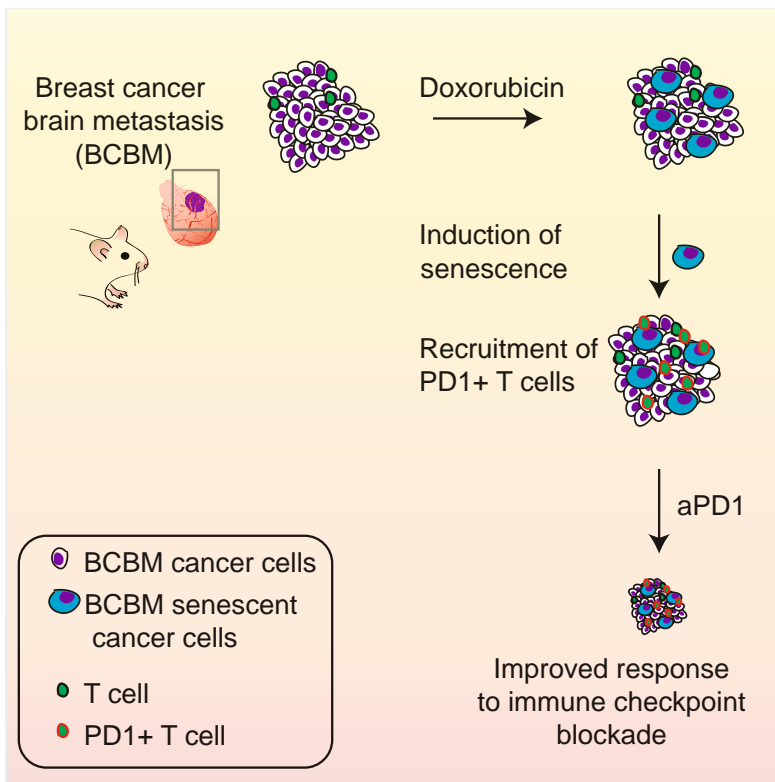
<sup>\*</sup> Equal contribution

Published in Cell Report Medicine 2022



## ABSTRACT

An increasing number of breast cancer patients develop brain metastases (BM). Standard-of-care treatments are largely inefficient, and breast cancer brain metastasis (BCBM) patients are considered untreatable. Immunotherapies are not successfully employed in BCBM, in part because breast cancer is a 'cold' tumor and also because the brain tissue has a unique immune landscape. Here, we used two immunocompetent models of BCBM derived from PyMT and Neu mammary tumors to test how harnessing the pro-senescence properties of doxorubicin can be used to prime the specific immune BCBM microenvironment. We reveal that BCBM senescent cells, induced by doxorubicin, trigger the recruitment of PD1-expressing T cells to the brain. Importantly, we demonstrate that induction of senescence with doxorubicin improves the efficacy of immunotherapy with anti-PD1 in BCBM in a CD8 T cell-dependent manner, thereby providing an optimized strategy to introduce immune-based treatments in this lethal disease.



## INTRODUCTION

BCBM is a leading cause of death for breast cancer (BC) patients. A recent meta-analysis has shown that for patients with metastatic BC, BCBM affects 31% of patients from the Her2<sup>+</sup> subtype, 32% of patients with triple-negative BC and 15% of patients with hormone receptor positive/Her2<sup>-</sup> disease, and their overall survival is dire [1,3]. Standard-of-care treatments for BCBM comprise systemic therapies with chemotherapies and targeted agents, radiotherapy and neurosurgical resection. Additionally, for Her2<sup>+</sup> BCBM patients, treatment with trastuzumab-deruxtecan has shown some clinical benefits [4]. However standard-of-care treatments are largely unsuccessful. This is in part due to the presence of the impermeable blood brain barrier (BBB) and the blood brain tumor barrier (BTB) as well as important resistance to chemotherapy and radiotherapy [5]. Consequently, survival of BCBM patients remains dreary and there is an urgent need to develop better, alternative therapeutic strategies for this disease [1,2].

Immunotherapies have revolutionized cancer treatment in several solid tumor types [6-10], however only a limited number of clinical trials have explored the efficacy of immunotherapy in BC patients. Additionally, BCBM patients have historically been excluded from those trials, due to the brain tissue that has long been depicted as an immune-privileged site [11,12]. However, specific immune reactions still occur in brain tumors and are commonly characterized by a high contribution of tumor-promoting myeloid cells, a low penetrance of cytotoxic T cells and high T-cell exhaustion, which hinder the efficacy of immunotherapies [13,14]. Recent findings in melanoma and lung BM have however challenged this view by demonstrating that some of those patients may benefit from immunotherapy [6]. Those encouraging findings are concomitant with the recent inclusion of BCBM patients in a number of clinical trials assessing the efficacy of immune-based treatments or other therapies [15-17]. Nevertheless, to date, nab-paclitaxel combined with anti-PD-L1 is the only FDA approved strategy for immunotherapy in triple negative BCBM, however patients' response to the treatment remains limited [15]. Consequently, exploring new opportunities to prime the specific immune BCBM environment is required to introduce immunotherapy in this disease.

Several studies report attempts to render 'cold' tumors more prone to respond to immunotherapies. For example, conventional chemotherapies can display immunomodulatory properties and influence immune responses. On the one hand, chemotherapies may modify the immune-properties of cancer cells, for instance by increasing cytokine production or provoking chromosomal instability or immunogenic cell death (reviewed in [18,19]). On the other hand, chemotherapies can also directly influence the properties of immune cells such as regulatory T cells (Tregs), tumor-associated myeloid cells or Natural Killer (NK) cell [20-23]. These findings have recently led to clinical applications,

where the immunomodulatory properties of chemotherapies are exploited to recruit immune cells to tumor sites and to sensitize 'cold' tumors to immunotherapies [15,24-26].

In addition to killing cancer cells, chemotherapeutics can also induce a senescence state in the cancer cell population. Importantly, senescent cells are known to trigger a remodeling of the tumor microenvironment (TME) as well as of the tumor immune landscape *via* secretion of factors that belong to the Senescence Associated Secretory Phenotype (SASP) [27,28]. Multiple senescence phenotypes have been characterized and vary depending on the senescence-induction modalities. Additionally, the effects of senescence and of the SASP on the immune TME are context- and tumor type-dependent [29,30]. However, the effects of chemotherapy-induced senescent cells on shaping the immune landscape of BCBM have not been assessed before.

The rareness of clinical trials in BCBM, the historical exclusion of BCBM patients from most immunotherapy trials [1,5], and the scarcity of immunocompetent BCBM animal models limit the study of strategies to prime the specific immune microenvironment of BCBM. Here, we test whether inducing senescence in BCBM may be used to introduce immunotherapy in this disease. We used a PyMT BCBM pre-clinical mouse model, which harbors an intact immune system and recapitulates key immune features of human BCBM. We assessed the ability of doxorubicin to remodel the BCBM immune landscape. Doxorubicin is an anthracycline antibiotic that has been shown to induce senescence in a range of cancer types in a BMP4-Smad, p21 and p16-dependent manner [31,32]. Additionally, liposomal-doxorubicin can cross the BBB and the BTB [33-35]. We demonstrate that inducing senescence with doxorubicin in BCBM tumor cells triggers a recruitment of PD1-expressing T cells to BCBM lesions, and this can be used to subsequently improve the efficacy of immunotherapy with anti-PD1. We confirm the efficacy of this therapeutic strategy in a second BCBM model derived from NeuT mammary tumors. Together, we present evidence that chemotherapy-induced senescence renders BCBM sensitive to immunotherapy with checkpoint inhibitors, thereby opening new avenues for improved clinical management of this dreadful disease.

## RESULTS

### ***Generation and characterization of a novel PyMT BCBM model.***

In order to identify new approaches to render BCBM sensitive to immunotherapy, we employed a mouse BCBM model generated *via* serial intracranial transplantations and carotid injections in immunocompetent Friend Virus B (FVB) inbred mice of tumor pieces derived from MMTV-PyMT mice that carry an E-cadherin-mCFP transgene [36] (**see Method section, Fig. 1A and [37]**). Following six rounds of enrichment in the brain, we generated organoids from the BCBM and we engineered them with H2B-Dendra2

and luciferase constructs for imaging purposes (from herein referred to as 'PyMT BCBM organoids'). Organoids are self-assembling miniature organ-like 3D *in vitro* structures that recapitulate with a high fidelity features of *in vivo* tumors such as cellular heterogeneity [38], and which can be manipulated *in vitro* to express for instance fluorescent reporters. Tumor organoids have been recently used to accurately model cancer biology and to perform *in vitro* pre-clinical testings [39]. The PyMT BCBM organoids were cultured in 3D basal membrane extract (BME) matrices to avoid inducing artificially high metastatic properties which may arise upon 2D culturing [40]. We dissociated the PyMT BCBM organoids into single cells and injected them in the mouse carotid. In this context, the brain enriched tumor cells were able to extravasate and to survive as single cells in the brain or to form BCBM in 3 out of 13 mice. This moderate metastatic efficiency is in line with a fairly sporadic spread to the brain in patients with metastatic breast cancer but demonstrates the ability of the PyMT BCBM organoids to home in this organ (**Fig. 1B**). Intracranial injections of the PyMT BCBM organoids led to a human end point of 33 days, providing a time window for therapeutic testing in contrast to other models that often cause death within two to three weeks after injection. Although these characteristics are required for pre-clinical studies like ours, a large number of animals is needed to study early BCBM formation.

Upon intracranial transplantations of the PyMT BCBM organoids, we observed BCBM formation in 100% of the mice. We monitored BCBM progression upon intracranial and carotid injections by IVIS imaging in a small cohort of mice (**Supplementary Fig. 1A, B**). Although a number of other BCBM models have been reported to develop in the brain dura [41], the PyMT BCBM was found to grow in the brain parenchyma upon carotid injection (**Supplementary Fig. 1C**). Additionally, multiple lesions of various sizes were found in the brain of mice injected in the carotid at humane endpoint, however we cannot exclude that large metastases result from the fusion of multiple smaller metastases (**Supplementary Fig. 1C**). Moreover, injection of PyMT BCBM organoids into the carotid resulted in the development of metastasis in the abdominal cavity near the uterus horn and in the spleen in 7% of mice (**Supplementary Fig. 1D**). Histological assessments demonstrated that BCBMs that are formed upon carotid or intracranial transplantations display similar histopathological features (Fig. 1C). Furthermore, mice that developed BCBM upon carotid injection had a mean survival of 70 days compared to 33 days for mice injected intracranially (**Supplementary Fig. 1E**).

In order to test whether the immune landscape evolves naturally in PyMT BCBM derived from intracranial injections, we compared immune infiltrates in PyMT BCBM derived from carotid *versus* intracranial injections using immunohistochemistry analyses. We did not find significant differences in cell number and tissue distribution of CD4 T cells, CD8 T cells, macrophages (F4/80), neutrophils (Ly6G) and regulatory T cells (Foxp3) (**Supplementary Fig. 2A**). Additionally, we did not observe significant differences in the number of PD1

expressing cells in BCBM generated by both procedures (**Supplementary Fig. 2A**). Therefore, considering the similarities between PyMT BCBMs derived from intracranial and intracarotid injections and for improved experimental reproducibility and standardization, we used intracranial injections of PyMT BCBM organoids derived from the sixth round of enrichment for the rest of our study.

We next tested whether our mouse model of PyMT BCBM recapitulates features of the human disease. Immunohistopathological analyses demonstrated that the PyMT mouse BCBM resembled the human counterpart (**see Method section, Fig. 1C, and Supplementary Fig. 2B**). Additionally, Magnetic Resonance Imaging (MRI) and Spectroscopy (MRS) confirmed that the mouse BCBM model mimics features of human brain metastasis (**Supplementary Fig. 2C, D and Methods**) [42,43]. Next, we performed immunohistochemical analyses of immune cell infiltration in human BCBM. Tumor-infiltrating lymphocytes (TILs, arrows), CD4 and CD8 T cells as well as cells expressing PDL1 were observed in human BCBM sections (**Fig. 1D, top panel**). High TILs content and PDL1 expression are prognostic markers for good response to immunotherapy [44], consequently this suggests that human BCBM may be targeted with immune-based treatments such as checkpoint inhibitors. Importantly, TILs, T cells and PD1-positive cells were also found to infiltrate the mouse PyMT BCBM (**Fig. 1D, lower panel**), however it is unknown whether the level of PD1<sup>+</sup> T cell infiltration is sufficient to elicit a response to immune checkpoint blockade. We next mapped the immune landscape of the mouse PyMT BCBM derived from intracranial injections using flow cytometry (**see Supplementary Fig. 3 for gating strategies**). The mouse PyMT BCBM was infiltrated with both immune cells of myeloid origin (neutrophils, monocytes, microglia, monocyte-derived macrophages (MDMs)), as well as lymphoid cells such as T and B cells (**Fig. 1E**). This is in line with previously published work in human BCBM [13,45,46] and warrants the use of the PyMT BCBM mouse model for designing innovative strategies for immunotherapies in this disease.

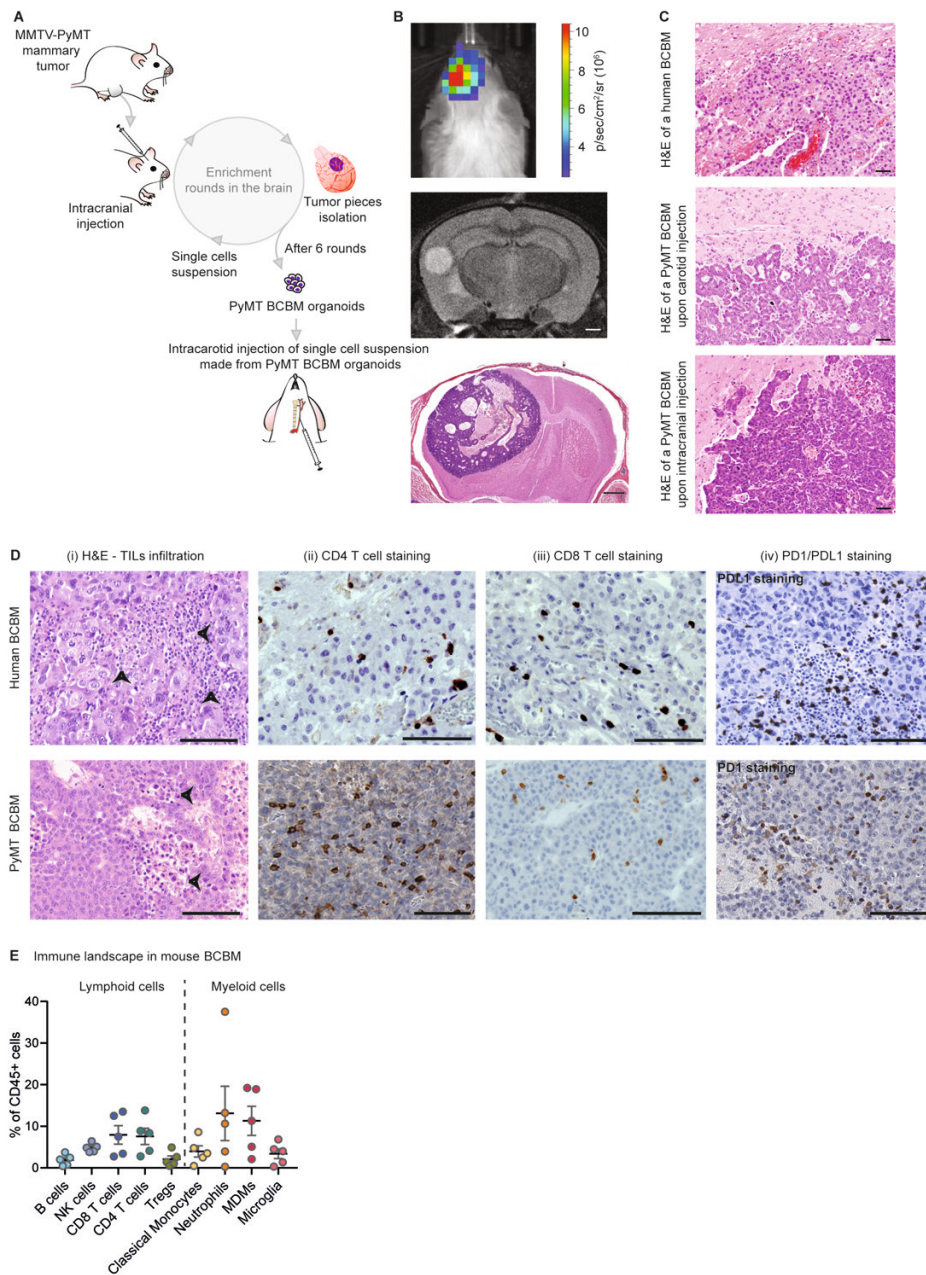


**Figure 1. The mouse BCBM mimics immune features of the human disease. A.** Schematic representation of the generation of the mouse PyMT BCBM model. **B.** Representative images of a metastasis formation upon carotid injection. BCBM organoids were made as single cells just before injection in the carotid. Metastasis formation was confirmed by bioluminescence (upper panel), MRI (medium panel) and H&E staining (lower panel). Scale bar:1 mm. **C.** Representative images of H&E staining of human BCBM (upper panel) and of mouse PyMT BCBMs generated upon carotid (middle



panel) and intracranial (lower panel) injections of PyMT BCBM organoids. Scale bar: 50  $\mu\text{m}$ . **D.** Representative images of H&E and immunohistochemistry staining for CD4, CD8 and PDL1/PD1 in human (top panel) and PyMT BCBM derived from intracranial injection (lower panel). On H&E images, black arrows point to tumor infiltrated lymphocytes (TILs). Scale bar: 100  $\mu\text{m}$ . **E.** Quantification of immune cell populations infiltrated into the mouse BCBM, as assessed by flow cytometry.  $n=5$  mice, data are presented as averaged percentage cells out of CD45<sup>+</sup> immune cells.

### ***Doxorubicin induces senescence in BCBM tumor cells.***

We next investigated whether doxorubicin can trigger senescence in BCBM. Doxorubicin is an anthracycline antibiotic, which has been shown to induce senescence in a variety of cell lines both *in vitro* and *in vivo* [31,32]. First, we treated PyMT BCBM organoids with low-dose doxorubicin (10 nmol/L) for 7 days *in vitro*. Over the course of the treatment, control-treated organoids continuously grew while doxorubicin-treated organoids remained small (**Fig. 2A**). Treatment with low dose doxorubicin led to a minor, non-statistically significant increase of apoptosis (**Fig. 2B**), suggesting that other mechanisms may cause the stalling of organoid growth. Indeed, the expression of the senescence-related genes *CDKN2A* and *FOXO4* [47] [1] [191] [191] [191] was enhanced while the expression of the proliferative marker *Ki67* was reduced (**Fig. 2C**). Next, PyMT BCBM organoids were engineered to express a luciferase construct and were intracranially injected into recipient FVB mice. Upon BCBM formation, as assessed by IVIS imaging, mice were administered three times with a control saline vehicle or with doxorubicin (5mg/kg), with a 4-day interval between treatments (**Fig. 2D**). In this context, *in vivo* treatment with doxorubicin induced an increase of senescence-associated (SA)  $\beta$ -Galactosidase activity in BCBM lesions compared to control (**Fig. 2E**), while the loss of lamin B1, a feature of senescent cells [48-50], was observed (**Supplementary Fig. 4A**) upon *in vivo* treatment with doxorubicin. Additionally, the number of apoptotic BCBM cells was non-statistically significantly increased upon doxorubicin treatment compared to control *in vivo* (**Supplementary Fig. 4B**). Together, this demonstrates that doxorubicin treatment correlates with the induction of a senescence program in our PyMT BCBM model both in *in vitro* organoids and *in vivo*.

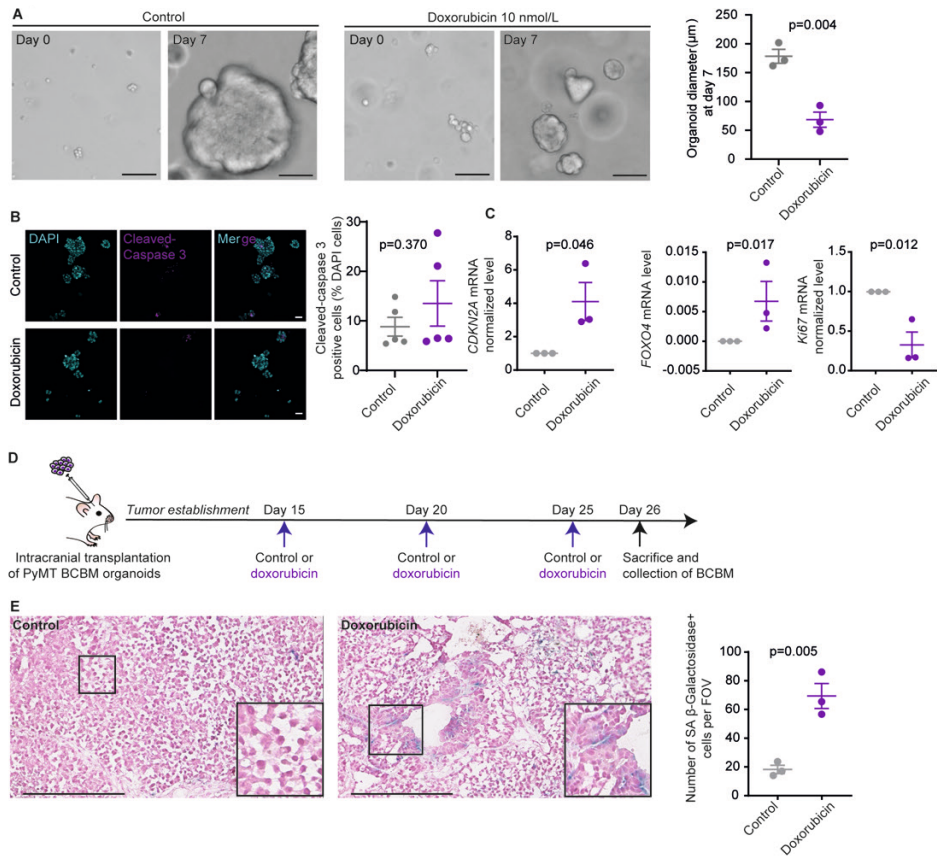


**Figure 2. Doxorubicin induces senescence in PyMT BCBM.** **A.** Representative images of PyMT BCBM organoids and quantification of organoid diameter after 7 days of treatment with vehicle (saline) or with doxorubicin 10 nmol/L.  $n=3$  biological repeats with three technical replicates *per* repeat. Data are presented as mean  $\pm$  standard-error-of-the-mean (SEM). Scale bar: 50  $\mu$ m. **B.** Representative images and quantification of cleaved-caspase 3 immunofluorescent staining in mouse BCBM organoids treated with vehicle (PBS) or with doxorubicin 10 nmol/L for 7 days.  $n=5$  biological repeats. Data are presented as mean  $\pm$  SEM. Scale bar: 50  $\mu$ m. **C.** RT-qPCR analysis of CDKN2A, FOXO4 and Ki67 mRNA levels normalized to GAPDH in PyMT BCBM organoids treated with vehicle (PBS) or doxorubicin 10 nmol/L for 7 days.  $n=3$  biological repeats with three technical replicates *per* repeat. Data are presented as mean  $\pm$  SEM. **D.** Schematic representation of experimental design and treatment timeline. **E.** Representative images and quantification of SA  $\beta$ -Galactosidase staining in *in vivo* PyMT BCBM treated with control vehicle (saline) or with doxorubicin.  $n=3$  mice *per* groups, with 5 fields of view analyzed and averaged *per* mouse. Data are presented as mean  $\pm$  SEM. Scale bar: 200  $\mu$ m.

### ***Doxorubicin reshapes the immune landscape of BCBM.***

Employing the immunomodulatory properties of chemotherapy is emerging as a potent strategy to increase immune infiltration into otherwise ‘cold’ tumors [19,51]. Additionally, senescent cells can remodel their environment *via* secretion of SASP factors [27]. We therefore next assessed the effects of doxorubicin on the immune landscape of the PyMT BCBM model. Mice bearing BCBM were subjected to the same treatment with doxorubicin or saline as before (**Fig. 2D**). To map the effects of doxorubicin on the PyMT BCBM immune landscape, mice were sacrificed 24h after the last treatment and BCBM lesions were collected for analyses. Flow cytometry analyses revealed an increased infiltration of CD4 and CD8 T cells to BCBMs grown in mice treated with doxorubicin compared to control (**Fig. 3A (i) and 3B (i)**). Immunofluorescence analyses confirmed that infiltration of CD4 and CD8 T cell was increased in PyMT BCBMs upon treatment with doxorubicin (**Supplementary Fig. 5A, B**). Activated CD4 T cells expressing CD69, Ki67 and Granzyme A as well as CD8 T cells expressing Ki67 were also found to be more abundant in PyMT BCBMs upon treatment with doxorubicin (**Fig. 3A (ii-iv) and 3B (ii)**). Lastly, treatment with doxorubicin induced an increased infiltration of CD4 T cells, CD8 T cells and NK cells expressing PD1 (**Fig. 3A (v), 3B (iii) and 3C**). We observed minor, non-statistically significant differences for the content of B cells, Tregs, neutrophils, macrophages and monocytes upon treatment with doxorubicin (**Supplementary Fig. 5C, D**).

### ***Senescent cells are not cleared by infiltrated T cells upon chemotherapy.***

Intricate crosstalk between immune cells and senescent cells can direct the fate of either populations [52-54], for instance immune cells may be recruited to clear senescent cells from aging or cancerous tissues [55]. Considering the increased infiltration of T cells upon doxorubicin, we next investigated whether T-cell recruitment to PyMT BCBMs led to clearance of senescence cells. Mice bearing BCBM were treated with saline or with doxorubicin, in combination with an IgG control or with depleting antibodies against CD4 or CD8 as previously described [56] (**Fig. 3D**). Successful depletion of CD4 and CD8 cells in the PyMT BCBM was confirmed by immunohistochemistry (Supplementary Fig. 5E, F). In line with previous work showing that CD8 T cells can clear senescent cells [55], depleting CD8 T cells in control-treated mice increased the number of SA  $\beta$ -Galactosidase positive cells (**Fig. 3E**). However, the number of senescent cells in doxorubicin-treated mice administered with depleting antibodies against CD4 or CD8 was not significantly different than for doxorubicin-treated mice that received the IgG control (**Fig. 3E, compare purple with greens**). This indicates that the recruitment of T cells to the PyMT BCBM upon doxorubicin treatment does not lead to clearance of senescent cells in our settings.

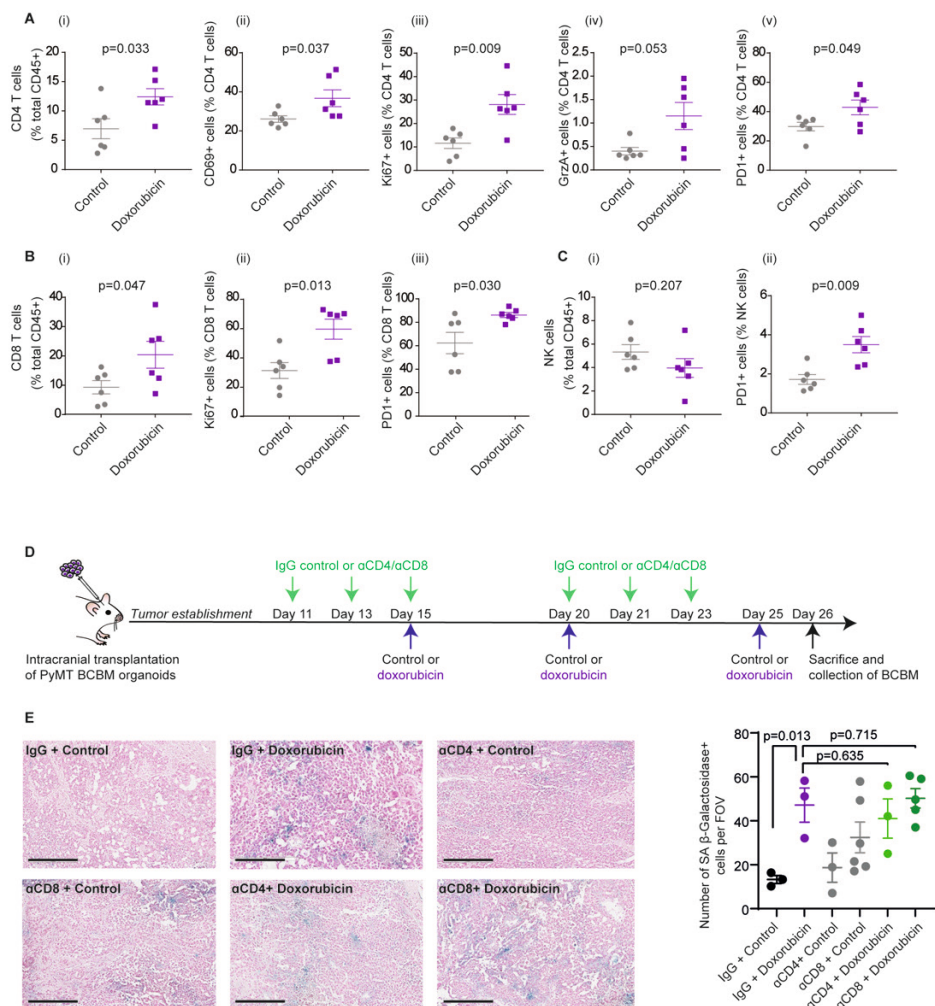


**Figure 3. Doxorubicin re-shapes the immune landscape in PyMT BCBM, yet recruited T cells do not clear senescent cancer cells. A.** Quantification of CD4 T cells as a percentage of CD45<sup>+</sup> cells (i), CD69<sup>+</sup> cells as a percentage of CD4 T cells (ii), Ki67<sup>+</sup> cells as a percentage of CD4 T cells (iii), Granzyme-A<sup>+</sup> cells as a percentage of CD4 T cells (iv) and PD1<sup>+</sup> cells as a percentage of CD4 T cells (v) infiltrated in PyMT BCBMs upon treatment with control vehicle (saline) or with doxorubicin. CD4 T cells were gated as CD45<sup>+</sup>/CD11b<sup>-</sup>/NK1.1<sup>-</sup>/CD19<sup>+</sup>/CD4<sup>+</sup> cells. Please also see Supplementary Fig. 3A for gating strategy. **B.** Quantification of CD8 T cells as a percentage of CD45<sup>+</sup> cells (i), Ki67<sup>+</sup> cells as a percentage of CD8 T cells (ii) and PD1<sup>+</sup> cells as a percentage of CD8 T cells (iii) infiltrated in PyMT BCBM upon treatment with control or with doxorubicin. CD8 T cells were gated as CD45<sup>+</sup>/CD11b<sup>-</sup>/NK1.1<sup>-</sup>/CD19<sup>+</sup>/CD8<sup>+</sup> cells. Please also see Supplementary Fig. 3A for gating strategy. **C.** Quantification of NK cells as a percentage of CD45<sup>+</sup> cells (i) and PD1<sup>+</sup> cells as percentage of NK cells (ii) infiltrated in PyMT BCBM upon treatment with control or with doxorubicin. NK cells were gated as CD45<sup>+</sup>/CD11b<sup>-</sup>/NK1.1<sup>+</sup> cells. Please also see Supplementary Fig. 3A for gating strategy. For A-C, data are presented as mean  $\pm$  SEM.  $n=6$  mice *per* group. **D.** Schematic representation of experimental design and treatment timeline. **E.** Representative images and quantification of SA  $\beta$ -Galactosidase

staining in PyMT BCBM treated with control IgG or depleting antibodies against CD4 or CD8 T cells, prior to treatment with control or with doxorubicin. n=3 mice for all group expect for anti-CD8 followed by control with n=6 and anti-CD8 followed by doxorubicin with n=5. Data are presented as mean +/- SEM. Scale bar: 200  $\mu$ m.

### **Senescent cells drive the recruitment of T cells to the BCBM without altering the tumor vasculature.**

We next assessed whether doxorubicin-induced senescent cells are involved in the recruitment of T cells to the PyMT BCBM upon treatment with doxorubicin. We used ABT263, a potent senolytic BH3 mimetic drug that inhibits the anti-apoptotic proteins BCL-2 and BCL-xL and which has been recently used to selectively ablate senescent cells in p53 proficient cellular models [57,58]. Small molecule Bcl-2 inhibitors have previously been used to successfully deplete senescent cells in primary and metastatic brain tumors in pre-clinical rodent models, demonstrating their ability to pass the BTB [59-61]. *In vitro*, treatment with ABT263 for 48h induced cell death specifically in organoids pre-treated with low dose doxorubicin for 7 days (**Supplementary Fig. 6A, B**). Moreover, to test whether ABT263 kills senescent cells, we generated a cell line from the PyMT BCBM organoids to perform an SA  $\beta$ -Galactosidase assay. In this setting, while doxorubicin significantly increased SA  $\beta$ -Galactosidase activity in PyMT BCBM cells, the population of SA  $\beta$ -Galactosidase<sup>+</sup> cells was ablated in BCBM cells treated with doxorubicin followed by ABT263, confirming the elimination of senescent cells by this senolytic agent (**Supplementary Fig. 6C**). Next, we tested the ability of ABT263 to deplete senescent cells *in vivo* (**Fig. 4A**). Administration of ABT263 did not alter tumor progression (**Supplementary Fig. 6D**). Tumor cell morphology and tumor size were not significantly altered; however, we observed a mild reduction of necrosis and of inflammation upon treatment with ABT263 compared to vehicle control (**Supplementary Fig. 6E**). Importantly, treatment with ABT263 in mice bearing PyMT BCBM reverted the increase of SA  $\beta$ -Galactosidase activity induced by doxorubicin, to a similar level as untreated conditions (**Fig. 4B**), confirming the activity and specificity of this senolytic agent against senescent cells in our PyMT BCBM model.

Next, we tested whether clearance of senescent cells with ABT263 would affect the recruitment of T cells to the PyMT BCBM. Quantification of immunofluorescent staining for CD4 and CD8 in *in vivo* PyMT BCBMs revealed that the recruitment of T cells to the BCBM triggered by doxorubicin treatment is reverted upon treatment with ABT263 (**Fig. 4C, D**). To control for a potential direct effect of ABT263 on T cell behavior, we isolated T cells from the mouse spleen and treated them *in vitro* with DMSO or ABT263. We neither found significant differences in T cell proliferation nor alterations in their migrating capability upon treatment with ABT263 compared to DMSO (**Supplementary Fig. 6 F, G and Supplementary Movies 1 and 2**), confirming that the observed reduction in T cell recruitment to the BCBM upon ABT263 is not due to a direct effect of the senolytic agent on T cell viability or migration.

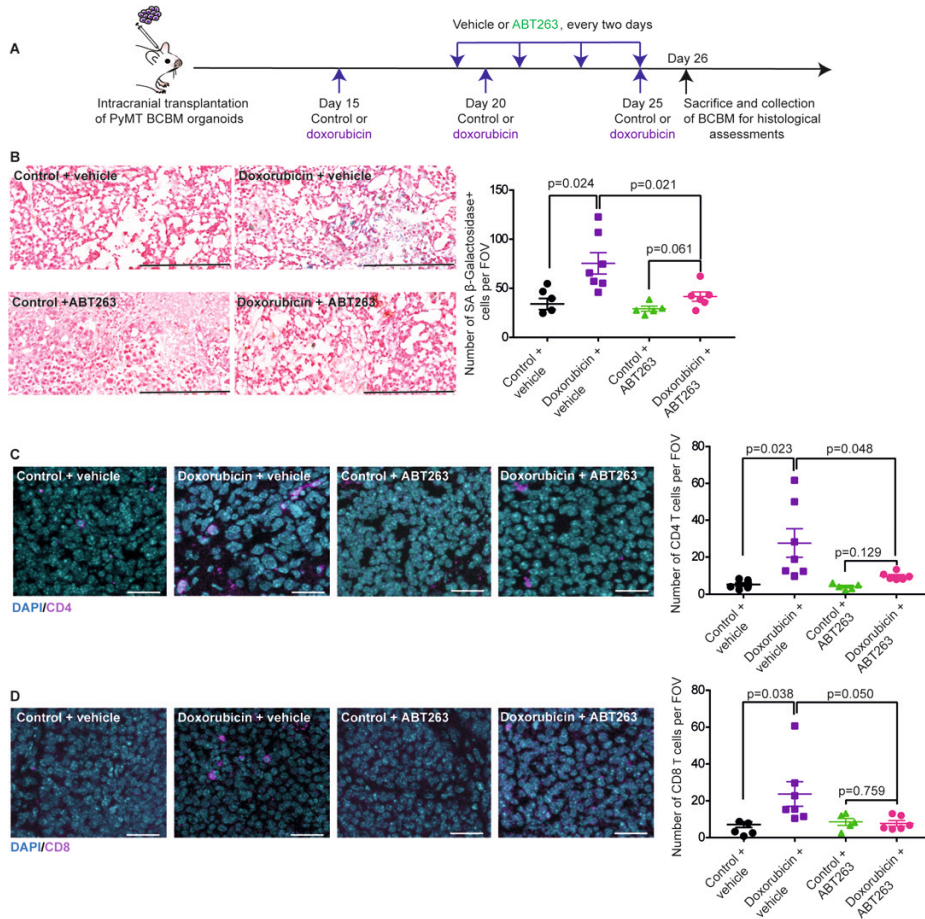


**Figure 4. Senescent cells drive the recruitment of T cells to PyMT BCBM.** **A.** Schematic representation of experimental design and treatment timeline. **B.** Representative images and quantification of SA β-Galactosidase staining in *in vivo* PyMT BCBMs upon treatment with control vehicle (saline) and with a chromophore vehicle (n=5), doxorubicin and a chromophore vehicle (n=5), saline control and ABT263 (n=5) or doxorubicin and ABT263 (n=6). Data are presented as mean +/- SEM. Scale bar: 200 μm. **C.** Representative images and quantification of immunofluorescence staining for CD4 and **D.** for CD8 upon treatment with control vehicle (saline) and a chromophore vehicle (n=5), doxorubicin and a chromophore vehicle (n=7), saline control and ABT263 (n=5) or doxorubicin and ABT263 (n=6). Data are presented as mean +/- SEM. Scale bar: 100 μm.

Lastly, induction of senescence can lead to a remodeling of the tumor vasculature, which has been shown to participate in the recruitment of T cells to the tumor mass [28]. We therefore evaluated whether doxorubicin triggered a remodeling of the BCBM vasculature. While we did not observe changes in blood vessel content in PyMT BCBM upon treatment with doxorubicin compared to control (**Supplementary Fig. 7A**), we found higher levels of  $\alpha$ -smooth muscle actin ( $\alpha$ SMA) expression in the blood vessels of doxorubicin-treated BCBM compared to control (**Supplementary Fig. 7B**). However, we neither detected statistically significant changes in pericyte (NG2<sup>+</sup> cells) recruitment close to the vasculature (**Supplementary Fig. 7C**) nor statistically significant alterations of the expression levels of ICAM nor VCAM in the endothelial cells, two immunomodulatory cell surface molecules which have been linked with tissue inflammation and immune cell recruitment [62] (**Supplementary Fig. 7D, E**).

Together, this demonstrates the role of doxorubicin-induced senescent cells in re-shaping the BCBM immune landscape and driving the recruitment of T cells to the BCBM, without significantly altering features of the BTB at the studied timepoint.

### ***Inducing senescence in BCBM improves the efficacy of anti-PD1.***

The presence of intratumoral PD1 positive T cells is commonly used as a prognostic marker of good response to immune checkpoint inhibition with anti-PD1 [44]. In addition, the observed recruitment of PD1<sup>+</sup> T cells to the mouse PyMT BCBM triggered by doxorubicin is in line with observations reported for extracranial breast tumors in the TONIC trial [51]. This prompted us to test whether recruiting PD1<sup>+</sup> T cells to the PyMT BCBM *via* doxorubicin treatment could be employed to improve anti-PD1 efficacy. To test this, FVB mice bearing PyMT BCBM were pre-treated with three administrations of a control saline vehicle or with doxorubicin, prior to continuous treatment with an IgG control or with an anti-PD1 antibody, twice weekly (**Fig. 5A**). Tumor response to treatment was monitored using whole body bioluminescent imaging (**Fig. 5B, C**), and mice were sacrificed when they showed signs of sickness. Doxorubicin treatment alone and anti-PD1 treatment alone neither significantly altered BCBM growth nor improved mouse survival compared to control treatment (**Fig. 5B-D**), in line with the lack of induction of apoptosis by doxorubicin in the PyMT BCBM (**Supplementary Fig. 4B**) and with the poor response to monotherapies reported in BCBM patients [1]. However, pre-treatment with doxorubicin prior to PD1 blockade altered tumor growth and significantly prolonged mouse survival compared to control and to single treatment with either doxorubicin or anti-PD1 (**Fig. 5B-D**). Mean survivals for each treatment group are depicted in Fig. 5E.

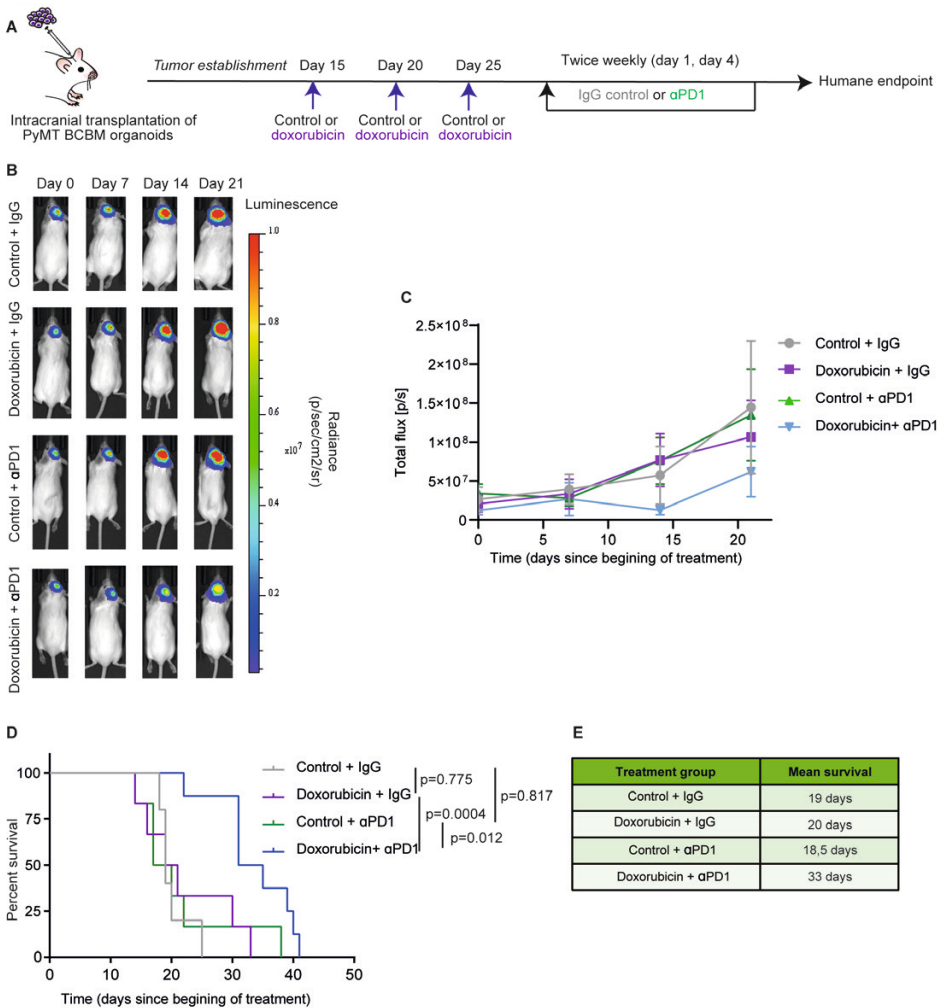


**Figure 5. Pre-induction of senescence with doxorubicin improves the efficacy of anti-PD1.**

**A.** Schematic representation of experimental design and treatment timeline. Upon establishment of BCBM, mice were randomized into treatment groups based on IVIS measurements and monitored using whole-body bioluminescence imaging until reaching humane endpoint. **B.** Representative images of whole-body IVIS bioluminescence monitoring of BCBM response to treatment. For each treatment group, images of a representative mouse followed over time from the beginning of the treatment (day 0) are depicted. **C.** IVIS bioluminescence flux averaged signal since the beginning of treatment in mice bearing BCBM and treated with vehicle control (saline) followed by IgG control (n=5); pre-treatment with saline followed by anti-PD1 antibody (n=6); pre-treatment with doxorubicin followed by IgG (n=6) or pre-treatment with doxorubicin followed by anti-PD1 antibody (n=8). **D.** Kaplan-Meier analyses of time to humane endpoint and mean survival from the beginning of the treatment and **E.** mean survival for mice treated with either pre-treatment with vehicle control (saline) followed by IgG control (n=5); pre-treatment with vehicle control (saline) followed by anti-PD1 antibody (n=6); pre-treatment with doxorubicin followed by IgG control (n=6) or pre-treatment with doxorubicin followed by anti-PD1 antibody (n=8).



Next, we evaluated whether the T cells that are recruited to the PyMT BCBM following doxorubicin treatment (Fig. 3) underly the improved survival upon anti-PD1 therapy. We first studied CD44 expression, a marker of mature T cells [63], in intratumoral T cells. The percentage of T cells that express CD44 was increased in the PyMT BCBM of mice treated with the combined treatment compared to monotherapies (**Fig. 6A, B**), suggesting that T cells found in the PyMT BCBM have potent anti-tumor activity upon treatment with doxorubicin followed by anti-PD1. Notably, the percentage of CD8 T cells positive for CD44 was significantly higher compared to the CD4 T cells in this treatment group (Fig. 6A, B). We then functionally tested the role of T cells in driving the response to anti-PD1 upon doxorubicin using depleting antibodies. Following pre-treatment with doxorubicin, mice bearing PyMT BCBM were continuously treated with IgG control or with depleting antibodies against CD4 or CD8, in combination with IgG control or anti-PD1 antibody twice weekly (as depicted in **Fig. 6C**). Mice were sacrificed when symptomatic, as previously (Fig. 5). Depleting CD8 cells significantly reduced mouse survival in response to doxorubicin followed by anti-PD1, while CD4-depletion did not (**Fig. 6D**). Considering that doxorubicin also induces a recruitment of PD1<sup>+</sup> NK cells to the BCBM (**Fig. 3C (ii)**), and in light of previous work indicating that NK cells can express CD8 [64], we next evaluated the percentage of the PD1<sup>+</sup> NK cell population that also expresses CD8. We found that out of the total CD45<sup>+</sup> cells in the PyMT BCBM, only 0.085% are NK cells that co-express PD1 and CD8, while 17.8% are CD8 T cells that express PD1 (**Supplementary Fig. 7F**). Since depletion of CD8 cells blocks the improved response to the treatment combination, the role of PD1<sup>+</sup> NK cells in the improved response to anti-PD1 upon doxorubicin is therefore likely limited. Together, our data confirms that CD8 T cells have a key role in driving the prolonged survival observed upon doxorubicin pre-treatment followed by anti-PD1 in PyMT BCBM.

We subsequently tested whether continuous administration of doxorubicin during anti-PD1 treatment would further improve survival outcomes compared to pre-treatment alone. Mice bearing PyMT BCBM lesions were pre-treated with control or with doxorubicin prior to treatment with anti-PD1 alone or with anti-PD1 combined with doxorubicin (**Supplementary Fig. 7D**). Pre-treatment with doxorubicin followed by continuous treatment with doxorubicin had no advantage over pre-treatment with doxorubicin alone when combined with anti-PD1 (**Supplementary Fig. 7E**), demonstrating that pre-treatment with doxorubicin can improve anti-PD1 therapy without the need for long-term exposure to doxorubicin with increased toxicity.

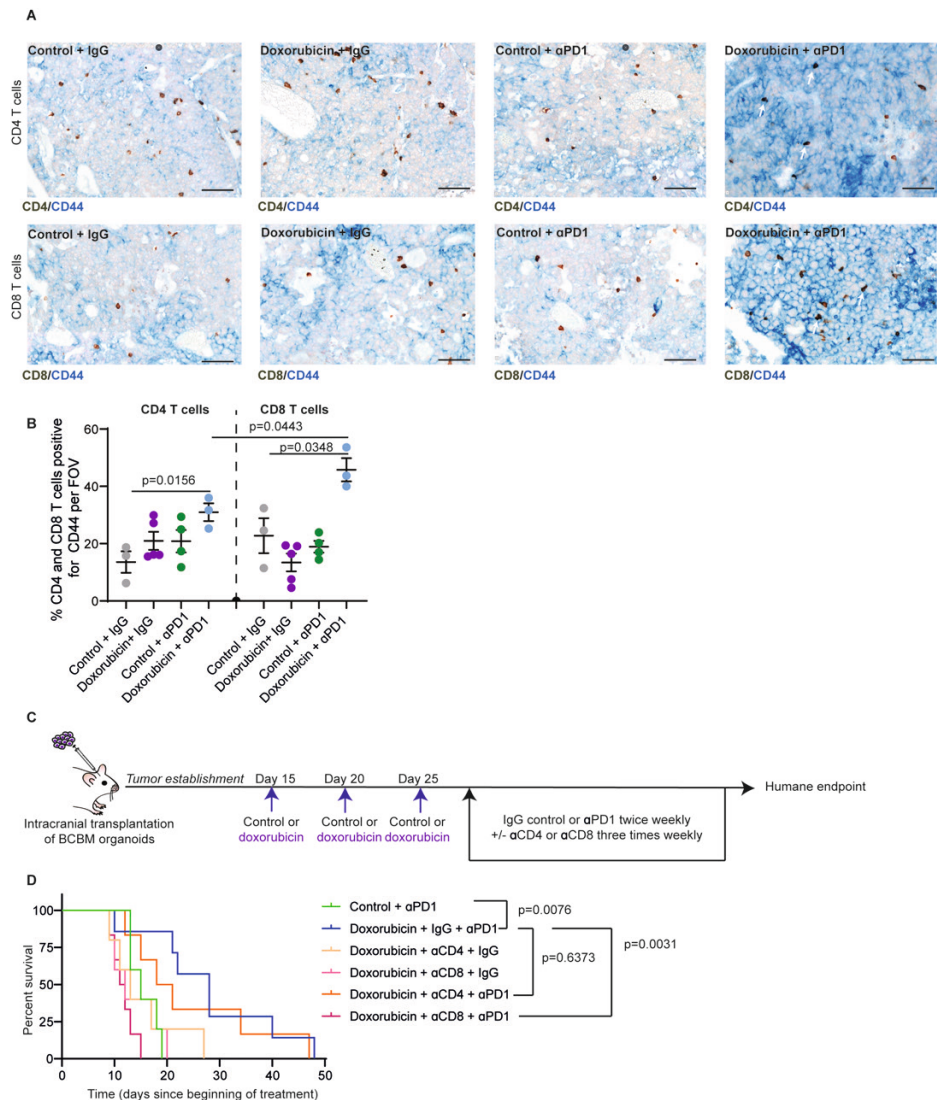


**Figure 6. CD8 T cells drive the improved response to doxorubicin followed by anti-PD1. A.**

Representative images of dual staining for CD4 and CD44 (top panel) and CD8 and CD44 (lower panel) in the PyMT BCBM upon treatment with vehicle control (saline) followed by IgG control; pre-treatment with vehicle control (saline) followed by anti-PD1 antibody; pre-treatment with doxorubicin followed by IgG control or pre-treatment with doxorubicin followed by anti-PD1 antibody. White arrows point to double positive cells, scale bar: 100  $\mu$ m. **B.** Quantification of CD44<sup>+</sup> CD4 and CD44<sup>+</sup> CD8 T cells as a percentage of total CD4 or CD8 T cells respectively in the PyMT BCBM upon treatment with vehicle control (saline) followed by IgG control (n=3 mice), doxorubicin followed by IgG control (n=5 mice), vehicle control (saline) followed by anti-PD1 (n=4 mice) or doxorubicin followed by anti-PD1 (n=3 mice), at endpoint (relates to the mouse cohort depicted in Fig. 5A-C). *Per tumor section*, 4-5 FOV were analyzed and averaged. Data are mean +/- SEM. **C.** Schematic representation of experimental design

and treatment timeline. **D.** Kaplan-Meier analyses of time to humane endpoint for mice treated with either vehicle control (saline) followed by anti-PD1 antibody (n=5 mice); pre-treatment with doxorubicin followed by IgG control and anti-PD1 antibody (n=6 mice); pre-treatment with doxorubicin followed by anti-CD4 or anti-CD8 antibody and IgG control (n=5 mice) or pre-treatment with doxorubicin followed by anti-CD4 or anti-CD8 antibody and anti-PD1 antibody (n=5 mice for CD4-depletion and n=6 mice for CD8-depletion).

Lastly, to test whether the combination treatment can be efficacious beyond the PyMT BCBM model, we generated a second BCBM model derived from mammary tumors from MMTV-NeuT mice, which harbors an overexpression of Her2 [65]. This model is clinically relevant considering that 31% of Her2<sup>+</sup> metastatic BC patients develop BCBM [3]. We established the NeuT BCBM model using six rounds of enrichment in the brain, and we generated organoids (from herein called 'NeuT BCBM organoids') from the last round of enrichment, similarly to the PyMT BCBM. Treating NeuT BCBM organoids with low dose doxorubicin stalled organoid growth but only moderately induced apoptosis by 3% (**Fig. 7A, B**). Next, we made a cell line from the NeuT BCBM organoids and we confirmed that doxorubicin treatment induces SA beta-galactosidase activity *in vitro* (**Fig. 7C**). Lastly, we intracranially injected NeuT BCBM organoids and upon BCBM formation, mice were randomized into treatment groups with control followed by IgG, doxorubicin followed by IgG, control followed by anti-PD1 or doxorubicin followed by anti-PD1, as for the PyMT BCBM model (Fig. 5). Mice were monitored until showing signs of sickness. Treatment with doxorubicin followed by IgG or with control followed by anti-PD1 did not significantly alter mouse survival compared to control followed by IgG (**Fig. 7D**). However, similarly to the PyMT BCBM, treatment with doxorubicin prior to anti-PD1 significantly improved mouse survival compared to monotherapies and to control prior to IgG (**Fig. 7D**). Together, this demonstrates the efficacy of pre-treatment with doxorubicin prior to anti-PD1 in a second model of BCBM and warrants further consideration to introduce our combination therapy for BCBM patients.

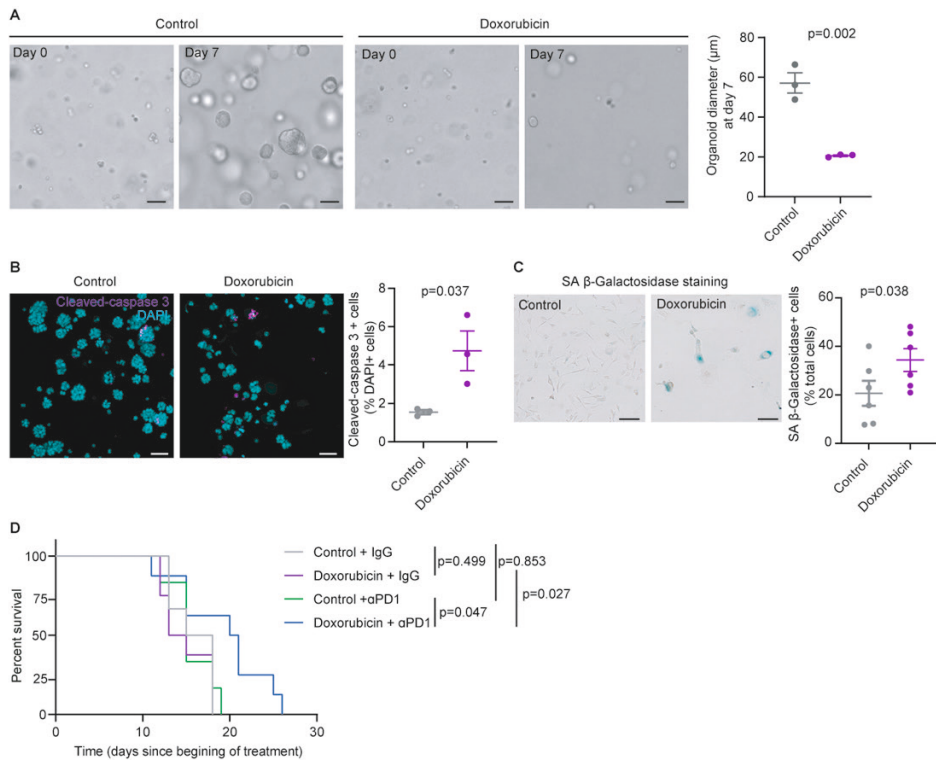


**Figure 7. Doxorubicin induces senescence and improves the response to anti-PD1 in the NeuT BCBM model.** **A.** Representative images and of NeuT BCBM organoids at day 0 and day 7 of treatment with control (PBS) or with doxorubicin 20 nmol/L and quantification of organoid diameter at day 7.  $n=3$  biological repeats. Scale bar: 50  $\mu\text{m}$ . **B.** Representative images and quantification of cell apoptosis using immunofluorescence staining for cleaved-caspase 3 in NeuT BCBM organoids after 7 days of treatment with control (PBS) or doxorubicin 20 nmol/L.  $n=3$  biological repeats. Scale bar: 50  $\mu\text{m}$ . **C.** Representative images of SA  $\beta$ -Galactosidase staining and quantification of the percentage of NeuT BCBM cells positive for SA  $\beta$ -Galactosidase after 7 days of treatment with control (PBS) or with doxorubicin 20 nmol/L.  $n=6$  biological repeats. Scale bar: 100  $\mu\text{m}$ .  $p$ -values were determined using a paired nonparametric t-test with a Mann-Whitney U correction. **D.** Kaplan-Meier analyses of time to humane endpoint for mice bearing NeuT BCBM and from the beginning of the treatment for mice treated with either pre-treatment with vehicle control (saline) followed by IgG control ( $n=6$ ); pre-treatment with vehicle control (saline) followed by anti-PD1 antibody ( $n=6$ ); pre-treatment with doxorubicin followed by IgG control ( $n=8$ ) or pre-treatment with doxorubicin followed by anti-PD1 antibody ( $n=8$ ). For Fig. 7, data are presented as mean  $\pm$  SEM.

## DISCUSSION

Improving the outcomes of BCBM patients necessitates more systematic pre-clinical testing and optimization of therapeutic regimens. Immunotherapy has shown positive outcomes in solid cancer types including brain metastasis derived from melanoma or lung cancer, but this remains limited for breast tumor [6,66-68]. Here, we used two preclinical immunocompetent mouse models of the disease to streamline immune-based treatments. Our PyMT BCBM model recapitulates key features of human BCBM in respect to intracranial growth, histopathological morphology, MRI profile and immune landscape. Importantly, our novel mouse BCBM models can be used in the future to further design immune-based treatments in this disease and to explore mechanisms driving BCBM progression. As such, our combined treatment data demonstrates that inducing senescence *via* pre-treatment with doxorubicin triggers a recruitment of PD1<sup>+</sup> T cells to the BCBM, which subsequently can be used to improve the efficacy of anti-PD1 treatment. Specifically, we found that CD8<sup>+</sup> T cells are key drivers of the enhanced survival upon doxorubicin and anti-PD1. Additionally, induction of senescence with doxorubicin did not correlate with important remodeling of the BTB, suggesting that other SASP factors are responsible for recruiting T cells to the BCBM.

Leveraging on the presence of senescent cells within a tumor mass to improve cancer treatment has previously been explored by us and others. For instance, inducing senescence has been shown to increase overall survival in lymphoma [30], and can be combined with glucose blockade to specifically eliminate senescent cells [69]. Similarly in liver cancer, the induction of senescence combined with administration of senolytic agents can significantly reduce tumor growth [70]. In addition, the use of CAR T cells that specifically target senescent cancer cells has been shown to prolong survival in mice bearing lung adenocarcinoma [71]. Senescence can be induced in various ways, such as telomeric or genomic alterations, oncogene activation, epigenomic remodeling or oxidative stress (reviewed in [27]). These various inducers of senescence will trigger the secretion of distinct SASP factors, and this can partly explain the various and somewhat opposite effects of senescence in cancer. The influence of senescent cells on cancer progression remains however controversial, since previous studies have shown that SASP factors can both promote and halt cancer progression [27,72]. Additionally, the role of cancer senescent cells in brain tumors remains under-studied. Here, we demonstrate that doxorubicin can be used to trigger senescence in BCBM, which in turn triggers a remodeling of the tumor immune landscape that can be employed to improve immunotherapy in BCBM.

While we report an induction of senescence upon doxorubicin *in vivo*, we do not observe an effect of doxorubicin treatment on BCBM growth or mouse survival. Doxorubicin-induced senescence was previously shown to be accompanied by a mitogenic SASP [73], therefore it is possible that senescent cells induce proliferation of their neighboring cells, which could explain the lack of effect of doxorubicin on tumor growth. Additionally, considering

that the recruited T cells upon doxorubicin express PD1, they may have reduced cytotoxic capacity and therefore not be capable of eradicating BCBM cells, which can explain the lack of efficacy of doxorubicin treatment alone.

In addition to the recruitment of T cells, we observed an increased number of NK cells expressing PD1 upon doxorubicin treatment, which has previously been linked to functional exhaustion of these cells [74]. NK cells can be recruited to clear senescent cells as a mechanism to maintain tissue integrity [75] and may therefore become exhausted when the number of senescent cells rise upon doxorubicin treatment. On the other hand, PD1<sup>+</sup> NK cells can also be cytotoxic [76], however, we found that CD8<sup>+</sup> cells are critical drivers of the response to the combination treatment, and only a small percentage of PD1<sup>+</sup> NK cells recruited to the BCBM upon doxorubicin express CD8. Therefore, the contribution of NK cells to the improved survival upon doxorubicin followed by anti-PD1 appears limited.

Doxorubicin has been used to treat BC with extracranial disease, however it has failed to improve outcomes in BCBM. Attempts to improve the efficacy of doxorubicin in BCBM have been reported. For instance, engineering doxorubicin with liposomes to pass the BBB and the BTB is currently being assessed in the clinic (NCT01818713). Here, our data reveal that re-purposing the pro-senescence properties of doxorubicin can be used to successfully introduce immunotherapy with immune-checkpoint blockade in BCBM. Additionally, the improved efficacy of anti-PD1 following doxorubicin pre-treatment in our BCBM model is in line with findings from the TONIC trial in extracranial breast tumors [51], and demonstrates that harnessing the immunomodulating, pro-senescence properties of doxorubicin can be used to improve checkpoint inhibitor treatments in BCBM.

There are some limitations to our study. Firstly, our PyMT BCBM model does not spontaneously metastasize to the brain upon cardiac injection of the BCBM organoids. Indeed, no tumor were formed, and we did not observe single tumor cells six months after intracardiac injection. Secondly, further research is needed to test whether BCBM can be sensitized to immune checkpoint inhibitors using other chemotherapies such as nab-paclitaxel and carboplatin/gemcitabine, which are currently being tested in combination with immunotherapy in BC patients with extracranial lesions [15,51,77]. Additionally, radiotherapy which is a standard-of-care for BCBM, can also induce senescence and may therefore also sensitize BCBM to immunotherapy [78,79]. Although our data suggest that doxorubicin pre-treatment could improve immunotherapy in BCBM, this strategy has yet to be employed in the clinic. BCBM patients are not currently treated with doxorubicin, consequently validating our findings in the human setting is not yet possible. Nevertheless, doxorubicin is already safely used in patients, and clinical trials would allow assessment of the efficacy of doxorubicin pre-treatment before anti-PD1 therapy for BCBM patients. Additionally, it remains to be investigated whether first-line treatments for primary breast cancer or for patients with undetected BM, employed in the clinic but not tested in our settings, have affected the ability of doxorubicin to recruit T cell to BCBMs and subsequently the efficiency

of anti-PD1 treatment. Lastly, we used an anti-PD1 antibody which in addition to acting as an immune checkpoint inhibitor can also trigger depletion of specific PD1<sup>+</sup> T cell and NK cell subsets [80]. Further work is required to test the efficacy of Fc inactive anti-PD1 antibody upon treatment with doxorubicin.

In summary, our study provides evidence that inducing senescence using doxorubicin pre-treatment can sensitize BCBM to PD1 blockade. This opens novel avenues to introduce, for the first time, immune-based treatments for BCBM patients. Our data also provides insights into how chemotherapy-induced senescence can be employed to improve immunotherapy, which may have important implications for strategies to combine induction of pro-senescence programs and immunotherapy in other cancer types.

## MATERIAL AND METHODS

### ***Animals***

Animal experiments were performed at The Hubrecht Institute and the Netherlands Cancer Institute in accordance with national regulations and ethical guidelines. Experiments were approved by the Dutch Central Authority for Scientific Procedures on Animals (CCD) and the local animal experimental committees at The Hubrecht Institute and The Netherlands Cancer Institute. FVB females (Janvier) were used at 8-20 weeks of age at the time of intracranial or carotid injections. All mice were maintained in the Laboratory Animal Facilities of the Hubrecht and of the Netherlands Cancer Institute under specific pathogen free conditions. Mice were housed in individually ventilated cages, food and water were provided *ad libitum*.

### ***Primary tumor material digestion for the generation of the PyMT BCBM and Neu BCBM***

For the first round of enrichment in the brain, primary breast tumors from MMTV-PyMT mice or from MMTV NeuT mice that carry E-cadherin-mCFP transgene and that had reached humane endpoint were harvested. Tumor pieces from breast tumors and from the rounds of enrichment were preserved in freezing medium (Gibco, Cat. No. 12648-010) at -80°C. Before intracranial injections, tumor pieces were thawed and minced on ice using sterile knives and enzymatically digested at 37°C for 20-30 min while shaking at 900 rpm. The digestion mix was composed of 10 mg collagenase A (Roche, Cat. No. 10103586001), 2 mL TrypLE Express (Gibco, Cat. No. 12605010) and 3 mL DMEM/F12 GlutaMAX (Gibco, Cat. No. 10565018) supplemented with 10 mmol/L HEPES (Gibco, Cat. No. 15630106), 100 µg/mL streptomycin and 100 U/mL penicillin (Gibco, Cat. No. 15140122). Undigested tumor pieces were removed by spinning down at 800 rcf at 4°C and for 5 min. The pellet was treated with 10 µg/mL DNase I (Roche, Cat. No. 10104159001) in DMEM/F12 GlutaMAX

medium and the tube was manually shaken for 5 min. The sample was washed three times in DMEM/F12 GlutaMAX and the final pellet was resuspended in 2  $\mu$ L of **phosphate-buffered saline (PBS)** *per* intracranial injection. There was no *in vitro* culture steps between rounds of enrichment in the brain.

### ***Intracranial injection***

For intracranial surgeries, mice were treated with 0.067 mg/mL rimadyl (carprofen, Zoetis) in drinking water 1 day before injection and for 3 days following surgery. Furthermore, mice were treated with 0.1 mg/kg temgesic (buprenorphine, Indivior Europe Limited) *via* subcutaneous injection 30 min before and 8h to 12h after surgery. Mice were anesthetized *via* inhalation of 2% (v/v) isoflurane and eyes were covered with duratears (Alcon). The head was shaved and disinfected using betadine. Scissors were used to make an incision in the skin over the cranium to reveal the periosteum, which subsequently was dissected away to reveal the bregma. Local anesthetic (0.01-0.02 mL) made of NaCl supplemented with 1 mg/mL Lidocaine (Fresenius Kabi) and 0.25 mg/mL Bupivacaine (Actavis, Aurobindo Pharma B.V.) was applied to the skull. The bregma was used as a 0 reference point to determine the position for intracranial injection: 1.5 mm to the right, 1.5 mm caudal and 1.5 mm deep. At this position a hole in the skull was drilled using a sterile compact drill bit. BCBM organoids expressing H2B-Dendra2 or Luciferase were dissociated into single cells with TrypLE Express (Gibco Cat. No. 12605010) at 37°C for approximately 10-20 min at 900 rpm until single cells were observed and were injected using a 10  $\mu$ L glass Hamilton syringe with a 30G and point 4 style needle at a speed of 1  $\mu$ L/min. *Per* mouse, 40,000 single cells derived from dissociated PyMT BCBM organoids and 50,000 single cells derived from dissociated NeuT BCBM organoids in 2  $\mu$ L were injected intracranially. We waited 2 minutes before retracting the needle to avoid spillage of cells outside the injection site. The wound was pressed with a sterile cotton tip and the skin was sutured. Mice were allowed to recover on a heating pad and closely monitored during the days following surgery.

### ***Carotid injection***

Similarly, as for intracranial injection, PyMT BCBM organoids were collected and washed from the **Basal Membrane Extract (BME)** and digested with TrypLE Express (Gibco Cat. No. 12605010) at 37°C for 10-20 min at 900 rpm. Digestion was stopped by adding DMEM/F12 GlutaMAX medium (Gibco, Cat. No. 10565018) and organoids were dissolved in PBS and filtered through a Falcon™ Round-Bottom Polystyrene Test Tubes with Cell Strainer Snap Cap (Fisher Scientific, Cat. No. 352235). Mice were treated with 0.067 mg/mL rimadyl (carprofen, Zoetis) in the drinking water 1 day before injection and for 3 days post-surgery. Furthermore, mice were treated with 0.1 mg/kg temgesic (buprenorphine, Indivior Europe Limited) *via* subcutaneous injection 30 min before and 8h to 12h after surgery. Mice were anesthetized *via* inhalation of 2% (v/v) isoflurane and eyes were covered with duratears



(Alcon). Surgery was performed as described in Zhang et al. [81]. *Per mice*, 10,000 PyMT BCBM single cells (made from dissociated PyMT BCBM organoids) were resuspended in 100  $\mu$ L of PBS and were injected in the carotid. Mice were allowed to recover on a heating pad and closely monitored during the following days.

### ***PyMT and Neu BCBM organoids preparation, culturing and lentiviral transduction***

From the last enrichment round in the brain, brain tumor pieces were isolated to generate tumor organoids. All steps were performed inside a flow cabinet and digestion was done as described in section “Primary tumor material digestion”. Once the pellet was washed and spun down, it was resuspended in BME type 2 (R&D systems Cat. No. 3533-005-02) diluted at a 2:1 ratio with DMEM/F12 GlutaMAX medium (Gibco, Cat. No. 10565018). Drops of 50  $\mu$ L of organoids with BME were plated in a pre-warm 24 well plate (Greiner bio-one, Cat. No. 662160) and inverted while solidifying for 30 min at 37°C, 5% CO<sub>2</sub>. Organoids were maintained in complete DMEM/F12 GlutaMAX medium (Gibco, Cat. No. 10565018), supplemented with 10 mmol/L Hepes (Gibco, Cat. No. 15630106), 100  $\mu$ g/ml streptomycin, 100 U/mL penicillin (Gibco, Cat. No. 15140122), 10.08 ng/ml FGF (Gibco, Cat. No. PHG0261) and B27 supplement (Gibco, Cat. No. 17504001) and incubated at 37°C, 5% CO<sub>2</sub>. To confirm Mycoplasma-free culturing of the organoids, the MycoAlert PLUS Kit (Lonza Cat. No. LT07-118) was used according to the manufacturer’s protocol. Organoids were split with TrypLE Express (Gibco, Cat. No. 12605010) while shaking for 10-20 min at 900 rpm and 37°C. In order to visualize tumor cells *in vivo* we transduced these organoids with a lentiviral vector for stable expression of UBC-Firefly-Luciferase. Additionally, to visualize tumor cells in immunofluorescent assays, we transduced organoids with a construct for stable expression of UBC-H2B-Dendra2-puromycin. For production of the lentivirus, human embryonic kidney (HEK) 293T cells at a confluence of 80% were used. *Per* 10 cm dish (Greiner, Cat. No. 664160) of HEK 293T cells, 7.5  $\mu$ g of psPAX2, 2.5  $\mu$ g PMD2.G and 10  $\mu$ g of our luciferase or H2B-Dendra constructs were mixed in 1 mL Opti-MEM (ThermoFisher Scientific, Cat. No. 31985070). After mixing, 1 mL of Opti-MEM with 40  $\mu$ L lipofectamine 2000 (ThermoFisher Scientific, Cat. No. 11668019) were added to the plasmid mix and incubated at room temperature for 15 min. The mix was carefully added to the HEK 293T cells and next morning medium was refreshed with DMEM GlutaMAX (Gibco, Cat. No. 31966047) supplemented with 100  $\mu$ g/mL streptomycin, 100 U/mL penicillin (Gibco, Cat. No. 15140122). After 48h, medium was collected and filtered through a 0.22  $\mu$ m filter (Milipore, Cat. No. SLGS033SS). Filtered medium was concentrated with an Amicon Ultra-15 10k column (Milipore, Cat. No. UFC905024) for 1h at 4000 rcf. Organoids were trypsinized into smaller clusters of approximately 8 cells and incubated with 250  $\mu$ L virus, 100  $\mu$ g/mL polybrene (Sigma, Cat. No. TR-1003-G) and 10  $\mu$ mol/L Y-27632 (Bio Connect, Cat. No. S1049) on a 48 well plate low adherence (Greiner, Cat. No. 677970). Spin infection was

done at 36°C, 600 rcf for 1h and organoids were subsequently incubated at 37°C for 6 h. Next, organoids were washed twice with DMEM/F12 GlutaMAX medium (Gibco, Cat. No. 10565018) and plated in BME. Complete DMEM/F12 GlutaMAX medium (Gibco, Cat. No. 10565018), supplemented with 10 mmol/L HEPES (Gibco, Cat. No. 15630106), 100 µg/mL streptomycin, 100 U/mL penicillin (Gibco, Cat. No. 15140122), 10.08 ng/mL FGF (Gibco, Cat. No. PHG0261), B27 supplement (Gibco, Cat. No. 17504001) and 10 µmol/L Y-27632 (Bio Connect, Cat. No. S1049) was added to the organoids for 2 days. Organoids were selected with 0.5 µg/mL puromycin (Gibco Cat. No. A1113803).

## ***Immunohistochemistry***

### ***Mouse samples***

Brain samples were collected and fixed in formalin or EAF (ethanol/acetic acid/ formaldehyde/ saline at 40:5:10:45 v/v/v/v) and embedded in paraffin. Sections were stained with hematoxylin and eosin (H&E) according to standard procedures. For immunohistochemistry, 4 µm-thick sections were made on which either E-cadherin (Cell Signaling, Cat. No. 3195, 1:100); Keratin 8 (DSHB University of Iowa, Troma 1, 1:1500); Glial Fibrillary Acidic Protein (GFAP) (BioTrend, Cat. No. BT46-5002-04, 1:500); Pankeratin (ThermoFisher, Cat. No. MS-343-P, 1:100); CD4 (eBiosciences, Cat. No.14\_9766\_80, 1:2000); CD8 (eBiosciences, Cat. No. 14-0808, 1:1000); PD-1 (Cell Signaling, Cat. No. Cat. No. 84651, 1:1000); F4/80 (Cell Signaling, Cat. No. 70076, 1:1000); Ly6G (BD Biosciences, Cat. No. 551459, 1:500) and Foxp3 (eBiosciences Cat. No. 14-5773, 1:500) primary antibodies were applied. The sections were reviewed with a Zeiss Axioskop2 Plus microscope (Carl Zeiss Microscopy, Jena, Germany) and images were captured with a Zeiss AxioCam HRc digital camera and processed with AxioVision 4 software (both from Carl Zeiss Vision, München, Germany). For dual staining for CD4/CD44 and CD8/CD44, CD4 (eBiosciences, Cat. No.14\_9766\_80, 1:2000); CD8 (eBiosciences, Cat. No. 14-0808, 1:1000) were first applied and detected with a Goat-α-Rat-Biotynated secondary antibody (SouthernBiotech; 3052-08) which was revealed with an HRP visualization in NovaRed (Vector Laboratories; SK-4800). Next, CD44 (Santa Cruz, sc-18849, 1:100) was applied and detected with a an Goat-α-Rat-Biotynated secondary antibody (SouthernBiotech; 3052-08) prior to being revealed with an AP visualization in blue (Vector Laboratories; SK-5300).

### ***Human samples***

Samples were fixed in 4% formaldehyde and embedded in paraffin. 4 µm-thick sections were stained with CD4 (Cell Marque, clone SP35), CD8 (Dako, clone C8/144B), PD1 (Dako, clone 22C3), GFAP (Dako, polyclonal (for Dako Omnis)), E-cadherin (Dako, clone NCH-38), pankeratin (Dako, clone AE1/AE3), Keratin 18 (Dako, clone DC10). The sections were reviewed with a Zeiss Axioskop2 Plus microscope (Carl Zeiss Microscopy, Jena, Germany)

and images were captured with a Zeiss AxioCam HRc digital camera and processed with AxioVision 4 software (both from Carl Zeiss Vision, München, Germany).

### **Generation of the PyMT and Neu BCBM models**

Tumor pieces derived from mammary tumors grown in MMTV-PyMT mice or in MMTV-Neu mice were digested as described in “Primary tumor material digestion” and intracranially injected. From the tumor generated, we isolated tumor pieces and after tumor digestion into single cells we performed another round of intracranial injection. This *in vivo* selection was performed without any *in vitro* step in between and for six successive rounds. Organoids from the last brain enrichment round were generated as described in “Organoids preparation”.

### **Characterization of the PyMT BCBM model**

Mice bearing PyMT BCBM generated by intracranial injections had an average survival latency of 4-5 weeks. Histopathological analyses demonstrated that PyMT BCBM derived from intracarotid injection are moderately to poorly differentiated adenocarcinomas with solid and/or lobular growth pattern and accompanied by thin fibrous vascular stroma and multifocal necrosis (Fig. 1C). The tumor cells were round to polygonal in shape and had relatively large nuclei and conspicuous nucleoli. All these features resembled the human counterpart of BCBM (Fig. 1C). Immunohistochemistry of markers that are not expressed in the brain, such as E-cadherin and pankeratin were strongly positive in PyMT BCBM and in human BCBMs while keratin 8/18 showed multifocal staining in PyMT BCBM and a strong staining in human BCBM (Supplementary Fig. 1B). In addition, GFAP, which is expressed in healthy brain tissue and in primary brain tumors but not in BM, was negative for both PyMT BCBM and human BCBMs (Supplementary Fig. 1B). Taken together, our mouse PyMT BCBM is comparable to human BCBMs in both histopathology and immunohistochemistry.

To further test whether our PyMT BCBM model mimics the human disease, we employed Magnetic Resonance Imaging (MRI) and performed T1-weighted post-contrast MRI of mice bearing a PyMT BCBM tumor (Supplementary Fig. 1B). Human BCBMs are characterized on MRI by well-defined tumor margins [82], which was also observed in our mouse model (Supplementary Fig. 1C, solid arrow). In addition, we observed some heterogeneity within the tumor caused by the necrotic areas (in black) (Supplementary Fig. 1C), which is often used in the clinic as an indication of high proliferation in the tumor [82]. Next, we employed the single-voxel PRESS technique [82] and acquired Magnetic Resonance Spectroscopy data from a volume of interest (VOI) of the contralateral healthy brain and the tumor (Supplementary Fig. 1D). In the tumor area, we observed a small decrease in the N-acetylaspartate (NAA) peak, a metabolite present in healthy neurons, which is typically decreased in human brain tumors [82,83]. An increase in the lactate + lipids peak was also detected in the tumor area compared to the contralateral healthy brain.

Lactate is a marker of anaerobic metabolism occurring in fast proliferative tumors in human [82], while the observed increase in the lipids peak is a result of cellular breakdown and consequent byproduct of necrosis. We observed in the tumor spectrum an increase in the choline peak compared to creatine, which is also found in human brain tumors and may be an indication of cellular proliferation and increased membrane turnover [43].

Together, our data show that our novel mouse PyMT BCBM model displays key histological, MR imaging and MR spectroscopy characteristics of human BCBMs, and this warrants the use of our model to study this disease in pre-clinical settings.

### ***In vitro* drug treatment**

BCBM organoids and cell lines were treated with 10 nmol/L (PyMT BCBM model) or with 20 nmol/L (Neu BCBM model) doxorubicin (Actavis) for 7 days, with a drug and medium renewal at day 4 after treatment initiation. PyMT BCBM organoids and cells, and mouse splenic T cells were treated with 10  $\mu$ mol/L ABT263 (MedKoo, Cat. No. 201970) diluted in dimethylsulfoxide (DMSO) for 48h following pre-treatment with doxorubicin.

### ***In vivo* drug treatment**

Mice were intracranially injected with 40,000 cells obtained from dissociated PyMT BCBM organoids or 50,000 cells from Neu BCBM organoids (**see Material and Methods, Intracranial injection**). Before initiation of treatment, mice were randomized based on IVIS total flux values into treatment groups with the following drug dosage. Timeline of treatment can be seen on the corresponding figures.

*Saline vehicle (control for doxorubicin):* three times every 5 days, same volume of saline as doxorubicin, administered *via* intravenous injection.

*Doxorubicin treatment:* For doxorubicin pre-treatment, mice were treated three times every 5 days with doxorubicin (Actavis, 5 mg/kg) administered *via* intravenous injection. For continuous treatment, mice were also treated once weekly on day 1 with doxorubicin (Actavis, 5 mg/kg) administered *via* intravenous injection until reaching humane endpoint.

*IgG treatment:* As controls for depletion of T cells, on days 1, 3 and 5 prior to treatment with vehicle or with chemotherapy, mice were treated with 400  $\mu$ g (day 1) or 200  $\mu$ g (day 3 and day 5) with *InVivoMAB* rat IgG2b isotype control (BioXCell, clone LTF-2, Cat. No. BE0090). As controls for anti-PD1 treatment, mice were treated twice weekly with 400  $\mu$ g (day 1) and 200  $\mu$ g (day 4) with *InVivoMAB* rat IgG2b isotype control (BioXCell, clone 2A3, Cat. No. BE0089). Both IgG controls were administered by intraperitoneal injection.

*anti-CD4 treatment:* on days 1, 3 and 5 prior to treatment with vehicle or with chemotherapy, mice were treated with 400  $\mu$ g (day 1) or 200  $\mu$ g (day 3 and day 5) with *InVivoMAB* anti-mouse CD4 (BioXCell, clone GK1.5, Cat. No. BE003-1) which was administered by intraperitoneal injection.

*anti-CD8 treatment:* on days 1, 3 and 5 prior to treatment with vehicle or with chemotherapy, mice were treated with 400  $\mu\text{g}$  (day 1) or 200  $\mu\text{g}$  (day 3 and day 5) with *InVivoMAb* anti-mouse CD8 (BioXCell, clone YTS 169.4, Cat. No. BP0117) and administered by intraperitoneal injection.

*Anti-PD1 treatment:* mice were treated twice weekly with 400  $\mu\text{g}$  (day 1) or 200  $\mu\text{g}$  (day 4) of *InVivoMAb* anti-mouse PD1 (BioXCell, clone RMP1-14, Cat. No. BE0146) which was administered by intraperitoneal injection.

*Cremophore EL vehicle:* As a control for ABT263 treatment, mice were treated every second days, for 7 days, with a cremophore EL vehicle (DMSO:Cremophore EL:saline as 1:1:8 (v:v:v)) and with the same volume as ABT263, by oral gavage.

*ABT263 treatment:* mice were treated every second days, for 7 days, with 50 mg/kg of ABT263 (Medkoo, Cat. No. 201970) by oral gavage.

We want to disclaim that we observed that treatment with doxorubicin and with doxorubicin and anti-PD1 triggered toxicity such as weight loss and paleness in some mice. Therefore, we found that 2/8 mice with PyMT BCBM and 3/8 mice with NeuT BCBM treated with doxorubicin followed by anti-PD1 (Fig. 5 and Fig. 7D) had a smaller tumor when sacrificed compared to mice receiving monotherapies, suggesting that the anti-tumor effects of the combination therapy are actually larger than the survival data shown in Fig. 5 and Fig. 7.

### ***Flow cytometry analysis of immune panels in the PyMT BCBM***

BCBM were dissociated into single-cell suspensions using a Brain Tumor Dissociation kit (Miltenyi Biotec, Cat. No. 130-095-942) and according to the manufacturer's instructions. Subsequently, samples were blocked in FACS buffer containing 1:50 Fc block CD16/CD32 (BD Biosciences, Clone 2.4G2, Cat. No. 553141) for 20 min at room temperature, and then stained with the indicated antibodies (see details in Supplementary Table 1). Samples were permeabilized and fixed with a fixation and permeabilization kit (Thermo Fisher Scientific, Cat. No. 00-5523-00), according to the manufacturer's protocol, and then stained with intracellular antibodies (see details in Supplementary Table 1). Signals were detected on a four-laser Fortessa flow cytometer (Becton Dickinson) and analyses were performed with FlowJo software, with the gating strategy presented in Supplementary Fig. 3.

### ***Statistical analysis***

Unless mentioned otherwise, p-values were determined by unpaired, nonparametric t-test with a Mann-Whitney U correction. Kaplan Meier survival curves were analyzed with a log-rank Mantel-Cox test.

## **Supplementary Material and Method**

### **IVIS imaging**

Bioluminescence imaging was performed with an IVIS200 camera (PerkinElmer; Waltham, MA USA) 10 min after intraperitoneal injection of 150 mg/kg Beetle Luciferin (Promega, Cat. No. E1605). Mice were anesthetized with 2% (v/v) isoflurane prior and during imaging. Signal flux was obtained using open filters and high binning for mice injected in the carotid (Fig. 1B and Supplementary Fig. 1A, B), and with small binning for mice bearing BCBM derived from intracranial injections (Fig. 5).

### **Magnetic resonance imaging**

Magnetic resonance imaging was performed with a 7 Tesla BioSpec 70/20 USR (Bruker; Billerica, MA USA). Fig. 1B was imaged with a T2 RARE sequence with a 3.9 ms echo-time, 2200 ms repetition time and 8 averages. Supplementary Fig. 1C, D was imaged with a T1-weighted post-contrast sequence with a 3 ms echo-time, 235 ms repetition time and a flip angle of 30 degrees. PRESS sequence was performed with a 17ms echo-time, 2500 ms repetition time, 256 averages and a volume-of-interest of 1.8x1.8x1.8 mm size. Paravision software (v6.0.1; Bruker) was used for image acquisition. The contrast agent used was Gadoterate meglumine (Dotarem®; 0.5 mmol/mL; Guerbet; Villepinte, France) diluted 5 times with saline and injected intravenously through a cannula *via* tail vein. Mice were anesthetized with 2% (v/v) isoflurane during imaging and the heart rate was monitored throughout the procedure.

### **Immunofluorescence staining, microscopy and image analysis**

*For organoids:* organoids were fixed in 4% paraformaldehyde for 20 min at room temperature, followed by permeabilization in 0.2% TritonX-100 in PBS for 15 min at room temperature. A block was next performed in 5% **bovine serum albumin (BSA)** diluted in PBS (wt:v) for 2h at room temperature, followed by staining overnight at 4°C with anti-Cleaved Caspase 3 (1:400, Asp175, Cell Signalling, Cat. No. 9661). Appropriate Alexa Fluor labelled secondary antibody (Thermo Fisher Scientific) was combined with DAPI (1 µg/mL) and incubated for 2h in the dark at room temperature.

*For BCBM sections:* samples were fixed in a PLP buffer containing 1% paraformaldehyde, 0.2% NaIO<sub>4</sub>, 37.5% L-lysine and 37.5% P-buffer (containing 81% of Na<sub>2</sub>HPO<sub>4</sub>, 19% of NaH<sub>2</sub>PO<sub>4</sub> diluted in water, pH=7.4) for 24 h at 4°C. Subsequently, samples were moved to a sucrose solution for 12 h, at 4°C, prior to being embedded in OCT Tissue Tek (ThermoFischer Scientific, Cat. No. 11381785) and stored at -80°C.

5 µm sections were rehydrated in PBS for 10 min at room temperature. Samples were subsequently permeabilized and blocked for 30 min at room temperature in a buffer made of 5% normal goat serum in PBS (v:v), 2.5% BSA in PBS (wt:v) and 0.5% Triton X-100 (v:v)

diluted in PBS. Samples were washed twice in PBS containing 3% BSA, prior to incubation with antibodies against T cells (anti-mouse CD4-eFluor660, 1:200; eBioscience, clone GK1.5, Cat. No. 50-0041-82; anti-mouse CD8-eFluor660, 1:200, eBioscience, clone 53-6.7, Cat. No. 50-0081-82; anti-mouse CD31, 1:100, BD Pharmingen, clone MEC 13.3, Cat. No. 550274; anti-mouse VCAM-1/CD106, 1:100, R&D Systems, Cat. No. AF643-SP; anti-mouse ICAM/CD54, 1:100 R&D Systems AF796-SP, anti-mouse NG2 Chondroitin Sulfate Proteoglycan (1:250, Millipore, Cat. No. AB5320) or anti- $\alpha$ -smooth muscle actin (1:100, Sigma-Adrich, Cat. No. A5228) at 4°C overnight. Samples were then washed three times in PBS and incubated for 5 min at room temperature with DAPI (0.1  $\mu\text{g}/\text{mL}$ ) in the dark. Slides were washed three times in PBS and mounted with Vectashield hard set (Vectorlab, Cat. No. H-1400-10).

For organoids, images were acquired on an inverted Leica TCS SP5 confocal microscope (Mannheim, Germany), in 8 bits with a 20x objective. Fiji was used for quantification. Quantification of cleaved-caspase 3 staining was performed as follows: the number of cleaved-caspase 3 positive cells was quantified in 3 representative fields of view *per* replicate and was counted as a percentage of all (DAPI<sup>+</sup>) cells. The experiment was performed in 5 biological repeats (PyMT BCBM) and in 3 biological repeats (NeuT BCBM). Each dot presented on the graphs represents the averaged value *per* biological repeat of the percentage of cleaved-caspase 3<sup>+</sup> cells *per* repeat.

For slides stained with anti-CD4 and anti-CD8 antibodies, images were acquired on an inverted Leica TCS SP5 confocal microscope (Mannheim, Germany), in 8 bits with a 20x objective. For slides stained with cleaved-caspase 3, images were acquired on an inverted Leica TCS SP8 confocal microscope (Mannheim, Germany) in 8 bits with a 40x objective.

For slides stained with CD31, ICAM, VCAM, NG2 and  $\alpha$ -smooth muscle actin, slides were scanned on an AxioscanZ1 microscope (Zeiss) in 8 bit with a 20x objective. Images were deconvoluted and stitched in Huygens software and converted to a 16 bits format in Fiji. Using Imaris, CD31<sup>+</sup> vessels present inside the BCBM (H2B-Dendra<sup>+</sup> area) were segmented and staining intensity of VCAM, ICAM and  $\alpha$ -smooth muscle actin were quantified inside the segmented vessels. Intensity of NG2 was quantified in the vicinity (0-10  $\mu\text{m}$ ) of the segmented vessels. Data were normalized to the area covered by CD31<sup>+</sup> vessels in each BCBM.

For staining for LaminB1, 5  $\mu\text{m}$  sections were dried for 15 min at room temperature, rehydrated in PBS for 10 min at room temperature and permeabilized and blocked for 30 min at room temperature in a buffer made of 2.5% (v/v) normal goat serum, 1% (wt/v) BSA and 0.1% (v/v) Triton X-100 diluted in PBS. Samples were washed twice in PBS containing 1% (wt/v) BSA, prior to incubation with the antibody against Lamin B1 (1:500, Abcam, clone GR3244890-2, Cat. No. ab16048) for 2h at room temperature. Samples were then washed twice in PBS containing 1% BSA and incubated for 1h at room temperature with appropriate secondary antibody and Hoechst 33342 (Thermo Fischer, Cat. No. H3570,

5 µg/mL) in the dark. Slides were washed three times in PBS, once in water and mounted with hard set ProLong Glass Antifade Mountant (Thermo Fischer, Cat. No. P3680). Images were acquired on a Zeiss LSM 880 confocal microscope (Jena, Germany), in 16 bit with a 40x objective. Fiji was used for quantification.

### **Flow cytometry analysis of cell apoptosis**

Cell death was analyzed by quantification of cells positive for the death marker 7-AAD. Organoids were collected and dissociated into single cells by incubating them in TrypLE Express (Gibco Cat. No. 12605010) at 37°C for approximately 20 min at 900 rpm. The cell suspension was filtered on a cell strainer and incubated with 7-AAD dye (Biolegend, Cat. No. 420404) for 10 min, on ice in the dark. Samples were processed on a Fortessa flow cytometer (Becton Dickinson) and analyses were performed with FlowJo software.

### **Assessments of SA $\beta$ -Galactosidase activity in tissue sections**

SA  $\beta$ -galactosidase staining was performed on 5-µm-thick cryo-sections of BCBM tumors using a commercial kit (Sigma Aldrich, Cat. No. 11828673001) and according to the manufacturer's instructions. SA  $\beta$ -galactosidase activity was quantified by manually counting the number of SA- $\beta$ -galactosidase<sup>+</sup> cells *per* field of view, as depicted in the figures. *Per* tumor, 5 FOV were quantified. Data depicted on the graphs are averaged values of all FOV *per* mouse.

### **Generation of BCBM cell lines**

Cell lines were generated by trypsinizing the BCBM organoids with TrypLE Express (Gibco, Cat. No. 12605010) while shaking for 10-20 min at 37°C. Cells were plated in 2D on plastic-bottom plates and were cultured in DMEM, supplemented with 100 U/mL penicillin (Gibco, Cat. No. 15140122), streptomycin 10 mmol/L, FBS (10%, Thermo Fisher Scientific, Cat. No. A4766801), EGF (5 ng/ml, Thermo Fisher Scientific, Cat. No. 53003018) and Insulin (5 µg/ml, Sigma Aldrich, Cat. No. I0516) in 20% O<sub>2</sub>, 5% CO<sub>2</sub> and at 37°C.

### **Assessments of SA $\beta$ -Galactosidase activity in vitro**

200,000 cells were seeded in 6-well plates and treated with PBS or with doxorubicin 10 nmol/L (PyMT BCBM) or doxorubicin 20 nmol/L (NeuT BCBM model) for 7 days. Cells were passaged once in the PBS condition over this 7-day period. Next, for the PyMT BCBM model, medium was renewed and cells were treated with DMSO or with ABT263 10 µmol/L for 48 h. Cells were subsequently stained using the Senescence Cells Histochemical Staining Kit (Sigma-Aldrich, Cat. No. CS0030) according to the manufacturer's instructions. Cells were imaged on a bright field CCD2-color microscope equipped with a Zeiss high resolution AxioCam 512 color camera. The total number of cells and the SA  $\beta$ -galactosidase<sup>+</sup> cells were counted from 5 representative fields of view *per* condition.



### **Real-time quantitative polymerase chain reaction (RT-qPCR)**

RNA samples were isolated using Trizol (Invitrogen Life Technology, Cat. No. 15596018), according to the manufacturer's protocol and stored at -80°C. Complementary DNA was synthesized using 1 µg of RNA *per* sample and with the High-Capacity cDNA Reverse Transcription kit (ThermoFischer Scientific, Cat. No. 4368814), according to the manufacturer's protocol. Reverse transcription was performed in a PCR machine following these steps: 10 min at 25°C, 120 min at 37°C and 5 min at 85°C. qPCR was performed using Power SYBR Green PCR Master Mix (ThermoFischer Scientific, Cat. No. A25777) in a QuantStudio Real-Time qPCR machine. Thermal cycle conditions were as follows: 2 min at 50°C, 2 min at 95°C followed by 45 cycles consisting of denaturation for 15 sec at 95°C, annealing for 1 min at 60°C, and extension for 1 min at 72°C. PCR reactions were concluded with incubation for 10 min at 72°C. Relative values were quantified using the ddCt method and mean values were plotted with SEM. Sequences of primers used in this study are as follows: *FOXO4*: forward: TCTACGAATGGATGGTCCGCAC, reverse: CTTGCTGTGCAAGGACAGGTTG; *CDKN2A*: forward: TGTTGAGGCTAGAGAGGATCTTG, reverse: CGAATCTGCACCGTAGTTGAGC; *Ki67*: forward: CTGCCTGCGAAGAGAGCATC, reverse: AGCTCCACTTCGCCTTTTGG; *GAPDH*: forward: GGGTTCCTATAAATACGGACTGC, reverse: CCATTTTGTCTACGGGACGA.

### **Effects of ABT263 on T cells**

#### ***Ki67-assessment:***

Splenocytes were isolated from tumor naïve, untreated FVB female mice (aged 8-20 weeks) and cultured in Roswell Park Memorial Institute (RPMI) 1640 Medium (Thermo Fisher Scientific, Cat. No. 21875034) containing FBS (10%, Thermo Fisher Scientific, Cat. No. A4766801), Penicillin/streptomycin (10,000 U/mL; Thermo Fisher Scientific, Cat. No. 15140-122), IL2 (Thermo Fisher Scientific, Cat. No. PMC0025, 10U/mL), β-mercaptoethanol (50 µmol/L), Ultraglutamine (2 mmol/L, Lonza, Cat. No. BE17-605E/U1), PMA (50 ng/mL, SigmaAldrich), ionomycin (1 µg/mL, SigmaAldrich), in plate pre-coated with anti-CD3 (1 µg/ml, BD Bioscience, clone 17A2, Cat. No. 564008). Splenocytes were cultured in the presence of DMSO or ABT263 (10 µmol/L) for 48 h. Next, splenocytes were washed twice in FACS buffer and were blocked for 5 min at room temperature in a blocking buffer (FACS buffer containing 1:50 Fc block CD16/CD32 (BD Biosciences, Clone 2.4G2, Cat. No. 553141)) prior to staining with an anti-CD3 antibody (BD Bioscience, clone 17A2, Cat. No. 564008, 1:100). Next, splenocytes were incubated with DAPI (1 µg/mL) and permeabilized in a Foxp3 fixation/permeabilization buffer (eBioscience, Cat. No. 00-5523-00) for 30 min, in the dark and at 4°C. Cells were washed twice in permeabilization buffer (eBioscience, Cat. No. 00-8333-56), blocked for 5 min in FACS buffer containing 1:50 Fc block and stained with an anti-Ki67 antibody (1:100, BD Pharmigen, Cat. No. 558615). Splenocytes were

analyzed on a Fortessa flow cytometer (Becton Dickinson) and analyses were performed with FlowJo software.

### ***Assessment of T cell migration***

T cells were isolated by flow cytometry from the spleen of tumor naïve, untreated ROSA26<sup>mTmG</sup> FVB female mice, aged 8-20 weeks. Spleens were gently mechanically dissociated using a scalpel blade and glass slides and single cells were incubated in a red cell lysis buffer (NH<sub>4</sub>Cl 155 mmol/L, KHCO<sub>3</sub> 1 mmol/L, 0.1 mmol/L EDTA diluted in MilliQ water, pH=7.4) for 5 min at room temperature. Next, splenocytes were blocked for 5 min at room temperature in a blocking buffer (FACS buffer containing 1:50 Fc block CD16/CD32 (BD Biosciences, Clone 2.4G2, Cat. No. 553141)) and incubated with primary antibodies in the dark for 45 min at 4°C (anti-CD11b-BV650 (1:1200, BD Bioscience, clone M1/70, Cat. No. 563402); anti-CD4-eFluor660 (1:300, BD Bioscience, clone GK1.5, Cat. No. 50-0041-82); anti-CD8-eFluor660 (1:100, ThermoFisher, clone 53-6.7, Cat. No. 50-0081-82). Samples were sorted on a Fusion Cell Sorter, DAPI<sup>+</sup> (dead cells) and CD11b<sup>+</sup> cells (myeloid cells) were excluded and T cells were isolated based on CD4/CD8 expression. Following isolation, T cells were cultured in plates coated with an anti-CD3 antibody (1 µg/mL, BD Bioscience, clone 17A2, Cat. No. 564008) in RPMI 1640 Medium (Thermo Fisher Scientific, Cat. No. 21875034) containing FBS (10%, Thermo Fisher Scientific, Cat. No. A4766801), Penicillin/streptomycin (10,000 U/mL; Thermo Fisher Scientific, Cat. No. 15140-122), IL2 (10 U/mL, Thermo Fisher Scientific, Cat. No. PMC0025), β-mercaptoethanol (50 µmol/L), Ultraglutamine (2 mmol/L, Lonza, Cat. No. BE17-605E/U1), PMA (50 ng/mL, SigmaAldrich), ionomycin (1 µg/mL, SigmaAldrich). T cells were treated with DMSO or ABT263 (10 µmol/L) for 48h. Subsequently, T cells were embedded in a mix of BME and T cell medium (1:1 ratio) and plated in a glass-bottom chamber. T cells were imaged on an inverted Leica SP8 Dive system (Leica, Mannheim, Germany) with an InSight X3 laser (Spectra-Physics). ROSA26<sup>mTmG</sup> was excited with 960 nm (InSight X3) and detected at 564-698 nm (HyD-RLD4). Time-lapse movies were acquired with a 5 µm z-step and imaged every 10 min for a total of 5 or 6h. All images were acquired in 12 bit and with a 25x / 0.95 NA water immersion objective. T cell migration was analyzed in Imaris using the spot function.

### ***Acknowledgements:***

The authors thank all members of the van Rheenen laboratory for critical reading of the manuscript. The authors also thank the Pathology Department, the Animal Research facility, the Flow cytometry facility and the Bioimaging facility of the Netherlands Cancer Institute and Pablo Lopez-Jimenez for technical and scientific supports.

***Fundings:***

This work was supported by the European Research Council Grant CANCER-RECURRENCE 648804, the CancerGenomics.nl (Netherlands Organization for Scientific Research) program, the Josef Steiner Cancer Research Foundation and the Dutch Cancer Society (grant 12049 (LA)). ASM is the recipient of a fellowship from the Portuguese Foundation for Science and Technology (FCT, GABBA program-PD/BD/105748/2014). CV is funded by a fellowship from the Human Frontiers in Science Program. DAP was supported by the Dutch Cancer Society (KWF) grant UMCU-7141 awarded to PLJdK. KH received funding from the Swiss National Science Foundation. The funders had no role in the study design; in the collection, analysis, and interpretation of data; in the writing of the paper; or in the decision to submit the paper for publication.

***Authors contribution:***

**Conceptualization and study design:** ASM, RUC, MLDB, CV and JvR

**Methodology, investigation and analysis:** ASM, CV, LC, SV, RUC, JYS, DAP, KH, PLJdK, MvG, CC, LtB, GB, LA, OvT

**Writing:** ASM, RUC, CV and JvR

**Funding acquisition:** ASM, CV, JvR

**Competing interests:** PLJdK is a co-founder and shareholder of Cleara Biotech BV, The Netherlands. The authors have no other competing interests to declare.

***Data and materials availability:***

All data and materials used in this study are available upon request. Transfer of organoids from the BCBM generated in this study is subjected to a material transfer agreement.

## REFERENCES

- Lin, N.U., Bellon, J.R., and Winer, E.P. (2004). CNS metastases in breast cancer. *Journal of Clinical Oncology* 22 (17), 3608-3617.
- Bowman, K.M., and Kumthekar, P. (2018). Medical management of brain metastases and leptomeningeal disease in patients with breast carcinoma *Future Oncology* 14, 391-407.
- Markus Kuksis, Y.G., William Tran, Christiane Hoey, Alex Kiss, Adam S Komorowski, Aman J Dhaliwal, Arjun Sahgal, Sunit Das, Kelvin K Chan (2021). The incidence of brain metastases among patients with metastatic breast cancer: a systematic review and meta-analysis. *Neuro-Oncology* 23, 894-904.
- Jacobson, A. (2022). Trastuzumab Deruxtecan Improves Progression-Free Survival and Intracranial Response in Patients with HER2-Positive Metastatic Breast Cancer and Brain Metastases. *Oncologist* 27, S3-S4. 10.1093/oncolo/oyac009.
- O'Sullivan, C.C., Davarpanah, N.N., Abraham, J., and Bates, S.E. (2017). Current challenges in the management of breast cancer brain metastases. *Semin Oncol* 44, 85-100. 10.1053/j.seminoncol.2017.06.006.
- Goldberg, S.B., Gettinger, S.N., Mahajan, A., Chiang, A.C., Herbst, R.S., Sznol, M., Tsiouris, A.J., Cohen, J., Vortmeyer, A., Jilaveanu, L., et al. (2016). Pembrolizumab for patients with melanoma or non-small-cell lung cancer and untreated brain metastases: early analysis of a non-randomised, open-label, phase 2 trial. *Lancet Oncol* 17, 976-983. 10.1016/S1470-2045(16)30053-5.
- Hodi, F.S., O'Day, S.J., McDermott, D.F., Weber, R.W., Sosman, J.A., Haanen, J.B., Gonzalez, R., Robert, C., Schadendorf, D., Hassel, J.C., et al. (2010). Improved survival with ipilimumab in patients with metastatic melanoma. *N Engl J Med* 363, 711-723. 10.1056/NEJMoa1003466.
- Marshall, H.T., and Djamgoz, M.B.A. (2018). Immuno-Oncology: Emerging Targets and Combination Therapies. *Front Oncol* 8, 315. 10.3389/fonc.2018.00315.
- Waldman, A.D., Fritz, J.M., and Lenardo, M.J. (2020). A guide to cancer immunotherapy: from T cell basic science to clinical practice *Nature Review Immunology* 17, 651-668.
- Couzin-Frankel, J. (2013). Breakthrough of the year 2013. *Cancer immunotherapy. Science*
- Engelhardt, B., Vajkoczy, P., and Weller, R.O. (2017). The movers and shapers in immune privilege of the CNS. *Nat Immunol* 18, 123-131. 10.1038/ni.3666.
- Louveau, A., Harris, T.H., and Kipnis, J. (2015). Revisiting the Mechanisms of CNS Immune Privilege. *Trends Immunol* 36, 569-577. 10.1016/j.it.2015.08.006.
- Klemm, F., Maas, R.R., Bowman, R.L., Kornete, M., Soukup, K., Nassiri, S., Brouland, J.P., Iacobuzio-Donahue, C.A., Brennan, C., Tabar, V., et al. (2020). Interrogation of the Microenvironmental Landscape in Brain Tumors Reveals Disease-Specific Alterations of Immune Cells. *Cell* 181, 1643-1660.
- Quail, D.F., and Joyce, J.A. (2017). The Microenvironmental Landscape of Brain Tumors. *Cancer Cell* 31, 326-341. 10.1016/j.ccell.2017.02.009.
- Schmid, P., Adams, S., Rugo, H.S., Schneeweiss, A., Barrios, C.H., Iwata, H., Dieras, V., Hegg, R., Im, S.A., Shaw Wright, G., et al. (2018). Atezolizumab and Nab-Paclitaxel in Advanced Triple-Negative Breast Cancer. *N Engl J Med* 379, 2108-2121. 10.1056/NEJMoa1809615.
- Murthy, R.K., Loi, S., Okines, A., Paplomata, E., Hamilton, E., Hurvitz, S.A., Lin, N.U., Borges, V., Abramson, V., Anders, C., et al. (2020). Tucatinib, Trastuzumab, and Capecitabine for HER2-Positive Metastatic Breast Cancer. *N Engl J Med* 382, 597-609. 10.1056/NEJMoa1914609.
- Tolaney, S.M., Sahebjam, S., Le Rhun, E., Bachelot, T., Kabos, P., Awada, A., Yardley, D., Chan, A., Conte, P., Dieras, V., et al. (2020). A Phase II Study of Abemaciclib in Patients with Brain Metastases Secondary to Hormone Receptor-Positive Breast Cancer. *Clin Cancer Res* 26, 5310-5319. 10.1158/1078-0432.CCR-20-1764.

18. Galluzzi, L., Humeau, J., Buqué, A., Zitvogel, L., and Kroemer, G. (2020). Immunostimulation with chemotherapy in the era of immune checkpoint inhibitors. *Nat Rev Clin Oncol* 12, 725-741.
19. Kersten, K., Salvagno, C., and de Visser, K.E. (2015). Exploiting the Immunomodulatory Properties of Chemotherapeutic Drugs to Improve the Success of Cancer Immunotherapy. *Front Immunol* 6, 516. 10.3389/fimmu.2015.00516.
20. Olson, O.C., Kim, H., Quail, D.F., Foley, E.A., and Joyce, J.A. (2017). Tumor-Associated Macrophages Suppress the Cytotoxic Activity of Antimitotic Agents. *Cell Rep* 19, 101-113. 10.1016/j.celrep.2017.03.038.
21. Zingoni, A., Fionda, C., Borrelli, C., Cipitelli, M., Santoni, A., and Soriani, A. (2017). Natural Killer Cell Response to Chemotherapy-Stressed Cancer Cells: Role in Tumor Immunosurveillance. *Front Immunol* 8, 1194. 10.3389/fimmu.2017.01194.
22. Ruffell, B., Chang-Strachan, D., Chan, V., Rosenbusch, A., Ho, C.M., Pryer, N., Daniel, D., Hwang, E.S., Rugo, H.S., and Coussens, L.M. (2014). Macrophage IL-10 blocks CD8+ T cell-dependent responses to chemotherapy by suppressing IL-12 expression in intratumoral dendritic cells. *Cancer Cell* 26, 623-637. 10.1016/j.ccell.2014.09.006.
23. Junankar, S., Shay, G., Jurczyk, J., Ali, N., Down, J., Pocock, N., Parker, A., Nguyen, A., Sun, S., Kashemirov, B., et al. (2015). Real-time intravital imaging establishes tumor-associated macrophages as the extraskelatal target of bisphosphonate action in cancer. *Cancer Discov* 5, 35-42. 10.1158/2159-8290.CD-14-0621.
24. Page, D.B., Beal, K., Linch, S.N., Spinelli, K.J., Rodine, M., Halpenny, D., Modi, S., Patil, S., Young, R.J., Kaley, T., et al. (2022). Brain radiotherapy, tremelimumab-mediated CTLA-4-directed blockade +/- trastuzumab in patients with breast cancer brain metastases. *NPJ Breast Cancer* 8, 50. 10.1038/s41523-022-00404-2.
25. Sevenich, L. (2019). Turning "Cold" into "Hot" Tumors-opportunities and challenges for radio-immunotherapy against primary and metastatic brain cancers. *Front Oncology* 9, 1963.
26. Priya Kumthekar 1, S.-C.T., Andrew J Brenner 3, Santosh Kesari 4, David E Piccioni 5, Carey Anders 6, Jose Carrillo 7, Pavani Chalasani 8, Peter Kabos 9, Shannon Puhalla 10, Katherine Tkaczuk 11, Agustin A Garcia 12, Manmeet S Ahluwalia 13, Jeffrey S Wefel 14, Nehal Lakhani 15, Nuhad Ibrahim 16 (2020). ANG1005, a Brain-Penetrating Peptide-Drug Conjugate, Shows Activity in Patients with Breast Cancer with Leptomeningeal Carcinomatosis and Recurrent Brain Metastases. *Clinical Cancer Research* 26, 2789-2799.
27. Faget, D.V., Ren, Q., and Stewart, S.A. (2019). Unmasking senescence: context-dependent effects of SASP in cancer. *Nat Rev Cancer* 19, 439-453. 10.1038/s41568-019-0156-2.
28. Ruscetti, M., Morris, J.P.t., Mezzadra, R., Russell, J., Leibold, J., Romesser, P.B., Simon, J., Kulick, A., Ho, Y.J., Fennell, M., et al. (2020). Senescence-Induced Vascular Remodeling Creates Therapeutic Vulnerabilities in Pancreas Cancer. *Cell* 181, 424-441 e421. 10.1016/j.cell.2020.03.008.
29. Ewald, J.A., Desotelle, J.A., Wilding, G., and Jarrard, D.F. (2010). Therapy-induced senescence in cancer. *J Natl Cancer Inst* 102, 1536-1546. 10.1093/jnci/djq364.
30. Schmitt, C.A., Fridman, J.S., Yang, M., Lee, S., Baranov, E., Hoffman, R.M., and Lowe, S.W. (2002). A senescence program controlled by p53 and p16INK4a contributes to the outcome of cancer therapy. *Cell* 109, 335-346. 10.1016/s0092-8674(02)00734-1.
31. Ruscetti, M., Leibold, J., Bott, M.J., Fennell, M., Kulick, A., Salgado, N.R., Chen, C.C., Ho, Y.J., Sanchez-Rivera, F.J., Feucht, J., et al. (2018). NK cell-mediated cytotoxicity contributes to tumor control by a cytostatic drug combination. *Science* 362, 1416-1422. 10.1126/science.aas9090.
32. Su, D., Zhu, S., Han, X., Feng, Y., Huang, H., Ren, G., Pan, L., Zhang, Y., Lu, J., and Huang, B. (2009). BMP4-Smad signaling pathway mediates adriamycin-induced premature senescence in lung cancer cells. *J Biol Chem* 284, 12153-12164. 10.1074/jbc.M807930200.

33. Chastagner, P., Sudour, H., Mriouah, J., Barberi-Heyob, M., Bernier-Chastagner, V., and Pinel, S. (2015). Preclinical studies of pegylated- and non-pegylated liposomal forms of doxorubicin as radiosensitizer on orthotopic high-grade glioma xenografts. *Pharm Res* 32, 158-166. 10.1007/s11095-014-1452-x.
34. Liu, Y., Yang, Y., Liu, X., and Jiang, T. (2008). Quantification of pegylated liposomal doxorubicin and doxorubicinol in rat plasma by liquid chromatography/electrospray tandem mass spectroscopy: Application to preclinical pharmacokinetic studies. *Talanta* 74, 887-895. 10.1016/j.talanta.2007.07.022.
35. Vail, D.M., Amantea, M.A., Colbern, G.T., Martin, F.J., Hilger, R.A., and Working, P.K. (2004). Pegylated liposomal doxorubicin: proof of principle using preclinical animal models and pharmacokinetic studies. *Semin Oncol* 31, 16-35. 10.1053/j.seminoncol.2004.08.002.
36. Beerling, E., Seinstra, D., de Wit, E., Kester, L., van der Velden, D., Maynard, C., Schafer, R., van Diest, P., Voest, E., van Oudenaarden, A., et al. (2016). Plasticity between Epithelial and Mesenchymal States Unlinks EMT from Metastasis-Enhancing Stem Cell Capacity. *Cell Rep* 14, 2281-2288. 10.1016/j.celrep.2016.02.034.
37. Margarido, A.S., Uceda-Castro, R., Hahn, K., de Bruijn, R., Kester, L., Hofland, I., Lohuis, J., Seinstra, D., Broeks, A., Jonkers, J., et al. (2022). Epithelial-to-Mesenchymal Transition Drives Invasiveness of Breast Cancer Brain Metastases. *Cancers (Basel)* 14.
38. Debnath, J., and Brugge, S.J. (2005). Modelling glandular epithelial cancers in three-dimensional cultures. *Nat Rev Cancer* 9, 675-688. 10.1038/nrc1695.
39. Drost, J., and Clevers, H. (2018). Organoids in cancer research. *Nat Rev Cancer* 18, 407-418. 10.1038/s41568-018-0007-6.
40. Weaver, V., Lelièvre, S., Lakin, J.N., Chrenek, M.A., Jones, J.C.R., Giancotti, F., Werb, Z., and Bissell, M.J. (2002). beta4 integrin-dependent formation of polarized three-dimensional architecture confers resistance to apoptosis in normal and malignant mammary epithelium. *Cancer Cell* 3, 205-216. 10.1016/s1535-6108(02)00125-3.
41. Rippaus, N., Taggart, D., Williams, J., Andreou, T., Wurdak, H., Wronski, K., and Lorger, M. (2016). Metastatic site-specific polarization of macrophages in intracranial breast cancer metastases. *Oncotarget* 7, 41473-41487. 10.18632/oncotarget.9445.
42. Howe, F.A., Barton, S.J., Cudlip, S.A., Stubbs, M., Saunders, D.E., Murphy, M., Wilkins, P., Opstad, K.S., Doyle, V.L., McLean, M.A., et al. (2003). Metabolic profiles of human brain tumors using quantitative in vivo 1H magnetic resonance spectroscopy *Magn Reson Med* 49, 223-232.
43. Miller, B.L. (1991). A review of chemical issues in 1H NMR spectroscopy: N-acetyl-L-aspartate, creatine and choline. *NMR Biomed* 4, 47-52. 10.1002/nbm.1940040203.
44. Topalian, S., Taube, J.M., Abders, R.A., and Pardoll, D.M. (2016). Mechanism-driven biomarkers to guide immune checkpoint blockade in cancer therapy. *Nature Review Cancer* 16, 275-287.
45. Iwamoto, T., Niikura, N., Ogiya, R., Yasojima, H., and Iwata, H. (2019). Distinct gene expression profiles between primary breast cancers and brain metastases from pair-matched samples. *Scientific Report* 7, 13343.
46. Duchnowska, R., Peksa, R., Radecka, B., Mandat, T., Trojanowski, T., Jarosz, B., and Jassem, J. (2016). Immune response in breast cancer brain metastasis and their microenvironment: the role of the PD-1/PD-L axis. *Breast cancer research* 1, 43.
47. Baar, M.P., Brandt, R.M.C., Putavet, D.A., Klein, J.D.D., Derks, K.W.J., Bourgeois, B.R.M., Stryeck, S., Rijksen, Y., van Willigenburg, H., Feijtel, D.A., et al. (2017). Targeted Apoptosis of Senescent Cells Restores Tissue Homeostasis in Response to Chemotoxicity and Aging. *Cell* 169, 132-147 e116. 10.1016/j.cell.2017.02.031.
48. Wang, A.S., Ong, P.F., Chojnowski, A., Clavel, C., and Dreesen, O. (2017). Loss of lamin B1 is a biomarker to quantify cellular senescence in photoaged skin. *Sci Rep* 7, 15678. 10.1038/s41598-017-15901-9.

49. Coffinier, C., Jung, H.J., Nobumori, C., Chang, S., Tu, Y., Barnes, R.H., 2nd, Yoshinaga, Y., de Jong, P.J., Vergnes, L., Reue, K., et al. (2011). Deficiencies in lamin B1 and lamin B2 cause neurodevelopmental defects and distinct nuclear shape abnormalities in neurons. *Mol Biol Cell* 22, 4683-4693. 10.1091/mbc.E11-06-0504.
50. Freund, A., Laberge, R.M., Demaria, M., and Campisi, J. (2012). Lamin B1 loss is a senescence-associated biomarker. *Mol Biol Cell* 23, 2066-2075. 10.1091/mbc.E11-10-0884.
51. Voorwerk, L., Slagter, M., Horlings, H.M., Sikorska, K., van de Vijver, K.K., de Maaker, M., Nederlof, I., Kluijn, R.J.C., Warren, S., Ong, S., et al. (2019). Immune induction strategies in metastatic triple-negative breast cancer to enhance the sensitivity to PD-1 blockade: the TONIC trial. *Nat Med* 25, 920-928. 10.1038/s41591-019-0432-4.
52. Toso, A., Revandkar, A., Di Mitri, D., Guccini, I., Proietti, M., Sarti, M., Pinton, S., Zhang, J., Kalathur, M., Civenni, G., et al. (2014). Enhancing chemotherapy efficacy in Pten-deficient prostate tumors by activating the senescence-associated antitumor immunity. *Cell Reports* 9, 75-89.
53. Dou, Z., Ghos, K., Grazia Vizioli, M., Zhu, J., Sen, P., Wangenstein, K.J., Simithy, J., Lan, Y., Lin, Y., Zhou, Z., et al. (2017). Cytoplasmic chromatin triggers inflammation in senescence and cancer *Nature* 550, 402-406.
54. Gluck, S., Guey, B., Gulen, M.F., Wolter, K., Kang, T.W., Schmacke, N.A., Bridgeman, A., Rehwinkel, J., Zender, L., and Ablasser, A. (2017). Innate immune sensing of cytosolic chromatin fragments through cGAS promotes senescence. *Nat Cell Biol* 19, 1061-1070. 10.1038/ncb3586.
55. Kang, T.W., Yeves, T., Woller, N., Hoenicke, L., Wuestefeld, T., Dauch, D., Hohmeyer, A., Gereke, M., Rudalska, R., Potapova, A., et al. (2011). Senescence surveillance of pre-malignant hepatocytes limits liver cancer development. *Nature* 479, 547-551. 10.1038/nature10599.
56. Ritsma, L., Steller, E.J., Ellenbroek, S.I., Kranenburg, O., Borel Rinkes, I.H., and van Rheeën, J. (2013). Surgical implantation of an abdominal imaging window for intravital microscopy. *Nat Protoc* 8, 583-594. 10.1038/nprot.2013.026.
57. Lagares, D., Santos, A., Grasberger, P.E., Liu, F., Probst, C.K., Rahimi, R.A., Sakai, N., Kuehl, T., Ryan, J., Bhola, P., et al. (2017). Targeted apoptosis of myofibroblasts with the BH3 mimetic ABT-263 reverses established fibrosis. *Sci Transl Med* 9. 10.1126/scitranslmed.aal3765.
58. Chang, J., Wang, Y., Shao, L., Laberge, R.M., Demaria, M., Campisi, J., Janakiraman, K., Sharpless, N.E., Ding, S., Feng, W., et al. (2016). Clearance of senescent cells by ABT263 rejuvenates aged hematopoietic stem cells in mice. *Nat Med* 22, 78-83. 10.1038/nm.4010.
59. Yu, X., Dobrikov, M., Keir, S.T., Gromeier, M., Pastan, I.H., Reisfeld, R., Bigner, D.D., and Chandramohan, V. (2019). Synergistic antitumor effects of 9.2.27-PE38KDEL and ABT-737 in primary and metastatic brain tumors. *PLoS One* 14, e0210608. 10.1371/journal.pone.0210608.
60. Tarantini, S., Balasubramanian, P., Delfavero, J., Csipo, T., Yabluchanskiy, A., Kiss, T., Nyul-Toth, A., Mukli, P., Toth, P., Ahire, C., et al. (2021). Treatment with the BCL-2/BCL-xL inhibitor senolytic drug ABT263/Navitoclax improves functional hyperemia in aged mice. *Geroscience* 43, 2427-2440. 10.1007/s11357-021-00440-z.
61. Lim, S., Kim, T.J., Kim, Y.J., Kim, C., Ko, S.B., and Kim, B.S. (2021). Senolytic Therapy for Cerebral Ischemia-Reperfusion Injury. *Int J Mol Sci* 22. 10.3390/ijms222111967.
62. Hunt, B.J., and Jurd, K.M. (1998). Endothelial cell activation. A central pathophysiological process. *BMJ* 316, 1328-1329. 10.1136/bmj.316.7141.1328.
63. Huet, S., Groux, H., Caillou, B., Valentin, H., Prieur, A.M., and Bernard, A. (1989). CD44 contributes to T cell activation. *J Immunol* 143, 798-801.

64. McKinney, E.F., Cuthbertson, I., Harris, K.M., Smilek, D.E., Connor, C., Manferrari, G., Carr, E.J., Zamvil, S.S., and Smith, K.G.C. (2021). A CD8(+) NK cell transcriptomic signature associated with clinical outcome in relapsing remitting multiple sclerosis. *Nat Commun* 12, 635. 10.1038/s41467-020-20594-2.
65. Boggio, K., Nicoletti, G., Di Carlo, E., Cavallo, F., Landuzzi, L., Melani, C., Giovarelli, M., Rossi, I., Nanni, P., De Giovanni, C., et al. (1998). Interleukin 12-mediated prevention of spontaneous mammary adenocarcinomas in two lines of Her-2/neu transgenic mice. *J Exp Med* 188, 589-596. 10.1084/jem.188.3.589.
66. Vilarino, N., Bruna, J., Bosch-Barrera, J., Valiente, M., and Nadal, E. (2020). Immunotherapy in NSCLC patients with brain metastases. Understanding brain tumor microenvironment and dissecting outcomes from immune checkpoint blockade in the clinic. *Cancer Treat Rev* 89, 102067. 10.1016/j.ctrv.2020.102067.
67. Tawbi, H.A., Forsyth, P.A., Algazi, A., Hamid, O., Hodi, F.S., Moschos, S.J., Khushalani, N.I., Lewis, K., Lao, C.D., Postow, M.A., et al. (2018). Combined Nivolumab and Ipilimumab in Melanoma Metastatic to the Brain. *N Engl J Med* 379, 722-730. 10.1056/NEJMoa1805453.
68. Cloughesy, T.F., Mochizuki, A.Y., Orpilla, J.R., Hugo, W., Lee, A.H., Davidson, T.B., Wang, A.C., Ellingson, B.M., Rytlewski, J.A., Sanders, C.M., et al. (2019). Neoadjuvant anti-PD-1 immunotherapy promotes a survival benefit with intratumoral and systemic immune responses in recurrent glioblastoma. *Nat Med* 25, 477-486. 10.1038/s41591-018-0337-7.
69. Dorr, J.R., Yu, Y., Milanovic, M., Beuster, G., Zasada, C., Dabritz, J.H., Lisec, J., Lenze, D., Gerhardt, A., Schleicher, K., et al. (2013). Synthetic lethal metabolic targeting of cellular senescence in cancer therapy. *Nature* 501, 421-425. 10.1038/nature12437.
70. Wang, C., Vegna, S., Jin, H., Benedict, B., Liefstink, C., Ramirez, C., de Oliveira, R.L., Morris, B., Gadiot, J., Wang, W., et al. (2019). Inducing and exploiting vulnerabilities for the treatment of liver cancer. *Nature* 574, 268-272. 10.1038/s41586-019-1607-3.
71. Amor, C., Feucht, J., Leibold, J., Ho, Y.J., Zhu, C., Alonso-Curbelo, D., Mansilla-Soto, J., Boyer, J.A., Li, X., Giavridis, T., et al. (2020). Senolytic CAR T cells reverse senescence-associated pathologies. *Nature* 583, 127-132. 10.1038/s41586-020-2403-9.
72. Wang, B., Kohli, J., and Demaria, M. (2020). Senescent Cells in Cancer Therapy: Friends or Foes? *Trends in Cancer* 6, 838-857.
73. Jackson, J.G., Pant, V., Li, Q., Chang, L.L., Quintas-Cardama, A., Garza, D., Tavana, O., Yang, P., Manshouri, T., Li, Y., et al. (2012). p53-mediated senescence impairs the apoptotic response to chemotherapy and clinical outcome in breast cancer. *Cancer Cell* 21, 793-806. 10.1016/j.ccr.2012.04.027.
74. Beldi-Ferchiou, A., Lambert, M., Dogniaux, S., Vely, F., Vivier, E., Olive, D., Dupuy, S., Lévassieur, F., Zucman, D., Lebbe, C., et al. (2016). PD-1 mediates functional exhaustion of activated NK cells in patients with Kaposi sarcoma. *Oncotarget* 7, 72961-72977. 10.18632/oncotarget.12150.
75. Pesce, S., Greppi, M., Grossi, F., Del Zotto, G., Moretta, L., Sivori, S., Genova, C., and Marcenaro, E. (2019). PD-1-PD-Ls Checkpoint: Insight on the Potential Role of NK Cells. *Front Immunol* 10, 1242. 10.3389/fimmu.2019.01242.
76. Hsu, J., Hodgins, J.J., Marathe, M., Nicolai, C.J., Bourgeois-Daigneault, M.C., Trevino, T.N., Azimi, C.S., Scheer, A.K., Randolph, H.E., Thompson, T.W., et al. (2018). Contribution of NK cells to immunotherapy mediated by PD-1/PD-L1 blockade. *J Clin Invest* 128, 4654-4668. 10.1172/JCI99317.
77. Cortes, J., Cescon, D.W., Rugo, H.D., Nowecki, Z., Im, S.-A., Md Yusof, M., Gallardo, C., Lipatov, O., Barrios, C.H., Holgado, E., et al. (2020). KEYNOTE-355: Randomized, double-blind, phase III study of pembrolizumab + chemotherapy versus placebo + chemotherapy for previously untreated locally recurrent inoperable or metastatic triple-negative breast cancer. *Journal of Clinical Oncology* 38.
78. Tabasso, A.F.S., Jones, D.J.L., Jones, G.D.D., and Macip, S. (2019). Radiotherapy-Induced Senescence and its Effects on Responses to Treatment. *Clin Oncol (R Coll Radiol)* 31, 283-289. 10.1016/j.clon.2019.02.003.



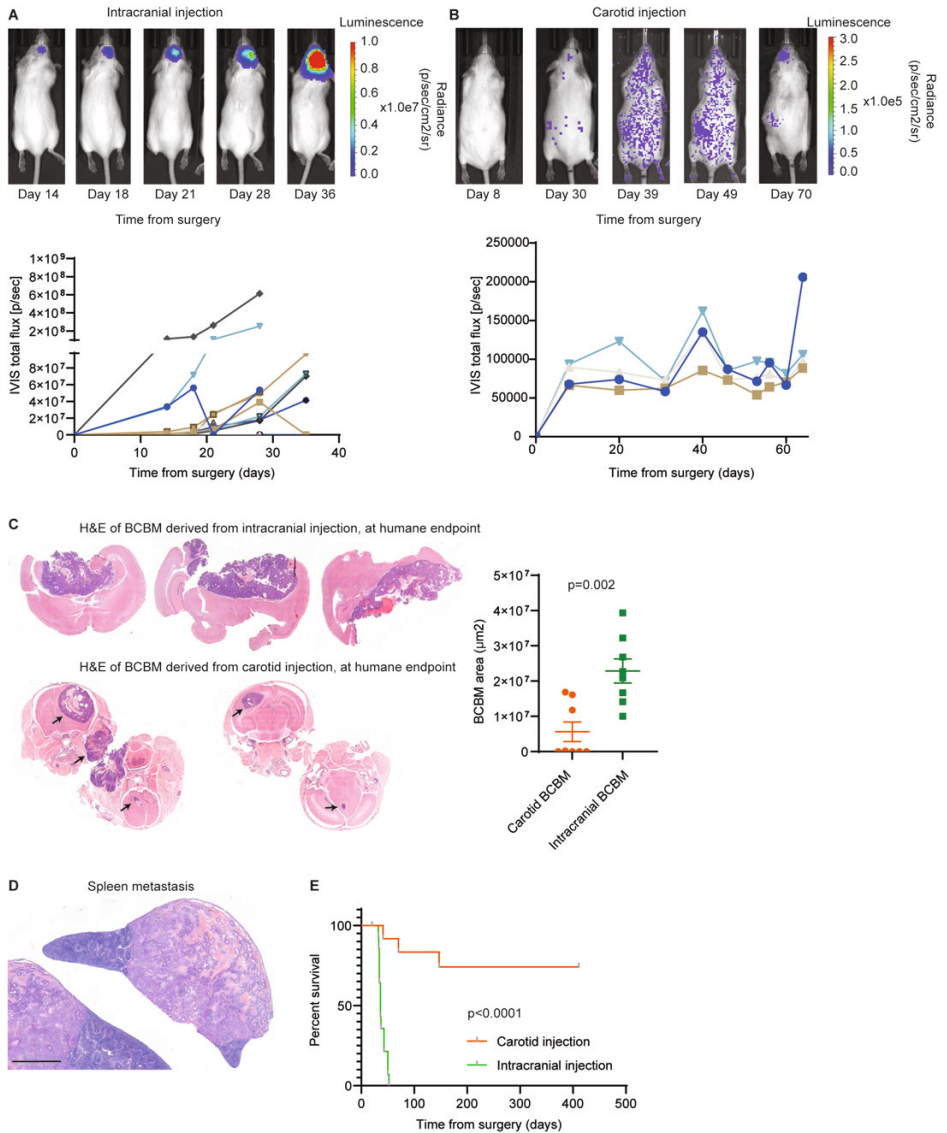
79. Putavet, D.A., and de Keizer, P.L.J. (2021). Residual Disease in Glioma Recurrence: A Dangerous Liaison with Senescence. *Cancers (Basel)* 13. 10.3390/cancers13071560.
80. Dahan, R., Sega, E., Engelhardt, J., Selby, M., Korman, A.J., and Ravetch, J.V. (2015). FcγRs Modulate the Anti-tumor Activity of Antibodies Targeting the PD-1/PD-L1 Axis. *Cancer Cell* 28, 285-295. 10.1016/j.ccell.2015.08.004.
81. Lignelli, A., and Khandji, A.G. (2011). Review of Imaging Techniques in the Diagnosis and Management of Brain Metastases. *Neurosurgery Clinics of North America* 22, 15-25.
82. Hourani, R., Brant, L.J., Rizk, T., Weingart, J.D., Barker, P.B., and Horska, A. (2008). Can Proton MR Spectroscopic and Perfusion Imaging Differentiate Between Neoplastic and Nonneoplastic Brain Lesions in Adults? *American Journal of Neuroradiology* 29, 366-372.
83. Zhang, C., Lowery, F.J., and Yu, D. (2017). Intracarotid Cancer Cell Injection to Produce Mouse Models of Brain Metastasis. *J Vis Exp* 120.

## SUPPLEMENTARY FILES

**Supplementary Table 1 – Details of antibodies used for flow cytometry.**

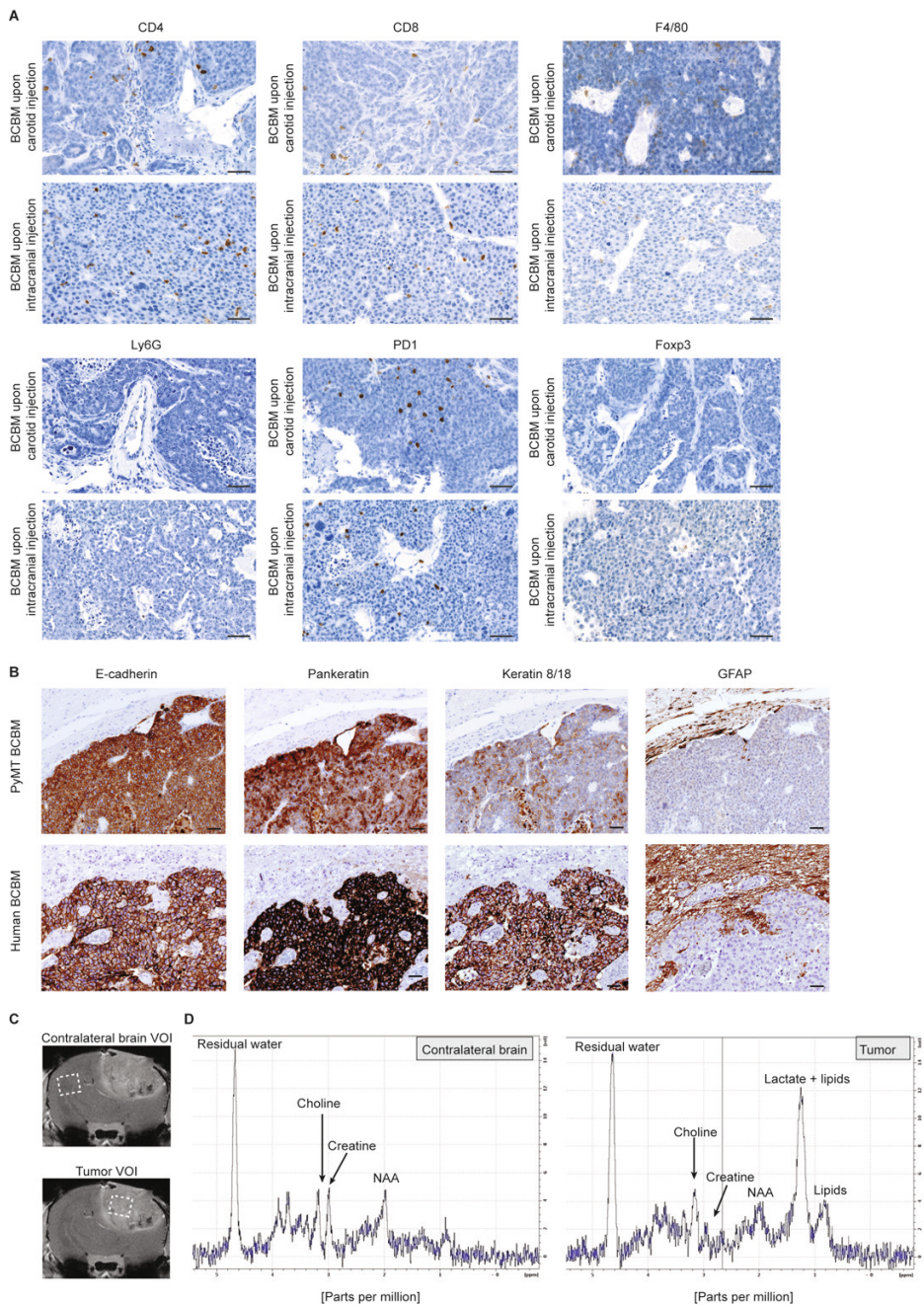
Marker	Fluorophore	Clone	Company	Cat. No.	Dilution
CD45	AF700	30-F11	Biolegend	103123	1/200
CD4	APC	GK 1.5	Biolegend	100412	1/300
CD8	FITC	53-6.7	eBioscience	11-0081-82	1/200
NK1.1	PE/Cy7	PK136	Biolegend	108713	1/600
CD11b	BV650	M1/70	Biolegend	101259	1/1200
Ki67	BV786	B56	BD Bioscience	558615	1/200
PD-1	BV421	J43	BD Bioscience	562584	1/200
CD69	PE-DAZZLE	H1.2F3	Biolegend	104335	1/200
FoxP3	PE-Cy5.5	FJK-16s	Biolegend	35-5773-82	1/200
Ly6G	APC	1A8	Biolegend	127613	1/150
Ly6C	BV605	HK1.4	Biolegend	128035	1/400
CD49D	PE-Cy7	9C10	Biolegend	103705	1/200
GranzymeA	Pacific blue	GB11	Biolegend	515407	1/100

## SUPPLEMENTARY FIGURES

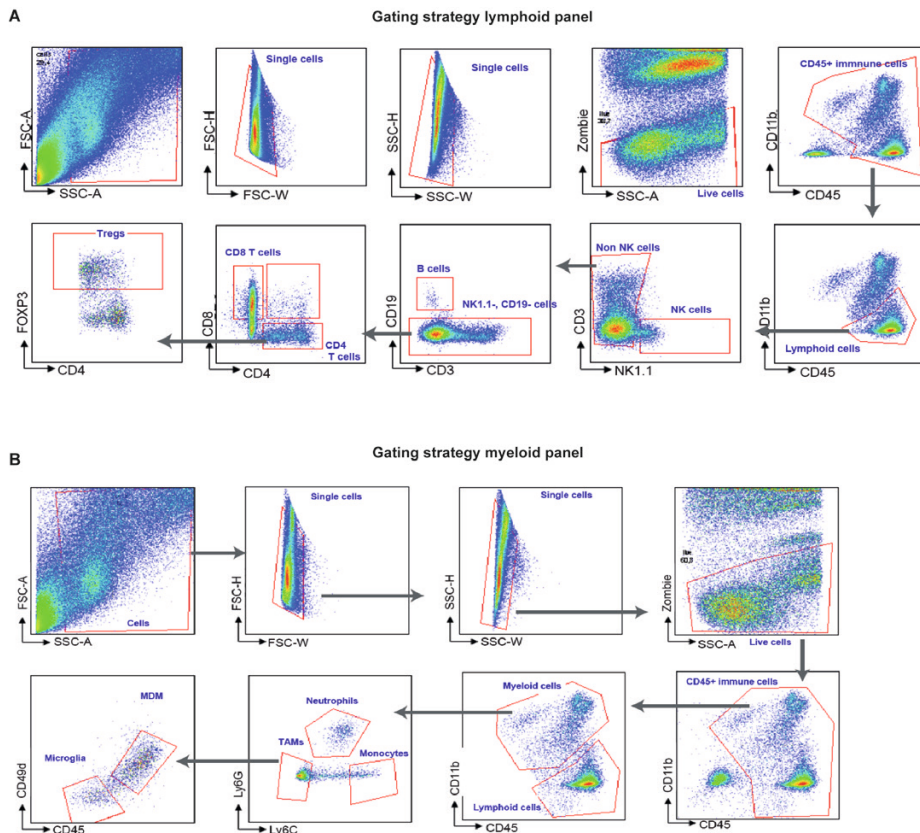


**Supplementary Figure 1. Characterization of BCBM generated upon intracarotid or intracardiac injections of the PyMT BCBM organoids.** **A.** Representative images and quantification of whole-body IVIS bioluminescence of BCBM upon intracranial injection or **B.** carotid injection of PyMT organoids made as single cells before injection. The same mouse, representative of the cohort, is displayed over time. Time in days displayed on the figure are from the time of surgery. The numbers of mice followed by whole-body IVIS bioluminescence were intracranial injection: n=10 mice, carotid injection: n=4 mice.

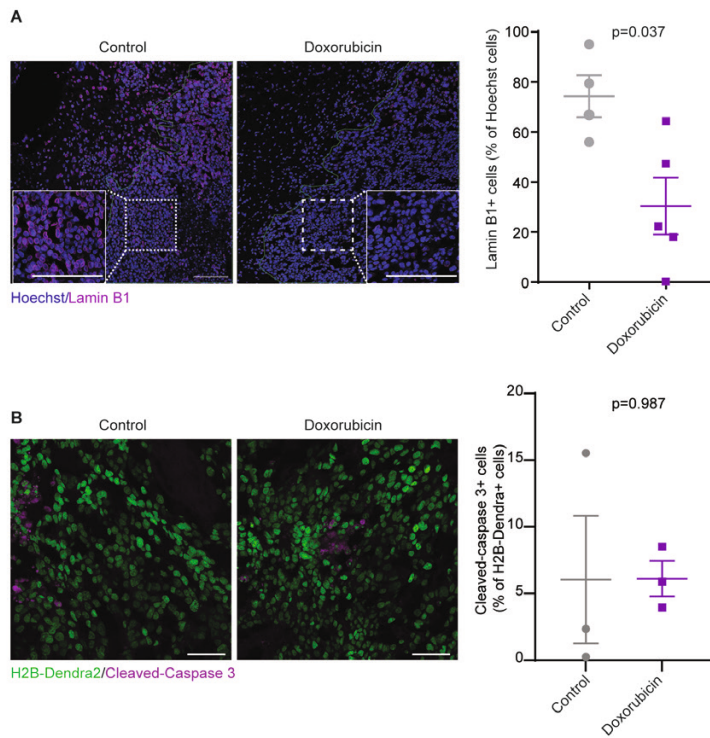
**Supplementary Figure 1. Continued. C.** Representative images and quantification of PyMT BCBM area at humane endpoint upon intracranial or carotid injections of the PyMT BCBM organoids. The graph illustrates the area of single BCBM found in 8 mice injected intracranially and in 13 mice injected in the carotid. Note that we found BCBMs in 2 out of 13 mice injected in the carotid, however this number of BCBMs may be underestimated since we analyzed only one H&E section per brain. Blue and orange dots depict BCBM found in independent mice. **D.** Representative pictures of extracranial metastases in the spleen (scale bar: 2 mm) in mice injected with PyMT BCBM organoids in the carotid. **E.** Kaplan-Meier analysis of survival for mice bearing BCBM upon intracranial or carotid injection. n=13 mice *per* group.



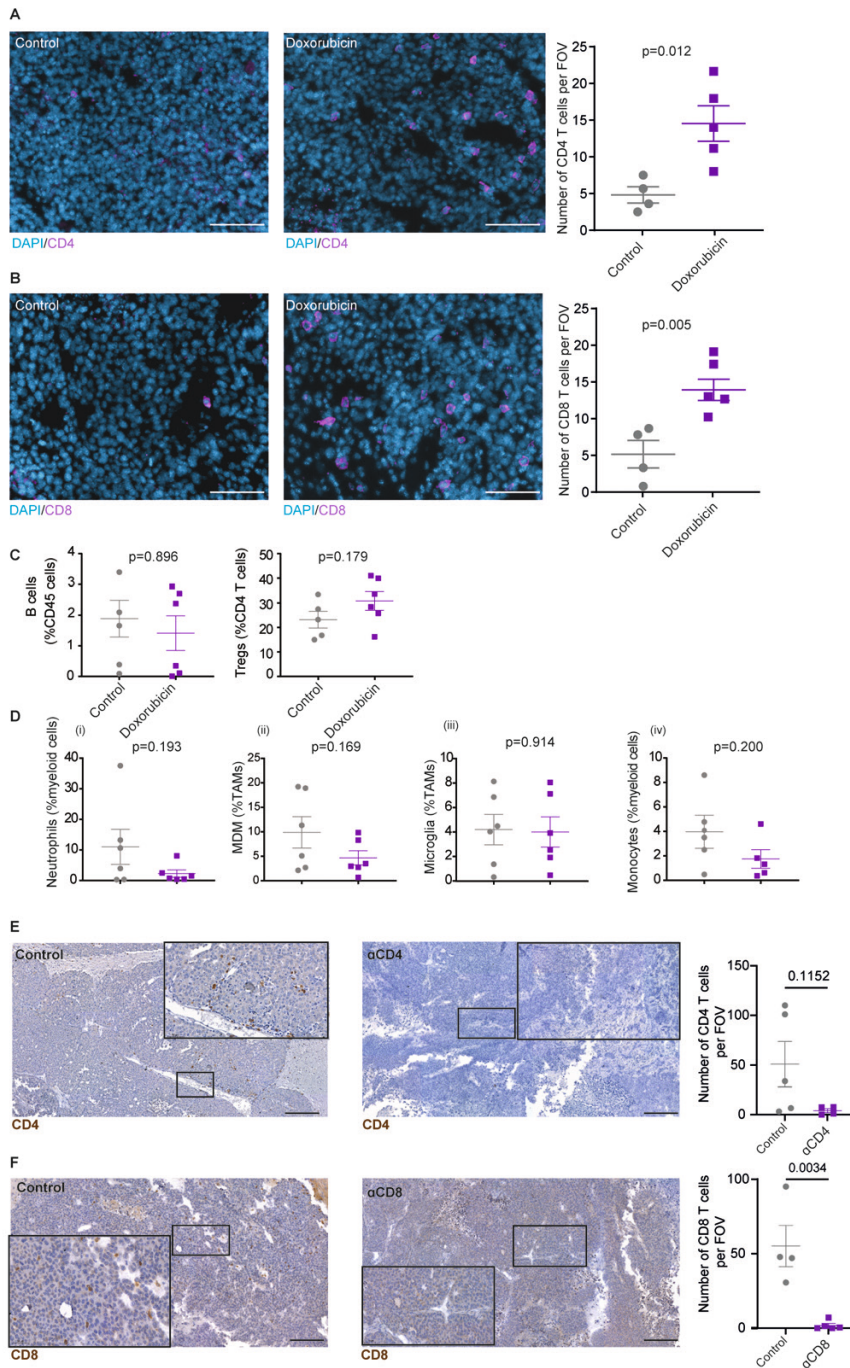
**Supplementary Figure 2. Continued. B.** Immunohistochemistry staining in PyMT BCMB (upper panel) and human BCMB (lower panel) for GFAP, pankeratin, E-cadherin and Keratin 8/18. Scale bar: 50  $\mu$ m. **C.** Representative images of a T1-weighted post-contrast MRI in contralateral brain and in the PyMT BCMB. The black arrow indicates edema. Dashed squares represent the volume of interest (VOI) measured in **D**. **D.** Spectra of the area depicted in **C**, obtained by MRS for both contralateral brain tissue and PyMT BCMB.



**Supplementary Figure 3. Flow cytometry analysis of infiltrated lymphoid cells. A.** Gating strategy applied to mouse BCMB to characterize the content of lymphoid cells. **B.** Gating strategy applied to mouse BCMB to characterize the content of myeloid cells.



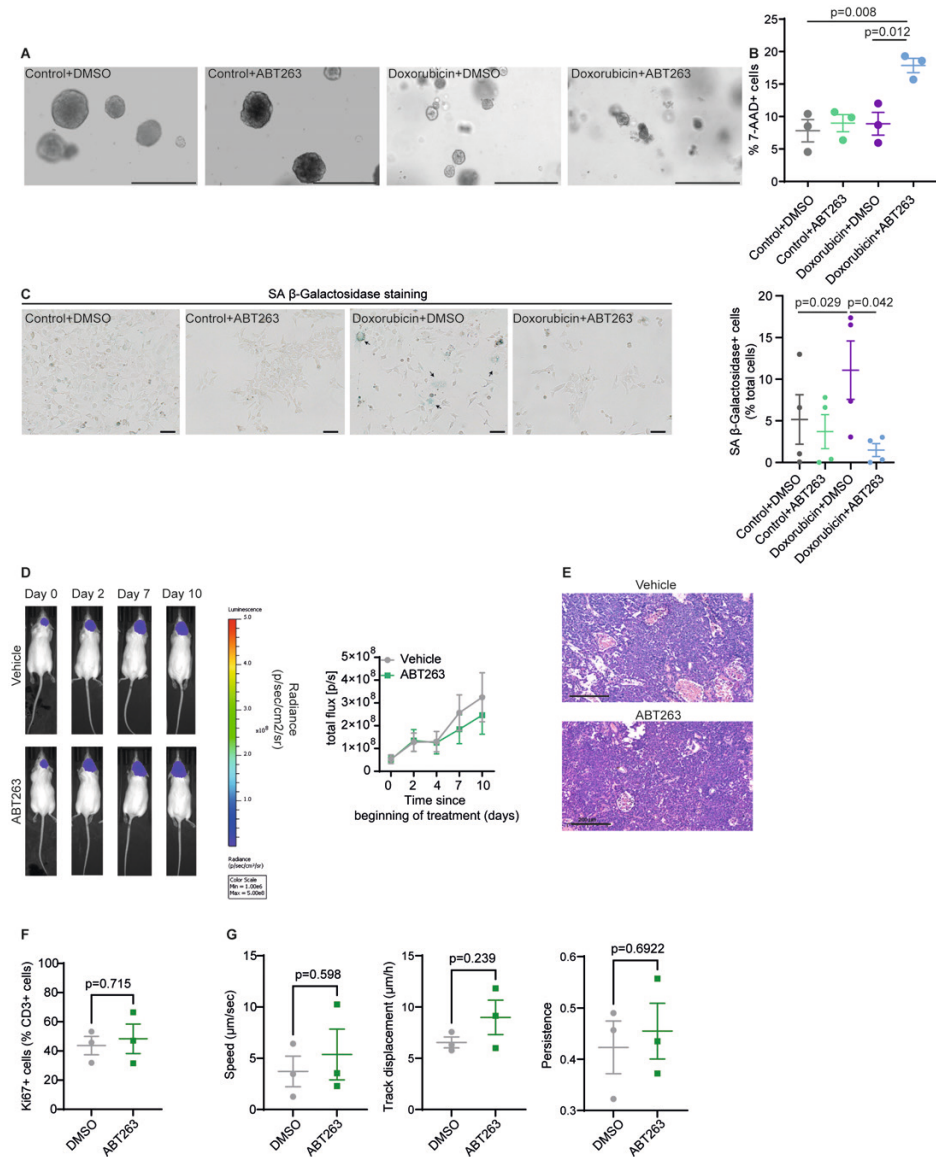
**Supplementary Figure 4. Immunofluorescence staining of lamin B1 and cleaved-caspase 3 in *in vivo* BCBM treated with doxorubicin. A.** Representative images and quantification of Lamin B1<sup>+</sup> cells in *in vivo* BCBMs treated with control vehicle (saline) or with doxorubicin. Data are presented as mean  $\pm$  SEM, n=4 mice (saline) and n=5 mice (doxorubicin). Scale bar: 100  $\mu$ m. **B.** Representative images and quantification of the percentage of BCBM tumor cells positive for cleaved-caspase 3<sup>+</sup> in *in vivo* BCBMs treated with control vehicle (saline) or with doxorubicin. Data are presented as mean  $\pm$  SEM, n=3 mice *per* group. Whole BCBM sections were quantified in Fiji. Scale bar: 50  $\mu$ m.



**Supplementary Figure 5. Immunofluorescence staining of CD4 and CD8 in *in vivo* BCBM treated with doxorubicin and validation of depletion of CD4 and CD8 using depleting antibodies. A.** Representative images and quantification of immunofluorescent staining for CD4 or B. for

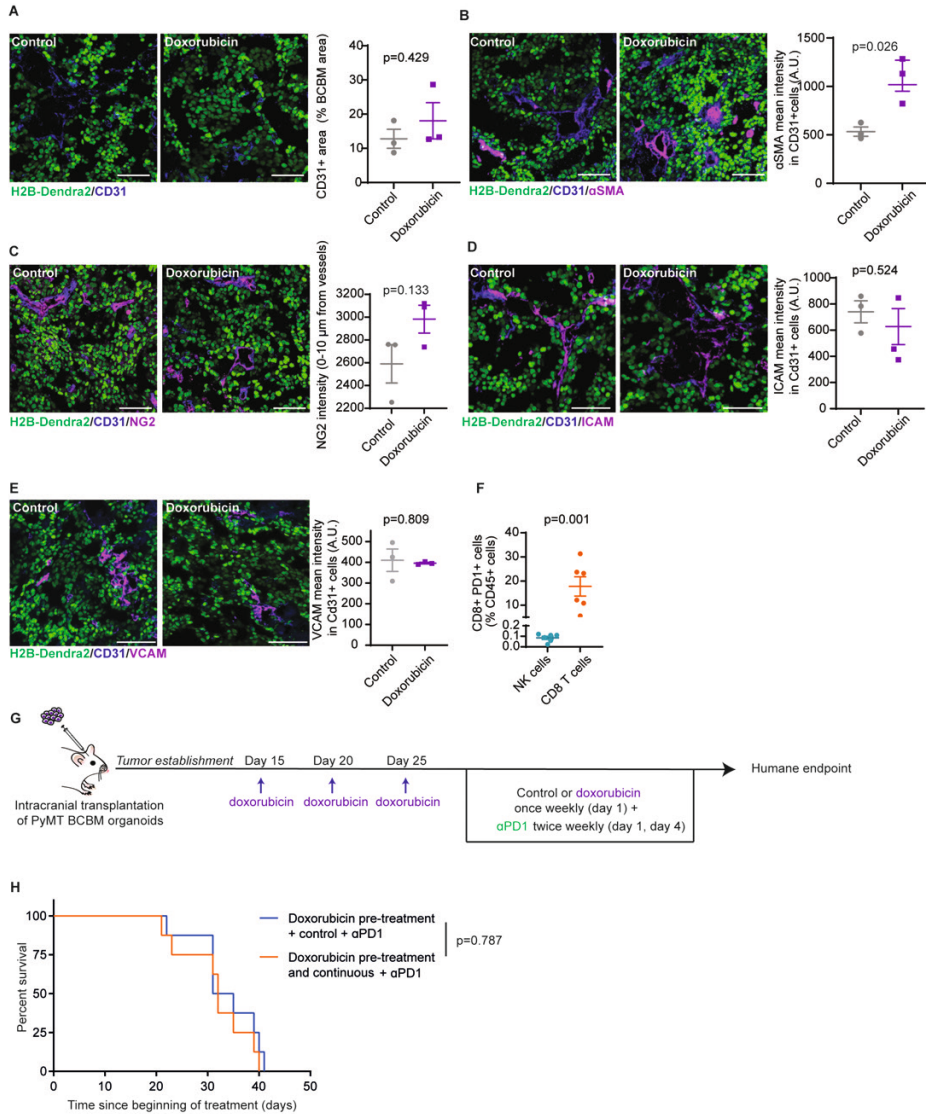


CD8 T cells in *in vivo* BCBMs treated with control vehicle (saline) or doxorubicin. n= 4 mice (saline) and n=5 mice (doxorubicin), data are presented as mean +/- SEM. Scale bar: 100  $\mu$ m. *Per* tumor section, 4-5 FOV were analyzed and averaged. **C.** Quantification of B cells as a percentage of CD45+ cells (i) and regulatory T cells as a percentage of CD4+ cells (ii) infiltrated in mouse BCBM treated with vehicle control (n=6) or with doxorubicin (n=6). Data are presented as mean +/- SEM. Data were obtained by flow cytometry. **D.** Quantification of neutrophils as a percentage of myeloid cells (i), MDMs as a percentage of TAMs (ii), microglia as a percentage of TAMs (iii) and monocytes as a percentage of myeloid cells (iv) infiltrated in mouse BCBM treated with vehicle control (n=6) or with doxorubicin (n=6). Data are presented as mean +/- SEM. Data were obtained by flow cytometry. Representative images and quantification of immunohistochemistry staining for CD4 (**E.**) and CD8 (**F.**) T cells in BCBM from mice treated with IgG control or with depleting antibodies against CD4 or CD8. n=3 mice *per* group, data are presented as mean +/- SEM. Scale bar: 200  $\mu$ m. *Per* tumor section, 4-5 FOV were analyzed.



**Supplementary Figure 6. ABT263 induces cells death in PyMT BCMB organoids and PyMT BCMB cells pre-treated with doxorubicin but does not directly affect BCMB tumor growth, T cell proliferation or migration. A.** Representative images and **B.** quantification of cell death with flow cytometry (7-AAD<sup>+</sup> cells as a percentage of all single cells) for PyMT BCMB organoids treated with vehicle (PBS) followed by DMSO, with doxorubicin alone followed by DMSO, with vehicle (PBS) followed by ABT263 or pre-treated with doxorubicin followed by ABT263.  $n=3$  biological repeats. Data are presented as mean  $\pm$  SEM. Scale bar: 400  $\mu$ m. **C.** Representative images and quantification of SA  $\beta$ -Galactosidase staining in the PyMT BCMB cell line treated with vehicle (PBS) followed by DMSO, with doxorubicin alone followed by DMSO, with vehicle (PBS) followed by ABT263 or pre-treated with

doxorubicin followed by ABT263. n=4 biological repeats. Data are presented as mean +/- SEM. Scale bar: 50  $\mu\text{m}$ . p-values were determined using a paired nonparametric t-test with a Mann-Whitney U correction. **D.** Whole-body bioluminescence images of representative mice for each treatment group followed over time and quantification of IVIS bioluminescence in mice bearing BCBM and treated with a vehicle or with ABT263. n=4 mice *per* group. **E.** Representative images of H&E staining of BCBM treated with a vehicle or with ABT263. n=4 mice *per* group. Scale bar: 200  $\mu\text{m}$ . **F.** Quantification of proliferative T cells (Ki67<sup>+</sup> as a percentage of CD3<sup>+</sup> positive cells) treated with DMSO or with ABT263 (10  $\mu\text{mol/L}$ ) for 48h. Data are mean +/- SEM, n=3 biological repeats. Data were obtained using flow cytometry. **G.** Quantification of T cell speed, track displacement and persistence upon *in vitro* treatment with DMSO or with ABT263 (10  $\mu\text{mol/L}$ ) for 48h. Data are mean +/- SEM, n=3 biological repeats. T cell migration was quantified in Imaris in 5 fields of view *per* condition and *per* biological repeat.



**Supplementary Figure 7. Recruitment of T cells upon induction of senescence by doxorubicin is not accompanied by a strong remodeling of the BTB in the PyMT BCBM, and continuous treatment with doxorubicin does not further improve anti-PD1 efficacy.** **A.** Representative images and quantification of area covered by vessels lined with CD31<sup>+</sup> cells normalized to the PyMT BCBM area upon treatment with control (saline) or with doxorubicin. **B.** Representative images and quantification of αSMA staining intensity in CD31<sup>+</sup> cells present in PyMT BCBM upon treatment with control (saline) or with doxorubicin. **C.** Representative images and quantification of NG2 staining intensity in the vicinity (0-10 μm) of vessels lined with CD31<sup>+</sup> cells in PyMT BCBM upon treatment with control (saline) or with doxorubicin. **D.** Representative images and quantification of ICAM staining intensity and **E.** VCAM staining intensity in CD31<sup>+</sup> cells in PyMT BCBM upon treatment with control (saline) or with doxorubicin. For A-E, n=3 mice *per* group, stainings were analysed in Imaris.

For each slide, the entire BCBM was analyzed. Please also see Method section for more details on data analysis. For B-E, data are normalized to the area covered by vessels lined with CD31<sup>+</sup> cells. Data are presented as mean  $\pm$  SEM. Scale bar: 150  $\mu$ m. **F.** Quantification by flow cytometry of the percentage of NK cells that express CD8 and PD1 and of CD8 T cells that express PD1 out of total CD45<sup>+</sup> cells, in the PyMT BCBM upon treatment with doxorubicin. n=6 mice, data are presented  $\pm$  SEM. **G.** Schematic representation of experimental design and treatment timeline. **H.** Kaplan-Meier analyses of time to humane endpoint for mice treated with either pre-treatment with doxorubicin followed by anti-PD1 (n=8) or pre-treatment with doxorubicin followed by anti-PD1 and continuous doxorubicin treatment (n=8).

### ***Supplementary Movie 1***

**Time-lapse imaging of T cell migration in BME upon treatment with DMSO.**

### ***Supplementary Movie 2***

**Time-lapse imaging of T cell migration in BME upon treatment with ABT263.**



# Chapter 4

**GFAP splice variants fine-tune glioma cell invasion and tumour dynamics by modulating migration persistence.**

**Rebeca Uceda-Castro**<sup>\*</sup>, Jessy V. van Asperen<sup>\*</sup>, Claire Vennin, Jacqueline Sluijs, Emma J. van Bodegraven, Andreia S. Margarido, Pierre A.J. Robe, Jacco van Rheenen<sup>#‡</sup>, Elly M. Hol<sup>#‡</sup>

<sup>\*</sup> Contributed equally

<sup>‡</sup> Shared senior authorship

<sup>#</sup> correspondence author

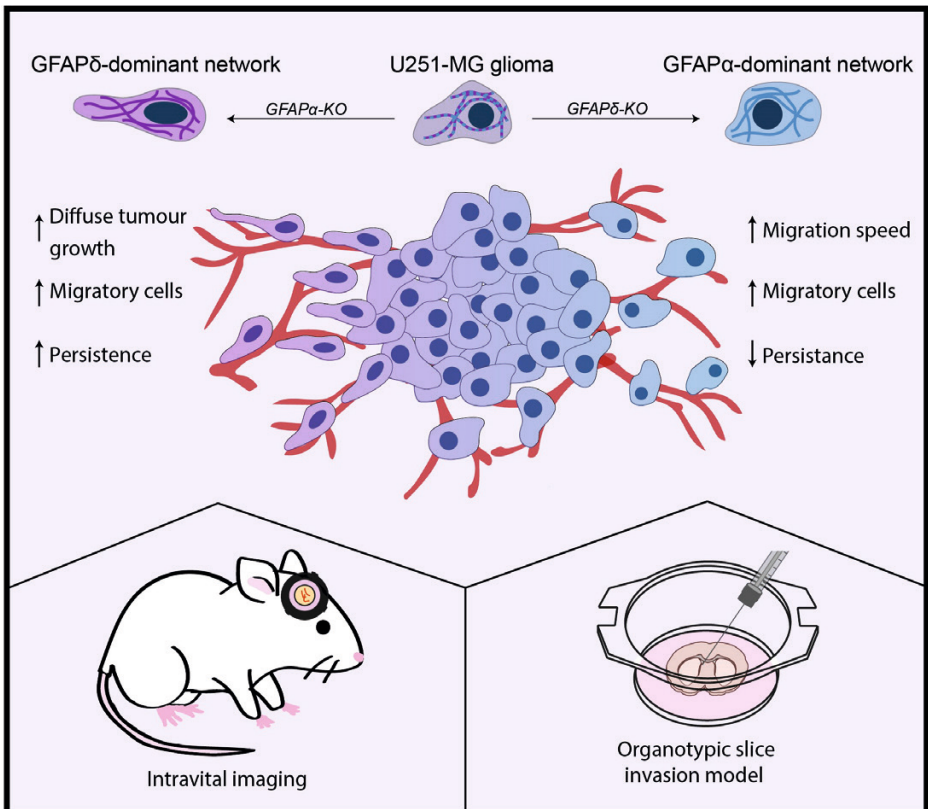
Published in Scientific Reports 2022





## ABSTRACT

Glioma is the most common form of malignant primary brain tumours in adults. Their highly invasive nature makes the disease incurable to date, emphasizing the importance of better understanding the mechanisms driving glioma invasion. Glial fibrillary acidic protein (GFAP) is an intermediate filament protein that is characteristic for astrocyte- and neural stem cell-derived gliomas. Glioma malignancy is associated with changes in GFAP alternative splicing, as the canonical isoform GFAP $\alpha$  is downregulated in higher-grade tumours, leading to increased dominance of the GFAP $\delta$  isoform in the network. In this study, we used intravital imaging and an *ex vivo* brain slice invasion model. We show that the GFAP $\delta$  and GFAP $\alpha$  isoforms differentially regulate the tumour dynamics of glioma cells. Depletion of either isoform increases the migratory capacity of glioma cells. Remarkably, GFAP $\delta$ -depleted cells migrate randomly through the brain tissue, whereas GFAP $\alpha$ -depleted cells show a directionally persistent invasion into the brain parenchyma. This study shows that distinct compositions of the GFAP-network lead to specific migratory dynamics and behaviours of gliomas.



## INTRODUCTION

Glioblastoma multiforme (GBM, grade IV glioma) is the most common and most aggressive tumour of the central nervous system, with an incidence of 3 per 100,000 people and a crude median survival of 9 months after diagnosis [1]. GBM is currently incurable and this is for a large part due to the highly invasive nature of glioma cells [2-4]. Standard-of-care treatment for GBM consists of surgical tumour resection, followed by chemo- and radiotherapy, but fails to fully eradicate highly invasive glioma cells. As a consequence, patients often relapse after treatment and the tumour rapidly re-grows.

The intermediate filament (IF) protein glial fibrillary acid protein (GFAP) is a signature type III IF protein of glioma cells that has been implicated in tumour migration [5-7]. The role of IFs in glioma invasion and migration has only gained attention recently [8]. With over 70 genes encoding different IF proteins, the IF family is one of the largest human gene families and IF expression patterns are highly cell- and tissue type-specific [9]. Changes in the composition of the IF-network are associated with alterations in malignancy. For example, during the epithelial-to-mesenchymal (EMT) transition, a process linked to increased cellular invasiveness and cancer progression [10], the IF-network of cancer cells with an epithelial origin changes from a keratin-dominant to a vimentin-dominant network [11-13]. In addition, breast cancer invasion is linked to changes in the IF-network, with a switch from keratin 8 to keratin 14 expression in invasive cells [14]. GFAP is an IF protein that is classically used to identify malignancies of glial origin, such as astrocytomas and glioblastomas [15]. In addition to GFAP, gliomas can heterogeneously express a combination of IFs including vimentin, synemin, and nestin [16], which are located within the same filament in the cell [17]. GFAP is differentially spliced, and GFAP $\alpha$  and GFAP $\delta$  are the two isoforms that are most highly expressed and best studied. The GFAP $\delta$  isoform results from alternative splicing with a 3' polyadenylation event, where the last two exons 8 and 9 of GFAP $\alpha$  are replaced by exon 7a, leading to an alternative 42 amino acid C-terminal tail [18,19]. The two isoforms have different assembly properties [20], protein interactions [19,21], and differ in their expression patterns, with GFAP $\alpha$  predominantly expressed in mature astrocytes and GFAP $\delta$  in the neurogenic niches of the human brain [22,23].

In previous studies, we and others have shown that glioma malignancy is associated with alterations in GFAP splice isoform levels [6,24-29]. As such, RNA sequencing analysis of the cancer genome atlas (TCGA) database showed that increasing glioma malignancy grades are associated with a lower overall expression of GFAP and a shift towards higher levels of the alternative splice variant GFAP $\delta$  relative to GFAP $\alpha$  [6]. Increasing the GFAP $\delta$ / $\alpha$  ratio *in vitro* leads to an upregulation of genes encoding proteins that are involved in the interactions between cells and the extracellular matrix (ECM) such as laminins, integrins, and matrix metalloproteinase 2 (MMP-2) [5-7,20]. Besides, immunohistochemical analysis of glioma tissue samples linked GFAP $\delta$  expression to an altered cellular morphology [28-28] and to more invasive tumours based on neuroimaging [27]. Although these observations are

suggestive for changed glioma cell behaviour upon alterations in GFAP-isoform expression, a full characterization of changed behaviour has not yet been performed.

In this study, we investigated how manipulation of GFAP-isoform expression affects human glioma cell invasion and growth dynamics *ex vivo* and *in vivo*. We longitudinally monitored the growth patterns of a total of twelve clones of U251-MG glioma cells depleted from either the GFAP $\alpha$  or the GFAP $\delta$  isoform in *ex vivo* organotypic mouse brain slices and in mouse brains *in vivo* with intravital imaging. We show that manipulation of the GFAP-network strongly affects the motility of glioma cells and tumour growth patterns. GFAP $\delta$ -KO cells form denser tumours, have increased motility compared to control tumours and migrate randomly, whereas GFAP $\alpha$ -KO cells show a more diffuse growth pattern and migrate more persistently towards the brain parenchyma.

## RESULTS

### ***GFAP-isoform expression differs between low- and high-grade gliomas.***

Using differential gene expression analysis of RNA sequencing data from the TCGA database, we previously showed that the ratio of splice variants GFAP $\alpha$  and GFAP $\delta$  differs between low grade- and high-grade gliomas [6]. Since this publication, 37 additional patient samples were included in the TCGA database. We therefore re-analysed the RNA sequencing data of the updated TCGA cohort and confirmed our previously reported findings. Whereas canonical splice variant GFAP $\alpha$  was significantly decreased in grade IV glioma compared to lower grades glioma (grade II and III) (**Supp. Fig. 1a**), the expression of alternative splice variant GFAP $\delta$  was not different between the different grades (**Supp. Fig. 1b**). Thus, there is an increased dominance of GFAP $\delta$  in high- versus lower-grade glioma, as illustrated by the significant increase in the GFAP $\delta/\alpha$  ratio (**Fig. 1a**).

### ***Modification of GFAP-isoform expression using CRISPR-Cas9.***

To understand how the different ratios of GFAP $\delta/\alpha$  affect the behaviour of the tumour cells, we modified GFAP-isoform expression in the U251-MG human glioma cell line using CRISPR-Cas9 technology, as previously performed in ref. [7]. A set of two single guide RNAs (sgRNAs) were used to delete the DNA region encoding the 41 or 42 amino acid tail of GFAP $\alpha$  and GFAP $\delta$ , respectively. To create a GFAP $\alpha$  knockout (KO), the intronic regions before and after exon 8 and 9 were targeted, whereas the GFAP $\delta$ -KO cells were created by flanking the intronic regions before and after exon 7a (**Fig.1b, Supp. Fig. 2b,d**). In addition to the six cell clones previously generated in ref 7 (CRISPR set A: CTL1, CTL2, GFAP $\delta$ -KO1, GFAP $\delta$ -KO2, GFAP $\alpha$ -KO1, GFAP $\alpha$ -KO2), we engineered six extra cell clones using a different set of sgRNAs (CRISPR set B: CTL3, CTL4, GFAP $\delta$ -KO3, GFAP $\delta$ -KO4, GFAP $\alpha$ -KO3, GFAP $\alpha$ -KO4) to create a total of twelve clones. Exonic depletion was confirmed with polymerase

chain reaction (PCR) (**Supp. Fig. 2a,c**) and sequencing (**Supp. Fig. 2b,d**). Targeting the exonic region led to a significant decrease in mRNA levels of the corresponding isoform (**Supp. Fig. 2e,f,g**) and an increase (GFAP $\alpha$ -KO) or decrease (GFAP $\delta$ -KO) of the GFAP $\delta$ / $\alpha$  mRNA ratio (**Fig. 1c**) and the GFAP $\delta$ /GFAPpan protein ratio (**Fig. 1d,e, Supp. Fig. 2h,i**). The cell clones showed normal IF-network formation, except for GFAP $\alpha$ -KO clone 3, where occasional network collapses were observed (**Supp. Fig. 2j**). This GFAP $\alpha$ -KO clone 3 had the highest GFAP $\delta$ /GFAPpan protein ratio (**Fig. 1d**), confirming that there is a limit to the level of GFAP $\delta$  that can be incorporated into the network [20,30].

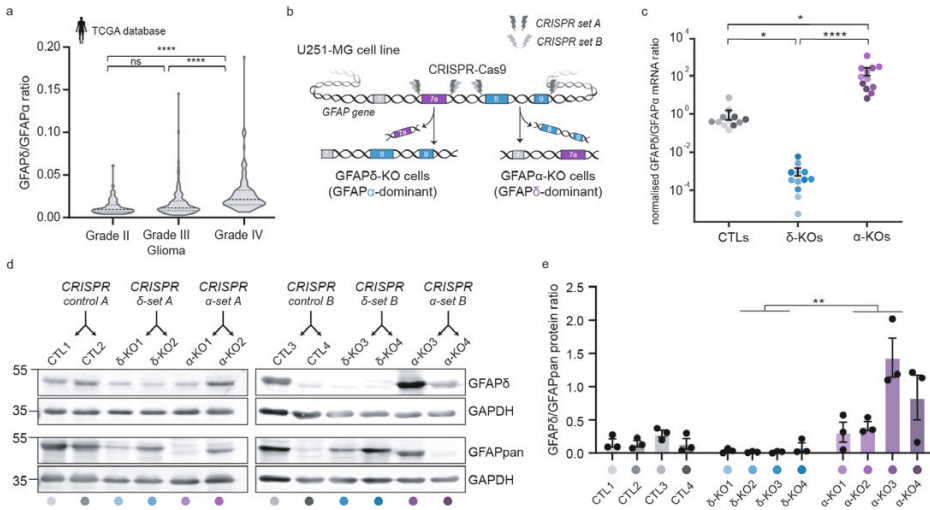


**Figure 1. GFAP $\delta$ /GFAP $\alpha$  ratio in the TCGA database and generation of GFAP isoform KO clones to regulate the GFAP $\delta$ /GFAP $\alpha$  ratio in U251-MG glioma cells.** (a) Violin plots of the GFAP $\delta$ /GFAP $\alpha$  ratio in tumour samples of grade II (n= 64), grade III (n= 130), and grade IV (n= 153) astrocytoma, obtained from normalised isoform expression data of the TCGA database. Significance was determined using a Kruskal-Wallis test followed by a Dunn's multiple comparisons test. (b) Schematic illustration of the GFAP gene with the Cas9-targeted locations to generate GFAP $\delta$ - and GFAP $\alpha$ -KO cell clones. GFAP $\delta$ -KO and GFAP $\alpha$ -KO cell clones were generated using two sets of sgRNAs (CRISPR set A and B) and four clones per isoform-KO were selected and characterised, leading to a total of 12 cell clones. (c) GFAP $\delta$ /GFAP $\alpha$  mRNA ratio of the GFAP isoform KO cells and controls, represented on a log<sub>10</sub> scale. Depletion of exon 7a (GFAP $\delta$ -KO) leads to a decrease in the GFAP $\delta$ /GFAP $\alpha$  ratio compared to the control cells, whereas depletion of exons 8 and 9 (GFAP $\alpha$ -KO) leads to an increase in the ratio. n=12 biological repeats per group, derived from 4 clones per condition represented with different colour hues. Significance was determined using a Kruskal-Wallis test followed by a Dunn's multiple comparisons test. (d) Protein levels of GFAP $\delta$  and all GFAP isoforms (GFAPpan) in the 12 different cell clones generated with the different CRISPR sets (CRISPR control A, CRISPR  $\delta$ -set A, CRISPR  $\alpha$ -set A, CRISPR control B, CRISPR  $\delta$ -set B, CRISPR  $\alpha$ -set B) determined with Western blot. Full-length blots are presented in Supp.Fig.6 (e) Quantification of GFAP $\delta$ /GFAPpan levels in the 12 different cell clones. Significance was determined using a Kruskal-Wallis test followed by a Dunn's multiple comparisons test. The data is shown as mean  $\pm$  S.E.M, \*p < 0.05, \*\*p < 0.01, \*\*\*p < 0.001, \*\*\*\*p < 0.0001, ns = not significant.

## Depletion of GFAP-isoforms increases cell invasion in *ex vivo* organotypic brain slices.

To study how modulation of the GFAP-network affects cell invasion in a physiologically relevant environment, we adapted the *ex vivo* organotypic brain slice model described by ref. 31. *Ex vivo*, 350  $\mu\text{m}$  thick brain slices of p15-17 mouse pups were prepared and cultured in an air-liquid interface. The twelve cell clones were transduced with H2B-mNeonGreen to visualise the nuclei and were injected into the lateral ventricles of the organotypic brain slice using a micromanipulator. The twelve H2B-mNeonGreen expressing cells (4 CTLs, 4 GFAP $\delta$ -KOs, 4 GFAP $\alpha$ -KOs) were co-injected with an internal control line (I-CTL, CRISPR set A: CTL1, CRISPR set B: CTL3) that expressed H2B-mCherry. The brain slices injected with U251-MG cells were kept in culture for one week (**Fig. 2a**). Upon fixation of the *ex vivo* slices, we applied whole-mount immunofluorescent staining for laminin and used RapiClear tissue clearing<sup>32</sup>. Subsequently, we used confocal imaging to create a 3D-reconstruction of the invasion patterns of the cells in the brain slice (**Fig. 2b, Supp. Fig. 3**). Laminin expression was not only observed along the blood vessels but deposits produced by the glioma cells were also observed at the injection site where the cell density was the highest (**Fig. 2b, Supp. Fig. 3**). We used this laminin expression pattern to distinguish cells within the tumour core from cells that had invaded into the mouse brain tissue (**Supp. Fig. 3**).

First, we compared the distribution of nuclei of the CTLs, GFAP $\delta$ -KOs, and GFAP $\alpha$ -KOs to that of the I-CTLs. We calculated the distance of every individual nucleus from the boundary of the tumour core and plotted the distribution of the cells within different distance bins (**Fig. 2c**). As expected, the distribution plot of H2B-mNeonGreen expressing CTLs overlapped with that of the H2B-mCherry expressing I-CTLs (**Fig. 2d, Supp Fig. 4a**). The distribution of nuclei of the GFAP $\delta$ -KO cells slightly deviated from the I-CTL line (**Fig. 2e,f, Supp Fig. 4b**), but the clearest alteration in distribution was observed in the GFAP $\alpha$ -KO cells. Whereas I-CTL cells have the highest density of cells in the tumour core, the GFAP $\alpha$ -KO cells showed a more diffuse growth pattern (**Fig. 2g, Supp Fig. 4c**). When plotting the distribution of cells, a shift in cell density towards the tumour border and tissue was observed (**Fig. 2h**), indicating more invasion. We next quantified the percentage of cells in the tissue as a measure for invasion and indeed observed a higher percentage of invading GFAP $\alpha$ -KO cells in comparison to its I-CTL and in comparison to the CTLs (**Fig. 2i**). Whereas GFAP $\delta$ -KO had similar percentages of invading cells compared to its I-CTL, a higher percentage of invading cells was measured in comparison to the CTLs (**Fig. 2i**).

To confirm the effect of downregulating GFAP $\alpha$  on tumour distribution patterns, we repeated the *ex vivo* organotypic brain slice invasion experiment with U251-MG cells transduced with an shRNA against the 3'UTR of GFAP $\alpha$  (**Supp. Fig. 5a**), as earlier published in ref. 5. Targeting GFAP $\alpha$  at the mRNA level led to a diffuse growth pattern and more invading cells, similar to the observations seen in CRISPR-Cas9 modified cells (**Supp. Fig. 5**).

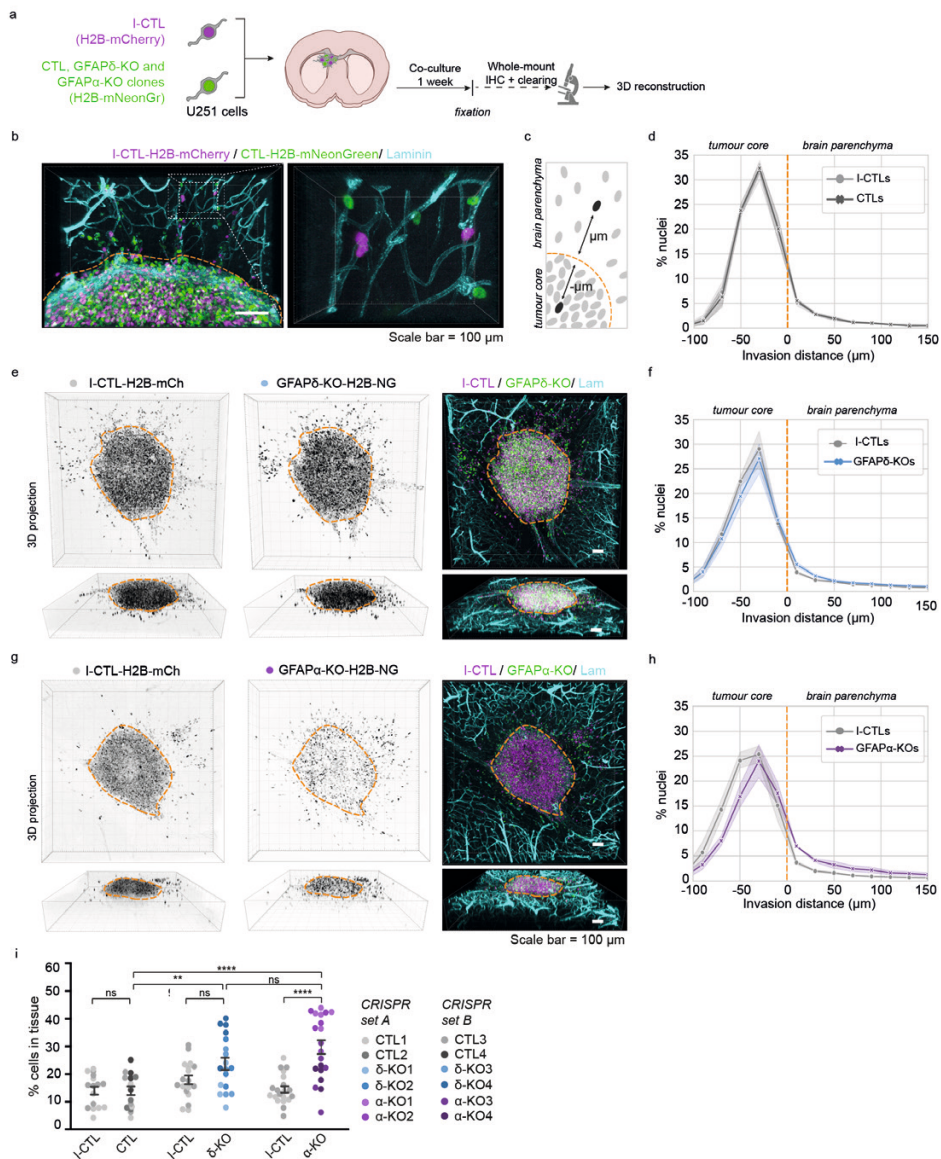


**Figure 2. Modification of GFAP isoform expression affects macroscopic growth patterns in organotypic brain slice cultures.** (a) Schematic of experimental set-up: H2B-NeonGreen expressing control (CTL), GFAP $\delta$ -KO and GFAP $\alpha$ -KO cell clones are injected in organotypic brain slices together with an H2B-mCherry expressing internal control (I-CTL) and co-cultured for one week. After fixation, whole-mount immunofluorescent staining, and clearing, confocal images are used to create a 3D reconstruction of the invasion patterns. (b) Representative image of I-CTL1 (magenta) and CTL1 (green) cells within the organotypic brain slice model. Invading cells are mainly found around the mouse brain vasculature (laminin, cyan). Laminin deposits in the tumour core can be used to distinguish stationary cells from cells invading the tissue, indicated by the orange dotted line. (c) Schematic depicting the method used to quantify the distribution of nuclei in the organotypic brain

slices. (d) Distribution of nuclei of all I-CTL and CTL cells in the organotypic brain slices (n=16 independent experiments, 4 different clones). (e) Representative images of invasion pattern of GFAP $\delta$ -KO clone 1 and I-CTL 1. (f) Distribution of nuclei of all GFAP $\delta$ -KO and I-CTL cells in the organotypic brain slices (n=18 independent experiments, 4 different clones). (g) Representative image of the invasion pattern of GFAP $\alpha$ -KO clone 2 and I-CTL 1. (h) Distribution of nuclei of all GFAP $\alpha$ -KO cells and I-CTL cells in the organotypic brain slices (n= 20 independent experiments, 4 different clones). (i) Quantification of the percentage of invaded cells per condition, n= 16 (CTLs), n=18 (GFAP $\delta$ -KO), and n= 20 (GFAP $\alpha$ -KO) injected organotypic brain slices derived from 4 different clones (CRISPR set A and B) per condition. Significance was determined using a two-way ANOVA followed by Tukey's multiple comparisons test. Scale bar = 100  $\mu$ m. The data is shown as mean  $\pm$  S.E.M, \*p < 0.05, \*\*p < 0.01, \*\*\*p < 0.001, \*\*\*\*p < 0.0001, ns = not significant. NG= mNeonGreen, mCh = mCherry, Lam = laminin.

### ***Depletion of GFAP $\alpha$ isoform leads to more diffuse tumours in vivo.***

Next, we aimed to study the GFAP modulated cells in an *in vivo* setting where a functional vasculature is present, and where it is possible to follow tumour progression over time. We used intravital microscopy (IVM), which allows to longitudinally visualise tumour cell behaviour at the single-cell level in a living organism [33]. Per condition, we separately injected two H2B-mNeonGreen expressing clones with the most extreme GFAP $\delta/\alpha$  ratio (CTL 1, GFAP $\delta$ -KO 2, and GFAP $\alpha$ -KO 2 from CRISPR set A, CTL 3, GFAP $\delta$ -KO 3, and GFAP $\alpha$ -KO 4 from CRISPR set B) into NOD-Scid IL2R $\gamma$  null mice. Tumour development was followed using a cranial imaging window (CIW). An overview image of the tumour at the endpoint was taken, when a well-established tumour with similar size had formed (**Fig. 3a, b**). To quantify the tumour density, we calculated the number of individual cells in the total tumour area. We observed that tumours generated by the GFAP $\delta$ -KO were significantly denser than tumours generated by the GFAP $\alpha$ -KO cells (**Fig. 3b, c**). This suggested that GFAP $\alpha$ -KO cells have a more diffuse growth pattern compared to GFAP $\delta$ -KO cells.

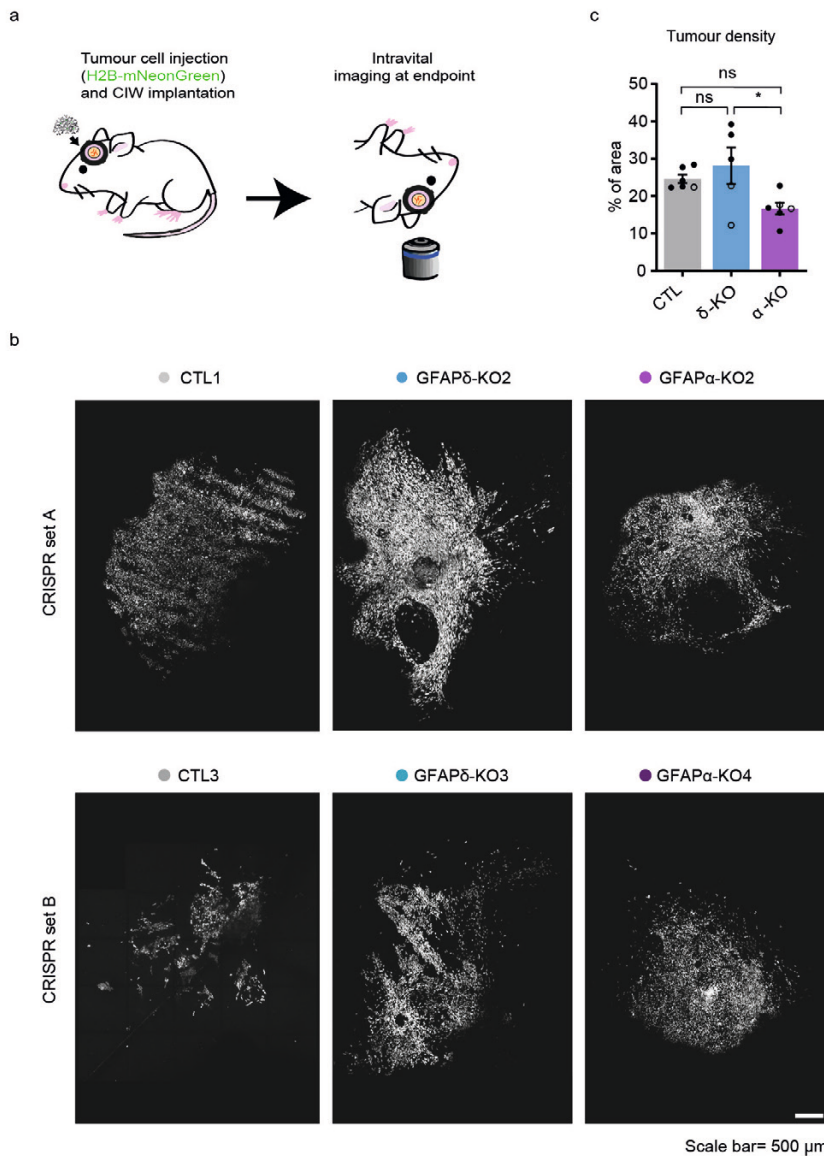


**Figure 3. *In vivo* tumour growth dynamics in GFAP modulated tumours.** (a) Schematic overview of the experimental setup. U251-MG GFAP-modulated cell clones expressing H2B-NeonGreen were implanted in the brain of NSG mice under a CIW. Time-lapse intravital imaging was performed through a CIW to study the tumour growth dynamics of each tumour type. (b) Representative 3D reconstructed tile-scans showing distinct tumours generated by different GFAP-modulated clones. Two clones engineered with different CRISPR-Cas9 sgRNAs are presented (CTL1, GFAP $\delta$ -KO2 and GFAP $\alpha$ -KO2 from CRISPR set A and CTL3, GFAP $\delta$ -KO3 and GFAP $\alpha$ -KO4 from CRISPR set B). Scale bar = 500  $\mu$ m. (c) Quantification of tumour density for each indicated tumour type.  $n=6$  (CTLs),  $n=5$  (GFAP $\delta$ -KO) and  $n=6$  (GFAP $\alpha$ -KO) mice. All tumours were imaged when they had filled half the imaging window (end-



point), which was between 13 and 35 days after the cranial window implantation, except for one CTL1 tumour which reached endpoint after 72 days. Black dots represent clones from CRISPR set A (CTL1, GFAP $\delta$ -KO2, GFAP $\alpha$ -KO2) and white dots represent clones from CRISPR set B (CTL3, GFAP $\delta$ -KO3, GFAP $\alpha$ -KO4). The data is shown as mean  $\pm$  S.E.M, \* $p < 0.05$ , \*\* $p < 0.01$ , \*\*\* $p < 0.001$ , \*\*\*\* $p < 0.0001$ , ns = not significant, one-way ANOVA followed by Tukey's multiple comparisons test.

### ***Depletion of GFAP isoforms increases motility and alters invasion patterns in vivo***

To further gain insight into the migratory behaviour of GFAP-modulated glioma cells *in vivo*, we again made use of the CIW to longitudinally study invasive behaviours at the single-cell level. At endpoint, a series of time-lapse z-stack images of the tumour was acquired for 6 hours with a time interval of 45 minutes (**Fig. 4a**). The movement of individual glioma cells was determined by tracking their migration path over time in 3D-reconstructed time-lapse movies (**Fig. 4b**). Data concerning migration velocity, speed, persistence, and directionality were extracted from the tracks. This showed that depletion of either GFAP $\delta$  or GFAP $\alpha$  isoform leads to an increase in the percentage of motile cells compared to the CTL (**Fig. 4c**). While the GFAP $\delta$ -KO cells migrate faster than the CTL cells (**Fig. 4d, e**), they move with less persistence compared to the GFAP $\alpha$ -KO and CTL cells (**Fig. 4f**). Considering that directionality is an important factor for invasion, we analysed the directionality patterns in each tumour type and determined whether the cells were migrating towards the tumour core or the brain parenchyma [34]. This demonstrated that GFAP $\alpha$ -KO cells migrate more towards the brain parenchyma while the CTL cells and GFAP $\delta$ -KOs migrate more randomly (**Fig. 4 b,g**). Indeed, this data is in line with our observation that GFAP $\alpha$ -KO tumours are more diffuse than GFAP $\delta$ -KO tumours (**Fig. 3b, c**).

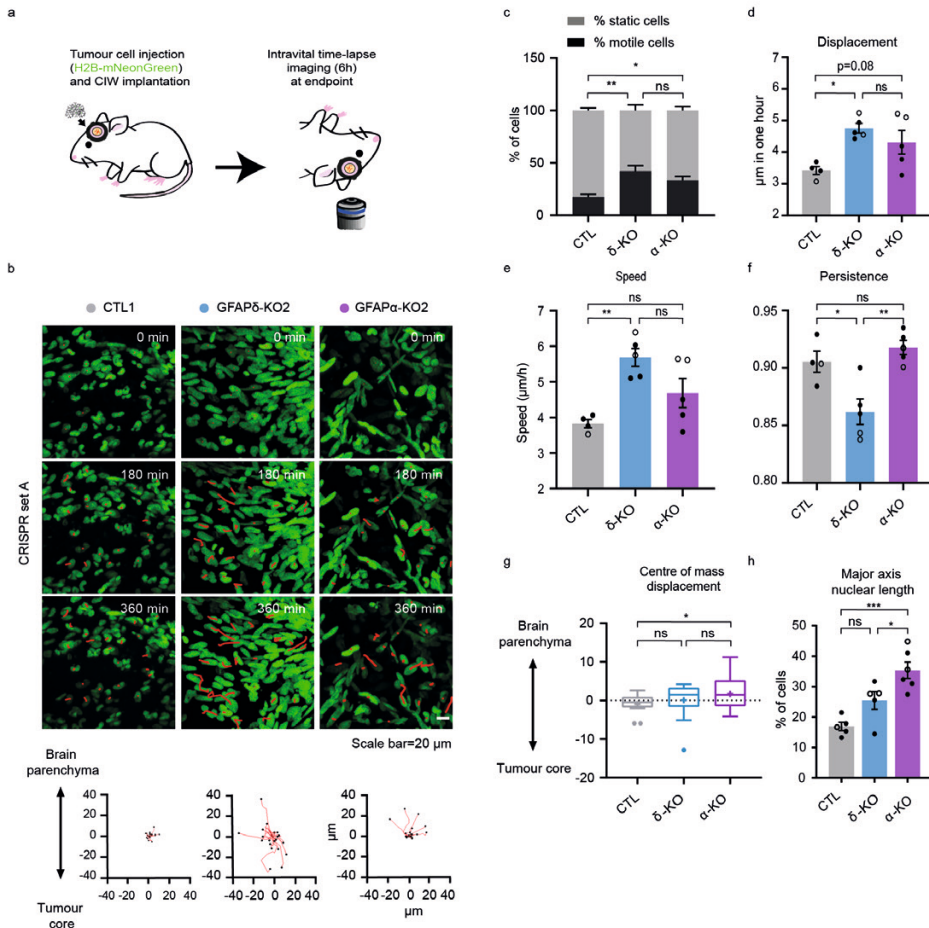


**Figure 4. *In vivo* migratory behaviour of tumour cells with different GFAP $\delta$ / $\alpha$  ratios.** (a) Schematic representation of implantation of CIW and intravital time-lapse imaging over 6 hours with an interval of 45 minutes. (b) Representative still images from a time-lapse movie showing migratory tumour cells in different GFAP modulated tumours (CTL1, GFAP $\delta$ -KO2, GFAP $\alpha$ -KO2). Red lines highlight individual tumour cell tracks. Scale bar=20  $\mu$ m. Corresponding plots represent tracks from a common origin showing the direction of the tumour cells either towards the tumour core or the brain parenchyma. (c) Percentage of motile (cell displacement  $>2\mu$ m/hour) and static cells for each tumour type. (d) Quantification of cell displacement of motile cells for the indicated tumour type. (e) Cell speed of motile cells for the different cell clones ( $\mu$ m/h). (f) Cell persistence of motile cells in the different cell clones. Black dots represent clones from CRISPR set A (CTL1, GFAP $\delta$ -KO2, GFAP $\alpha$ -KO2) and white dots clones from CRISPR set B (CTL3, GFAP $\delta$ -KO3, GFAP $\alpha$ -KO4). (g) Tukey-style whiskers plot of the centre of mass displacement of individual positions of each condition. (h) Quantification of nuclear cell length in the different cell clones. % of cells with a length higher than 30  $\mu$ m is represented.  $n=4$  (CTLs),  $n=5$  (GFAP $\delta$ -KO), and  $n=5$  (GFAP $\alpha$ -KO) CIW mice implanted with 2 different cell clones, one of each CRISPR set. The data is shown as mean  $\pm$  S.E.M, \* $p < 0.05$ , \*\* $p < 0.01$ , \*\*\* $p < 0.001$ , \*\*\*\* $p < 0.0001$ , ns = not significant, one-way ANOVA or two-way ANOVA followed by Tukey's multiple comparisons test.

It has been recently shown that nucleus stiffness and cell deformability play an important role in cell motility. For instance, to move in a three-dimensional ECM, the nucleus of a cell must squeeze through the narrow spacing within the brain parenchyma [35-37]. In our model, we observed a significant increase in the nuclear axis length of GFAP $\alpha$ -KOs compared to CTLs (**Fig. 4h**), which may contribute to the increased ability of GFAP $\alpha$ -KO to infiltrate the brain parenchyma.

## DISCUSSION

The invasive nature of glioma makes the disease highly aggressive and hard to treat. Therefore, precisely understanding the mechanisms driving invasion of glioma cells is crucial for the development of new anti-invasive treatment strategies. In this study, we investigated the role of GFAP-isoforms in glioma cell invasion, using an organotypic brain slice invasion model and intravital imaging through a CIW. We show that the GFAP $\delta$ / $\alpha$  ratio affects the macroscopic growth patterns of glioma cells both *ex vivo* and *in vivo* by regulating cell migration speed, directionality, and persistence. Importantly, we demonstrate that GFAP $\delta$ -KO cells show increased motility compared to CTL and GFAP $\alpha$ -KO cells *in vivo*, but move randomly. GFAP $\alpha$ -KO cells, on the other hand, move more persistently and have a strong tendency to migrate towards the brain parenchyma. These dynamics of the GFAP $\alpha$ -KO cells lead to a more diffuse infiltration pattern into the brain parenchyma.

Earlier studies that investigated the role of GFAP in cell motility and migration have been somewhat inconsistent. As such, GFAP expression has been linked to both higher [38,39] and lower [5,40,41] velocities of cell migration. Also, shRNA mediated knockdown of GFAP $\alpha$  decreased cell velocity in an earlier *in vitro* study [5], which is inconsistent with the phenotype we describe here. The effect of GFAP depletion on cell behaviour might not only be isoform dependent, but also influenced by the cell-environmental context [34], which may explain discrepancies between earlier studies performed in 2D. Our study is the first, to our knowledge, to investigate the role of GFAP and its isoforms within the physiological context of the brain. We find that depletion of both isoforms leads to an increase in the number of motile cells, as well as an increase in cell displacement and speed (Fig. 4c, d, e). Therefore, cell-intrinsic motility and velocity may not be dependent on the GFAP $\delta$ / $\alpha$  ratio, but on modification of the GFAP-network in general. In contrast to motility and velocity, we demonstrate that directionality and persistence of cell migration is GFAP-isoform dependent. Previous studies have shown that the IF-network can promote migration persistence by modulating microtubule organization and cell polarity [38,42-44]. Whether the absence of GFAP $\alpha$  or dominance of GFAP $\delta$  regulates directional migration similarly remains to be elucidated. The directionality of migration and invasion can also be steered by extrinsic factors<sup>45</sup> such as ECM composition and topology [45]. For instance, adhesive

interaction of the cell with the extracellular microenvironment as well as remodelling of the ECM are required to migrate efficiently through the extracellular space [46]. MMPs are responsible for the degradation of a large range of ECM proteins and GBM cells have been shown to overexpress MMP2 and 9 [47]. In line with this, we showed in our previous work that modulation of the GFAP $\alpha$  isoform affects genes involved in the compositions of the ECM and extracellular space<sup>6</sup>. In addition, we previously demonstrated that GFAP $\alpha$ -KO cells produce more laminin and overexpress MMP2 by activating signaling pathways up- and downstream of dual-specificity phosphatase 4 (DUSP4)<sup>5,7</sup>. This might contribute to the higher ability of these cells to invade the brain parenchyma persistently. Additionally, it has been shown that immune cells, including macrophages and microglia, also promote glioma invasion [48-50]. Considering that our experiments were performed in immunodeficient NOD-SCID mice, it remains to be elucidated whether interactions with immune cells potentially affect the invasive behaviour of glioma cells with different GFAP $\delta/\alpha$  ratios.

The findings of this study contribute to our understanding on how a switch in the GFAP $\delta/\alpha$  ratio in grade IV glioma patients may affect the aggressiveness of these tumours. Increased dominance of GFAP $\delta$  in grade IV glioma tumours has been reported by multiple studies [6,25,26,28] (reviewed in ref. 29), and was confirmed by analysis of the updated TCGA database (Fig. 1a). Similarly, Brehar and colleagues reported that patients with highly invasive tumours, based on pre-operative MRI, had increased percentages of GFAP $\delta$  positive cells [27]. Glioma tumours are known to be highly heterogeneous. This heterogeneity appears to be not only between patients but also between single cells within a tumour [51-53], therefore it is likely that the same tumour is composed of a mix of cells with a high and low GFAP- $\delta/\alpha$  ratio and these distinct cell populations may contribute to different behaviour. Together, it can be hypothesised that a larger population of high GFAP $\delta/\alpha$  ratio cells in grade IV tumours contributes to infiltration of the brain parenchyma and subsequent relapse after therapy. Further work is needed to understand the contribution of the GFAP $\delta/\alpha$  ratio to the infiltrative growth of low and high-grade glioma tumours in clinical samples, for instance using intravital imaging in patient-derived xenografts [54].

How the shift in GFAP-isoform expression is established in grade IV tumours is currently unknown. Alternative splice events are known to occur more frequently in tumour tissue in comparison to non-malignant cells [55], and dysregulation of the splicing machinery drives glioma aggressiveness [56]. Recently, it was discovered that hypoxia can induce adult-to-foetal splicing transitions in glioma, regulated by muscle blind-like proteins (MBNL) [57]. Hypoxia is considered an important driver of glioma invasion and is typically associated with grade IV gliomas [58,59]. GFAP has multiple predicted binding motifs for the hypoxic-associated splicing factor MBNL [60]. The link between hypoxia, GFAP alternative splicing, and cell invasion remains to be investigated.

In summary, our work demonstrates the importance of GFAP-isoforms in fine-tuning glioma invasion and tumour dynamics. Together, the increased understanding of the

mechanisms driving the invasive behaviours of different GFAP positive populations that form glioma tumours will help develop better anti-invasive therapeutic strategies in the future.

## MATERIALS AND METHODS

### Cell lines and culture

The cell identity of malignant glioma cell line U251-MG (obtained from Lars Ruether, Institut für Neuropathologie, Universitätsklinikum Münster, Münster, Germany) was confirmed by short terminal repeat analysis (Eurofins Scientific, Luxembourg city, Luxembourg). All cells were cultured in DMEM high glucose (Gibco 41966052) mixed 1:1 with Ham's F10 nutrient mix (Gibco 22390025) supplemented with 10% fetal bovine serum (Gibco 10270106/Biowest S181H) and 1% penicillin/streptomycin (Gibco 15140122) at 37 °C in a humidified incubator with 5% CO<sub>2</sub>. Cells were routinely tested negative for mycoplasma contamination.

### Mice

For the generation of organotypic slice cultures, 15-17 day- old C57BL6J male and female mice were used. C57BL6J mice were obtained from Charles Rivers Laboratories and bred in-house. The animals were kept under a normal 12:12h light-dark cycle with lights off at 19:00, at room temperature (21 +/- 2 °C) and at 40-70% humidity conditions and were fed with chow and water *ad libitum*.

For intravital imaging experiments, NOD-Scid IL2Rgnull male and female mice (NSG), aged 8 to 20 weeks at the time of cranial window implantation were used. Mice were housed in individually ventilated cage and received food and water *ad libitum*.

All experimental protocols used in this manuscript were in accordance with ARRIVE guidelines, national regulations, and ethical guidelines and were approved by the Centrale Commissie Dierproeven (CCD) and the Instantie voor Dierenwelzijn (IvD).

### TCGA RNA sequencing data collection and analysis

Expression data of GFAP splice variants from the Cancer Genome Atlas (TCGA) was extracted using the TSVdb webtool (<http://tsvdb.com>)<sup>61</sup>. Normalised RSEM (RNA-Seq by Expectation maximization) count estimates from TCGA Lower Grade Glioma (TCGA-LGG) and glioblastoma multiforme (TCGA-GBMs) projects were extracted and matched with the sample ID to clinical data on histological subtype and malignancy grade downloaded from the TCGA database: <https://www.cancer.gov/tcga>. The GFAP $\alpha$  and GFAP $\delta$  normalised expression levels and GFAP $\delta/\alpha$  ratios were compared in data from 64 grade II astrocytomas, 130 grade III astrocytomas and 153 GBMs.

## Generation of CRISPR-Cas9 plasmids

Single guide RNAs (sgRNAs) targeting the intronic regions before and after exon7a (GFAP $\delta$ -KO) or exon 8 and 9 (GFAP $\alpha$ -KO) were designed using web resources of the Broad Institute (<http://tools.genome-engineering.org/>)<sup>62</sup> or CRISPOR.org (<http://crispor.tefor.net/>)<sup>63</sup> and were selected based on proximity to exons and MIT and CFD specificity score<sup>64</sup>. The sgRNA complementary oligonucleotide templates (Supp. Table 1) were cloned into pSpCas9(BB)-2A-Puro (Addgene, #48139) or pSpCas9(BB)-2A-GFP (Addgene, #48138) plasmids after BbsI (Thermo Fisher Scientific) digestion. Plasmids were isolated using a Maxiprep kit (LabNed) and the sequence was verified by Sanger sequencing (Macrogen, Amsterdam, The Netherlands). Per GFAP-isoform, two sets of CRISPR-Cas9 plasmids were generated (CRISPR  $\delta$ -set A, CRISPR  $\delta$ -set B, CRISPR  $\alpha$ -set A, CRISPR  $\alpha$ -set B, Supp. Table 1). Empty plasmids were used as a control (CRISPR control A and CRISPR control B). The sgRNAs cloned into the pSpCas9(BB)-2A-Puro plasmid (CRISPR control A,  $\delta$ -set A,  $\alpha$ -set A) and the cell clones generated with these plasmids (CTL1, CTL2,  $\delta$ -KO1,  $\delta$ -KO2,  $\alpha$ -KO1,  $\alpha$ -KO2) have been described in ref. 7. The sgRNA pairs cloned into the pSpCas9(BB)-2A-GFP plasmid (CRISPR control B,  $\delta$ -set B,  $\alpha$ -set B) and the cell clones generated with these plasmids (CTL3, CTL4,  $\delta$ -KO3,  $\delta$ -KO4,  $\alpha$ -KO3,  $\alpha$ -KO4) are first described in this paper.

For cell transfection of the CRISPR-Cas9 construct and clonal expansion, U251-MG cells were seeded at a density of 0.8 to 1.2 x 10<sup>5</sup> cells in an uncoated 6-well plate. Twenty-four hours after seeding, the sets of CRISPR-Cas9 plasmids (1  $\mu$ g DNA total) with the sgRNAs upstream and downstream of the targeted exons of the GFAP isoforms were co-transfected using polyethylenimine (PEI, 166 ng/mL final concentration). Cells transfected with the pSpCas9(BB)-2A-Puro plasmids (CRISPR set A) were treated with 1  $\mu$ g/mL puromycin (Sigma-Aldrich, 58-58-2) 24 hours after transfection and were selected for 96 hours. The drug-resistant pool was expanded and cell clones were generated by single-cell sorting cells into 96-well plates using fluorescence-activated cell sorting (FACS; FACSAria II Cell Sorter). Cells transfected with the pSpCas9(BB)-2A-GFP plasmids (CRISPR set B) were selected for GFP using FACS (FACSAria II Cell Sorter) 48 hours after transfection. The GFP-positive pool was expanded and cell clones were generated by plating cells at low densities in 96-well plates (0.5 cell/well). The 96-well plates were inspected for colony formation and cell clones were expanded.

## Selection of CRISPR-Cas9 targeted cell clones

PCR screening was used to identify cell clones in which the targeted DNA region in the GFAP gene was depleted. Genomic DNA was isolated from cell pellets of the cell clones. Cells were lysed in 5 mM Tris HCl (pH 8.8) at 95°C for 10 minutes and treated with proteinase K at 56°C for 30 minutes. The CRISPR-Cas9 targeted DNA region was amplified using primers described in Supp. Table 1, using the FirePol PCR Master Mix (Solis BioDyne, 04-12-00S15). PCR products were separated on a 1.5% agarose gel containing SYBR Safe

(Thermo Fisher Scientific, S33102) and GFAP-isoform KO clones were identified based on the presence of predicted smaller PCR products. Depletion of the targeted DNA region was confirmed by isolating the amplified DNA of the PCR product using the PureLink Quick Gel Extraction Kit (Thermo Fisher Scientific, K210012) and Sanger sequencing (Macrogen, Amsterdam, The Netherlands).

### shRNA construct design

Lentiviral shRNA expression plasmids targeting GFAP $\alpha$  or non-targeting controls were generated as described in ref. 5. In short, lentiviral shRNA expression plasmids from the RNAi Consortium (TRC) Mission library were obtained from Sigma-Aldrich (TRCN0000083733) [65]. A human shRNA construct against nucleotides 2674-2694 in the 3' untranslated region of the GFAP $\alpha$  transcript or a SHC002 non-targeting construct (NTC) with no homology to human sequences were cloned into the pLKO.1 backbone. It was attempted to create shRNAs targeting the transcript of GFAP $\delta$ , however we were unsuccessful in significantly downregulating this isoform (data not shown).

### Lentiviral production and transduction of cells

Lentiviruses encoding NTC or GFAP $\alpha$  shRNA were produced as described in ref 5. U251-MG cells were transduced with lentiviral particles encoding NTC or GFAP $\alpha$  shRNA with a multiplicity of infection (MOI) of 0.5. Three days after transduction, cells were selected by treatment with 1  $\mu$ g/mL puromycin (Gibco, A1113803) to create stable cell lines.

All U251-MG GFAP-modulated cells (with CRISPR-Cas9 or shRNAs) and controls were transduced with lentiviruses to induce expression of H2B-mNeonGreen or H2B-mCherry. The pLV-H2B-mNeonGreen-IRES-puro plasmid was a gift from Dr. Hugo Snippert [66], the pLenti6-H2B-mCherry plasmid was a gift from Torsten Wittmann (Addgene plasmid # 89766). Lentiviral particles were produced with standard third-generation lentiviral protocol. In short,  $2 \times 10^7$  293T cells (ATCC, ATCC-CRL-11268) were plated in a 15 cm<sup>2</sup> dish and transfected the next day with a total of 51.6  $\mu$ g DNA of an envelope plasmid (pMD2.G), packaging plasmids (pMDLg/pRRE and pRSV-Rev) and pLV-H2B-mNeonGreen-IRES-puro or pLenti6-H2B-mCherry plasmid using PEI (166 ng/mL final concentration). The medium was replaced 24 hours after transfection. After 48 hours, the medium containing virus particles were collected and filtered through a 0.22  $\mu$ m filter. The supernatants were ultracentrifuged at 22,000 rpm (rotor 70Ti, Beckman ultracentrifuge) at 16 °C for 2 hours and 40 minutes. The pellet was resuspended in PBS + 0.5% BSA (Sigma), aliquoted and stored at -80°C until further use. The viral titre was determined by transducing 293T cells with a dilution series of the virus. The viral titre was estimated in transducing units (TU) / mL by counting the number of transduced fluorescent cells 48 hours after transduction. The GFAP modulated cells were transduced with H2B-mNeonGreen and H2B-mCherry lentiviral particles with an MOI of 1. Cells were passaged once and positive cells were selected by

keeping the cells in medium containing 1.5 µg/mL puromycin (H2B-mNeonGreen clones) or 10 µg/mL blasticidin (H2B-mCherry clones) for three days.

### **Western blot analysis**

Total protein was extracted from cultured cells scraped in suspension buffer [0.1M NaCl, 0.01 M Tris HCl (pH 7.6), 0.001 M EDTA, and Complete EDTA-free protease inhibitor cocktail (Roche)] and sonicated (2x 10 seconds) in an ultrasonic bath. An equal amount of 2x SDS loading buffer [100 µM Tris (pH 6.8), 4% SDS, 20% glycerol, 5% 2-ME, and bromophenol blue] was added to the cell suspension, samples were heated at 95 °C for 5 minutes and DNA was broken down by pushing the sample through a 25-gauge needle. Equal amounts of sample were loaded on a 10% SDS-page gel and proteins were separated by electrophoresis. Proteins were then blotted on a 0.45-µm pore size nitrocellulose membrane (GE Healthcare) using a wet/tank transfer blotting system (Biorad, 170390). Membranes were blocked in blocking buffer (50 mM Tris pH 7.4, 150 mM NaCl, 0.25% (w/v) gelatin, 0.5% Triton-X100) for 10 minutes and incubated with primary antibodies (Supp. Table 2) in blocking buffer overnight at 4 °C. Membranes were washed with TBS with 1% Tween (TBS-T) three times for 10 minutes and then incubated with secondary antibodies (Supp. Table 2) in blocking buffer at room temperature for 1 hour. After three washing steps with TBS-T and one washing step with MilliQ, the membrane blots were scanned with the Odyssey Clx Western Blot Detection System (Li-Cor Biosciences). The background-corrected signal intensity of bands corresponding to the GFAP $\alpha$  and GFAP $\delta$  proteins were measured and normalised against the intensity levels of glyceraldehyde 3- phosphatedehydrogenase (GAPDH) bands on the same blots.

### **RNA isolation, cDNA isolation and real-time quantitative PCR**

For RNA extraction of cultured cells, cells were seeded on poly-D lysine (PDL)-coated wells of a 24-well plate at a density of  $4 \times 10^4$  cells. After three days in culture, cells were lysed in TRIzol (Thermo Fisher Scientific, 15596026) and RNA was extracted using standard TRIzol-chloroform extraction methods. RNA concentration and purity were measured using Varioscan Flash (Thermo Fisher Scientific). 200 to 500 ng of RNA were used to prepare cDNA using the QuantiTect Reverse Transcription Kit (Qiagen, 205311) according to the manufacturer's protocol. The generated cDNA was used for real-time quantitative PCR using the SYBR Green Master mix in a QuantStudio 6 Flex Real-Time PCR system (Thermo Fisher Scientific, 4309155) using the primers listed in Supp. Table 1. Expression values were calculated by transforming Ct values ( $2^{-Ct}$ ) and were normalised to the mean value of the transformed Ct values of the reference genes GAPDH and Alu element Jurka (Alu- J).



## Immunocytochemistry

For immunocytochemistry on cultured cells, cells were seeded on PDL-coated coverslips in a 24-well plate at a density of  $2 \times 10^4$  cells. After three days in culture, the cells were fixed in 4% paraformaldehyde (PFA) dissolved in phosphate buffer saline (PBS), pH 7.4 for 30 minutes. Cells were washed in PBS, incubated in a blocking buffer (50 mM Tris pH 7.4, 150 mM NaCl, 0.25% (w/v) gelatine, and 0.5% triton X-100) at room temperature for 15 min, and afterwards with primary antibodies (Supp. Table 2) in blocking buffer overnight at 4°C. Coverslips were washed with PBS and incubated with secondary antibodies (Supp. Table 2) and Hoechst 33528 (1:1000, Thermo Fisher Scientific, H3569) in blocking buffer at room temperature for 1 hour. After washing steps with PBS, the coverslips were mounted on microscopy slides with Mowiol (0.1 M tris-HCl pH 8.5, 25% glycerol, 10% Mowiol (Merck Millipore, 81381). The samples were imaged using a Zeiss AxioScope A1 microscope with a 40x objective.

## Generation of Organotypic Brain Slices

For the generation of organotypic brain slices, the protocol of Pencheva et al., 2017 was adapted<sup>31</sup>. Postnatal day 15 – 17 C57BL6J pups were decapitated, the brains were dissected and captured in ice-cold artificial cerebrospinal fluid (aCSF, pH7.2: 10 mM Hepes, 21 mM NaHCO<sub>3</sub>, 1.2 mM NaH<sub>2</sub>PO<sub>4</sub>, 2.5 mM KCl, 2 mM MgCl<sub>2</sub>, 2 mM CaCl<sub>2</sub>, 5 mM D-glucose, 250 mM glycerol in milliQ). The brains were transferred to a petri dish and cerebellum and olfactory bulbs were removed. The cerebrum was glued to the vibratome cutting stage using a drop of Loctite 401 glue (Henkel Adhesives) with the rostral part facing upwards. The vibratome cutting stage was mounted on a VT1000S vibratome (Leica Biosystems, 1404723512) and tissue was fully submerged in carbonated ice-cold aCSF. Coronal brain slices of 350 µm were cut with a speed of 0.1 mm/s and a frequency of 7 Hz. Slices with visible lateral ventricles were transferred to 1.0-µm porous membrane inserts (Corning®, 353102) in a 6-well plate with slicing medium [DMEM:F12 (Gibco, 11320), 1% L-Glutamine (Gibco, 25030123), 5 mM HEPES, 21 mM NaHCO<sub>3</sub> and 1% pen/strep (Gibco, 15140122)], with a maximum of 4 slices per transwell insert. Residual aCSF was removed from the inserts, the brain slices were washed with PBS and the transwells were transferred to 1.5 mL recovery medium (DMEM:F12, 25% FBS, 1% L-Glutamine, 5 mM HEPES, 21 mM NaHCO<sub>3</sub> and 1% P/S) below the transwells, allowing the slices to be cultured at the air-liquid interface. The slices were cultured at 37 °C in a humidified incubator with 5% CO<sub>2</sub> overnight. The next day, the transwells were dipped twice in PBS and transferred to a 6-well plate containing NSC medium (DMEM:F12 – glutamax, 1% pen/strep, 10 ng/mL EGF (Peprotech, AF-100-15-A), 10 ng/mL FGF (Peprotech, AF-100-18B) before injection of cells.

### **Organotypic brain slice invasion assay**

Cells were counted using the Countess 3 FL Automated Cell Counter (Thermo Fischer Scientific, AMQAF2000) and suspensions of  $2.5 \times 10^5$  cells/  $\mu\text{L}$  were prepared. For the mixed cell injections, H2B-mNeonGreen expressing cells were mixed at a 1:1 ratio with H2B-mCherry expressing internal control cells. For the CRISPR-Cas9 modulated cells, CTL-1-H2B-mCherry was used as an internal control (I-CTL1) for the CRISPR-set-A clones (CTL 1 and 2, GFAP $\delta$ -KO 1 and 2, GFAP $\alpha$ -KO 1 and 2), and CTL-3-H2B-mCherry was used as an internal control (I-CTL2) for the CRISPR- set-B clones (CTL 3 and 4, GFAP $\delta$ -KO 3 and 4, GFAP $\alpha$ -KO 3 and 4). For the shRNA modulated cells, NTC-H2B-mCherry was used as an internal control. A Hamilton 0.5  $\mu\text{L}$  syringe model 7000.5 KH (Hamilton, 86250) was assembled on a Narishige micromanipulator model MM-3 (Narishige group) and was placed on the magnetic board of a Leica MS5 dissection microscope (Leica Biosystems), using a Narishige GJ-8 magnetic stand (Narishige group). The syringe was rinsed with acetone, 70% ethanol, and PBS before use. Before injection, the cell suspension was mixed and 0.5  $\mu\text{L}$  was taken up by the syringe. The needle was placed into the lateral ventricle of the brain slice by moving 50  $\mu\text{m}$  into the tissue and 40  $\mu\text{m}$  out. The cell suspension was slowly injected into the lateral ventricle of the mouse brain tissue, filling up the lateral ventricle without overflowing on the tissue. The medium of the organotypic brain slices was replaced every 2-3 days. One week after injection of the cells, the brain slices were washed with PBS and fixed in 4% PFA in PBS at 4 °C overnight.

### **Whole-mount immunostaining and RapiClear clearing**

For whole-mount immunostaining of the organotypic brain slices, we used the method described in Belle et al., 2014 [67]. The porous membrane surrounding the brain tissue was cut out and transferred to a 24-well dish. The tissue was permeabilised in 2% Triton-X-100 (Roche, 40319421) in PBS and subsequently incubated in PBSGT blocking solution (0.2% gelatin, 0.5% Triton-X-100, 0.01 % thimerosal or 0.2 % sodium azide in 1x PBS), for a minimum of 4 hours at room temperature. Primary antibodies were diluted in PBSGT + 0.1% saponin, 300  $\mu\text{L}$  was added to the tissue and incubated on a horizontal shaker (70 rpm) at 37 °C for 3 days. Tissue injected with mixed H2B-mNeonGreen/ H2B-mCherry cells were incubated with rabbit anti-laminin antibodies (1:1000, Supp. Table 2). The empty wells were filled with PBS to avoid evaporation of the primary antibody mix. The tissue was washed 6 times in PBS with 0.25% Triton-X-100 for one hour. Secondary antibodies were diluted in PBSGT + 0.1% saponin and the mix was spun down to precipitate aggregates. 300  $\mu\text{L}$  was added to the tissue and incubated on a horizontal shaker (70 rpm) at 37 °C for 24h. The tissue was washed 6 times in PBS with 0.25% Triton-X-100 for one hour. For tissue clearing of the organotypic brain slices, we selected the RapiClear protocol developed by SunJin Lab, as this protocol does not lead to tissue shrinkage and the protocol is non-laborious [32,68]. For tissue clearing, the brain slices were transferred to iSpacers (SunJin Lab Co.,

#IS002) mounted on microscope slides and 300  $\mu\text{L}$  of RapiClear 1.47 (SunJin Lab Co, #RC147001) was added on the brain slices. The slices were cleared at 37 °C on a horizontal shaker (30 rpm) for 45 minutes, mounted with a coverslip in RapiClear 1.47, and sealed with transparent nail polish. The cleared brain slices were imaged using an LSM 880 (Zeiss) confocal microscope equipped with a 3-channel QUASAR Detection Unit (000000-2078-293). The entire population of injected cells was imaged with a 10x objective (N-Achroplan 10x, 420940-990-000) at 1.77  $\mu\text{m}$  pixel resolution Z-plane increments of 6.63  $\mu\text{m}$  and using image tiling. Smaller regions were imaged using a 20x objective (LD Plan-NEOFLUAR 20x, 421350-9970-000) at 0.42  $\mu\text{m}$  pixel resolution and 3.39  $\mu\text{m}$  Z-plane increments.

### ***Quantification of cell invasion in ex vivo slices***

Cell invasion in the organotypic brain slices was quantified in the confocal generated images using ImageJ (1.53c) and Imaris software (version 8.4). Upon blinding, images were excluded from analysis when errors had occurred during the injections of cells (overflowing of tissue, large populations of unhealthy-looking cells). Using ImageJ software, image tiling was used to reconstruct the entire population of injected cells. The tiled z-stack consisted of an H2B-mNeonGreen and H2B-mCherry channel with the nuclei of the injected glioma cells and a laminin channel staining the mouse vasculature. In addition to staining the vasculature, laminin also gave rise to a diffuse staining at the location where tumour density was highest, as shown by H2B-mCherry/ H2B-mNeonGreen signal. This staining of the ECM deposits generated by the tumour cells was used to draw a boundary between the tumour core and the mouse tissue (Supp. Fig.3) in the different z-planes. An additional channel was generated in which only the tumour core laminin staining was selected. The stitched images with additional laminin-channel were imported into the Imaris Software (version 8.4). The 'create surface' function was used to generate a 3D surface of the laminin tumour core signal (background subtraction, estimated diameter 17.8, threshold =2, voxels =1). The 'create spots' function was used to generate individual spots (11  $\mu\text{m}$  + PSF-elongation along the Z-axis) of the H2B-mCherry nuclei using a standardised Quality threshold filter, adjusted so that cells in all z-planes were detected. Using the same function, the same number of H2B-mNeonGreen spots was generated. The 'distance transformation' function was used for the tumour core surface, generating a new channel where the intensity of the signal represented the distance from the 'outside surface object' or 'inside surface object'. The Imaris software was used to calculate for every H2B-mCherry and H2B-mNeonGreen nucleus the distance to the tumour core, using the 'intensity center' calculation within the "statistics" function. The excel file was exported and histograms of the distances (bin size 20  $\mu\text{m}$ ) were created using the NumPy package of the Python software [69].

### **Tumour cell injection and cranial window implantation (CWI) surgery**

Two clones per condition generated by two different sgRNA were used for the *in vivo* experiments: CTL 1 (CRISPR-set-A) and 3 (CRISPR-set-B), GFAP $\delta$ -KO 2 (CRISPR-set-A) and 3 (CRISPR-set-B), and GFAP $\alpha$ -KO 2 (CRISPR-set-A) and 4 (CRISPR-set-B). Clones with the most extreme GFAP $\delta/\alpha$  ratio were selected, except for the GFAP $\alpha$ -KO clone 3 as network collapses were observed in this line. Per injection, 100,000 U251-MG cells were resuspended in 3 $\mu$ l of PBS and injected the same day as the cranial window was implanted. CWI was performed as previously described<sup>70</sup>. In short, mice were sedated with 4% isoflurane inhalation for inducing anaesthesia and 1.5-2% during surgery. The hair from the back of the neck up to the eyes was shaved. Next, the mouse head was firmly fixed with ear bars in a stereotaxic device. Eye ointment was applied to prevent the animal's eyes from drying out. Next, the skin was cut circularly. After scraping the periosteum underneath to the edges of the skull, a circular groove of 5 mm diameter was drilled over the right parietal bone. After craniotomy, the dura mater was removed with a fine forceps. Next, tumour cells were injected stereotactically using a 10 $\mu$ l Hamilton syringe with a 2 pt style needle in the middle of the craniotomy at a depth of 0.5 mm. The exposed brain was sealed with silicone oil and a 6 mm coverslip glued on top. Dental acrylic cement (Vertex) was applied on the skull surface to cover the edge of the coverslip and a 3D printed plastic ring was glued around the coverslip to provide fixation to the microscope. A single dose of 100 $\mu$ g/kg of buprenorphine (Temgesic, Indivior Europe Limited) was administered before the surgery and the day after surgery. In addition Rimadyl in water was administered 24 hours before CIW implantation and for a total of 72 hours (Zoetis). After surgery, the mice were provided food and water *ad libitum*. Mice were closely monitored twice per week.

### **Intravital imaging**

Mice were anaesthetised in an induction chamber with 4.0% isoflurane. Next, they were placed face-up in a custom-designed imaging box. A 3D printed imaging plate facilitated CWI fixation. Isoflurane was introduced through the facemask and ventilated by an outlet on the other side of the box. To study cell migration, time-lapse images of several positions of the tumour volume were acquired every 45 minutes for a maximum of 6 hours, during which the climate chamber surrounding the microscope was kept at 37 °C and the mouse body temperature was monitored with a rectal thermometer. For each position, images of the complete z stack of the tumour were acquired, with a step size of 3 $\mu$ m. Imaging was performed on an inverted Leica SP8 multiphoton microscope with a chameleon Vision-S (Coherent Inc., Santa Clare, CA, [www.coherent.com](http://www.coherent.com)). This microscope is equipped with a 25x (HCX IRAPO NA0.95 WD 2.5mm) water objective with four non-descanned detectors (NDDs). The NDDs detected the following wavelengths: NDD1 <455 nm, NDD2 455–505 nm, NDD3 500–550 nm, NDD4 555–680 nm. H2B-mNeonGreen was excited with 944 nm and

detected with NDD3. Scanning was performed in a bidirectional mode at 400Hz and 12bit, with a zoom of 1, and 512 × 512 pixels.

### Quantification of tumour density

Density was calculated at endpoint. A tumour was considered endpoint when approximately 50% or more of the cover slip of the imaging window was covered with tumour cells. All tumours included in the analysis were imaged between 13 and 35 days after the cranial window was implanted, except for one CTL1 which reached endpoint 72 days after window implantation due to a miss injection. To quantify the tumour density, we calculated the number of individual cells in the total tumour area. The quantification was done using ImageJ (U. S. NIH, Bethesda, Maryland, USA).

### Tracking migration of tumour cells

All mice that were successfully imaged for 6 hours were included in the analysis. The analysis were done in a blinded manner. The tracking of migratory cells was done as previously described [70]. After imaging, acquired z-stacks were corrected for z and xy shifts with Huygens Professional software program (version20.10). Up to 300 cells per mouse were tracked manually with an ImageJ plugin ("MTrackJ" Rasband, W.S., ImageJ, U. S. NIH, Bethesda, Maryland, USA). At the start of each movie, a random cell was selected. The XY position was determined over time and the displacement, speed and persistence for each cell were calculated by Excel (Microsoft).

The spatial average of all cell positions was used to measure the centre of mass displacement. For each border position, the centre of mass along the Y-axis was measured by the 'Chemotaxis and Migration Tool'. Calculation of the centre of mass ( $M_{end}$ ).  $i$ = index of single cells,  $n$ = number of cells,  $X_{i,end}$   $Y_{i,end}$  = coordinates of the respective endpoint.

$$M_{end} = \frac{1}{n} \sum_{i=1}^n (X_{i,end}, Y_{i,end})$$

### Statistical analysis

The normality of data was tested using the Shapiro-Wilk test. For all normally distributed measurements, one-way ANOVA (when >2 means were compared) or two-way ANOVA followed by Tukey's multiple comparisons test were used to determine significance, set to  $p < 0.05$ . For non-normally-distributed measurements, a Kruskal-Wallis test (when >2 means were compared) followed by Dunn's multiple comparisons test were used to determine significance. All p values were two-tailed. Levels of significance were set as follows: ns > 0.05, \*0.05 ≤ p < 0.01, \*\*0.01 ≤ p < 0.001, \*\*\*0.001 ≤ p < 0.0001, \*\*\*\*p ≤ 0.0001. Error bars are presented as mean ± S.E.M. All statistical analyses were performed using GraphPad Prism software (version 9.1.2, GraphPad Software, USA).

## REFERENCES

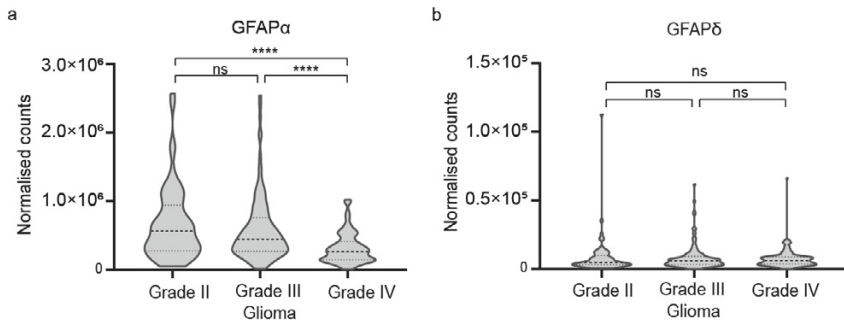
1. Ho, V. K. Y. *et al.* Changing incidence and improved survival of gliomas. *Eur. J. Cancer* 50, 2309–2318 (2014).
2. Bellail, A. C., Hunter, S. B., Brat, D. J., Tan, C. & Van Meir, E. G. Microregional extracellular matrix heterogeneity in brain modulates glioma cell invasion. *Int. J. Biochem. Cell Biol.* 36, 1046–1069 (2004).
3. Hatoun, A., Mohammed, R. & Zakieh, O. The unique invasiveness of glioblastoma and possible drug targets on extracellular matrix. *Cancer Manag. Res.* 11, 1843–1855 (2019).
4. Birbrair, A. *2017\_Book\_StemCellMicroenvironmentsAndBe.* (2017).
5. Moeton, M. *et al.* Silencing GFAP isoforms in astrocytoma cells disturbs laminin-dependent motility and cell adhesion. *FASEB J.* 28, 2942–2954 (2014).
6. Stassen, O. M. J. A. *et al.* GFAP $\delta$ /GFAP $\alpha$  ratio directs astrocytoma gene expression towards a more malignant profile. *Oncotarget* 8, 88104–88121 (2017).
7. van Bodegraven, E. J. *et al.* GFAP alternative splicing regulates glioma cell-ECM interaction in a DUSP4-dependent manner. *FASEB J.* 33, 12941–12959 (2019).
8. Leduc, C. & Etienne-Manneville, S. Intermediate filaments in cell migration and invasion: The unusual suspects. *Curr. Opin. Cell Biol.* 32, 102–112 (2015).
9. Peter, A. & Stick, R. Evolutionary aspects in intermediate filament proteins. *Curr. Opin. Cell Biol.* 32, 48–55 (2015).
10. Zhang, Y. & Weinberg, R. A. Epithelial-to-mesenchymal transition in cancer: complexity and opportunities EMT: a naturally occurring transdifferentiation program. *Front. Med.* 12, 1–13 (2018).
11. Thiery, J. P., Acloque, H., Huang, R. Y. J. & Nieto, M. A. Epithelial-Mesenchymal Transitions in Development and Disease. *Cell* 139, 871–890 (2009).
12. Mendez, M. G., Kojima, S.-I. & Goldman, R. D. Vimentin induces changes in cell shape, motility, and adhesion during the epithelial to mesenchymal transition. *FASEB J.* 24, 1838–51 (2010).
13. Sharma, P., Alsharif, S., Fallatah, A. & Chung, B. M. Intermediate Filaments as Effectors of Cancer Development and Metastasis: A Focus on Keratins, Vimentin, and Nestin. *Cells* 8, 497 (2019).
14. Cheung, K. J., Gabrielson, E., Werb, Z. & Ewald, A. J. Collective invasion in breast cancer requires a conserved basal epithelial program. *Cell* 155, 1639–1651 (2013).
15. Duffy, P. E. & Rapport, M. M. Experimental Cell Research 139 (1982) 145-157 THE Relationship To The Shape , Of Glial Motility , Acidic Protein And Differentiation Of Human Astrocytoma. 139, (1982).
16. Skalli, O. *et al.* Astrocytoma grade IV (glioblastoma multiforme) displays 3 subtypes with unique expression profiles of intermediate filament proteins. *Hum. Pathol.* 44, 2081–2088 (2013).
17. Leduc, C. & Manneville, S. E. Regulation of microtubule-associated motors drives intermediate filament network polarization. 216, 1689–1704 (2017).
18. Blechingberg, J., Lykke-andersen, S., Jensen, T. H., Jørgensen, A. L. & Nielsen, A. L. Regulatory mechanisms for 3'-end alternative splicing and polyadenylation of the Glial Fibrillary Acidic Protein, GFAP, transcript. *Nucleic Acids Res.* 35, 7636–7650 (2007).
19. Nielsen, A. L. *et al.* A new splice variant of glial fibrillary acidic protein, GFAP epsilon, interacts with the presenilin proteins. *J. Biol. Chem.* 277, 29983–29991 (2002).
20. Moeton, M. *et al.* GFAP isoforms control intermediate filament network dynamics, cell morphology, and focal adhesions. *Cell. Mol. Life Sci.* 73, 4101–4120 (2016).
21. Nielsen, A. L. & Jørgensen, A. L. Self-assembly of the cytoskeletal glial fibrillary acidic protein is inhibited by an isoform-specific C terminus. *J. Biol. Chem.* 279, 41537–41545 (2004).
22. van den Berge, S. A. *et al.* Longterm quiescent cells in the aged human subventricular neurogenic system specifically express GFAP- $\delta$ . *Aging Cell* 9, 313–326 (2010).

23. Roelofs, R. F. *et al.* Adult human subventricular, subgranular, and subpial zones contain astrocytes with a specialized intermediate filament cytoskeleton. *Glia* 52, 289–300 (2005).
24. Jenny Blechingberg, 1 Ida Elisabeth Holm, 2 Karsten Bork Nielsen, 1 Torben Heick Jensen, 3 Arne Lund Jørgensen, 1 & Nielsen1, A. A. L. Identification and Characterization of GFAPj, a Novel Glial Fibrillary Acidic Protein Isoform. *Am. J. Trop. Med. Hyg.* 51, 523–532 (1994).
25. Andreiuolo, F. *et al.* GFAP $\delta$  immunostaining improves visualization of normal and pathologic astrocytic heterogeneity. *Neuropathology* 29, 31–39 (2009).
26. Heo, D. H. *et al.* A histopathological diagnostic marker for human spinal astrocytoma: expression of glial fibrillary acidic protein- $\delta$ . *J. Neurooncol.* 108, 45–52 (2012).
27. Brehar, F. M., Arsene, D., Brinduse, L. A. & Gorgan, M. R. Immunohistochemical analysis of GFAP- $\delta$  and nestin in cerebral astrocytomas. *Brain Tumor Pathol.* 32, 90–98 (2015).
28. Choi, K.-C., Kwak, S.-E., Kim, J.-E., Sheen, S. H. & Kang, T.-C. Enhanced glial fibrillary acidic protein- $\delta$  expression in human astrocytic tumor. *Neurosci. Lett.* 463, 182–187 (2009).
29. van Bodegraven, E. J., van Asperen, J. V., Robe, P. A. J. & Hol, E. M. Importance of GFAP isoform-specific analyses in astrocytoma. *Glia* 67, 1417–1433 (2019).
30. Ming-Der Perng,\* Shu-Fang Wen,\* Terry Gibbon,\* Jinte Middeldorp, J. S. & Elly M. Hol, and R. A. Q. Glial Fibrillary Acidic Protein Filaments Can Tolerate the Incorporation of Assembly-compromised GFAP- $\delta$ , but with Consequences for Filament Organization and  $\alpha$ B-Crystallin Association. *Mol. Biol. Cell* 82, 327–331 (2009).
31. Pencheva, N. *et al.* Identification of a Druggable Pathway Controlling Glioblastoma Invasiveness. *Cell Rep.* 20, 48–60 (2017).
32. Bekkouche, B. M. B., Fritz, H. K. M., Rigosi, E. & O'Carroll, D. C. Comparison of Transparency and Shrinkage During Clearing of Insect Brains Using Media With Tunable Refractive Index. *Front. Neuroanat.* 14, 1–19 (2020).
33. Margarido, A. S., Bornes, L., Vennin, C. & van Rheenen, J. Cellular plasticity during metastasis: New insights provided by intravital microscopy. *Cold Spring Harb. Perspect. Med.* 10, 1–21 (2020).
34. Alieva, M. *et al.* Intravital imaging of glioma border morphology reveals distinctive cellular dynamics and contribution to tumor cell invasion. *Sci. Rep.* 9, 1–11 (2019).
35. McGregor, A. L., Hsia, C. R. & Lammerding, J. Squish and squeeze - the nucleus as a physical barrier during migration in confined environments. *Curr. Opin. Cell Biol.* 40, 32–40 (2016).
36. Wolf, K. *et al.* Physical limits of cell migration: Control by ECM space and nuclear deformation and tuning by proteolysis and traction force. *J. Cell Biol.* 201, 1069–1084 (2013).
37. Ivkovic, S. *et al.* Direct inhibition of myosin II effectively blocks glioma invasion in the presence of multiple motogens. *Mol. Biol. Cell* 23, 533–542 (2012).
38. De Pascalis, C. *et al.* Intermediate filaments control collective migration by restricting traction forces and sustaining cell–cell contacts. *J. Cell Biol.* jcb.201801162 (2018) doi:10.1083/jcb.201801162.
39. Lepekhin, E. A. *et al.* Intermediate filaments regulate astrocyte motility. *J. Neurochem.* 79, 617–625 (2001).
40. Rutka, J. T. *et al.* Effects of antisense glial fibrillary acidic protein complementary DNA on the growth, invasion, and adhesion of human astrocytoma cells. *Cancer Res.* 54, 3267–3272 (1994).
41. Elobeid, A., Bongcam-Rudloff, E., Westermark, B. & Nistér, M. Effects of inducible glial fibrillary acidic protein on glioma cell motility and proliferation. *J. Neurosci. Res.* 60, 245–256 (2000).
42. Gan, Z. *et al.* Vimentin Intermediate Filaments Template Microtubule Networks to Enhance Persistence in Cell Polarity and Directed Migration. *Cell Syst.* 3, 252–263.e8 (2016).
43. Shabbir, S. H., Cleland, M. M., Goldman, R. D. & Mrksich, M. Geometric control of vimentin intermediate filaments. *Biomaterials* 35, 1359–1366 (2014).
44. Schaedel, L., Lorenz, C., Schepers, A. V., Klumpp, S. & Köster, S. microtubules by direct interactions. *Nat. Commun.* doi:10.1038/s41467-021-23523-z.
45. Petrie, R. J., Doyle, A. D. & Yamada, K. M. Random versus directionally persistent cell migration. *Nat. Rev. Mol. Cell Biol.* 10, 538–549 (2009).

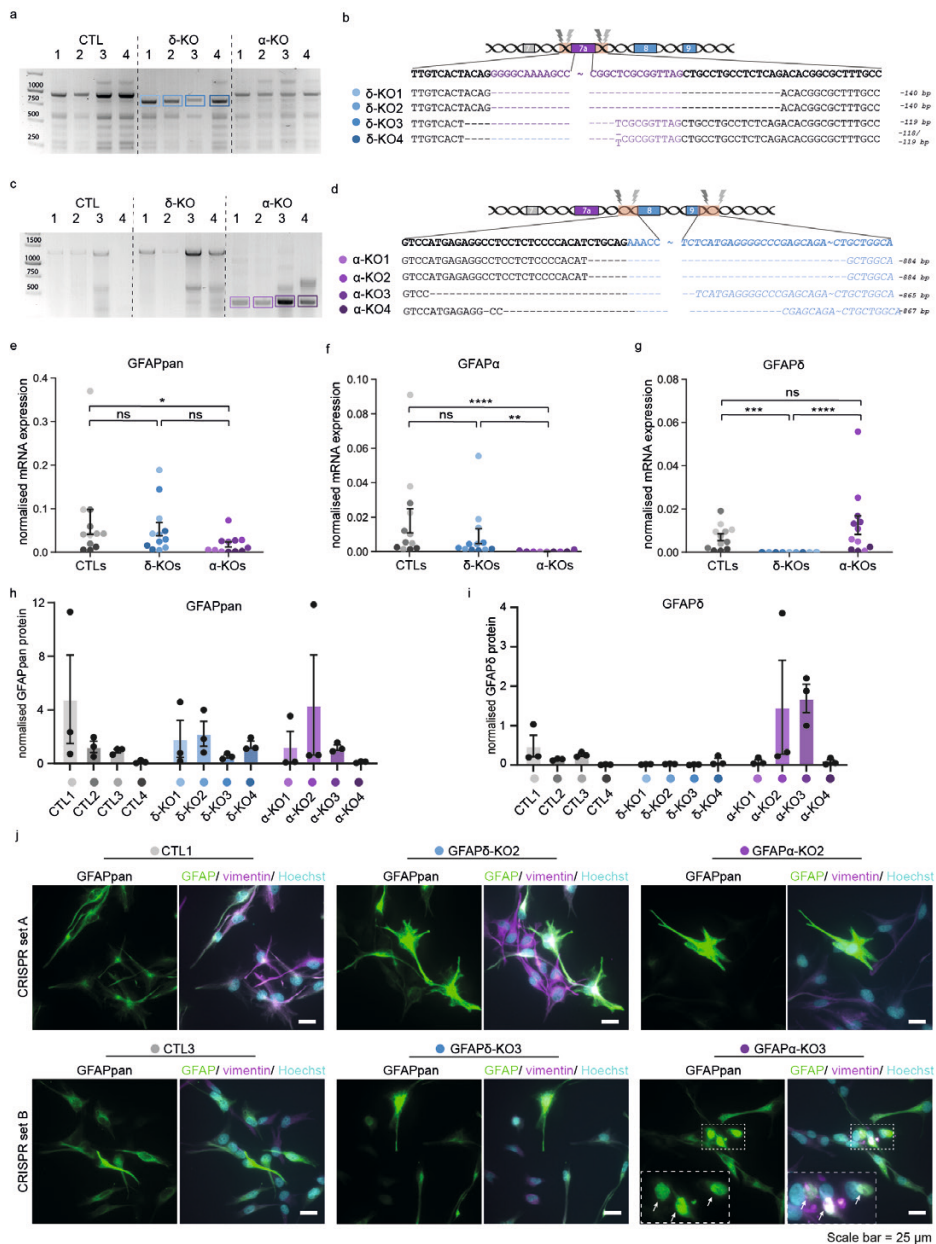
46. Trepap, X., Chen, Z. & Jacobson, K. Cell migration. *Compr. Physiol.* 2, 2369–2392 (2012).
47. Forsyth, P. A. *et al.* Gelatinase-A (MMP-2), gelatinase-B (MMP-9) and membrane type matrix metalloproteinase-1 (MT1-MMP) are involved in different aspects of the pathophysiology of malignant gliomas. *Br. J. Cancer* 79, 1828–1835 (1999).
48. Broekman, M. L. *et al.* Multidimensional communication in the microenvirons of glioblastoma. *Nat. Rev. Neurol.* (2018) doi:10.1038/s41582-018-0025-8.
49. Markovic, D. S., Glass, R., Synowitz, M., Van Rooijen, N. & Kettenmann, H. Microglia stimulate the invasiveness of glioma cells by increasing the activity of metalloprotease-2. *J. Neuropathol. Exp. Neurol.* 64, 754–762 (2005).
50. Chen, H. *et al.* Immune response in glioma's microenvironment. (2021).
51. Patel, A. P. *et al.* Single-cell RNA-seq highlights intratumoral heterogeneity in primary glioblastoma. *Science* (80-. ). 344, 1396–1401 (2014).
52. Szerlip, N. J. *et al.* Intratumoral heterogeneity of receptor tyrosine kinases EGFR and PDGFRA amplification in glioblastoma defines subpopulations with distinct growth factor response. *Proc. Natl. Acad. Sci. U. S. A.* 109, 3041–3046 (2012).
53. Meyer, M. *et al.* Single cell-derived clonal analysis of human glioblastoma links functional and genomic heterogeneity. *Proc. Natl. Acad. Sci. U. S. A.* 112, 851–856 (2015).
54. Zeng, W. *et al.* Patient-derived xenografts of different grade gliomas retain the heterogeneous histological and genetic features of human gliomas. *Cancer Cell Int.* 20, 1–12 (2020).
55. Kahles, A. *et al.* Comprehensive Analysis of Alternative Splicing Across Tumors from 8,705 Patients. *Cancer Cell* 34, 211–224.e6 (2018).
56. Fuentes-Fayos, A. C. *et al.* Splicing machinery dysregulation drives glioblastoma development/aggressiveness: oncogenic role of SRSF3. *Brain* 143, 3273–3293 (2020).
57. Voss, D. M., Sloan, A., Spina, R., Ames, H. M. & Bar, E. E. The Alternative Splicing Factor, MBNL1, Inhibits Glioblastoma Tumor Initiation and Progression by Reducing Hypoxia-Induced Stemness. *Cancer Res.* 80, 4681–4692 (2020).
58. Gérard, M. *et al.* Hypoxia Imaging and Adaptive Radiotherapy: A State-of-the-Art Approach in the Management of Glioma. *Front. Med.* 6, (2019).
59. Jensen, R. L. *et al.* Preoperative dynamic contrast-enhanced MRI correlates with molecular markers of hypoxia and vascularity in specific areas of intratumoral microenvironment and is predictive of patient outcome. *Neuro. Oncol.* 16, 280–291 (2014).
60. Paz, I., Akerman, M., Dror, I., Kosti, I. & Mandel-Gutfreund, Y. SFmap: A web server for motif analysis and prediction of splicing factor binding sites. *Nucleic Acids Res.* 38, 1–5 (2010).
61. Sun, W. *et al.* TSVdb: A web-tool for TCGA splicing variants analysis. *BMC Genomics* 19, 1–7 (2018).
62. Ran, F. A. *et al.* Genome engineering using the CRISPR-Cas9 system. *Nat Protoc* 8, 2281–2308 (2013).
63. Concordet, J. P. & Haeussler, M. CRISPOR: Intuitive guide selection for CRISPR/Cas9 genome editing experiments and screens. *Nucleic Acids Res.* 46, W242–W245 (2018).
64. Doench, J. G. *et al.* Optimized sgRNA design to maximize activity and minimize off-target effects of CRISPR-Cas9. *Nat. Biotechnol.* 34, 184–191 (2016).
65. Root, D. E., Hacohen, N., Hahn, W. C., Lander, E. S. & Sabatini, D. M. Genome-scale loss-of-function screening with a lentiviral RNAi library. *Nat. Methods* 3, 715–719 (2006).
66. Drost, J. *et al.* Sequential cancer mutations in cultured human intestinal stem cells. *Nature* 521, 43–47 (2015).
67. Belle, M. *et al.* A Simple Method for 3D Analysis of Immunolabeled Axonal Tracts in a Transparent Nervous System. *Cell Rep.* 9, 1191–1201 (2014).
68. www.sunjinlab.com. Mouse Brain Quick Guide :
69. Harris, C. R. *et al.* Array programming with NumPy. *Nature* 585, 357–362 (2020).
70. Alieva, M. *et al.* Preventing inflammation inhibits biopsy-mediated changes in tumor cell behavior. *Sci. Rep.* 7, 7529 (2017).



## SUPPLEMENTARY FILES

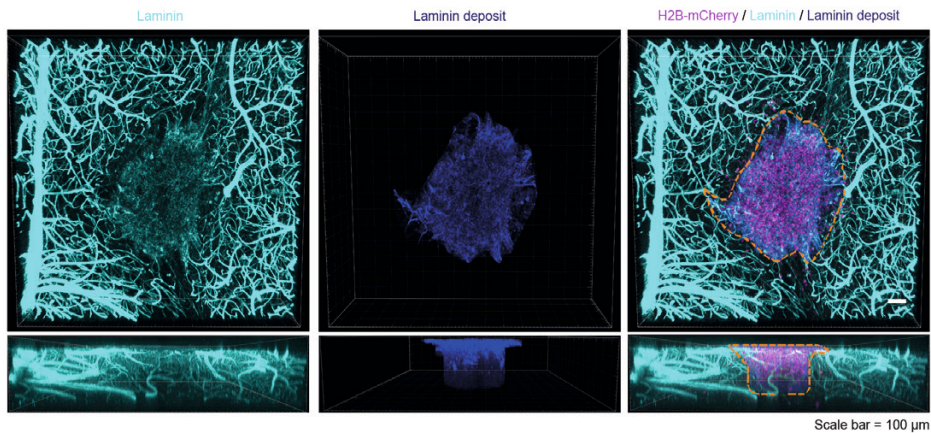


**Supplementary Figure 1. GFAP isoform expression in different grades of astrocytoma.** Violin plots of GFAP $\alpha$  and GFAP $\delta$  levels in tumour samples of grade II (n= 64), grade III (n= 130), and grade IV (n= 153) astrocytoma, obtained from normalised isoform expression data of the TCGA database. GFAP $\alpha$  levels (a) are decreased in grade IV astrocytoma, whereas GFAP $\delta$  levels (b) remain constant. Significance was determined using a Kruskal-Wallis test followed by Dunn's multiple comparisons test. The data is shown as mean  $\pm$  S.E.M, \*p < 0.05, \*\*p < 0.01, \*\*\*p < 0.001, \*\*\*\*p < 0.0001, ns = not significant.

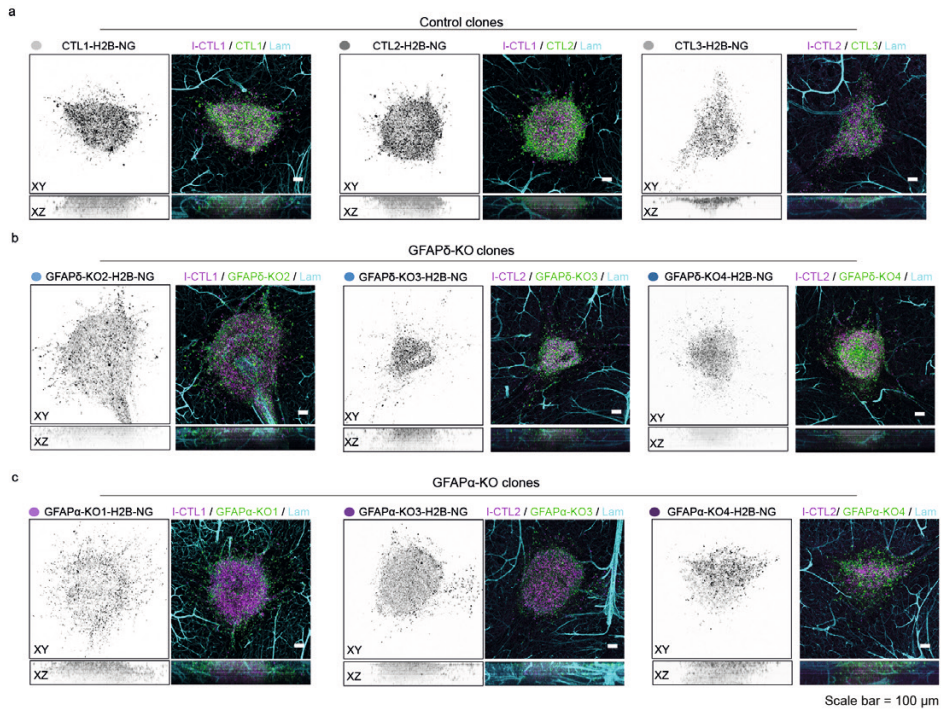


**Supplementary Figure 2. Characterisation of the GFAP-modulated cells.** (a,b) PCR amplification and sequencing of the GFAP gene around exon 7a. GFAP $\delta$ -KO cells have a deletion of 140 bp (GFAP $\delta$ -KO 1 and 2, CRISPR  $\delta$ -set A) or 118/119 bp (GFAP $\delta$ -KO 3 and 4, CRISPR  $\delta$ -set B) of exon 7a. (c,d) PCR amplification and sequencing of the GFAP gene around exons 8 and 9. GFAP $\alpha$ -KO cells have 884 bp deletion (GFAP $\alpha$ -KO 1 and 2, CRISPR  $\alpha$ -set A) or 865/867 bp deletion (GFAP $\alpha$ -KO 3 and 4, CRISPR  $\alpha$ -set B) of exons 8 and 9. (e-g) mRNA levels of GFAPpan (e), GFAP $\alpha$  (f), and GFAP $\delta$  (h) normalised against GAPDH and AluJ. Deletion of exon 7a (GFAP $\delta$ -KO cells) leads to a significant

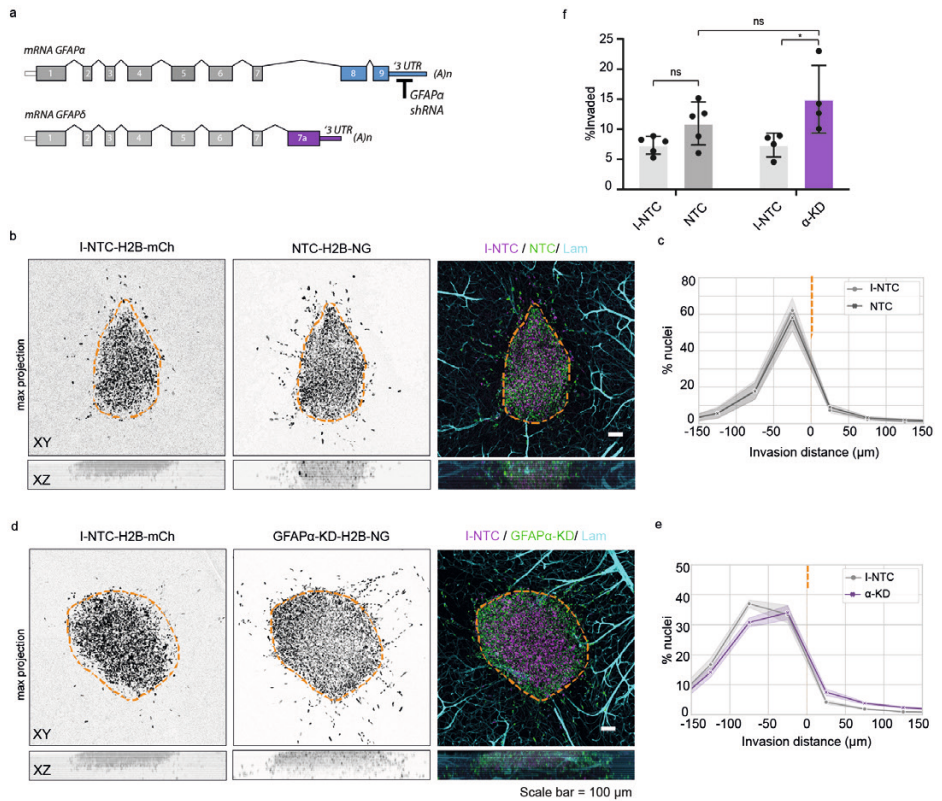
reduction in GFAP $\delta$  mRNA levels, but not to a reduction in GFAP $\alpha$  or GFAPpan. Deletion of exons 8 and 9 (GFAP $\alpha$ -KO cells) leads to a significant reduction in both GFAP $\alpha$  and GFAPpan levels, but not in GFAP $\delta$  mRNA levels.  $n = 12$  individual experiments per group, derived from 4 clones per condition represented with different colour hues. Significance was determined using a Kruskal-Wallis test followed by Dunn's multiple comparisons test. (h,i) Protein levels of GFAPpan (g) and GFAP $\delta$  (h) normalised against GAPDH. (j) The GFAP network in six different cell clones (CRISPR set A: CTL1, GFAP $\delta$ -KO3, GFAP $\alpha$ -KO3, CRISPR set B: CTL3, GFAP $\delta$ -KO2, GFAP $\alpha$ -KO2) shown with immunofluorescence. GFAP is integrated in the IF network (shown with vimentin) in all cell clones. IF network collapses were occasionally observed in GFAP $\alpha$ -KO3, indicated with white arrows. Scale bar = 25  $\mu\text{m}$ . The data is shown as mean  $\pm$  S.E.M, \* $p < 0.05$ , \*\* $p < 0.01$ , \*\*\* $p < 0.001$ , \*\*\*\* $p < 0.0001$ , ns = not significant.



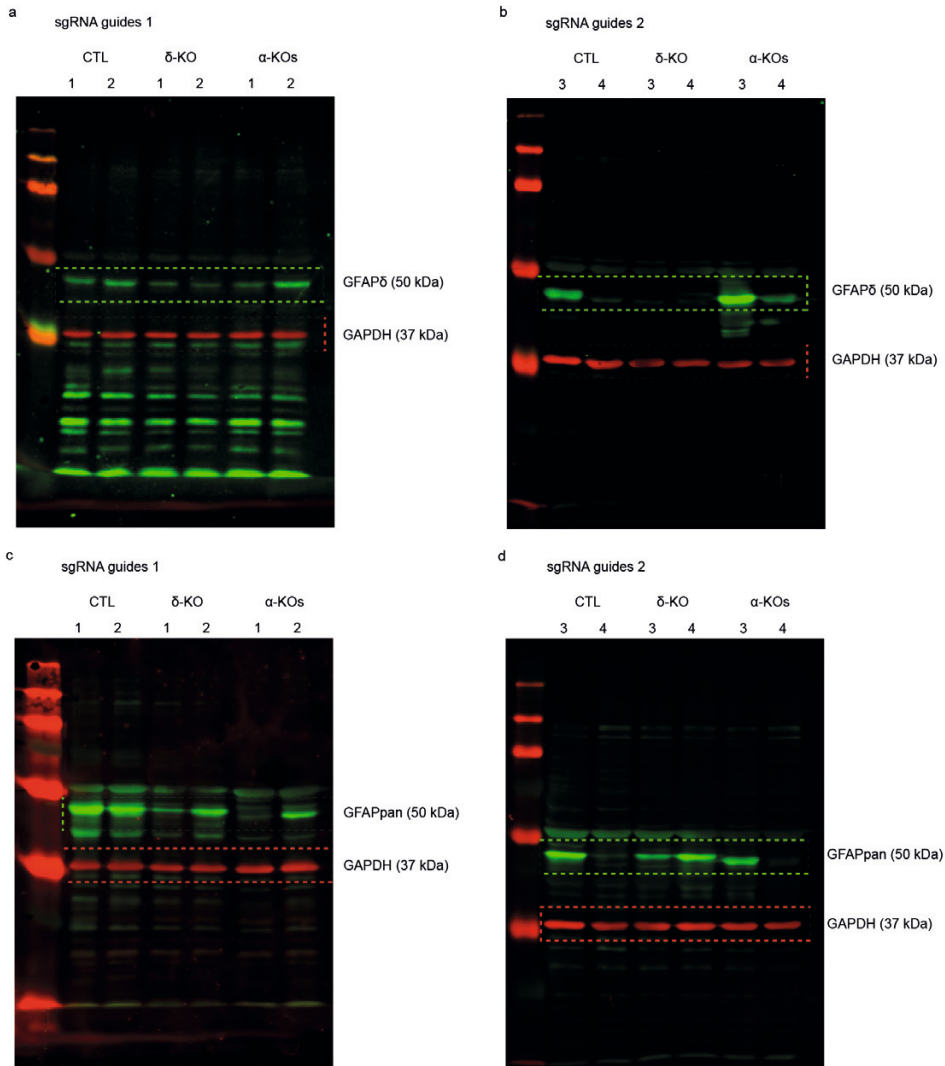
**Supplementary Figure 3. Laminin staining can be used to distinguish tumour core from invading cells.** Overexposure of laminin reveals background staining that colocalizes with the highest density of H2B-mCherry nuclei at the site of injection. This laminin deposit is used to distinguish cells in the tumour core versus cells that invaded the tissue, indicated with the orange dotted line. Scale bar = 100  $\mu\text{m}$ .



**Supplementary Figure 4. Representative images of organotypic slice cultures injected with the different cell clones.** Representative images of injected I-CTL-H2B-mCherry cells together with H2B-mNeonGreen expressing CTL clones (a), GFAP $\delta$ -KO clones (b) or GFAP $\alpha$ -KO clones (c). Scale bar = 100  $\mu$ m. NG= mNeonGreen, Lam = laminin.



**Supplementary Figure 5. Invasion patterns of GFAP $\alpha$ -KD cells.** (a) Schematic illustration of GFAP $\alpha$  shRNA target site. (b,c) I-NTC and NTC show similar distribution patterns of nuclei in organotypic brain slices. Histograms show the percentage of nuclei per 50  $\mu$ m bins, with negative values representing cells within the tumour core and positive values representing cells in the mouse brain tissue ( $n=5$  independent experiments). (d,e) GFAP $\alpha$ -KD cells show a more diffuse growth pattern in comparison to I-NTC cells and a shift in cell distribution towards the mouse tissue ( $n=4$  independent experiments). (f) Quantification of the percentage of invaded cells. GFAP $\alpha$ -KD cells show higher percentages of cell invasion in comparison to the I-NTCs, but not in comparison to the NTCs. Significance was determined using a two-way ANOVA followed by Tukey's multiple comparisons test. Scale bar = 100  $\mu$ m. The data is shown as mean  $\pm$  S.E.M, \*\* $p < 0.05$ , \*\* $p < 0.01$ , \*\*\* $p < 0.001$ , \*\*\*\* $p < 0.0001$ , ns = not significant. I-NTC = internal non-targeting control, NTC = non-targeting control, NG = mNeonGreen, mCh = mCherry, Lam = laminin, UTR = untranslated region.



**Supplementary Figure 6. Protein levels of GFAP $\delta$  and all GFAP isoforms (GFAPpan) in the 12 different cell clones determined with Western blot (a,b) Full-length blots of GFAP and GAPDH. Single blots were stained with primary antibodies rabbit anti-GFAP $\delta$  and mouse antiGAPDH and with secondary antibodies donkey anti-rabbit IRDye800 and donkey anti-mouse AF647 (Table S2). (c,d) Full-length blots of GFAP and GAPDH. Single blots were stained with primary antibodies rabbit anti-GFAPpan and mouse anti-GAPDH and with secondary antibodies donkey anti-rabbit IRDye800 and donkey anti-mouse AF647 (Supp. Table 2). All antibodies were characterised in Moeton et al., 2016.**

Supplementary Table 1. Overview of oligonucleotides

Name	Target	Oligonucleotide 1 (5' > '3)	Oligonucleotide 2 (5' > '3)
<i>CRISPR-guides</i>			
GFAP $\alpha$ -KO sgRNAs 1	GFAP gene intron 7	CACCGGGCTGGTT CTGCAGATGTG	AAACCACATCTGCA GAAACCAGCCC
	GFAP gene '3 UTR exon 9	CACCGGATAGTTGC TCCGCCTCTGC	AAACGCAGAGGGC GAGCAACTATCC
GFAP $\alpha$ -KO sgRNAs 2	GFAP gene intron 7	CACCGCAGGCTGGT TTCTGCAGATG	AAACCATCTGCAGA AACCAGCCTGC
	GFAP gene '3 UTR exon 9	CACCGCTCGGGCC CCTCATGAGACG	AAACCGTCTCATGAG GGGCCGAGC
GFAP $\delta$ -KO sgRNAs 1	GFAP gene intron 6	CACCGTAACTGCTTG TCACTACAGG	AAACCCCTGTAGTGA CAAGCAGTTAC
	GFAP gene intron 7	CACCGGGCAAAGCG CCGTGCTGAG	AAACCTCAGACACG GCGCTTTGCCC
GFAP $\delta$ -KO sgRNAs 2	GFAP gene intron 6	CACCGTTTAACTGCT TGTCACTACA	AAACTGTAGTGACAA GCAGTTAAAC
	GFAP gene intron 7	CACCGAATGGAACG CCGCCGGCTCG	AAACCGAGCCGGCG GCGTTCCATTTC
<i>shRNA-guides</i>			
shRNA GFAP $\alpha$	GFAP $\alpha$ transcript nt 2674-2694	CCCTTCTTACTACA CACAAA	na
NTC	na	CAACAAGATGAAGACACCAA	na

Supplementary Table 1. Continued.

Name	Target	Oligonucleotide 1 (5' > '3)	Oligonucleotide 2 (5' > '3)
<i>PCR primers</i>			
GFAP $\alpha$	GFAP gene 44,907,012- 44,908,284	TAGGCTCTCTGCTGGTT	GAGGGGATGTAGTAGGTGC
GFAP $\delta$	GFAP gene 44,910,531- 44,909,596	GTTGCTCCAGACTGGGACTG	CATTTCAGGGCCAATGCAAG
<i>qPCR primers</i>			
AluJ	Repeat sequence AluJ	CAACATAGTAAACCCGCTCTCT	GCCTCAGCCTCCCGAGTAG
GAPDH	GAPDH transcript	TGCACCCACCAACTGCTTAGC	GGCATGGACTGTGGTCATGA
GFAP $\alpha$	GFAP transcript 1 (a) 2776-2890	CCCACCTGCTTTGACTGAGC	CCTTCTTCGGCCTTAGAGGG
GFAP $\delta$	GFAP transcript 2 (b) 1167 - 1263	TCCAACCTGCAGATTGAGG	TTGGTATAACTCGTATTGTGAGGCTT
GFAPpan	GFAP transcript 1,2 453 - 551	GACCTGGCCACTGTGAGG	GGCTTCATCTGCTTCCTGTC

Abbreviations: AluJ = Alu element Jurka, GAPDH = Glyceraldehyde 3-phosphate dehydrogenase, GFAP = glial fibrillary acidic protein, qPCR = quantitative polymerase chain reaction, sgRNA = single guide RNA, shRNA = short hairpin RNA, PCR = polymerase chain reaction, UTR = untranslated region, na = not applicable.



**Supplementary Table 2. List of antibodies**

<b>Antibody</b>	<b>Product number, Company</b>	<b>(WM)-IF</b>	<b>WB</b>
Chicken anti-vimentin	AB5733, Chemicon, Temecula, CA, USA	1:1500	-
Mouse anti-GAPDH	MAB374, Chemicon, Temecula, CA, USA	-	1:2000
Rabbit anti-GFAP	#Z0334, Dako (Agilent), Santa Clara, CA, USA	1:1000	1:50000
Rabbit anti-GFAP $\delta$	Manufactured in house. Bleeding date: 27-11-2003 (purified in 2004)	-	1:2000
Rabbit anti-laminin	L9393, Sigma Aldrich, St Louis, MO, USA	1:1000	-
Donkey anti-chicken Cy3	703-175-155, Jackson Immuno Research, West Grove, PA, USA	1:1000	-
Donkey anti-mouse AF647	703-606-150, Jackson Immuno Research, West Grove, PA, USA	-	1:2000
Donkey anti-rabbit Cy3	711-166-152, Jackson Immuno Research, West Grove, PA, USA	1:1000	-
Donkey anti-rabbit AF647	711-606-152, Jackson Immuno Research, West Grove, PA, USA	1:1000	-
Goat anti-rabbit IRDye800	926-32211, LI-COR, 4647 Superior Street Lincoln, NE, USA	-	1:5000

Abbreviations: AF= Alexa Fluor, GAPDH= Glyceraldehyde 3-phosphate dehydrogenase, GFAP = glial fibrillary acidic protein, WB = Western blot, (WM)-IF = (whole-mount)-immunofluorescence



# Chapter 5

Epithelial-to-mesenchymal transition  
drives invasiveness of breast cancer brain  
metastases.

Margarido AS, **Uceda-Castro R**, Hahn K, de Bruijn R, Kester L, Hofland I, Lohuis J,  
Seinstra D, Broeks A, Jonkers J, Broekman MLD, Wesseling P, Vennin C, Vizoso M<sup>#</sup>,  
van Rheenen J<sup>#</sup>

<sup>#</sup> Correspondence

Published in **Cancers** 2022



## **ABSTRACT**

(1) Background: an increasing number of breast cancer patients develop lethal brain metastases (BM). The complete removal of these tumors by surgery becomes complicated when cells infiltrate into the brain parenchyma. However, little is known about the nature of these invading cells in breast cancer brain metastasis (BCBM). (2) Methods: we use intravital microscopy through a cranial window to study the behavior of invading cells in a mouse model of BCBM. (3) Results: we demonstrate that BCBM cells that escape from the metastatic mass and infiltrate into brain parenchyma undergo epithelial-to-mesenchymal transition (EMT). Moreover, cells undergoing EMT revert to an epithelial state when growing tumor masses in the brain. Lastly, through multiplex immunohistochemistry, we confirm the presence of these infiltrative cells in EMT in patient samples. (4) Conclusions: together, our data identify the critical role of EMT in the invasive behavior of BCBM, which warrants further consideration to target those cells when treating BCBM.

## INTRODUCTION

Although early detection of primary tumors and novel treatment strategies have improved outcomes of patients with breast cancer (BC), an increasingly large number of metastatic BC patients live long enough to develop lethal BM: 30–50% of patients with Her2+ BC and 25–45% of triple negative BC develop brain metastasis [1–5]. Standard-of-care treatments for BCBM include neurosurgical resection, systemic therapies and stereotactic radiotherapy. However, these treatments largely fail to improve patients' outcomes and BCBM remains a leading cause of BC-related death [5]. In particular, the ability of BCBM cells to infiltrate into the healthy brain tissue renders BCBM difficult to treat. Although tumor resection may seem complete by magnetic resonance imaging (MRI), the limited resolution of this technique does not allow the detection of individual cells that have invaded beyond the resection cavity. Consequently, overall survival rates following surgical removal of BCBM remain dismal, with 60% of patients with confirmed complete resection by MRI locally recurring within 1 year after surgery [6,7]. Nevertheless, the properties of BCBM cells that invade the brain parenchyma and drive patients' relapse remain under-studied. It is therefore critical to better understand the mechanisms that drive the invasive behavior of BCBM cells in order to design efficient treatment strategies for this dreadful disease. The migratory and infiltrative behaviors of BC cells that escape primary tumors have been extensively studied [8–13]. It is generally accepted that in order to become invasive, cells in the primary tumor hijack the developmental program known as EMT [14–24]. For instance, we and others previously used intravital microscopy to show that cells that escape from primary breast tumor and invade the healthy stroma undergo EMT [25–28]. During EMT, cells downregulate the expression of epithelial markers such as the cell–cell adhesion molecule E-cadherin (E-cad), thereby losing cell polarity and cell–cell adhesion. In parallel, cells undergoing EMT acquire mesenchymal markers that drive stemness and invasiveness such as Zeb1 and Twist [14,18,21,29–34]. To date, the role of EMT in BC has mainly been studied in the context of cancer cells disseminating from the primary tumor and during the outgrowth of extracranial metastases, but the existence and functions of EMT in BCBM remain unknown. We previously used the mouse mammary tumor virus polyoma middle-T antigen (PyMT) model crossed with fluorescent E-cadherin-mCFP (E-cad-mCFP) reporter mice to report EMT in ductal mammary carcinomas and lung metastases [26,27]. Here, we employed this EMT reporter mouse to generate a BCBM model in order to image, isolate and characterize cells that have undergone EMT in the context of brain metastasis. Using intravital imaging, we identify infiltrative tumor cells in BCBM which preclude the complete removal of the lesion by surgery, leading to increased BCBM recurrence in mice. Moreover, we demonstrate that in contrast to cells in the tumor mass, cells infiltrating into the brain tissue display a mesenchymal expression profile. Additionally, we find that mesenchymal cells can revert to an epithelial state during outgrowth of tumor masses in

the brain. Importantly, using multiplex immunohistochemistry, we also detect this infiltrating population of cells in EMT in the brain tissues of BCBM patients, illustrating the clinical relevance of our observations. Collectively, our data warrants further consideration to target EMT as part of the treatment of BCBM.

## RESULTS

### ***Intravital Microscopy Identifies Migratory Single Cells at the Invasive Front of BCBM***

To characterize BCBM cells that invade the brain parenchyma, we performed a total of 6 serial intracranial transplantations of tumor pieces originally derived from end-stage primary ductal carcinomas that had developed in the mammary glands of PyMT E-cad-mCFP reporter mice [27] (**Figure 1A**). Fast-growing brain metastases were established after the 6th round of transplantation in the brain. From these tumors, we derived organoids with the aim to maintain 3D heterogenic characteristics of brain metastases. From here on, tumors that develop upon intracranial injection of the single cell suspension of brain enriched organoids are referred to as BCBMs. To study the behavior of BCBM cells in vivo, we intracranially injected these organoids labelled with a nuclear fluorescent marker (H2B-Dendra2) in ROSA26<sup>mTmG</sup> FVB mice and monitored BCBM progression through a cranial imaging window using multi-photon microscopy. Two weeks after intracranial injection of BCBM organoids, we observed the formation of a tumor with individual lobes containing a high density of tumor cells (**Figure 1B**). Importantly, we observed single tumor cells outside of the tumor lobes (**Figure 1B**). These single tumor cells were associated with blood vessels (**Figure 1B, C**). To assess the behavior of these single cells, we performed time-lapse live imaging through the cranial imaging window for up to 12 h by multi-photon microscopy in ROSA26<sup>mTmG</sup> mice (**Figure 2A, B**). We tracked the position of 350 cells within the tumor lobes and 350 cells at the invasive front over time in a total of 16 positions in 3 mice (**Figure 2C, D**). Whilst the vast majority of cells in the tumor lobes were non-migratory, a large proportion of the cancer cells in the brain parenchyma were motile (defined by cells with a speed equal to or higher than 2.5  $\mu\text{m}$  per hour, **Figure 2C, D**). Moreover, cell migration in the parenchyma was highly persistent (**Figure 2E**). Additionally, we frequently observed cells migrating along structures such as type I collagen fibers as observed by second harmonic generation (SHG) (**Figure 2F**). Together, we identify a population of highly migratory cancer cells that escape from the BCBM lobes and invade the surrounding parenchyma.

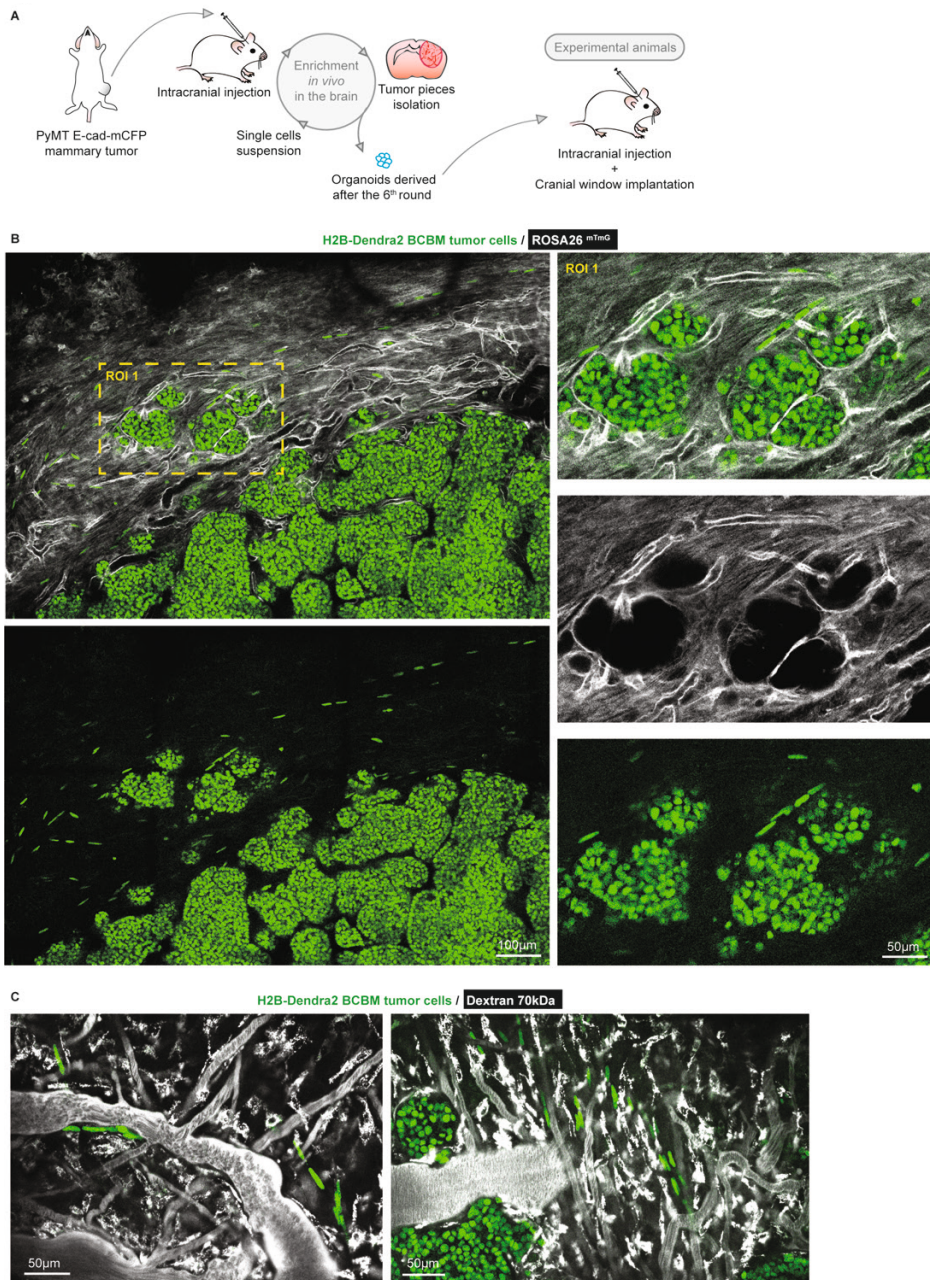


**Figure 1. Intravital microscopy reveals the presence of single tumor cells at the invasive front of BCBM.** (A) Schematic representation of the generation of a BCBM model derived from PyMT, E-cad-mCFP tumor. (B) Representative image ( $n = 4$  mice) obtained by multi-photon imaging through a cranial window of a BCBM invasive front, 2 weeks after tumor implantation. The image depicts tumor cells expressing H2B-Dendra2 (green) grown in ROSA26<sup>mTmG</sup> mice. The mouse brain



parenchyma expressed tdTomato (mTmG; grey). The invasion front shows the presence of single tumor cells expressing H2B-Dendra2 (green) that are disconnected from the tumor lobules and associated with the brain vasculature (mTmG, grey). **(C)** Representative pictures obtained by multi-photon imaging through a cranial window of BCBM 2 weeks after tumor implantation. Images show single tumor cells expressing H2B-Dendra2 (green) in close association with blood vessels. Blood vessels were imaged with 70 kDa fluorescent-dextran (grey).

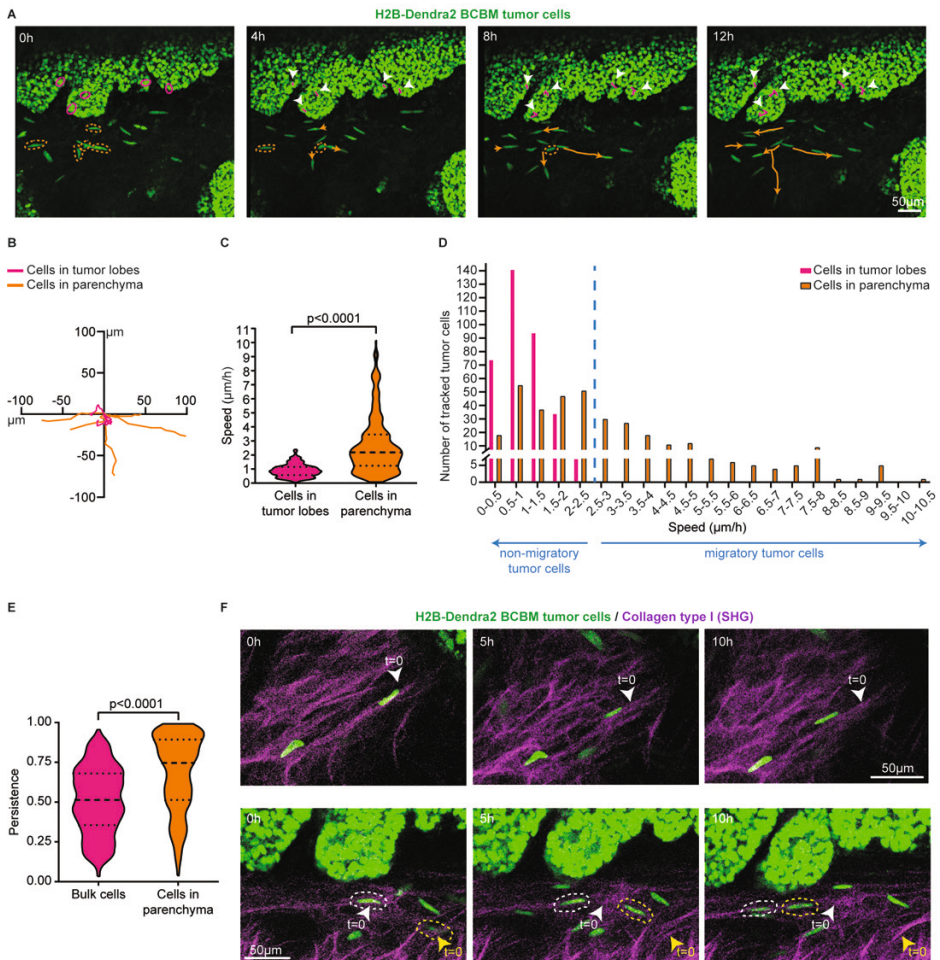


**Figure 2. Single cells at the invasive front of BCBM are highly migratory.** **(A)** Representative still images from a time-lapse multi-photon tracking of BCBM through a cranial window. BCBM tumor cells expressing H2B-Dendra2 were imaged every hour for up to 12 h. Randomly picked cancer cells located in the tumor lobe or brain parenchyma are marked with a circle in magenta and orange, respectively. Tracks are depicted once cells move. Migratory tracks depict the total movement of tumor cells in the tumor lobes (magenta tracks and white arrowheads) and brain parenchyma (orange tracks). **(B)** Rose plot representation of the migratory tracks with a common origin of tumor cells displayed in (A).

**Figure 2. Continued.** (C) Quantification of the speed of tumor cells in the tumor lobes (magenta) or brain parenchyma (orange);  $n = 350$  tumor cells per condition imaged in 3 mice; p-value was determined using a Mann–Whitney t-test, two-tailed. (D) Distribution of tumor cell speed for cells present in the tumor lobes and in the brain parenchyma. (E) Quantification of the persistence of migratory tracks from a total of 350 tumor cells per condition from 3 mice. p-value was determined with a Mann–Whitney t-test, two-tailed. (F) Representative still images of a time-lapse multi-photon movie showing the migration of BCBM tumor cells along crosslinked collagen type I fibers (SHG channel) in two distinct areas.

### ***Impeding Tumor Cell Migration Improves Surgical Resection***

Considering that cancer cell invasiveness hinders complete tumor resection and are associated with worse patient prognosis in BM and glioblastoma [49–51], we next tested whether impeding tumor cell migration would improve the efficiency of surgery in BCBM. Cell motility in BC, including PyMT breast tumors, was previously shown to be partly driven by the actin-related protein 2/3 complex (ARP2/3 complex), which mediates actin nucleation [52–54]. As such, reducing ARPC3 expression can impair cell migration without altering proliferation [55]. We therefore transduced our BCBM organoids with short-hairpin RNAs against ARPC3 (shARPC3). Western blot analysis confirmed the reduced expression of ARPC3 using two distinct shARPC3 (**Figures 3A,S1**). For further experiments, we worked with shARPC3 #2, which showed the highest knockdown efficiency. Next, we intracranially injected BCBM organoids engineered with either shScramble or shARPC3 in ROSA26<sup>mTmG</sup> FVB mice. We confirmed that reducing ARPC3 expression did not alter tumor cell proliferation, based on Ki67 expression (Figure 3B, C). Next, we used multiphoton microscopy to monitor BCBMs through a cranial window. In line with previous literature [52,53,55], reducing ARPC3 expression in BCBM cells significantly decreased the number of cells that invaded the surrounding parenchyma (**Figure 3D, E**).

Next, we tested whether impairing migration and invasion by ARPC3 knockdown would improve surgical removal of BCBM. We intracranially injected BCBM organoids engineered with either shScramble or shARPC3 in 16 FVB mice and monitored BCBM growth using MRI (**Figure 4A**). Whilst blinded for the experimental group, we performed surgical resection of the BCBM when tumors reached a volume of 10–18 mm<sup>3</sup>. The average tumor volume was equal between both groups (**Figure 4B**). Importantly, in line with the absence of significant changes in proliferation (**Figure 3B, C**), the time for tumors to reach the same average volume prior to resection did not differ between the shScramble and shARPC3 tumors, confirming that reducing ARPC3 expression does not influence tumor growth (**Figure 4B, C**). From the shARPC3 group, one mouse did not grow a BCBM, and another mouse was sacrificed for BCBM-unrelated reasons; therefore, we excluded those mice from the experiment. Since our BCBM cells express H2B-Dendra2, we used fluorescent microscopy to score the amount of tumor cells that were left behind after surgical resection of the BCBMs (**Figure 4D**). This revealed that in all mice of the shScramble group, some BCBM cells remained in the surgical cavity; however, this was not the case in the majority

of the shARPC3 mice (**Figure 4D,E**). Strikingly, even a week after surgical removal, those cells that were left behind were not detected by MRI (**Figure 4F**). This suggests that also in the clinic, where MRI is used as a measure of complete BCBM resection, single BCBM cells that invade the parenchyma and are left behind upon resection may not be detected. Additionally, similar to BCBM patients, we observed BCBM recurrence at later time-points with 50% of the shScramble mice recurring versus 33% in the shARPC3 group during the 11 weeks follow-up post-surgery (**Figure 4F, G**). Reduced expression of ARPC3 in the recurrent tumors was maintained, as confirmed by RT-qPCR (**Figure S2**). Together, these data suggest that blocking cell invasion may improve surgical resection of the BCBM.

### ***BCBM Invading Tumor Cells Are in a Mesenchymal State***

Next, we investigated the role of EMT in these invasive tumor cells using the E-cad-mCFP reporter, as we previously did in the primary tumor [26,27]. In the tumor lobes, cancer cells express E-cad-mCFP (**Figure 5A**). Importantly, we observed that all cells that invaded the parenchyma lost E-cad-mCFP expression (arrowheads, **Figure 5A, B**). From here on, we refer to cells with high E-cad-mCFP expression as E-cad<sup>HI</sup> cells and cells that lost E-cad-mCFP expression as E-cad<sup>LO</sup> cells. In line with our previous observations in primary PyMT breast tumors [26,27], E-cad<sup>HI</sup> cells were on average non-motile, whilst a large fraction of the E-cad<sup>LO</sup> cells were migratory (**Figure 5C, D**).

To characterize the Epithelial/Mesenchymal (E/M) states of E-cad<sup>HI</sup> cells and E-cad<sup>LO</sup> cells, we isolated both populations using fluorescence activated cell sorting (FACS) (**Figures 5E, S3**). Imaging analysis of E-cad-mCFP confirmed the successful isolation of E-cad<sup>HI</sup> and E-cad<sup>LO</sup> cells (**Figure S3**). Next, we performed bulk mRNA sequencing on both cell populations (**Figure 5F, G**) and analyzed the differentially expressed genes that we refer to as the E-cad<sup>LO</sup> gene set. The E-cad<sup>LO</sup> gene set contains typical EMT genes, such as E-cadherin (Cdh1), N-cadherin (Cdh2), Vimentin (Vim), Fibronectin (Fn1) and transcription factors such as Snail (Snai1), Zeb1 and Zeb2 (**Figure 5G**). We confirmed the bulk mRNA sequencing results by RT-qPCR (**Figure 5G**). In line with this data, the E-cad<sup>LO</sup> gene set was enriched for genes involved in the “Hallmark Epithelial\_Mesenchymal\_Transition” [42] (**Figure 5H**). Lastly, we compared the expression profile of E-cad<sup>LO</sup> cells isolated from BCBM to the expression profile of their counterparts isolated from primary PyMT tumors. Importantly, in our prior study, we showed that E-cad<sup>LO</sup> cells have low expression levels of the epithelial marker E-cadherin and high expression of the mesenchymal marker Vimentin [27].

In line with the enrichment of genes involved in EMT, we found that the E-cad<sup>LO</sup> gene set but not E-cad<sup>HI</sup> gene set of BCBM tumors is enriched in genes that were found to be significantly upregulated in the E-cad<sup>LO</sup> gene set of the primary breast tumor [27]. Collectively, these data show that the differential expression of E-cad-mCFP in E-cad<sup>HI</sup> and E-cad<sup>LO</sup> cells reports the epithelial and mesenchymal states of cells, respectively, in our PyMT BCBM model.

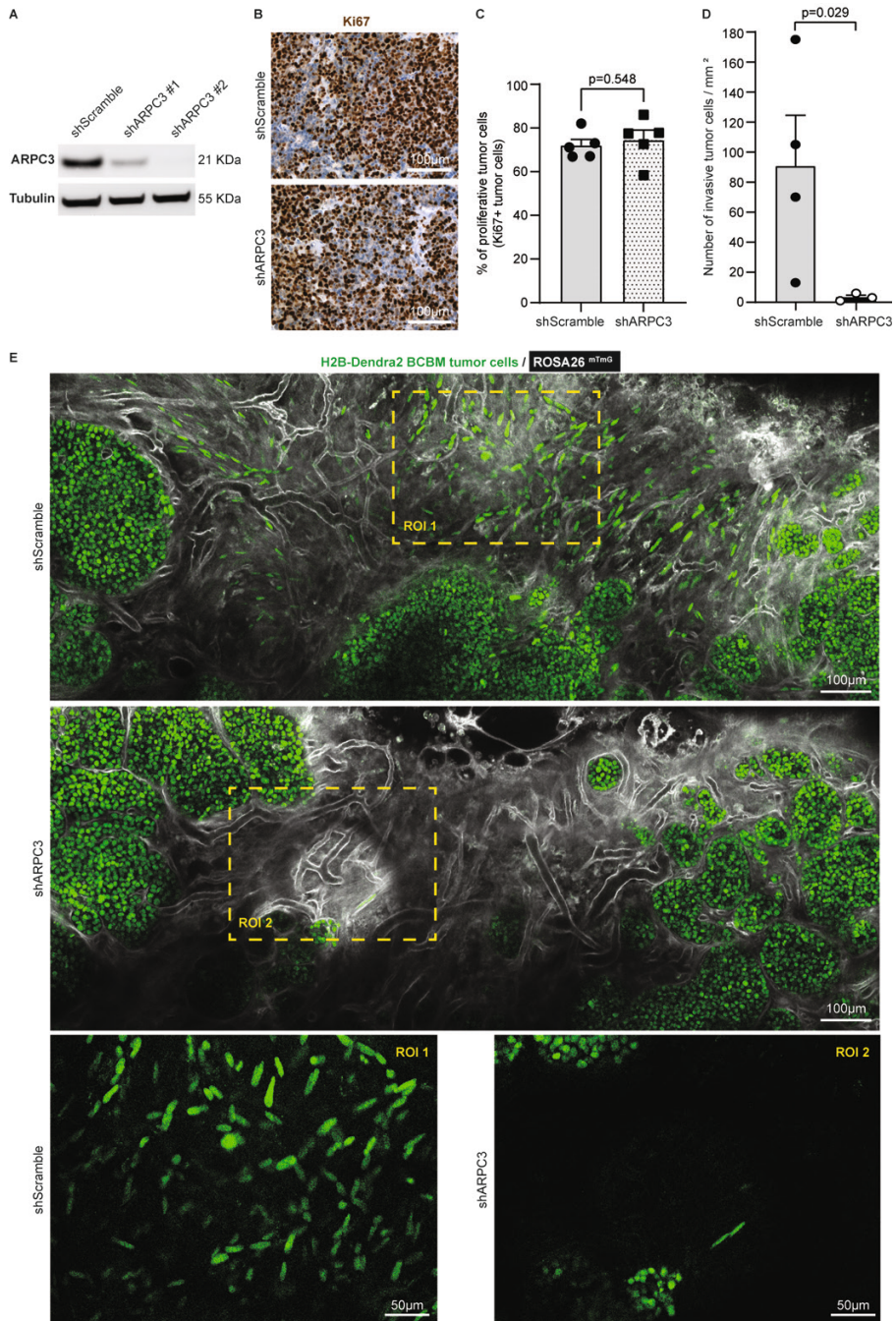


**Figure 3. Reducing ARPC3 expression decreases the number of invasive tumor cells.** (A) Western-blot of ARPC3 and Tubulin on BCBM tumor cells engineered with the shScramble or shARPC3 constructs. See Figure S1 for uncropped blot. (B) Representative images and (C) quantifica-

tion of Ki67 immunohistochemistry staining in BCBM derived from shScramble or shARPC3 organoids intracranially injected into recipient mice. Data are presented as mean  $\pm$  standard-error of the mean (SEM);  $n = 5$  mice per group;  $p$ -value was determined using a Mann–Whitney t-test, two-tailed. **(D)** Quantification of the number of invasive tumor cells observed by intravital imaging of ROSA26<sup>mTmG</sup> mice injected with shScramble or shARPC3 BCBM organoids. Data are presented as mean  $\pm$  SEM;  $n = 4$  mice for shScramble and  $n = 3$  mice for shARPC3 #2;  $p$ -value was determined using a Mann–Whitney t-test, one-tailed. **(E)** Representative multi-photon images of BCBM derived from shScramble and shARPC3 BCBM organoids intracranially injected into ROSA26<sup>mTmG</sup> mice.

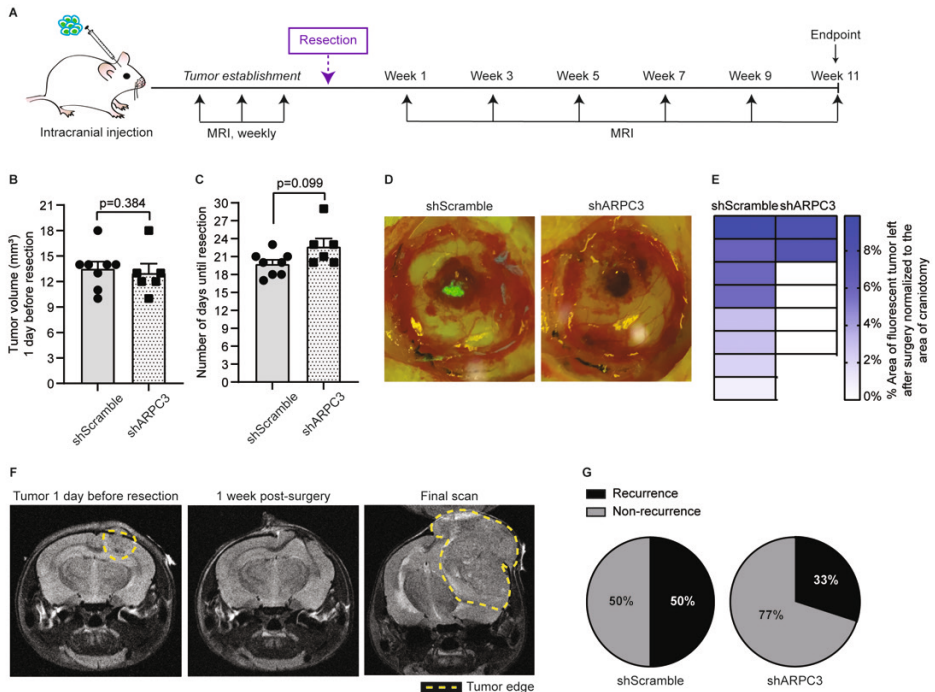


**Figure 4. Impeding tumor cells migration improves surgical resection.** **(A)** Schematic representation of experimental design. **(B)** Quantification of the tumor volume in mice intracranially injected with BCBM organoids engineered with the shScramble ( $n = 8$ ) and shARPC3 ( $n = 6$ ) constructs, one day before resection and as measured by MRI. Data are presented as mean  $\pm$  SEM;  $p$ -value was determined using a Mann–Whitney t-test, two-tailed. **(C)** Time between intracranial injection and resection for mice injected with BCBM organoids engineered with the shScramble ( $n = 8$ ) and shARPC3 ( $n = 6$ ) constructs. Data are presented as mean  $\pm$  SEM;  $p$ -value was determined using a Mann–Whitney t-test, two-tailed. **(D)** Representative images and **(E)** quantification of the percentage of tumor area (green fluorescent signal of H2B-Dendra2 expressed by all BCBM cells) left after resection. Each square represents one mouse. **(F)** Representative MRI images of a mouse brain at the various stages of the experiment. **(G)** Pie charts showing the percentage of mice that recurred until 11 weeks after resection. Additionally, see Figure S2.

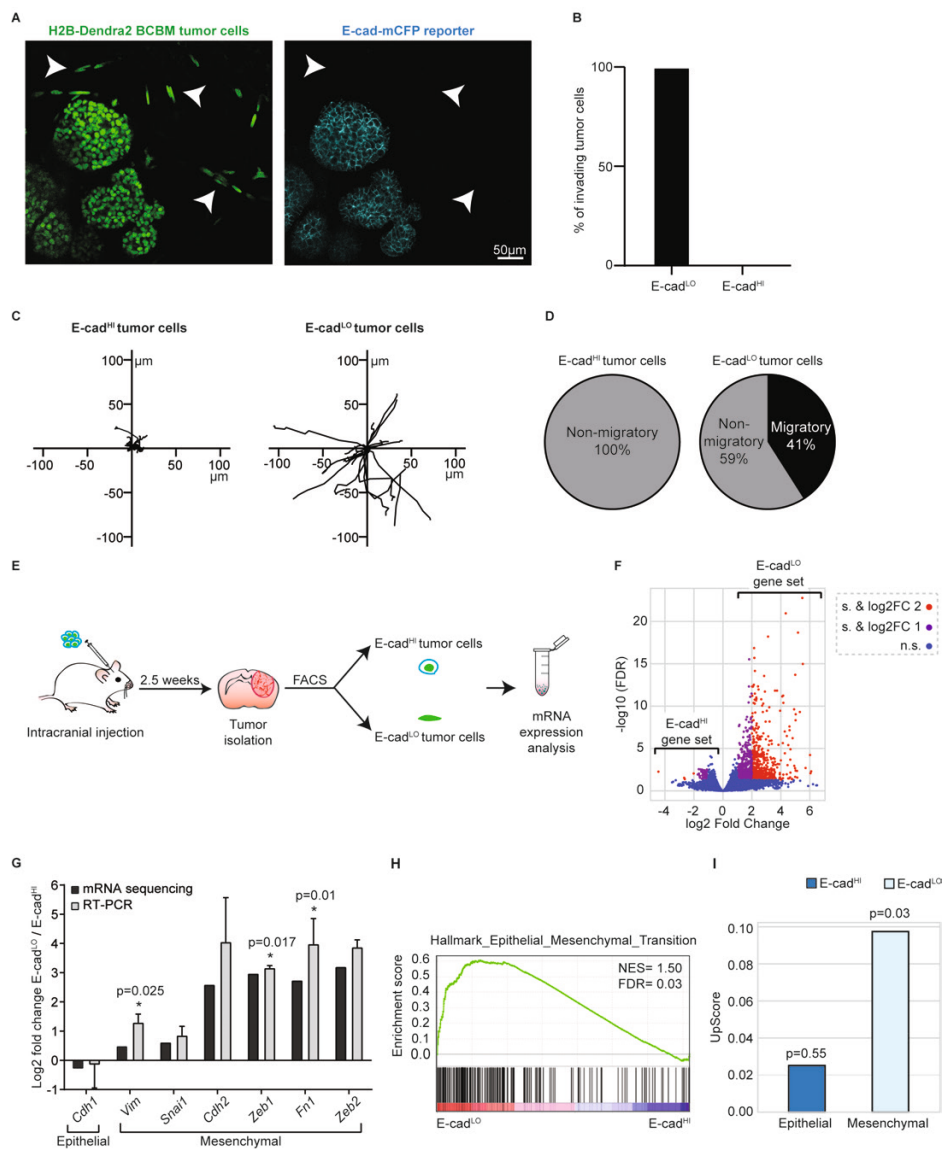


**Figure 5. BCBM invading tumor cells are in a mesenchymal state.** (A) Representative multi-photon images of BCBM tumor cells expressing H2B-Dendra2 (green) and endogenous E-cad-mCFP (turquoise). White arrowheads point to invading tumor cells. (B) Percentage of invading tumor cells that are E-cad<sup>L/O</sup> and E-cad<sup>H/L</sup>. (C) Representative rose plots of migratory tracks with a common origin of 20 E-cad<sup>H/L</sup> tumor cells and 20 E-cad<sup>L/O</sup> tumor cells imaged using multi-photon imaging through a cranial window. (D) Pie charts of migratory (speed  $\geq 2.5 \mu\text{m/h}$ ) E-cad<sup>H/L</sup> or E-cad<sup>L/O</sup> tumor cells. (E) Schematic representation of experimental design used for isolating E-cad<sup>H/L</sup> or E-cad<sup>L/O</sup> tumor cells for mRNA sequencing and RT-qPCR. (F) Volcano plot comparing the fold change and false discovery rate (FDR) of E-cad<sup>H/L</sup> and E-cad<sup>L/O</sup> BCBM tumor cells. (G) mRNA expression analysis of EMT related genes by mRNA sequencing and RT-qPCR;  $n = 4$  for mRNA sequencing and  $n = 3$  for RT-qPCR with

exception for *Cdh2* and *Zeb2*, which are  $n = 2$ . Data are presented as mean  $\pm$  SEM and standard deviation (SD) for *Cdh2* and *Zeb2*. *p-values* were determined with a one-sample t-test, one-tailed between E-cad<sup>LO</sup> and E-cad<sup>HI</sup> tumor cells. **(H)** Gene set enrichment analysis [41] showing enrichment of the signature “Hallmark Epithelial\_Mesenchymal\_Transition” in E-cad<sup>LO</sup> BCBM tumor cells. **(I)** Up-score enrichment of E-cad<sup>HI</sup> or E-cad<sup>LO</sup> BCBM tumor cells in E-cad<sup>LO</sup> breast tumor cells [27]. Value of 0 implies that there is no enrichment of one gene set over the other. *p-values* were determined with a one-sample t-test to calculate the significance to 0.

### ***Mesenchymal Cells Can Form New Tumors and Revert to an Epithelial State***

Since the presence of invasive BCBM cancer cells is involved in relapse following surgical resection (**Figure 4** and [49,51]), we next investigated whether the E-cad<sup>LO</sup> cells have the capacity to grow BCBMs. We isolated ~2000 E-cad<sup>LO</sup> cells from BCBM grown in ROSA26<sup>mTmG</sup> FVB mice by FACS and injected this population intracranially in tumor free FVB mice (**Figure 6A**). An assessment of the purity suggested a potential contamination of the sorted fraction of at most 2.5% with other cells. Therefore, we injected 2.5% of E-cad<sup>HI</sup> cells in tumor free mice to serve as a purity control group (**Figure S3**). In 75% of mice injected with E-cad<sup>LO</sup> cells, BCBMs had developed during approximately 7 weeks post-intracranial injection, while no tumors developed during the same follow-up period in the purity control group (**Figure 6B**). Next, we isolated the BCBMs generated by the E-cad<sup>LO</sup> cells and studied the expression of the E-cad-mCFP reporter (**Figure 6C**). In all tumors, we detected the E-cad-mCFP reporter in tumor cells, which was further validated by staining tumors with an E-cadherin antibody (**Figure 6C**). This demonstrated that in our BCBM model, mesenchymal cells have the ability to form new tumors and to concomitantly revert to an epithelial phenotype, a process often referred to as mesenchymal-to-epithelial transition (MET).

### ***Tumor Cells Undergoing EMT Are Present at the Invasion Front in Human BCBM***

Finally, we investigated whether mesenchymal infiltrative tumor cells are also present in BCBM patients (**Figure 7**). We obtained tumor resections from 8 patients with BCBM. Using multiplex immunohistochemistry, we simultaneously stained for Pankeratin and E-cad to mark cells in an epithelial state, and *Zeb1* to mark cells in a mesenchymal state (**Figure 7A**). In the tumor mass, we indeed observed that cancer cells stain positive for Pankeratin and E-cad and negative for *Zeb1*, as expected for epithelial cancer cells. Moreover, and in line with previous observations [56], the brain parenchyma that surrounds the BCBM contained cells that were positive for *Zeb1* and negative for E-cad. Yet, most of these cells were also negative for Pankeratin, suggesting that those cells belong to a population of glial and immune cells that also express *Zeb1* [57]. However, in seven out of eight patients, we also observed a population of *Zeb1* positive; E-cad negative cells with moderate to high expression of the epithelial marker Pankeratin (**Figure 7B**). In line with the data of the

infiltrative E-cad<sup>LO</sup> cells that are present in the brain parenchyma in our mouse model, these Pankeratin-positive, Zeb1-positive, E-cad-negative cells have a spindle shape nucleus, indicative of a migratory state (encircled in **Figure 7A**). Together, this suggests that BCBM patients also have infiltrative tumor cells in EMT in the brain parenchyma that surrounds the BCBM.

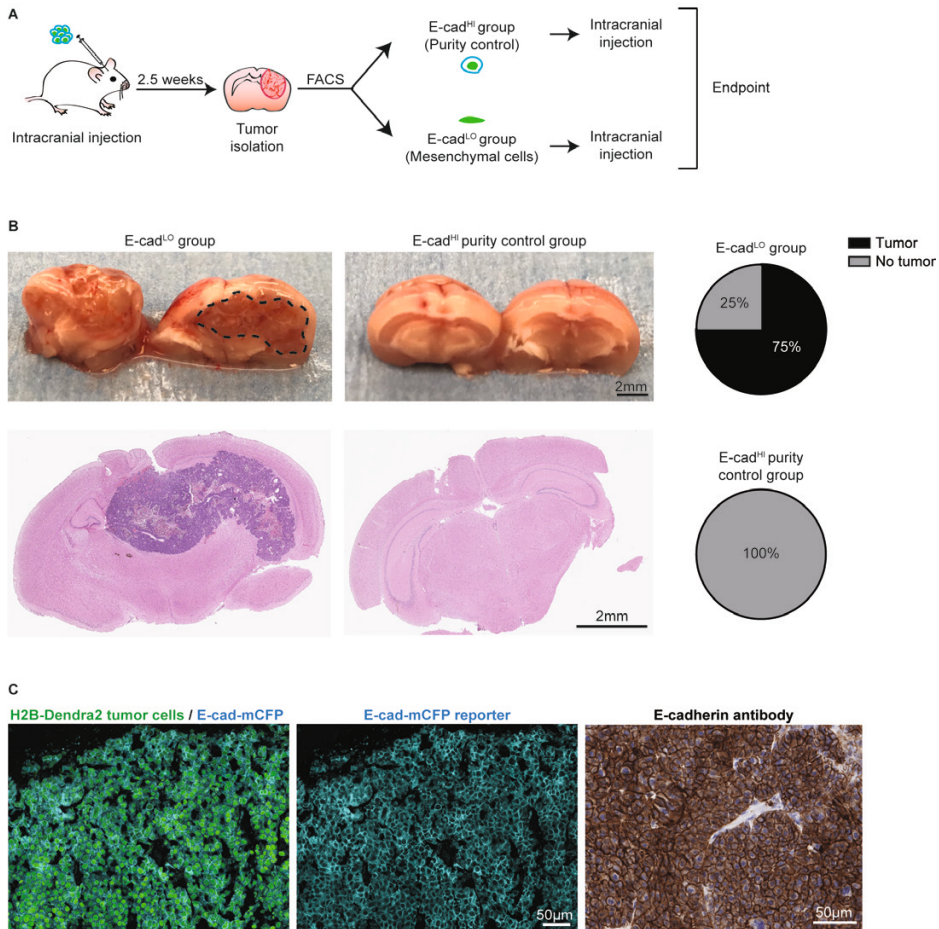


**Figure 6. Mesenchymal cells can grow tumors and revert to an epithelial state.** (A) Schematic representation of experimental design. (B) Representative pictures and H&E staining of the mouse brain. Pie charts show the percentage of BCBM tumors formed after intracranial injection of approximately 2000 E-cad<sup>LO</sup> tumor cells compared to the purity control group.  $n = 4$  mice per group. (C) Representative images of immunofluorescent staining (left and middle panels) of H2B-Dendra2 (green) and the endogenous E-cad-mCFP (turquoise) reporter in tumors formed after intracranial injection of E-cad<sup>LO</sup> tumor cells. The expression of E-cadherin was confirmed using immunohistochemistry with an E-cadherin antibody (right panel).  $n = 3$  mice.



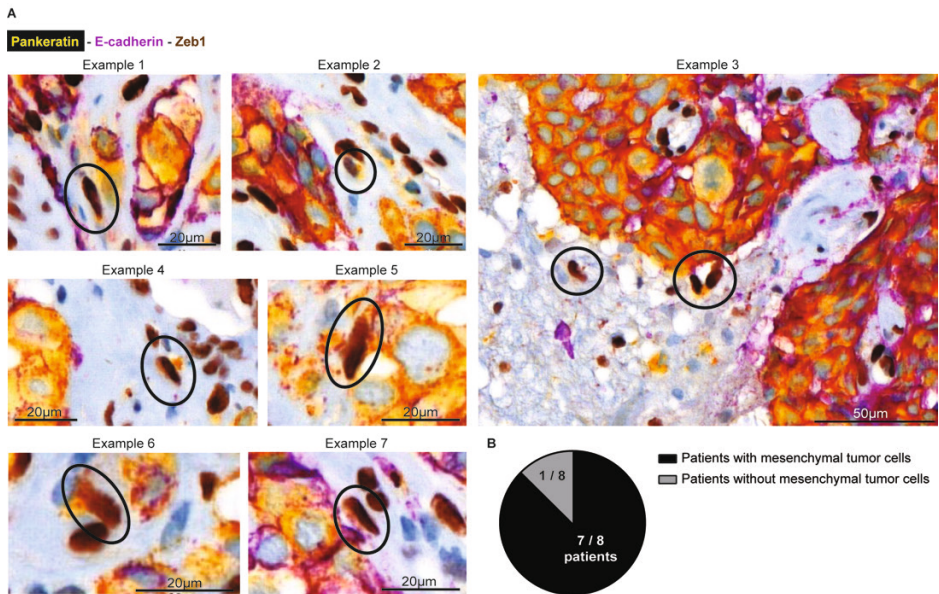


**Figure 7. Mesenchymal tumor cells are present at the invasive front in human BCBM. (A)** Multiplex immunohistochemistry imaging of PanKeratin (yellow), E-cadherin (purple) as markers for epithelial cells and Zeb1 (DAB) to mark cells in a mesenchymal state. **(B)** Quantification of the number of patients where mesenchymal tumor cells were observed in the brain parenchyma.

## CONCLUSIONS

The role of EMT in the formation of metastases has been heavily debated by the field. However, the role of EMT at later stages of the metastatic cascade in growing metastatic masses remains under-studied. Here, we used intravital microscopy combined with mRNA sequencing to demonstrate that cells undergoing EMT are present in established BCBM, invade the brain parenchyma and have the capacity to revert to an epithelial state when forming secondary lesions. We also reveal that the presence of these invasive cells impairs the successful removal of BCBM lesions. Importantly, even if surgery is followed by chemotherapy or radiotherapy, these invasive cells may not be efficiently depleted, since EMT endow cells with properties that can render them resistant to those therapies [21,58–60]. Therefore, targeting EMT can improve surgical resection and may sensitize cells that are left behind to subsequent therapies. In our study, we combined an E-cad fluorescent reporter with mRNA sequencing to study EMT in BCBM. We showed that the E-cad<sup>LO</sup> cells upregulate mesenchymal markers and are migratory. However, recent work has provided evidence that EMT is not a binary switch but that cells can adopt various hybrid E/M states with distinct metastatic and chemoresistance properties [17,19,25,61,62]. Here, in

our mouse experiments, we have neither investigated the presence nor the role of cells with different E/M states. However, in our analysis of human BCBM, we observed cancer cells that escaped from the tumor mass and invaded the brain parenchyma contained a typical mesenchymal profile of expressing *Zeb1* and losing E-cadherin, but interestingly still expressing the epithelial marker Pankeratin. Expression of the latter marker suggests that these infiltrating cells may not have lost all epithelial traits which can indicate a hybrid state. Future studies should shed light on the role of specific hybrid E/M states in BCBM and their distinct contributions to patient relapse following surgery. Additionally, developing therapeutic strategies to block EMT and/or mesenchymal cells is required to target this process and to ultimately improve BCBM patients' outcomes. Nevertheless, our data warrant future studies to target EMT processes for better treatment of BCBM.

## **MATERIALS AND METHODS**

### **Mice**

All experiments were performed under the guidelines of the Animal Welfare Committee of the Royal Netherlands Academy of Arts and the Netherlands Cancer Institute, in accordance with national guidelines. Animals were kept at the Hubrecht animal facility in Utrecht, the Netherlands or at the Netherlands Cancer Institute facility in Amsterdam, the Netherlands. All animals were housed in individually ventilated cages under specific pathogen-free conditions and received chow and water ad libitum. Female ROSA26<sup>mTmG</sup> C57BL/6J mice were purchased from Jackson Laboratory and backcrossed to FVB mice at the animal facility of the Hubrecht and of the Netherlands Cancer Institute. Female FVB mice were acquired from Janvier. All mice were injected with tumor cells when they were 8–20 weeks old.

### **Serial Intracranial Injections to Generate the BCBM Model**

End-stage primary breast tumors were isolated from PyMT E-cad-mCFP mice [27] and frozen in freezing medium (Gibco, Cat. No. 12648-010, ThermoFisher Scientific, Waltham, MA, USA). For the first intracranial injection, tumors were thawed and minced on ice with sterile knives and enzymatically digested at 37 °C for 20–30 min while shaking at 900 rpm. The digestion mix was composed of 0.01 g collagenase A (Roche, Cat. No. 10103586001, Basel, Switzerland), 2 mL TrypLE Express (Gibco, Cat. No. 12605010) and 3 mL DMEM/F12 GlutaMAX (Gibco, Cat. No. 10565018) supplemented with 10 mmol/L Hepes (Gibco, Cat. No. 15630106), 100 µg/mL streptomycin and 100 U/mL penicillin (Gibco, Cat. No. 15140122). Undigested tumor pieces were removed by spinning down at 800 rcf at 4 °C and for 5 min. Then, 10 µg/mL DNase I (Roche, Cat. No. 10104159001) in DMEM/F12 GlutaMAX medium were used to dissolve the pellet while manually shaking the tube for 5 min. The final pellet was resuspended in 3 µL per intracranial injection of PBS. After a tumor was formed in

the brain of the recipient mouse, the tumor was isolated and cut into smaller tumor pieces prior to freezing (Gibco, Cat. No. 12648-010). This whole process is considered as one enrichment round in the brain. We repeated this process for a total of 6 times using the tumor pieces from the previous serial enrichment round. At the 6<sup>th</sup> enrichment round, we derived organoids which are described in this study as 'BCBM organoids'.

### **Organoids Culturing**

PyMT E-cad-mCFP organoids were cultured in drops of 50  $\mu$ L of Basal Membrane Extract (BME) type 2 (R&D systems, Cat. No. 3533-005-02) diluted at a 2:1 ratio with DMEM/F12 GlutaMAX medium (Gibco, Cat. No. 10565018) in a pre-warm 24-well plate (Greiner bio-one, Cat. No. 662160) and inverted while solidifying for 30 min at 37 °C, 5% CO<sub>2</sub>. Organoids were cultured in complete DMEM/F12 GlutaMAX medium (Gibco, Cat. No. 10565018), supplemented with 10 mmol/L Hepes (Gibco, Cat. No. 15630106), 100  $\mu$ g/mL streptomycin, 100 U/mL penicillin (Gibco, Cat. No. 15140122), 10.08 ng/mL FGF (Gibco, Cat. No. PHG0261) and 1 $\times$  B27 supplement (Gibco, Cat. No. 17504001) and incubated at 37 °C, 5% CO<sub>2</sub>. To confirm Mycoplasma-free culturing of the organoids, the MycoAlert PLUS Kit (Lonza Cat. No. LT07-118, Basel, Switzerland) was routinely used according to the manufacturer's protocol.

### **Lentivirus Production and Transduction**

Generation of the PyMT E-cad-mCFP; H2B-Dendra2 line was performed using the vector plvx-UBC-H2B-Dendra2-puromycin. Human embryonic kidney (HEK) 293T cells at a confluence of 80% were used for lentivirus production. Per 10 cm dish (Greiner, Cat. No. 664160) of HEK 293T cells, 7.5  $\mu$ g of psPAX2, 2.5  $\mu$ g PMD2.G and 10  $\mu$ g of our H2B-Dendra2 construct were mixed in 1 mL Opti-MEM (ThermoFisher Scientific, Cat. No. 31985070, Waltham, MA, USA). After mixing, 1 mL of Opti-MEM with 40  $\mu$ L lipofectamine 2000 (ThermoFisher Scientific, Cat. No. 11668019) were added to the plasmid mix and incubated at room temperature for 15 min. The mix was carefully added to the HEK 293T cells. The following morning, medium was refreshed with DMEM GlutaMAX (Gibco, Cat. No. 31966047) supplemented with 100  $\mu$ g/mL streptomycin, 100 U/mL penicillin (Gibco, Cat. No. 15140122). After 48 h, medium was collected and filtered through a 0.22  $\mu$ m filter (Milipore, Cat. No. SLGS033SS, Burlington, MA, USA). Filtered medium was concentrated with an Amicon Ultra-15 10 k column (Milipore, Cat. No. UFC905024) for 1 h at 4000 rcf. Organoids were trypsinized into smaller clusters of approximately 8 cells and incubated with 250  $\mu$ L virus, 100  $\mu$ g/mL polybrene (Sigma, Cat. No. TR-1003-G, St. Louis, MO, USA) and 10  $\mu$ mol/L Y-27632 (Bio Connect, Cat. No. S1049) on a 48-well plate low adherence (Greiner, Cat. No. 677970). Spin infection was performed at 36 °C, 600 rcf for 1 h and organoids were subsequently incubated at 37 °C for 6 h. Organoids were washed twice with DMEM/F12 GlutaMAX medium (Gibco, Cat. No. 10565018) and plated in BME. Complete DMEM/

F12 GlutaMAX medium (Gibco, Cat. No. 10565018), supplemented with 10 mmol/L Hepes (Gibco, Cat. No. 15630106), 100 µg/mL streptomycin, 100 U/mL penicillin (Gibco, Cat. No. 15140122), 10.08 ng/mL FGF (Gibco, Cat. No. PHG0261), 1xB27 supplement (Gibco, Cat. No. 17504001) and 10 µmol/L Y-27632 (Bio Connect, Cat. No. S1049) was added to the organoids for 2 days maximum. Organoids selection was performed with 0.5 µg/mL puromycin (Gibco Cat. No. A1113803).

### **shRNAs Constructs Selection, Viruses Production and Transduction**

ARPC3 knockdown experiments were performed with shRNAs provided by The RNAi Consortium (TRC) mouse library. Their oligoIDs were the following: shRNA#1-TRCN0000110780, shRNA#2-TRCN0000110781, shRNA#3-TRCN0000110783 and shRNA#4-TRCN0000110784. Resistance cassette from these vectors was changed from puromycin to blasticidin and control pLKO.1-scramble-blasticidin was purchased from Addgene (plasmid 26701, Watertown, MA, USA). The puromycin cassette for the shARPC3 constructs was removed using restriction enzymes BamH1 and KpnI. Concentrated viruses were produced as described in [35] by co-transfection of 4 plasmids: VSV-G (9 µg), pMLD (12.5 µg), kREV (6.25 µg) and shARPC3 (32 µg) in HEK 293T cells. Organoid transduction was performed as described in 'Lentivirus production and transduction'. Virus titers were calculated with a qPCR lentivirus titration titer kit (abm, Cat. No. LV900, Richmond, BC, Canada) as per the manufacturer's protocol. Organoids were transduced with a multiplicity of infection (MOI) of 10. To determine the volume of virus to use during transductions, we used the formula:  $MOI = \text{number of viral units} / \text{number of cells}$ . Transduced organoids were selected with 10 µg/mL of blasticidin (Gibco, Cat. No. A1113903) and kept in culture with this selection.

### **Cranial Window Implantation and BCBM Injection under the Window**

BCBM derived organoids were digested with TrypLE Express (Gibco, Cat. No. 12605010) for ~20 min at 900 rpm and 37 °C to produce a single cell suspension. Digestion was stopped by adding DMEM F12 medium. Per injection, 100,000 cells were resuspended in 3 µL of PBS and injected just before the implantation of the cranial window. Cranial window implantation was performed as previously described [36]. In summary, mice were treated with 0.067 mg/mL rimadyl (carprofen, Zoetis) in drinking water 1 day before injection and for 3 days post-surgery. Furthermore, 30 min before surgery mice were subcutaneously injected with 0.1 mg/kg temgesic (buprenorphine, Indivior Europe Limited) and 8–12 h after window implantation. Mice were anesthetized via inhalation of 2% (v/v) isoflurane and eyes were covered with duratears (Alcon). Once placed in a stereotactic frame, the mouse head was shaved and the skin was cut in a circular manner. Once the skull was exposed, a local anesthetic (0.01–0.02 mL) made of NaCl supplemented with 1 mg/mL Lidocaine (Fresenius Kabi) and 0.25 mg/mL Bupivacaine (Actavis, Aurobindo Pharma B.V.) was applied. After removal of the periosteum, a 5 mm diameter circle was drilled on the right parietal bone.

The bone was removed following removal of dura mater with thin forceps. The tumor cell suspension was injected in the middle of the craniotomy at 0.5 mm depth with a 10  $\mu$ L glass Hamilton syringe, 30G and point 4-style needle at a speed of 1  $\mu$ L/minute. Silicone oil covered the exposed brain and a 6 mm coverslip was glued on top with histoacryl (Braun). Dental acrylic cement (Vertex) was applied on the skull surface to glue a 3D printed window which provides fixation when performing intravital microscopy. After surgery, mice were allowed to recover on a heating pad and were closely monitored the following days.

### **Intravital Imaging Microscopy**

Mice were sedated with 1% (v/v) isoflurane and placed in a custom-designed imaging box while kept under continuous anesthesia with isoflurane. Both the imaging box and microscope were adjusted to 36.5 °C using a climate chamber. During long-term imaging, mice were administered with 100  $\mu$ L/h of Nutriflex special 70/240 (Braun). Intravital images were acquired with both an inverted Leica SP8 Dive system (Leica, Mannheim, Germany) with a MaiTai eHP DeepSee laser (Spectra-Physics, Milpitas, CA, USA) and an InSight X3 laser (Spectra-Physics) or an inverted Leica SP8 Dive system (Leica, Mannheim, Germany) with only InSight X3 laser (Spectra-Physics). For both systems a Leica Application Suite X (LAS X) software (Mannheim, Germany) was used. For the system with 2 lasers, SHG (crosslinked collagen I), E-cad-mCFP and H2B-Dendra2 were simultaneous excited with 860 nm (Mai Tai) and detected at 420–442 nm (HyD-RLD1), 444–485 nm (HyD-RLD2) and 510–556 nm (HyD-RLD3), respectively. ROSA26<sup>mTmG</sup> was excited with 980 nm (InSight X3) and detected at 564–698 nm (HyD-RLD4). For the system with one laser, we performed sequential scanning; sequence 1 used an excitation of 930 nm (InSight X3) to detect SHG at 458–471 nm (HyD-RLD2), H2B-Dendra2 at 491–541 nm (HyD-RLD3) and ROSA26<sup>mTmG</sup> at 564–684 nm (HyD-RLD4); sequence 2 used an excitation of 840 nm to image E-cad-mCFP at 442–475 nm (HyD-RLD3). Three-dimensional tile scans were acquired with a 5  $\mu$ m z-step size. Time-lapse movies were acquired with a 5  $\mu$ m z-step and imaged every hour for a total of 8 to 12 h. All images were acquired in 12 bit and with a 25 $\times$ /0.95 NA water immersion objective. Dextran Texas Red 70,000 MW (Invitrogen, Cat. No. D1830) at a concentration of 10 mg/mL was intravenously injected prior imaging. Texas Red was excited at 980 nm and detected at 674–711 nm.

### **Movies Correction and xy Migration Analysis**

Time-lapse movies were corrected for xyz drift movements using Huygens Professional software program (version 20.10, Hilversum, Netherlands). For this correction we used the ROSA26<sup>mTmG</sup> channel as a reference. Per corrected position, we made a maximum projection of 3 consecutive z-planes throughout the complete z-stack for the analysis, thus covering the complete imaging depth. Cells were manually tracked using MTrackJ plugin from ImageJ. A total of 120 to 370 cells were tracked per mouse in 3 mice. For each

population (cells in tumor lobes or in the brain parenchyma), 350 cells were analyzed. The XY position was determined over time by the MTrackJ plugin and the speed and persistence for each individual cell was calculated with Excel (Microsoft, Redmond, DC, USA). For each population (cells in tumor lobes or in the brain parenchyma), we determined the percentage of migratory cells based on the number of tracked cells which speed was equal or higher than 2.5  $\mu\text{m}$  over the total number of tracked cells per population.

### **Western Blot**

Protein lysates were made using 20 mmol/L Tris-HCl pH 8.0, 150 mmol/L NaCl, 1% NP-40, 10% Glycerol in milli-Q water, complemented with protease and phosphatase inhibitors (Roche, Cat. No. 11697498001). Protein lysates were quantified using the Pierce BCA protein assay kit (Thermo Scientific, Cat. No. 23225) and loaded on a NUPAGE 4–12% gel Bis-Tris gradient gel (Invitrogen, Cat. No. NP0321PK2). Transfer onto a nitrocellulose membrane (Bio-Rad, Cat. No. 1620112) was performed overnight in 1 $\times$  transfer buffer (25 mmol/L Tris, 2 mol/L Glycine, 20% methanol in demineralized water). Membranes were blocked at room temperature for 1.5 h in 5% non-fat dry milk and incubated overnight at 4 °C with the antibodies diluted in 5% non-fat dry milk. Primary antibodies were ARPC3 (also denominated as p21-ARC; 1:1000; Invitrogen Cat. No. PA5-82253) and Tubulin (1:10 000; Abcam Cat. No. ab6160). Membranes were washed 3 $\times$  with TBS-T and incubated for 1 h at room temperature with adequate secondary antibodies: anti-rabbit HRP (1:3000; BioRad Cat. No. 1706515) or anti-rat HRP (1:3000; Invitrogen Cat. No. 62-9520) in 5% nonfat dry milk. Membranes were washed 3 $\times$  with TBS-T and developed using ECL-clarity (BioRad, Cat. No. 170-5060) on a Fusion FX7 edge (Vilber).

### **Intracranial Injection**

BCBM organoids were prepared as mentioned in ‘Cranial window implantation and BCBM injection under the window’. Prior to surgery, mice received 0.067 mg/mL rimadyl (carprofen, Zoetis) in drinking water 1 day before injection and for 3 days post-surgery. Additionally, 30 min before surgery and 8–12 h after surgery, mice were subcutaneously injected with 0.1 mg/kg temgesic (buprenorphine, Indivior Europe Limited). Mice were anesthetized via inhalation of 2% (v/v) isoflurane and eyes were covered with duratears (Alcon). After shaving the head, an incision was made in the skin to reveal the skull, followed by the application of a local anesthetic (0.01–0.02 mL). This was prepared with NaCl supplemented with 1 mg/mL Lidocaine (Fresenius Kabi) and 0.25 mg/mL Bupivacaine (Actavis, Aurobindo Pharma B.V.). After removal of the periosteum, a hole was drill 1.5 mm to the right and 1.5 mm posterior to the bregma. At a depth of 1 mm, we injected our tumor cells preparation (100,000 cells in 3  $\mu\text{L}$ ) with a 10  $\mu\text{L}$  glass Hamilton syringe, 30G and point 4-style needle at a speed of 1  $\mu\text{L}$ /minute. Skin was sutured after injection and the mouse was allowed to recover on a heating pad, being monitored closely the next days.

## Magnetic Resonance Imaging

Magnetic resonance imaging was performed with a 7 Tesla BioSpec 70/20 USR (Bruker; Billerica, MA, USA). Imaging was performed with a T2 RARE sequence with a 39 ms echotime, 2200 ms repetition time and 8 averages. Paravision software (v6.0.1; nBruker) was used for image acquisition and MIPAV NIH software (Bethesda, USA) was used for tumor volume measurements. Mice were anesthetized with 2% (v/v) isoflurane during imaging, eyes were covered with duratears (Alcon) and the heart rate was monitored throughout the procedure.

## Tumor Resection

This surgery was designed in close collaboration with a neurosurgeon to resemble the clinical setting. During this entire experiment, the researcher performing the surgery and MRI was not aware of the BCBM group from the time of intracranial injection until the 11 weeks after tumor resection. Mice were intracranially injected with 20,000 cells derived from either shScramble or shARPC3 BCBM organoids. The coordinates from the bregma were 1.5 mm to the right, 1.5 mm posterior and 0.5 mm depth. Once mice developed tumors with a volume of 10–18 mm<sup>3</sup>, BCBM resection was performed. Mice received 0.067 mg/mL rimadyl (carprofen, Zoetis) in drinking water 1 day before surgical resection and for 3 days post-surgery. Moreover, 30 min before surgery and 8 h after surgery, mice were subcutaneously injected with 0.1 mg/kg temgesic (buprenorphine, Indivior Europe Limited). Mice were anesthetized via inhalation of 2% (v/v) isoflurane and their eyes were covered with duratears (Alcon). The mouse head was shaved and Rymadil (5 mg/kg) and warm NaCl were subcutaneously injected. Once placed on the stereotactic frame, an incision was made in the skin to reveal the skull. A local anesthetic which consisted of NaCl supplemented with 1 mg/mL Lidocaine (Fresenius Kabi) and 0.25 mg/mL Bupivacaine (Actavis, Aurobindo Pharma B.V.) was applied on the skull. Removal of the periosteum was performed with a cotton swab, followed by drilling of a 5 mm diameter circle on the right parietal bone. Bone and meninges were removed with thin forceps. With a vacuum pump, the BCBM was aspirated with a 100 µL sterile tip until no more tumor was visible. To stop bleeding, we used cold NaCl with eyespear pointed tips (Sugi) and once mostly dried we applied spongstan (Ethicon). Once the bleeding stopped and the surgery finished, we used a fluorescent stereomicroscope system (Nightsea fluorescent adapter, Lexington, MA, USA) to visualize how much fluorescent tumor was left behind. Skin was sutured and glued with histoacryl (Braun).

After surgery, mice received subcutaneously warm NaCl while recovering on a heating pad. Mice were closely monitored over the following days.

## Fluorescence Activated Cell Sorting

BCBM were isolated from mouse brains and minced manually on ice using sterile scalpels. All of these steps were executed inside a flow cabinet. Minced tumors were collected in a 15

mL falcon and enzymatically digested in 3 mL PBS supplemented with 10 µg/mL DNase I (Roche, Cat. No. 10104159001) and 0.96 mg/mL Liberase TH (Roche, Cat. No. 5401151001) at 37 °C for 15 min at 1050 rpm. The remaining pieces were resuspended with a 20-gauge needle. Supernatant was spun down and washed twice with a FACS buffer made of PBS with 2 mmol/L EDTA (Lonza AccuGENE, Cat. No. 51234) and 1% B27 (50× Gibco, Cat. No. 17504044). After the last wash, the pellet was resuspended in FACS buffer and filtered through the lid of a falcon tube with a cell strainer (Falcon, Cat. No. 352235). Sample was transferred into a polypropylene falcon (Falcon, Cat. No. 352063) and just prior to sorting, 20 nmol/L of TO-PRO Iodide-3 642/661 was added (Invitrogen, Cat. No. T3605). Cells were sorted on a FACS Aria Fusion 1 (BD Biosciences) (San Jose, USA) and the gating strategy is illustrated in **Figure S3**. The purity check control was performed using the CFP positive population since we did not have enough CFP negative cells for this purpose (**Figure S3**).

### **RNA Isolation, cDNA Synthesis and Real Time PCR (RT-qPCR)**

RNA was isolated using TRIzol LS reagent (Invitrogen, Cat. No. 10296010) according to the manufacturer's protocol. To help with the visualization of the pellet, GlycoBlue Coprecipitant (Invitrogen, Cat. No. AM9516) was used as described by the manufacturer's protocol. The amount and purity of isolated RNA was analyzed with Nanodrop DS11/DS-11+ Spectrophotometer (DeNovix, Wilmington, DE, USA). RNA was pre-treated with RNase free-Dnase (Promega, Cat. No. M6101) followed by cDNA synthesis with high-capacity cDNA Reverse Transcription kit (Applied Biosystems, Cat. No. 4368814, Waltham, MA, USA). Both reactions were performed according to the manufacturer's instructions. qPCR was performed with PowerUp SYBR Green Master Mix (ThermoFischer Scientific, Cat. No. A25777) in a QuantStudio Real-Time qPCR machine (ThermoFischer Scientific, Waltham, MA, USA) and PPIA and RPL38 were used as housekeeping genes to enable normalization. Primers were used at a 150 nmol/L concentration and sequences are annotated in Table S1. Thermal cycle conditions were as follows: 2 min at 50 °C, 2 min at 95 °C followed by 45 cycles consisting of denaturation for 15 s at 95 °C, annealing for 1 min at 60 °C, and extension for 1 min at 72 °C. PCR reactions were concluded with incubation for 10 min at 72 °C. RDML raw data was processed using RDML-Ninja (version 0\_9\_3, Amsterdam, The Netherlands) and LinReg software (version 2020, Amsterdam, The Netherlands) to determine the baselines and obtain the empirical primer efficiencies. qPCR fold changes between samples were obtained by  $\Delta\Delta C_t$  calculations and corrected by primer efficiencies. Average values from the two housekeeping genes were calculated, normalized to E-cad<sup>hi</sup> tumor cells, log<sub>2</sub> transformed and the average plotted. Statistical significance was calculated with GraphPad Prism (San Diego, CA, USA) package using one sample t-test, one-tailed.



## RNA Bulk Sequencing and Bioinformatics

Illumina TruSeq mRNA libraries were generated and sequenced with 65 base single reads on a HiSeq 2500 using V4 chemistry (Illumina Inc., San Diego, CA, USA) as previously described [37]. Reads were mapped to the genome with Hisat version 2.1.0. (Amsterdam, Netherlands) Read counts were determined with lcount based on the mouse reference genome GRCm38\_87. To correct for sequencing depth variability between samples, a DESeq median-of-ratios approach was implemented [38] followed by a log-transformation of the normalized counts. These corrections were necessary in order to obtain the normalized expression values. The singscore package [39] was used to determine the EMT scores based on the EcadLO signature of PyMT breast tumors [27]. Statistical significance of both scores to 0 was calculated with one-sample t-test. DESeq2 [38] was used for the differential expression analysis. Pathway analysis was conducted with GSEA preranked [40] by using as metric  $-\log_{10}(\text{FDR})$  divided by the sign of the  $\log_2\text{FoldChange}$  and the Hallmark gene sets as pathways [41]. Samples of the Beerling *et al.* [27] were downloaded from GEO number GSE77107. The reads were trimmed using Cutadapt [42] to remove any remaining adapter sequences and to filter reads shorter than 20 base pairs. The trimmed reads were aligned to the GRCm38 reference genome using STAR [43]. Quality control (QC) statistics from FastQC [44] and the above-mentioned tools were collected and summarized using MultiQC [45]. Gene expression counts were generated by featureCounts [46] using gene definitions from Ensembl GRCm38 version 100. Normalized expression values were obtained as described above. The entire analysis was implemented by Julian de Ruiter using Snakemake (snakemake version 5.19.2; wrapper version 0.63.0) (Amsterdam, Netherlands) [47] and is freely available on GitHub (<https://github.com/jrderuiter/snakemake-rnaseq>) (accessed on 4 June 2020).

## Immunofluorescence and Confocal Imaging

Brain samples were fixed overnight in 4% periodate-lysine/4% paraformaldehyde [48] at 4 °C. The next day, tissues were washed with PBS, incubated overnight in 30% sucrose and frozen in OCT. Per tumor, 2 consecutive sections of 5  $\mu\text{m}$  thickness were cut. After cutting, sections were hydrated twice with PBS for 15 min and mounted with anti-fading mounting medium (Vectashield, Vector laboratories (Cat. No. H-1000-10). Slides were imaged using inverted Leica TCS SP8 confocal microscope. H2B-Dendra2 was excited at 488 nm and collected at 495–545 nm. E-cad-mCFP signal was excited at 442 nm and collected at 454–479 nm with a line accumulation of 3. All images were acquired with a 25 $\times$ /0.95 NA water immersion objective.

## Immunohistochemistry

Brain samples were collected and fixed in formalin or EAF (ethanol/acetic acid/ formaldehyde/ saline at 40:5:10:45 v/v) and embedded in paraffin. Immunohistochemistry was performed

on 4  $\mu\text{m}$ -thick sections for E-cadherin antibody (Cell Signaling, Cat. No. 3195, 1:100) and KI67 antibody (Abcam, Cat. No. ab15580, 1:1000). Sections were imaged using an Aperio AT2 digital scanner with a 20 $\times$  objective and processed with Aperio ImageScope software (both from Leica Biosystems, Wetzlar, Germany).

### **Human Samples and Multiplex Immunohistochemistry**

All the human BCBM biospecimens were isolated at the Amsterdam UMC (location VUMC). Before the surgery of the brain tumors, patients at the A-UMC/VUMC are informed and have always had the opportunity to object to the use of their biospecimens. For all samples used in our study, patients did not object, and hence, they did therefore agree to the use of their biospecimens. This opt-out procedure is pursuant to the ethical rules and regulations of the Amsterdam UMC, location VUMC. Hence, the procedures comply both with international legislative and ethical standards. In the database of the Amsterdam UMC, location VUMC, 8 samples of brain resections with a metastasis of mammary carcinoma were selected. These were all invasive ductal carcinomas, not otherwise specified, with a different receptor status: 2 ER-positive, 2 HER2-positive, 2 triple negative and 1 unknown receptor status. Immunohistochemistry of the Formalin Fixed Paraffin Embedded (FFPE) tumor samples was performed on a Discovery Ultra automated stainer (Ventana Medical Systems). Briefly, paraffin sections were cut with a 3  $\mu\text{m}$  thickness, heated at 75  $^{\circ}\text{C}$  for 28 min and deparaffinized with an EZ prep solution (Ventana Medical Systems). Heat-induced antigen retrieval was carried out using Cell Conditioning 1 (CC1, Ventana Medical Systems) for 64 min at 95  $^{\circ}\text{C}$ . For the triple panel Zeb1 (DAB), Pankeratin (Yellow) and E-cadherin (Purple): Zeb1 was detected in the first sequence using clone E2G6Y (Cell Signaling, 1:200 dilution, 60 min at room temperature). Zeb1 bound antibody was visualized using Anti-Rabbit HQ (Ventana Medical systems) for 12 min at 37  $^{\circ}\text{C}$  followed by Anti-HQ HRP (Ventana Medical systems) for 12 min at 37  $^{\circ}\text{C}$ , followed by the ChromoMap DAB Detection kit (Ventana Medical Systems). In the second sequence of the triple staining procedure, Pankeratin was detected using clone AE1/AE3 (Abcam, 1:400 dilution, 60 min at 37  $^{\circ}\text{C}$ ) Pankeratin was visualized using Anti-Mouse NP (Ventana Medical systems, Oro Valley, AZ, USA) for 12 min at 37  $^{\circ}\text{C}$  followed by Anti-NP AP (Ventana Medical systems) for 12 min at 37  $^{\circ}\text{C}$ , followed by Discovery Yellow Detection Kit (Ventana Medical Systems). For the third sequence, E-cadherin was detected using clone NCH-38 (Agilent/DAKO, 1:50 dilution, 60 min at 37  $^{\circ}\text{C}$ ). Ecadherin was visualized using Anti-Mouse HQ (Ventana Medical systems) for 12 min at 37  $^{\circ}\text{C}$  followed by Anti-HQ HRP (Ventana Medical systems) for 12 min at 37  $^{\circ}\text{C}$ , followed by the Discovery Purple Detection Kit (Ventana Medical Systems). Slides were counterstained with Hematoxylin and Bluing Reagent (Ventana Medical Systems) and imaged with a 40 $\times$  magnification with a PANNORAMIC<sup>®</sup> 1000 scanner (3DHISTECH, Budapest, Hungary).

## REFERENCES

1. Kadankulam Syriac, A.; Nandu, N.S.; Leone, J.P. Central Nervous System Metastases from Triple-Negative Breast Cancer: Current Treatments and Future Prospective. *Breast Cancer* 2022, *14*, 1–13.
2. Garcia-Alvarez, A.; Papakonstantinou, A.; Oliveira, M. Brain Metastases in HER2-Positive Breast Cancer: Current and Novel Treatment Strategies. *Cancers* 2021, *13*, 2927.
3. Achrol, A.S.; Rennert, R.C.; Anders, C.; Soffiatti, R.; Ahluwalia, M.S.; Nayak, L.; Peters, S.; Arvold, N.D.; Harsh, G.R.; Steeg, P.S.; et al. Brain metastases. *Nat. Rev. Dis. Primers* 2019, *5*, 5.
4. Bowman, K.M.; Kumthekar, P. Medical management of brain metastases and leptomeningeal disease in patients with breast carcinoma. *Future Oncol.* 2018, *14*, 391–407.
5. Lin, N.U.; Bellon, J.R.; Winer, E.P. CNS metastases in breast cancer. *J. Clin. Oncol.* 2004, *22*, 3608–3617.
6. Mahajan, A.; Ahmed, S.; McAleer, M.F.; Weinberg, J.S.; Li, J.; Brown, P.; Settle, S.; Prabhu, S.S.; Lang, F.F.; Levine, N.; et al. Post-operative stereotactic radiosurgery versus observation for completely resected brain metastases: A single-centre, randomised, controlled, phase 3 trial. *Lancet Oncol.* 2017, *18*, 1040–1048.
7. Patchell, R.A.; Tibbs, P.A.; Regine, W.F.; Dempsey, R.J.; Mohiuddin, M.; Kryscio, R.J.; Markesbery, W.R.; Foon, K.A.; Young, B. Postoperative radiotherapy in the treatment of single metastases to the brain: A randomized trial. *JAMA* 1998, *280*, 1485–1489.
8. Van Rheeenen, J.; Scheele, C. Intravital microscopy to illuminate cell state plasticity during metastasis. *Curr. Opin. Cell Biol.* 2021, *72*, 28–35.
9. Margarido, A.S.; Bornes, L.; Vennin, C.; van Rheeenen, J. Cellular Plasticity during Metastasis: New Insights Provided by Intravital Microscopy. *Cold Spring Harb. Perspect. Med.* 2020, *10*, a037267.
10. Chitty, J.L.; Filipe, E.C.; Lucas, M.C.; Herrmann, D.; Cox, T.R.; Timpson, P. Recent advances in understanding the complexities of metastasis. *F1000Res* 2018, *7*: 1169. <https://doi.org/10.12688/f1000research.15064.2>.
11. Van Helvert, S.; Storm, C.; Friedl, P. Mechanoreciprocity in cell migration. *Nat. Cell Biol.* 2018, *20*, 8–20.
12. Cheung, K.J.; Ewald, A.J. Illuminating breast cancer invasion: Diverse roles for cell-cell interactions. *Curr. Opin. Cell Biol.* 2014, *30*, 99–111.
13. Condeelis, J.; Segall, J.E. Intravital imaging of cell movement in tumours. *Nat. Rev. Cancer* 2003, *3*, 921–930.
14. Bornes, L.; Belthier, G.; van Rheeenen, J. Epithelial-to-Mesenchymal Transition in the Light of Plasticity and Hybrid E/M States. *J. Clin. Med.* 2021, *10*, 2403.
15. Luond, F.; Tiede, S.; Christofori, G. Breast cancer as an example of tumour heterogeneity and tumour cell plasticity during malignant progression. *Br. J. Cancer* 2021, *125*, 164–175.
16. Bhatia, S.; Wang, P.; Toh, A.; Thompson, E.W. New Insights Into the Role of Phenotypic Plasticity and EMT in Driving Cancer Progression. *Front. Mol. Biosci.* 2020, *7*, 71.
17. Li, Y.; Lv, Z.; Zhang, S.; Wang, Z.; He, L.; Tang, M.; Pu, W.; Zhao, H.; Zhang, Z.; Shi, Q.; Genetic Fate Mapping of Transient Cell Fate Reveals N-Cadherin Activity and Function in Tumor Metastasis. *Dev. Cell* 2020, *54*, 593–607.e5.
18. Dongre, A.; Weinberg, R.A. New insights into the mechanisms of epithelial-mesenchymal transition and implications for cancer. *Nat. Rev. Mol. Cell Biol.* 2019, *20*, 69–84.
19. Pastushenko, I.; Blanpain, C. EMT Transition States during Tumor Progression and Metastasis. *Trends Cell Biol.* 2019, *29*, 212–226.
20. Diepenbruck, M.; Christofori, G. Epithelial-mesenchymal transition (EMT) and metastasis: Yes, no, maybe? *Curr. Opin. Cell Biol.* 2016, *43*, 7–13.
21. Nieto, M.A.; Huang, R.Y.; Jackson, R.A.; Thiery, J.P. EMT: 2016. *Cell* 2016, *166*, 21–45.

22. Hanahan, D.; Weinberg, R.A. Hallmarks of cancer: The next generation. *Cell* 2011, *144*, 646–674.
23. Nieto, M.A. Epithelial plasticity: A common theme in embryonic and cancer cells. *Science* 2013, *342*, 1234850.
24. Ocana, O.H.; Corcoles, R.; Fabra, A.; Moreno-Bueno, G.; Acloque, H.; Vega, S.; Barrallo-Gimeno, A.; Cano, A.; Nieto, M.A. Metastatic colonization requires the repression of the epithelial-mesenchymal transition inducer Prx1. *Cancer Cell* 2012, *22*, 709–724.
25. Luond, F.; Sugiyama, N.; Bill, R.; Bornes, L.; Hager, C.; Tang, F.; Santacrose, N.; Beisel, C.; Ivanek, R.; Burglin, T.; et al. Distinct contributions of partial and full EMT to breast cancer malignancy. *Dev. Cell* 2021, *56*, 3203–3221 e11.
26. Bornes, L.; van Scheppingen, R.H.; Beerling, E.; Schelfhorst, T.; Ellenbroek, S.I.J.; Seinstra, D.; van Rheenen, J. Fsp1-Mediated Lineage Tracing Fails to Detect the Majority of Disseminating Cells Undergoing EMT. *Cell Rep.* 2019, *29*, 2565–2569.e3.
27. Beerling, E.; Seinstra, D.; de Wit, E.; Kester, L.; van der Velden, D.; Maynard, C.; Schafer, R.; van Diest, P.; Voest, E.; van Oudenaarden, A.; et al. Plasticity between Epithelial and Mesenchymal States Unlinks EMT from Metastasis-Enhancing Stem Cell Capacity. *Cell Rep.* 2016, *14*, 2281–2288.
28. Erami, Z.; Herrmann, D.; Warren, S.C.; Nobis, M.; McGhee, E.J.; Lucas, M.C.; Leung, W.; Reischmann, N.; Mrowinska, A.; Schwarz, J.P.; et al. Intravital FRAP Imaging using an E-cadherin-GFP Mouse Reveals Disease- and Drug-Dependent Dynamic Regulation of Cell-Cell Junctions in Live Tissue. *Cell Rep.* 2016, *14*, 152–167.
29. Krebs, A.M.; Mitschke, J.; Lasierra Losada, M.; Schmalhofer, O.; Boerries, M.; Busch, H.; Boettcher, M.; Mougialakos, D.; Reichardt, W.; Bronsert, P.; et al. The EMT-activator Zeb1 is a key factor for cell plasticity and promotes metastasis in pancreatic cancer. *Nat. Cell Biol.* 2017, *19*, 518–529.
30. Ye, X.; Tam, W.L.; Shibue, T.; Kaygusuz, Y.; Reinhardt, F.; Ng Eaton, E.; Weinberg, R.A. Distinct EMT programs control normal mammary stem cells and tumour-initiating cells. *Nature* 2015, *525*, 256–260.
31. Tsai, J.H.; Donaher, J.L.; Murphy, D.A.; Chau, S.; Yang, J. Spatiotemporal regulation of epithelial-mesenchymal transition is essential for squamous cell carcinoma metastasis. *Cancer Cell* 2012, *22*, 725–736.
32. Mani, S.A.; Guo, W.; Liao, M.J.; Eaton, E.N.; Ayyanan, A.; Zhou, A.Y.; Brooks, M.; Reinhard, F.; Zhang, C.C.; Shipitsin, M.; et al. The epithelial-mesenchymal transition generates cells with properties of stem cells. *Cell* 2008, *133*, 704–715.
33. Yang, J.; Mani, S.A.; Donaher, J.L.; Ramaswamy, S.; Itzykson, R.A.; Come, C.; Savagner, P.; Gitelman, I.; Richardson, A.; Weinberg, R.A. Twist, a master regulator of morphogenesis, plays an essential role in tumor metastasis. *Cell* 2004, *117*, 927–939.
34. Cano, A.; Perez-Moreno, M.A.; Rodrigo, I.; Locascio, A.; Blanco, M.J.; del Barrio, M.G.; Portillo, F.; Nieto, M.A. The transcription factor snail controls epithelial-mesenchymal transitions by repressing E-cadherin expression. *Nat. Cell Biol.* 2000, *2*, 76–83.
35. Follenzi, A.; Ailles, L.E.; Bakovic, S.; Geuna, M.; Naldini, L. Gene transfer by lentiviral vectors is limited by nuclear translocation and rescued by HIV-1 pol sequences. *Nat. Genet.* 2000, *25*, 217–222.
36. Alieva, M.; Ritsma, L.; Giedt, R.J.; Weissleder, R.; van Rheenen, J. Imaging windows for long-term intravital imaging: General overview and technical insights. *Intravital* 2014, *3*, e29917.
37. Henneman, L.; van Miltenburg, M.H.; Michalak, E.M.; Braumuller, T.M.; Jaspers, J.E.; Drenth, A.P.; de Korte-Grimmerink, R.; Gogola, E.; Szuhai, K.; Schlicker, A.; et al. Selective resistance to the PARP inhibitor olaparib in a mouse model for BRCA1-deficient metaplastic breast cancer. *Proc. Natl. Acad. Sci. USA* 2015, *112*, 8409–8414.
38. Anders, S. and W. Huber, Differential expression analysis for sequence count data. *Genome Biol.* 2010, *11*, R106.
39. Foroutan, M.; Bhuvu, D.D.; Lyu, R.; Horan, K.; Cursons, J.; Davis, M.J. Single sample scoring of molecular phenotypes. *BMC Bioinform.* 2018, *19*, 404.

40. Subramanian, A.; Tamayo, P.; Mootha, V.K.; Mukherjee, S.; Ebert, B.L.; Gillette, M.A.; Paulovich, A.; Pomeroy, S.L.; Golub, T.R.; Lander, E.S.; et al. Gene set enrichment analysis: A knowledge-based approach for interpreting genome-wide expression profiles. *Proc. Natl. Acad. Sci. USA* 2005, *102*, 15545–15550.
41. Liberzon, A.; Birger, C.; Thorvaldsdottir, H.; Ghandi, M.; Mesirov, J.P.; Tamayo, P. The Molecular Signatures Database (MSigDB) hallmark gene set collection. *Cell Syst.* 2015, *1*, 417–425.
42. Martin, M. Cutadapt removes adapter sequences from high-throughput sequencing reads. *EMBnet J.* 2011, *17*, 10–12. <https://doi.org/10.14806/ej.17.1.200>.
43. Dobin, A.; Davis, C.A.; Schlesinger, F.; Drenkow, J.; Zaleski, C.; Jha, S.; Batut, P.; Chaisson, M.; Gingeras, T.R. STAR: Ultrafast universal RNA-seq aligner. *Bioinformatics* 2013, *29*, 15–21.
44. Andrews, S. *FastQC: A Quality Control Tool for High Throughput Sequence Data*; GitHub Babraham Bioinformatics, 2010.
45. Ewels, P.; Magnusson, M.; Lundin, S.; Kaller, M. MultiQC: Summarize analysis results for multiple tools and samples in a single report. *Bioinformatics* 2016, *32*, 3047–3048.
46. Liao, Y.; Smyth, G.K.; Shi, W. featureCounts: An efficient general purpose program for assigning sequence reads to genomic features. *Bioinformatics* 2014, *30*, 923–930.
47. Koster, J.; Rahmann, S. Snakemake—A scalable bioinformatics workflow engine. *Bioinformatics* 2012, *28*, 2520–2522.
48. McLean, I.W.; Nakane, P.K. Periodate-lysine-paraformaldehyde fixative. A new fixation for immunoelectron microscopy. *J. Histochem. Cytochem.* 1974, *22*, 1077–1083.
49. Dankner, M.; Caron, M.; Al-Saadi, T.; Yu, W.; Ouellet, V.; Ezzeddine, R.; Maritan, S.M.; Annis, M.G.; Le, P.U.; Nadaf, J.; et al. Invasive growth associated with Cold-Inducible RNA-Binding Protein expression drives recurrence of surgically resected brain metastases. *Neuro Oncol.* 2021, *23*, 1470–1480.
50. de Gooijer, M.C.; Guillen Navarro, M.; Bernardis, R.; Wurdinger, T.; van Tellingen, O. An Experimenter’s Guide to Glioblastoma Invasion Pathways. *Trends Mol. Med.* 2018, *24*, 763–780.
51. Siam, L.; Bleckmann, A.; Chaung, H.N.; Mohr, A.; Klemm, F.; Barrantes-Freer, A.; Blazquez, R.; Wolff, H.A.; Luke, F.; Rohde, V.; et al. The metastatic infiltration at the metastasis/brain parenchyma-interface is very heterogeneous and has a significant impact on survival in a prospective study. *Oncotarget* 2015, *6*, 29254–29267.
52. Wang, W.; Wyckoff, J.B.; Goswami, S.; Wang, Y.; Sidani, M.; Segall, J.E.; Condeelis, J.S. Coordinated regulation of pathways for enhanced cell motility and chemotaxis is conserved in rat and mouse mammary tumors. *Cancer Res.* 2007, *67*, 3505–3511.
53. Yamaguchi, H. and J. Condeelis, Regulation of the actin cytoskeleton in cancer cell migration and invasion. *Biochim. Biophys. Acta* 2007, *1773*, 642–652.
54. Welch, M.D.; DePace, A.H.; Verma, S.; Iwamatsu, A.; Mitchison, T.J. The human Arp2/3 complex is composed of evolutionarily conserved subunits and is localized to cellular regions of dynamic actin filament assembly. *J. Cell Biol.* 1997, *138*, 375–384.
55. Frentzas, S.; Simoneau, E.; Bridgeman, V.L.; Vermeulen, P.B.; Foo, S.; Kostaras, E.; Nathan, M.; Wotherspoon, A.; Gao, Z.H.; Shi, Y.; et al. Vessel co-option mediates resistance to anti-angiogenic therapy in liver metastases. *Nat. Med.* 2016, *22*, 1294–1302.
56. Nagaishi, M.; Nakata, S.; Ono, Y.; Hirata, K.; Tanaka, Y.; Suzuki, K.; Yokoo, H.; Hyodo, A. Tumoral and stromal expression of Slug, ZEB1, and ZEB2 in brain metastasis. *J. Clin. Neurosci.* 2017, *46*, 124–128.
57. Euskirchen, P.; Radke, J.; Schmidt, M.S.; Schulze Heuling, E.; Kadikowski, E.; Maricos, M.; Knab, F.; Grittner, U.; Zerbe, N.; Czabanka, M.; et al. Cellular heterogeneity contributes to subtype-specific expression of ZEB1 in human glioblastoma. *PLoS ONE* 2017, *12*, e0185376.

58. Qiao, L.; Chen, Y.; Liang, N.; Xie, J.; Deng, G.; Chen, F.; Wang, X.; Liu, F.; Li, Y.; Zhang, J. Targeting Epithelial-to-Mesenchymal Transition in Radioresistance: Crosslinked Mechanisms and Strategies. *Front. Oncol.* 2022, *12*, 775238.
59. Dudas, J.; Ladanyi, A.; Ingruber, J.; Steinbichler, T.B.; Riechelmann, H. Epithelial to Mesenchymal Transition: A Mechanism that Fuels Cancer Radio/Chemoresistance. *Cells* 2020, *9*, 428.
60. Marie-Egyptienne, D.T.; Lohse, I.; Hill, R.P. Cancer stem cells, the epithelial to mesenchymal transition (EMT) and radioresistance: Potential role of hypoxia. *Cancer Lett.* 2013, *341*, 63–72.
61. Jolly, M.K.; Somarelli, J.A.; Sheth, M.; Biddle, A.; Tripathi, S.C.; Armstrong, A.J.; Hanash, S.M.; Bapat, S.A.; Rangarajan, A.; Levine, H. Hybrid epithelial/mesenchymal phenotypes promote metastasis and therapy resistance across carcinomas. *Pharmacol. Ther.* 2019, *194*, 161–184.
62. Kroger, C.; Afeyan, A.; Mraz, J.; Eaton, E.N.; Reinhardt, F.; Khodor, Y.L.; Thiru, P.; Bieri, B.; Ye, X.; Burge, C.B.; et al. Acquisition of a hybrid E/M state is essential for tumorigenicity of basal breast cancer cells. *Proc. Natl. Acad. Sci. USA* 2019, *116*, 7353–7362.

## SUPPLEMENTARY FILES

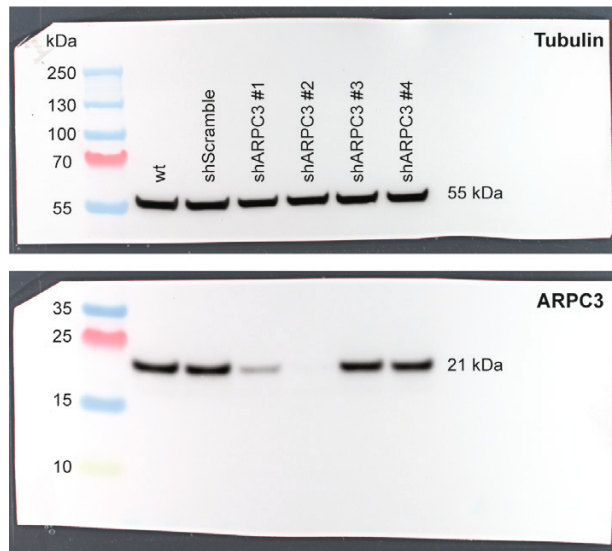


**Figure S1. Western blot analysis of ARPC3 knockdown in BCMB organoids.** Uncropped Western blot showing ARPC3 expression in BCMB organoids engineered with all ARPC3 shRNA's. Tubulin was used as a loading control.

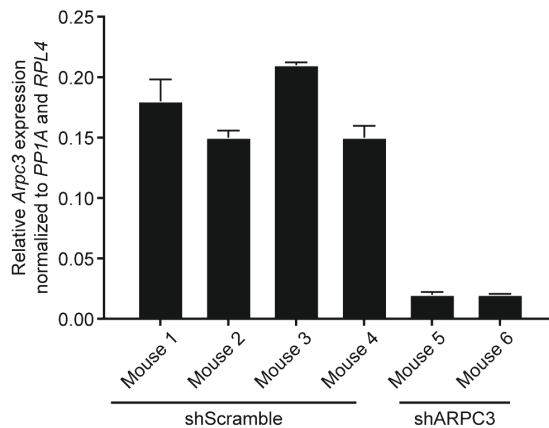


**Figure S2. ARPC3 knockdown validation by RT-qPCR in recurrent tumors.** Relative Arpc3 expression in recurrent tumors in mice injected with BCMB organoids engineered with either the shARPC3 or shScramble constructs. Data are presented as mean  $\pm$  SD.  $n = 1$  mouse with 3 technical replicates.

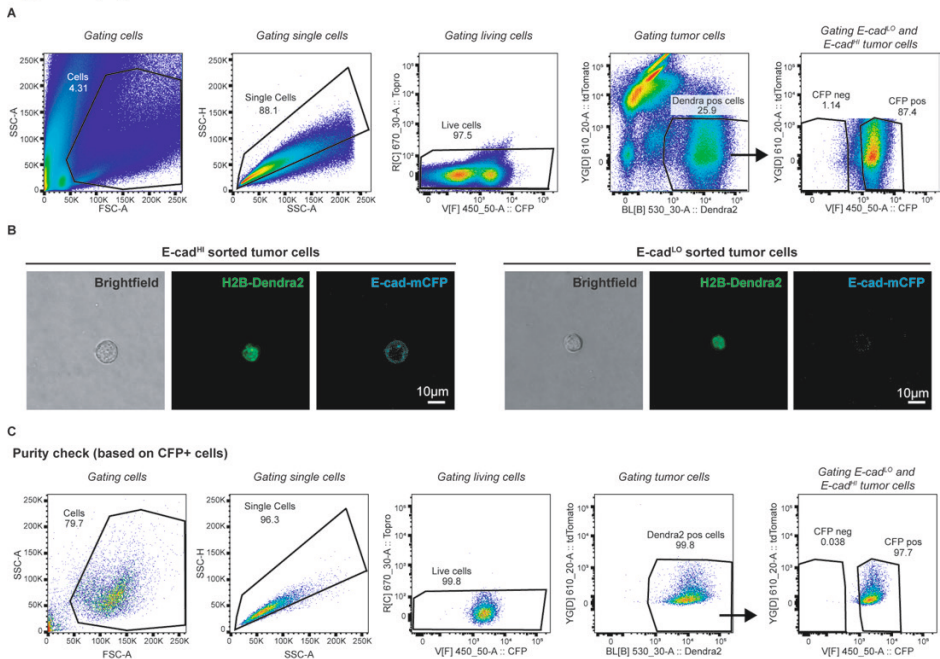


**Figure S3. Gating strategy of BCBM tumors FACS.** (A) Gating strategy applied to BCBM tumors to sort Ecad<sup>hi</sup> and Ecad<sup>Lo</sup> tumor cells. (B) Representative images of Ecad<sup>hi</sup> and Ecad<sup>Lo</sup> sorted tumor cells. (C) Gating strategy to analyze the purity of our FACS strategy. Due to the limited amount of Ecad<sup>Lo</sup> cells that we could obtain for this experiment, we performed the purity control using the Ecad<sup>hi</sup> tumor cells.



**Table S1. Primer sequences.**

<b>Primer</b>	<b>Sequence</b>
<i>RPL38_F</i>	5'-AGGATGCCAAGTCTGTCAAGA-3'
<i>RPL38_R</i>	5'-TCCTTGCTGTGATAACCAGGG-3'
<i>PPIA_F</i>	5'-GTTTCATGCCTTCTTTACCTTCCC-3'
<i>PPIA_R</i>	5'-CAAATGCTGGACCAAAACACAAACG-3'
<i>Vim-F</i>	5'-TGGTACAAGTCCAAGTTTGC-3'
<i>Vim-R</i>	5'-GTGAGTGACTGCACCTGTCT-3'
<i>Snai1-F</i>	5'-TTGTAAACAAGGAGTACCTCAGC-3'
<i>Snai1-R</i>	5'-GAGAATGGCTTCTCACCAGTG-3'
<i>Zeb1-F</i>	5'-GCTGGCAAGACAACGTGAAAG-3'
<i>Zeb1-R</i>	5'-GCCTCAGGATAAATGACGGC-3'
<i>Cdh1-F</i>	5'-CAGGTCTCCTCATGGCTTTC-3'
<i>Cdh1-R</i>	5'-CTTCCGAAAAGAAGGCTGTCC-3'
<i>Cdh2-F</i>	5'-AGCGCAGTCTTACCGAAGG-3'
<i>Cdh2-R</i>	5'-TCGCTGCTTTCATACTGAACCTT-3'
<i>Fn1-F</i>	5'-AGAGCAAGCCTGAGCCTGA-3'
<i>Fn1-R</i>	5'-GTCCCAGATCATGGAATCTT-3'
<i>Zeb2-F</i>	5'-ATTGCACATCAGACTTTGAGGAA-3'
<i>Zeb2-R</i>	5'-GAGTTCCAGGTGGCAGGTCAT-3'
<i>Arpc3-F</i>	5'-GGACACCGTCAAGATGCCG-3'
<i>Arpc3-R</i>	5'-GCCTTGAAGTAGTAGATGGCTT-3'



# Chapter 6

General discussion



The brain is the central organ of the CNS, controls most of our body functions and is therefore highly protected; mechanically by the skull and chemically by the BBB that selectively separates the brain from the blood circulation. When malignant neoplasms develop and grow in the brain, they are a significant threat to the overall functioning of the body, often leading to severe consequences.

Glioma is one of the most common and most malignant type of brain tumors [1]. The primary factors contributing to early relapse in cases of glioblastoma are the resistance of the tumor to radiotherapy and chemotherapy, and more important the incomplete surgical removal caused by the diffuse invasion of individual cells [2].

Another type of malignancies in the CNS, which also results in a significant rate of morbidity and mortality are brain metastases. They are observed in 15 to 40% of all metastatic cancer patients [3]. The primary cancers that most frequently metastasize to the brain are lung, breast, melanoma, and colorectal, accounting for ~45%, ~15%, ~10%, and ~5% of brain metastases, respectively [4]. Additionally, autopsy studies have revealed that 10% of breast cancer patients with stage 4 disease have developed brain metastases that were not clinically apparent yet [5, 6]. In the recent years there has been an increase in the incidence of brain metastases, possibly due to improved treatment regimens resulting in prolonged patient survival or greater detection of brain lesions through advanced imaging techniques. On average, the time between the initial diagnosis of the primary cancer and the development of CNS metastasis ranges from 2 to 3 years [7]. Systemic chemotherapy after diagnosis of brain metastasis was reported to be associated with prolonged survival. However, the prognosis of brain metastasis of breast cancer is very poor; median survival is 2.3 - 7.1 months [8, 9]. Therefore, there is an urgent need to understand the specific properties of the tumor and the unique microenvironment of the CNS. Hence, we need more systematic pre-clinical testing and optimization of therapeutic regimens to improve the outcome of patients.

This thesis emphasizes the significance of brain tumors and the challenges associated with tumor recurrence and current treatment approaches. It stresses the need for innovative therapies and provide new avenues to improve patient outcomes. I started by making use of the mouse models we generated in the laboratory to study the mechanism of intrinsic chemoresistance in brain metastasis. Tumor cells overexpress the breast cancer resistance protein (BCRP) as an adaptive response, leading to therapy resistance (chapter 2). In the following chapter, a novel treatment combination for managing brain metastases is proposed, involving immune checkpoint inhibition. Modulating the brain microenvironment using doxorubicin-induced senescence recruits cytotoxic T cells expressing PD1. Immune checkpoint blockade after doxorubicin treatment significantly improves mouse survival. This suggests the potential of immune checkpoint inhibitors specifically for brain metastases and may help the development of better therapeutic strategies (chapter 3). In the last two chapters I focused on one of the main problems in brain tumors: their invasive nature,

which correlates strongly with the elevated risk of tumor recurrence. In chapter 4, I explored the importance of GFAP-isoforms in glioma invasion and tumor dynamics using intravital microscopy. Understanding the mechanisms driving invasive behaviors of specific GFAP-positive populations can lead to more effective invasion-targeting therapies. Lastly, in Chapter 5 I investigate brain metastasis behavior without treatment through intravital microscopy. EMT is identified as a crucial driver of local invasion. Knocking down ARPC3, which affects the migration of mesenchymal tumor cells, reduces tumor recurrence.

## **LESSON LEARNED: WE NEED GOOD PRE-CLINICAL MODELS OF BCBM**

The increasing prevalence of brain metastases in clinical practice has gained significant attention for this fatal disease. In recent years, numerous researchers, both in the field of basic and clinical research, have dedicated their efforts to develop various preclinical models with the aim of gaining fundamental knowledge on this disease which will help to develop and improve therapeutic approaches. Metastasis is a complex process involving multiple steps like invasion, circulation survival, and adaptation to new environments. This process is notably inefficient, with most cells failing at different stages. Even at the final step of organ colonization, successful metastatic cells may constitute only 1 in 100 of those that completed brain extravasation [10]. The brain microenvironment is unique, featuring tissue-resident cells (microglia, oligodendrocytes, astrocytes, and neurons), distinct metabolic characteristics, and a protective BBB which selectively regulates the entry of substances from the bloodstream, including potential treatments [11]. To understand and find therapies for CNS metastasis, accurate preclinical models mimicking this complexity are crucial, although no single model can cover all the unanswered questions.

Historically, the study of BCBM faced challenges due to the complexity of replicating the unique microenvironment of the brain and the metastatic process in a laboratory setting. Early efforts primarily relied on *in vitro* models, which, while useful for studying basic cancer cell biology, fell short in mimicking the complex interactions between cancer cells and the brain microenvironment. The development of *in vivo* models, particularly mouse models, marked a significant advancement in the field.

Mouse models have been pivotal in studying the metastatic processes of BCBM, effectively replicating human tumor microenvironments and interactions [10, 12]. Techniques like the orthotopic or intracardiac injection of human or mouse cancer cells into mice have provided critical insights into metastatic progression, brain colonization mechanisms, and the interactions between cancer cells and brain, including the roles of the BBB and tumor microenvironment [13, 14]. Some of these models, include the B16 melanoma, MDA-MB-231-BR breast cancer, and modified Lewis Lung Carcinoma models.

Genetically engineered mouse models (GEMMs) have offered deeper insights into BCBM by allowing the study of specific genetic alterations in breast cancer and their role in brain metastasis. They have shed light on genetic drivers of metastasis and the roles of tumor suppressor genes and oncogenes [15, 16]. Furthermore, syngeneic models, where mouse cancer cells are injected into inbred recipient mice, and xenograft models, particularly patient-derived xenografts (PDX), have provided invaluable insights. While syngeneic models maintain an intact immune system, crucial for studies on tumor microenvironment interactions and immunotherapy responses, PDX models are essential for studying human-specific processes, despite their challenges in establishment and maintenance.

Traditionally, widely used BCBM models involved immortalized cell lines like MDA-MB-231BR and MDA-MB-231BR-HER2+ as mentioned above, administered to mice via intracardiac injections. However, these models present significant challenges, such as extensive passaging, clonal selections potentially causing genetic bottlenecks, limited tumor heterogeneity, and derivation from other sites than the brain, limiting their translational research potential. As a result, in this thesis, we report the development of three new syngeneic BCBM models derived from MMTV-PyMT, MMTV-Neu, and K14Cre, Brca1fl/fl, p53fl/fl (KB1P) mouse models. Derived directly from primary tumors without in vitro manipulation, these models offer a controlled environment for investigating tumor cells, immune system interactions, and the brain microenvironment. They provide a more accurate simulation of disease progression and treatment response, crucial elements often lacking in existing models. Additionally, features such as endogenous E-cadherin fluorescence in our PyMT and Neu models, combined with intravital microscopy, allow for a deeper understanding of tumor cell behavior, including the roles of epithelial or mesenchymal cells in brain invasion (Chapter 5).

Another important consideration is that the majority of BCBM models were generated using 2D lines instead of 3D. Organoids, in contrast to 2D cell lines, closely recapitulate the genetic and morphological heterogeneity observed on the tumor cells of the primary tumor [17] as well as tissue architecture and spatial complexity present in the in vivo microenvironment. Furthermore, brain tissue is softer than tissue culture plastics on the GPa scale, making them unsuitable for studying brain tissue [18-20]. Therefore, organoids are a step in between cell lines and mice. Despite their higher cost, lower tumor intake and more difficult to genetically engineer, organoids are considered more reliable than 2D cell lines due to their ability to retain the complex intra-tumor heterogeneity.

In summary, each model has its advantages and disadvantages, and the selection should be based on the research question.

## UNDERSTANDING CHEMORESISTANCE: A BARRIER TO EFFECTIVE CANCER TREATMENT

While studying the response to chemotherapies in our BCBM models (chapter 2), we came across with one of the main problems of this deadly disease: Chemoresistance, which refers to the ability of cancer cells to become resistant to the effects of chemotherapy drugs, leading to treatment failure and disease progression. Conventional therapies for BCBMs have been largely ineffective because of chemoresistance and impermeability of the BBB.

While analyzing the permeability of drugs through the BBB, which is influenced by factors such as drug solubility, plasma protein binding ratio, molecular weight, and the presence of ABC transporters, it became evident that conventional drugs like paclitaxel, docetaxel, and etoposide struggle to reach effective concentrations in brain tissue. However, clinical studies have indicated the effectiveness of other agents, like capecitabine, 5-fluorouracil, and platinum analogues [21-23], which suggest alternative pathways to drug delivery in brain tissue. My work, particularly with doxorubicin—a commonly used drug to treat breast cancer—showed that the lack of response in chemo-naïve BCBM was not solitary due to a lack of drug penetration but appeared to be pumped out by cancer cells upon expression of a drug export pump (chapter 2, figure 1 and 2). This was a key finding, as it directed the focus towards intrinsic factors of resistance.

I hypothesized that this resistance is connected to intrinsic factors, as indicated by the expression of p-gp and BCRP in the vasculature (chapter 2, figure 1). Intrinsic factors, in this context, refer to the inherent properties within the cancer cells themselves that contribute to their resistance against chemotherapeutic drugs. The observation that BCBM cells, despite being highly proliferative and typically more responsive to chemotherapies that induce DNA damage, were not responding to treatments, was contrary to expectations. This led to the finding of increased expression of BCRP in BCBM cells, both *in vivo* and *in vitro*, suggesting a mechanism of intrinsic resistance to BCRP-specific chemotherapy drugs.

Upregulation of ABC transporters upon drug exposure has been thoroughly investigated [24]. This phenomenon is particularly significant in the context of brain metastases, where tumor cells have typically encountered drugs prior to their late occurrence. There have been several attempts to increase the drug penetrability by inhibiting the ABC transporters present in the BBB but they have failed in the human setting [25-27]. Several factors could contribute to the explanation of these disappointing results. These factors include: the absence of target expression in patient tumors, unreliable tools for detecting ABC transporter expression, redundancy among ABC transporters, the necessity of dose reduction for cytotoxic agents due to the protective function of ABC transporters when inhibited in normal tissues, the use of chemotherapy cocktails containing drugs with low affinity for the targeted transporter, the inclusion of tumors where ATP-dependent drug efflux is not a significant mechanism of resistance, or a combination of these factors. Even



though the results of these clinical trials were not very successful potentially due to the factors mentioned above, I support the idea of assessing the BCRP and P-gp expression prior to initiating treatment. If their expression levels are high, the additional use of inhibitors of export pumps should be taken into consideration, as suggested by the preclinical studies. This approach has the potential to not only enhance the response to treatment by overcoming resistance but could also significantly reduce tumor size. Ultimately, this could increase the likelihood of these patients becoming eligible for surgery, potentially leading towards a curative outcome.

Moreover, in chapter 2, we present evidence that this upregulation of ABC transporters can occur even without drug exposure. Two primary hypotheses could explain the enrichment of BCRP in the brain. The first hypothesis is around the concept of positive selection. Here, we postulate that cells expressing BCRP might gain a survival advantage in the brain's unique microenvironment. This advantage could be attributed to BCRP's ability to actively efflux a variety of substances, including potential toxins and chemotherapeutic agents, thus enhancing the survival and proliferation of these cells in the brain. Concurrently, we also observe that the impact of BCRP on chemoresistance extends beyond its well-known efflux capabilities. BCRP appears to interact with other molecular pathways within the tumor microenvironment, significantly affecting tumor behavior and response to treatment. For instance, hypoxia, a prevalent condition in rapidly growing tumors, has been identified as a key factor inducing the expression of BCRP. The research of Comerford *et al.* [28] and Krishnamurthy *et al.* [29] highlights this relationship, demonstrating how hypoxia can lead to increased BCRP expression and consequently, enhanced resistance to chemotherapy. Moreover, the work of Ee, Pui Lai Rachel and colleagues [30] demonstrated that estrogens could stimulate the production of BCRP in hormone-responsive tumors. This is crucial, considering the hormone receptor status, including estrogen receptors, can change between primary tumors and brain metastases. Therefore, using antiestrogens could potentially reduce drug resistance in these tumors. Alternatively, it could be an adaptation of tumor cells to the brain, driven by genetic or epigenetic changes. The exact mechanisms leading to BCRP enrichment in the brain remain a subject of ongoing research. Consequently, it is essential to consider this supplementary barrier, beyond the BBB, when assessing the penetration of drugs into brain tumors. As novel approaches are being explored to facilitate the transportation of chemotherapeutic agents like doxorubicin across the BBB and BTB (for instance in clinical trials NCT01818713, NCT03387917 or NCT02536183), it becomes evident that overcoming intrinsic resistance to these compounds is another critical obstacle for achieving successful therapeutic outcomes. Promisingly, several studies have utilized PET tracers to evaluate the effectiveness of ABC transporter inhibitors in enhancing drug delivery to the brain [31, 32]. These findings indicate that alongside targeting the BBB and BTB, directing interventions towards ABC transporters in tumor cells could potentially bring positive outcomes in improving chemotherapy responses.

All these observed discrepancies raise questions about the underlying factors contributing to chemoresistance in BCBM. The high proliferation rate of BCBM cells, and the competition with neurons often resulting in hypoxic regions within the tumor [33], may induce a phenomenon called vascular mimicry [34]. Vascular mimicry involves tumor cells creating their pseudo-vasculature to ensure a continuous nutrient and oxygen supply. Hypoxia, which is common in rapidly growing tumors, has been shown to promote the upregulation of ABC transporters such as BCRP in ovarian tumors[29], further limiting drug effectiveness.

To address these challenges, personalized medicine approaches that consider individual BCRP expression levels may be essential. Profiling a patient's tumor biology, including BCRP expression, can guide more effective treatment strategies. Targeting ABC transporters, in addition to improving drug penetrability across the BBB, holds potential for enhancing chemotherapy responses in BCBM. Although these findings are encouraging, their practical implementation in clinical settings is essential for the effective benefit of patients. This is particularly important given the evident prominence of BCRP-mediated chemoresistance in murine models of BCBM, which shows BCRP's substantial role in contributing to chemoresistance. However, it's crucial to recognize that while mouse studies are invaluable, the translation of these findings to the human context warrants further investigation. One critical consideration is that BCRP expression and function may differ between mice and humans. In 2011, the group of Prof. Tesaraki used a quantitative proteomic approach to identify and quantify carriers and receptors of brain capillary endothelial cells from both human and mice, revealing differences in expression patterns [35]. Notably, the efflux transporter BCRP was essentially similar, even if slightly higher expressed in humans [35], whereas P-gp showed greater expression in mice [35, 36]. Therefore, thorough research is necessary ensure that the promising discoveries made in murine models can be successfully applied to human patients.

## **THE ROLE OF IFS AND EMT IN INVASION AND TUMOR RECURRENCE**

Tumor invasion and recurrence are critical factors that contribute to the progression and poor prognosis of cancer. The understanding of the underlying mechanisms involved in these processes is crucial for the development of effective therapeutic strategies.

Glioma cells tend to infiltrate the brain parenchyma being very difficult to resect and as a consequence there is a high chance of tumor recurrence. In the past years, there has been increasing attention for the role of IFs in cell invasion since cancer progression is frequently accompanied by alterations in its expression patterns, specifically linked to phenotypes that promote increased cellular migration and invasion. While vimentin is widely

recognized as the primary enhancer of migration [37-40], it is worth noting that another type III IF protein expressed in glioma cells, called glial fibrillary acid protein (GFAP), has also been implicated in tumor migration [41, 42]. In chapter 4 we showed that manipulating the GFAP network significantly impacts the motility of glioma cells and influences tumor growth patterns. Depletion of GFAP $\delta$  leads to the formation of denser tumors with increased motility, characterized by random migration. On the other hand, GFAP $\alpha$  knockout results in a more diffuse growth pattern and promotes persistent migration towards the brain parenchyma. This aspect of cell migration is a key determinant in the efficiency of metastatic spread and is often linked to poor prognosis in various cancers [43].

The findings in Chapter 4 increase our understanding of how alterations in the GFAP $\delta/\alpha$  ratio can impact the aggressiveness of grade IV gliomas. Previous studies and analysis of the updated TCGA database (chapter 4, Fig. 1a) have consistently reported an increased dominance of GFAP $\delta$  in grade IV glioma tumors [44]. Glioma tumors display significant heterogeneity, not only between patients but also within individual cells within a tumor [45]. Therefore, it is likely that a grade IV tumor comprises a mixture of cells with different GFAP $\delta/\alpha$  ratios, and these distinct cell populations may contribute to different behaviors. It can be hypothesized that a larger population of cells with a high GFAP $\delta/\alpha$  ratio in grade IV tumors contributes to the infiltration of the brain parenchyma and subsequent relapse following therapy. Therefore, it would potentially be beneficial to do regular assessments of the immunohistochemical expression of GFAP in patients. Our study suggest that it may be beneficial to closely monitor after the initial surgery procedure the increased GFAP $\delta$  expression observed in glioblastoma samples. This may enable us to categorize these patients as high-risk for early recurrence and subject them to regular neuroimaging investigations during follow-ups. However, clinical studies are required to establish whether determination of GFAP $\delta$  expression can be used for making such clinical beneficial decisions. Given that a high GFAP $\delta/\alpha$  ratio correlates with the expression of high-malignant genes and migratory dynamics of glioma cells [44], novel therapies may need to balance the ratio between GFAP $\alpha$  and GFAP $\delta$  to aim to reduce the motility and invasiveness of malignant glioma cells effectively.

As mentioned before, vimentin is a very well-know IF type III and that is constitutively expressed in mesenchymal cells [46]. It is known to maintain the cytoarchitecture and tissue integrity [47]. In the recent years, vimentin has gained much importance as a marker for EMT.

EMT is a biological process that plays a significant role in embryogenesis, wound healing, and cancer progression [48, 49]. EMT is characterized by the transformation of epithelial cells, which are normally tightly bound together, into mesenchymal cells that possess enhanced migratory and invasive capabilities. This phenotypic change contributes to the acquisition of aggressive qualities by cancer cells, promoting metastasis and leading to tumor recurrence. This transition is driven by a complex interplay of molecular signaling

pathways, transcription factors, and microenvironmental cues. Key regulators of EMT include transcription factors such as Snail, Slug, Twist, and Zeb, which repress the expression of epithelial markers (e.g., E-cadherin) and promote the expression of mesenchymal markers (e.g., N-cadherin, vimentin) [50, 51].

Even though a large number of studies have correlate poor prognosis with loss of E-Cadherin [52-57] and upregulation of Vimentin and Snai1 [58], the significance of EMT in the metastatic process is a topic of debate [59, 60]. Moreover, and despite extensive histopathological studies, there is a lack of convincing evidence for EMT in patient samples. Notably, histopathological images of metastasized primary breast tumors have revealed an absence of mesenchymal cells. Instead, both primary and metastatic tumor cells demonstrated positive staining for E-cadherin and displayed typical epithelial characteristics [61, 62]. Furthermore, recent research involving mouse studies has raised doubts on the role of EMT in the metastatic process, suggesting that EMT may not be a prerequisite for the establishment of metastasis [60, 63]. In one study, *in vivo* lineage tracing revealed that the EMT marker Fsp1 was not predominantly expressed in metastatic tumor cells [60]. Another study demonstrated that the knockout of EMT-associated genes Snail or Twist did not impact the formation of metastases in mouse pancreatic tumors [63]. Based on these findings, the authors of these studies concluded that EMT might not be a critical mechanism for the formation of metastases.

However, the scientific community has participated in extensive debate regarding the conclusions drawn from these two studies. Numerous research groups have presented results using the same mouse models, demonstrating that the EMT marker Fsp1 is expressed predominantly in the later stages of the EMT process. Furthermore, not all metastatic tumor cells in a mesenchymal state express Fsp1, as indicated by these findings [64]. This suggests that tumor cells can undergo EMT and metastasize without ever expressing Fsp1. Additionally, different research groups performed experiments involving the depletion of the mesenchymal marker SMA in the same pancreatic tumors as those in Zheng et al.'s study. They demonstrated that depleting a sole EMT marker does not lead to the complete inhibition of the entire EMT process [65]. Altogether, this debate and studies has led to a new concept where cells do not undergo a simple binary switch between epithelial and mesenchymal states; instead, they can exhibit a range of diverse hybrid E/M states, as well [66].

Until now, the majority of research on EMT and the formation of metastases has primarily focused on metastases occurring outside the brain. In Chapter 5, we showed the existence of EMT in BCBM in both human and mouse models. We made an interesting observation of BCBM tumor cells exhibiting EMT characteristics, as depicted in Figure 5 of Chapter 5 since it has been described that EMT is important for metastases [51] but we are the first ones that show that this process also plays an important role in the formation of new metastases in the same organ when metastases are already formed. These mesenchymal tumor cells are the invading population within the BCBM tumors. Importantly, even though

confirming the existence of tumor cells that have undergone EMT using conventional histopathology has been challenging, we successfully confirmed the presence of EMT tumor cells in BCBM patients, as illustrated in Figure 7 of Chapter 5 through the application of multiplex immunohistochemistry. However, we did not investigate the role of hybrid states in the invasion of cells from brain metastases. So it may well be that many more tumor cells undergo EMT that we could measure with our techniques, which should be further investigated in future studies. Yet, understanding why certain cancers, like breast cancer, preferentially metastasize to specific organs such as the brain, and the role of EMT and hybrid states in this organ-specific metastasis, remains a critical area of research.

Similarly, to what happens in glioma tumors, the infiltration of these tumor cells into the brain impeded complete tumor resection, ultimately leading to tumor recurrence in our BCBM model. While we could visually identify residual tumor cells using fluorescence after surgery, these cells remained undetectable by MRI, as shown in Figure 4 of Chapter 5. In clinical settings, approximately 60% of patients with brain metastases experience recurrence within a year following complete tumor resection [67, 68]. The standard treatment approach for these patients involves surgical intervention followed by radiotherapy, and sometimes chemotherapy. Although we did not specifically investigate the combined effects of surgery with radiotherapy or chemotherapy, previous studies suggest that mesenchymal tumor cells may exhibit resistance to these therapies [69-71]. For instance, it was shown in the study conducted by Fischer *et al.* [60], that mesenchymal cells were resistant to cyclophosphamide treatment. Another study from Xiaofeng Zheng *et al.*, showed similar results in a pancreatic model where mesenchymal cells were resistant to gemcitabine. Thus, there are significant challenges that must be overcome to obtain successful cancer treatment [63]. A large effort has been made to try to revert the EMT phenotype using a combination of inhibitors and standard chemotherapy. For instance, mocetinostat in combination with gemcitabine for metastatic leiomyosarcoma, metformin in combination with cisplatin/radiation for NSCLC, bufalin in combination with gemcitabine for pancreatic cancer, palbociclib in combination with tamoxifen for HR(+)/HER2(-) advanced breast cancer, and disulfiram in combination with gemcitabine for metastatic pancreatic cancer. However, it is not yet clear about the safety in the long-term use of the EMT inhibitors [72]. This is particularly important if the EMT inhibitors in turn activate MET process that is believed to be involved in cancer metastasis.

Another potentially safer strategy could be the manipulation of stromal cells, including CAFs or TAMs, since they contribute to the promotion of EMT [73-75]. An advantage of targeting stromal cells is that they are not malignant cells themselves. Therefore, they are less likely to undergo clonal selection and acquire new mutations, which are common routes of resistance in cancer treatment.

In conclusion, this thesis reveals a new role for EMT. Apart from its involvement in metastasis and drug resistance, we suggest that EMT plays a part in BCBM recurrence

after surgery. Future studies should explore using EMT inhibition alongside surgery to see if it reduces tumor recurrence.

## **IMMUNOTHERAPY'S IMPACT ON BRAIN METASTASES: ADVANCEMENTS AND CHALLENGES**

Immunotherapy has emerged as a revolutionary approach to cancer treatment, harnessing the power of the immune system to combat cancer cells. With the limitations of conventional therapies, such as chemotherapy and radiation, as discussed in Chapter 2, there is a growing need for more effective and targeted treatments. Chemotherapeutic agents can have beneficial effects in breast tumors but limited effect on BCBM, which is potentially partly due to the expression of drug export pumps on tumor cells (Chapter 2). Despite immunotherapy's successes in treating melanoma, non-small cell lung cancer, and renal cell carcinoma [76-78], challenges persist in the field of immunotherapy. Not all patients respond uniformly to immunotherapy; approximately 20% of patients show a response, highlighting a significant heterogeneity in treatment outcomes [79]. Adding to the complexity, the brain has long been seen as an immunologically privileged site due to the BBB and the absence of lymphatic drainage, which were thought to hinder immune cell entry. However, emerging research contradicts this notion, showing that immune cells can infiltrate the central nervous system [80, 81].

The immune dynamics in BM are less understood compared to primary brain cancers, particularly in how they affect systemic and central nervous system immunity. Current research is actively exploring whether immune responses in BM are influenced more by the tissue environment or by the type of the originating tumor, such as melanoma, lung, renal, or breast cancer. Notably, unlike GBM, BM often exhibit moderate to significant T cell infiltration, suggesting differing immune landscapes. Several studies have indicated that the degree and pattern of T cell infiltration in brain metastases vary depending on the type of primary tumor that has metastasized to the brain [82, 83]. Specifically, melanoma brain metastases exhibit the highest T cell density with a diffuse infiltration pattern across the metastatic lesion. In contrast, metastases from renal, lung, and breast cancers are characterized by a moderate influx of T cells, predominantly localized within the tumor's stromal compartments [82]. However, it has to be considered that mutations that are found in BM are often not present in matched primary tumors[84]. Furthermore, data on brain metastasis patients are limited since those patients are often excluded from clinical trials. Nonetheless, immunotherapies have shown to improve survival in patients with cancers like melanoma and non-small cell lung cancer (NSCLC) [76, 85], which often metastasize to the brain suggesting the potential for therapeutic intervention via checkpoint inhibition. However, clinical trials have shown that checkpoint inhibitors alone often do not significantly

improve survival rates [86]. This might be because the majority of T cells infiltrating these brain tumors are bystander cells, not targeting specific tumor antigens [87]. Alternatively, anti-tumor T cells might be present but are rendered ineffective due to local immune suppression, even with checkpoint inhibitors. Thus, blocking immune suppression could be key to making brain tumors more responsive to immunotherapy. Alongside ongoing clinical trials focused on evaluating the effectiveness of various checkpoint inhibitors' combinations, there's a growing interest in exploring the synergistic potential of combining chemotherapy or radiotherapy with immunotherapy.

These agents can induce immunogenic cell death, leading to the release of tumor antigens and danger signals, which, in turn, can stimulate an immune response against the cancer cells [88, 89]. Additionally, chemotherapy can deplete suppressive immune cells, such as regulatory T cells (Tregs) and myeloid-derived suppressor cells (MDSCs) [90], thus relieving immunosuppression within the tumor microenvironment. Furthermore, some chemotherapies such as cisplatin or fluorouracil, have been found to upregulate the expression of major histocompatibility complex (MHC) molecules on cancer cells [91-94], making them more visible to the immune system and enhancing immune recognition and response [94, 95]. Moreover, doxorubicin has been associated with MDSC depletion [96], an increase in the level of type I interferons [97] and induction of immunogenic cell death [98]. Moreover, chemotherapies can also induce senescence in the cancer cells which has been shown to trigger the remodeling of the tumor microenvironment. In chapter 3 we demonstrated that by inducing senescence in tumor cells we can increase immune infiltration, specifically of CD8 T-cells, and this can be used subsequently to improve response to ICIs. Furthermore, the increased effectiveness of anti-PD1 therapy following doxorubicin pre-treatment in our BCBM models parallels the results from the TONIC trial in extracranial breast tumors [99]. This highlights the potential of leveraging doxorubicin's immunomodulatory effects to enhance checkpoint inhibitor treatments in BCBM.

Chemotherapy alone or anti-PD1 alone did not show any benefit as it was previously reported by Niesel *et al.* [100]. Interestingly we both show different ways of increasing the effectiveness of immunotherapies in brain metastases. However, there is still room for new combinations with other chemotherapies or even radiotherapy and other ICIs such as anti-CTLA4. Chemotherapy agents like platinum-based drugs sensitize the tumor microenvironment, making it more responsive to ICIs. For instance, cisplatin, could be combine with ICIs to enhance the immune response against the tumor. In terms of radiotherapy, local radiation can induce tumor cell death and enhance antigen presentation. Moreover, irradiation has been shown to induce type I interferons via the stimulator of interferon genes (STING) pathway and consequently enhance T cell priming [101, 102]. Combining this with ICIs like nivolumab has shown improved outcomes, particularly in melanoma, where patients experienced enhanced response rates and prolonged progression-free survival [103]. Finding novel strategies for converting tumors with low

immune cell infiltration, known as “cold” to tumors with a high degree of immune infiltration and an inflamed microenvironment, referred “hot” will provide more desirable response rates ICI therapy.

## **CONCLUDING REMARKS**

The research presented in this thesis highlights the critical nature of brain tumors and the formidable challenges posed by tumor recurrence and existing treatment modalities. Central to this understanding is the urgent need for innovative therapeutic approaches aimed at significantly enhancing patient outcomes. Animal models have emerged as invaluable tools throughout this research, providing essential insights into the intricate dynamics of brain tumors, focusing on invasion mechanisms and treatment responses.

In this thesis I have focused on the two most common brain tumors, which are gliomas and brain metastases. Glioma, as one of the most common and malignant types of brain tumors, presents unique challenges due to incomplete surgical removal caused by the diffuse invasion of individual cells. Brain metastases, on the other hand, are observed in a significant percentage of patients with metastatic breast leading to poor prognosis, highlighting the need for improved therapeutic strategies.

During the course of the thesis, I have explored the mechanisms of chemoresistance in brain metastasis and proposed a novel treatment combination involving immune checkpoint inhibition. Additionally, the importance of GFAP-isoforms in glioma invasion and tumor dynamics has been investigated, along with the behavior of brain metastases without treatment through intravital microscopy. These findings contribute to our understanding of the specific properties of brain tumors and the unique microenvironment of the CNS.

Furthermore, the thesis discusses the development and characterization of preclinical models BCBM. These syngeneic models, derived from mouse models, provide valuable tools for studying BCBM and testing new therapeutic strategies. The unique features of these models offer a controlled environment to study tumor cell interactions with the immune system and the brain microenvironment. Also, enable precise control over disease onset, facilitating in-depth study of disease progression in the brain and treatment responses which make them particularly suitable for understanding tumor behavior and invasion in the brain.

Overall, this thesis serves as a significant reminder of the significance of brain tumors, the challenges associated with their treatment, and the importance of innovative approaches to improve patient outcomes. The use of animal models, the exploration of chemoresistance and ABC transporters, and the investigation of IFs and EMT contribute to our understanding of brain tumors and facilitate the way for the development of improved therapeutic strategies.



## REFERENCES

1. Philips, A., et al., *Authors' Comment on "Brain Tumours: Rise in Glioblastoma Multiforme Incidence in England 1995-2015 Suggests an Adverse Environmental or Lifestyle Factor"*. J Environ Public Health, 2018. 2018: p. 2170208.
2. Claes, A., A.J. Idema, and P. Wesseling, *Diffuse glioma growth: a guerilla war*. Acta Neuropathol, 2007. 114(5): p. 443-58.
3. Soffietti, R., A. Ducati, and R. Ruda, *Brain metastases*. Handb Clin Neurol, 2012. 105: p. 747-55.
4. Nayak, L., E.Q. Lee, and P.Y. Wen, *Epidemiology of brain metastases*. Curr Oncol Rep, 2012. 14(1): p. 48-54.
5. Nussbaum, E.S., et al., *Brain metastases. Histology, multiplicity, surgery, and survival*. Cancer, 1996. 78(8): p. 1781-8.
6. Tsukada, Y., et al., *Central nervous system metastasis from breast carcinoma. Autopsy study*. Cancer, 1983. 52(12): p. 2349-54.
7. DiStefano, A., et al., *The natural history of breast cancer patients with brain metastases*. Cancer, 1979. 44(5): p. 1913-8.
8. Lee, S.S., et al., *Brain metastases in breast cancer: prognostic factors and management*. Breast Cancer Res Treat, 2008. 111(3): p. 523-30.
9. Boogerd, W., et al., *Brain metastases in breast cancer; natural history, prognostic factors and outcome*. J Neurooncol, 1993. 15(2): p. 165-74.
10. Kienast, Y., et al., *Real-time imaging reveals the single steps of brain metastasis formation*. Nat Med, 2010. 16(1): p. 116-22.
11. Quail, D.F. and J.A. Joyce, *The Microenvironmental Landscape of Brain Tumors*. Cancer Cell, 2017. 31(3): p. 326-341.
12. Bos, P.D., et al., *Genes that mediate breast cancer metastasis to the brain*. Nature, 2009. 459(7249): p. 1005-9.
13. Valiente, M., et al., *The Evolving Landscape of Brain Metastasis*. Trends Cancer, 2018. 4(3): p. 176-196.
14. Sevenich, L., *Turning "Cold" Into "Hot" Tumors-Opportunities and Challenges for Radio-Immunotherapy Against Primary and Metastatic Brain Cancers*. Front Oncol, 2019. 9: p. 163.
15. Nguyen, D.X., P.D. Bos, and J. Massague, *Metastasis: from dissemination to organ-specific colonization*. Nat Rev Cancer, 2009. 9(4): p. 274-84.
16. Minn, A.J., et al., *Genes that mediate breast cancer metastasis to lung*. Nature, 2005. 436(7050): p. 518-24.
17. Weeber, F., et al., *Tumor Organoids as a Pre-clinical Cancer Model for Drug Discovery*. Cell Chem Biol, 2017. 24(9): p. 1092-1100.
18. Weigelt, B., C.M. Ghajar, and M.J. Bissell, *The need for complex 3D culture models to unravel novel pathways and identify accurate biomarkers in breast cancer*. Adv Drug Deliv Rev, 2014. 69-70: p. 42-51.
19. Duval, K., et al., *Modeling Physiological Events in 2D vs. 3D Cell Culture*. Physiology (Bethesda), 2017. 32(4): p. 266-277.
20. Wang, C., X. Tong, and F. Yang, *Bioengineered 3D brain tumor model to elucidate the effects of matrix stiffness on glioblastoma cell behavior using PEG-based hydrogels*. Mol Pharm, 2014. 11(7): p. 2115-25.
21. Jeon, J., et al., *Revisiting Platinum-Based Anticancer Drugs to Overcome Gliomas*. Int J Mol Sci, 2021. 22(10).
22. Wang, M.L., et al., *Capecitabine for 5-fluorouracil-resistant brain metastases from breast cancer*. Am J Clin Oncol, 2001. 24(4): p. 421-4.
23. Bachelot, T., et al., *Lapatinib plus capecitabine in patients with previously untreated brain metastases from HER2-positive metastatic breast cancer (LANDSCAPE): a single-group phase 2 study*. Lancet Oncol, 2013. 14(1): p. 64-71.
24. Abolhoda, A., et al., *Rapid activation of MDR1 gene expression in human metastatic sarcoma after in vivo exposure to doxorubicin*. Clin Cancer Res, 1999. 5(11): p. 3352-6.
25. Kelly, R.J., et al., *A pharmacodynamic study of docetaxel in combination with the P-glycoprotein antagonist tariquidar (XR9576) in patients with lung, ovarian, and cervical cancer*. Clin Cancer Res, 2011. 17(3): p. 569-80.

26. Pusztai, L., et al., *Phase II study of tariquidar, a selective P-glycoprotein inhibitor, in patients with chemotherapy-resistant, advanced breast carcinoma*. *Cancer*, 2005. 104(4): p. 682-91.
27. Cripe, L.D., et al., *Zosuquidar, a novel modulator of P-glycoprotein, does not improve the outcome of older patients with newly diagnosed acute myeloid leukemia: a randomized, placebo-controlled trial of the Eastern Cooperative Oncology Group 3999*. *Blood*, 2010. 116(20): p. 4077-85.
28. Krishnamurthy, P., et al., *The stem cell marker Bcrp/ABCG2 enhances hypoxic cell survival through interactions with heme*. *J Biol Chem*, 2004. 279(23): p. 24218-25.
29. He, M., et al., *Hypoxia-inducible factor-2alpha directly promotes BCRP expression and mediates the resistance of ovarian cancer stem cells to adriamycin*. *Mol Oncol*, 2019. 13(2): p. 403-421.
30. Ee, P.L., et al., *Identification of a novel estrogen response element in the breast cancer resistance protein (ABCG2) gene*. *Cancer Res*, 2004. 64(4): p. 1247-51.
31. Bauer, M., et al., *Approaching complete inhibition of P-glycoprotein at the human blood-brain barrier: an (R)-[11C]verapamil PET study*. *J Cereb Blood Flow Metab*, 2015. 35(5): p. 743-6.
32. Verheijen, R.B., et al., *Molecular Imaging of ABCB1 and ABCG2 Inhibition at the Human Blood-Brain Barrier Using Elacridar and (11)C-Erlotinib PET*. *J Nucl Med*, 2018. 59(6): p. 973-979.
33. Ebright, R.Y., et al., *HIF1A signaling selectively supports proliferation of breast cancer in the brain*. *Nat Commun*, 2020. 11(1): p. 6311.
34. Fu, R., et al., *HIF-1alpha promoted vasculogenic mimicry formation in lung adenocarcinoma through NRP1 upregulation in the hypoxic tumor microenvironment*. *Cell Death Dis*, 2021. 12(4): p. 394.
35. Uchida, Y., et al., *Quantitative targeted absolute proteomics of human blood-brain barrier transporters and receptors*. *J Neurochem*, 2011. 117(2): p. 333-45.
36. Verscheijden, L.F.M., et al., *Differences in P-glycoprotein activity in human and rodent blood-brain barrier assessed by mechanistic modelling*. *Arch Toxicol*, 2021. 95(9): p. 3015-3029.
37. Strouhalova, K., et al., *Vimentin Intermediate Filaments as Potential Target for Cancer Treatment*. *Cancers (Basel)*, 2020. 12(1).
38. Battaglia, R.A., et al., *Vimentin on the move: new developments in cell migration*. *F1000Res*, 2018. 7.
39. Mendez, M.G., S. Kojima, and R.D. Goldman, *Vimentin induces changes in cell shape, motility, and adhesion during the epithelial to mesenchymal transition*. *FASEB J*, 2010. 24(6): p. 1838-51.
40. Messica, Y., et al., *The role of Vimentin in Regulating Cell Invasive Migration in Dense Cultures of Breast Carcinoma Cells*. *Nano Lett*, 2017. 17(11): p. 6941-6948.
41. Moeton, M., et al., *Silencing GFAP isoforms in astrocytoma cells disturbs laminin-dependent motility and cell adhesion*. *FASEB J*, 2014. 28(7): p. 2942-54.
42. van Bodegraven, E.J., et al., *GFAP alternative splicing regulates glioma cell-ECM interaction in a DUSP4-dependent manner*. *FASEB J*, 2019. 33(11): p. 12941-12959.
43. Paul, C.D., P. Mistriotis, and K. Konstantopoulos, *Cancer cell motility: lessons from migration in confined spaces*. *Nat Rev Cancer*, 2017. 17(2): p. 131-140.
44. Stassen, O., et al., *GFAPdelta/GFAPalpha ratio directs astrocytoma gene expression towards a more malignant profile*. *Oncotarget*, 2017. 8(50): p. 88104-88121.
45. Patel, A.P., et al., *Single-cell RNA-seq highlights intratumoral heterogeneity in primary glioblastoma*. *Science*, 2014. 344(6190): p. 1396-401.
46. Satelli, A. and S. Li, *Vimentin in cancer and its potential as a molecular target for cancer therapy*. *Cell Mol Life Sci*, 2011. 68(18): p. 3033-46.
47. Eriksson, J.E., et al., *Introducing intermediate filaments: from discovery to disease*. *J Clin Invest*, 2009. 119(7): p. 1763-71.
48. Arnoux, V., et al., *Erk5 controls Slug expression and keratinocyte activation during wound healing*. *Mol Biol Cell*, 2008. 19(11): p. 4738-49.

49. Thiery, J.P., et al., *Epithelial-mesenchymal transitions in development and disease*. Cell, 2009. 139(5): p. 871-90.
50. Dongre, A. and R.A. Weinberg, *New insights into the mechanisms of epithelial-mesenchymal transition and implications for cancer*. Nat Rev Mol Cell Biol, 2019. 20(2): p. 69-84.
51. Beerling, E., et al., *Plasticity between Epithelial and Mesenchymal States Unlinks EMT from Metastasis-Enhancing Stem Cell Capacity*. Cell Rep, 2016. 14(10): p. 2281-8.
52. Beck, B., et al., *Different levels of Twist1 regulate skin tumor initiation, stemness, and progression*. Cell Stem Cell, 2015. 16(1): p. 67-79.
53. Berx, G., et al., *E-cadherin is a tumour/ invasion suppressor gene mutated in human lobular breast cancers*. EMBO J, 1995. 14(24): p. 6107-15.
54. Guilford, P., et al., *E-cadherin germline mutations in familial gastric cancer*. Nature, 1998. 392(6674): p. 402-5.
55. Kase, S., et al., *Expression of E-cadherin and beta-catenin in human non-small cell lung cancer and the clinical significance*. Clin Cancer Res, 2000. 6(12): p. 4789-96.
56. Pirinen, R.T., et al., *Reduced expression of alpha-catenin, beta-catenin, and gamma-catenin is associated with high cell proliferative activity and poor differentiation in non-small cell lung cancer*. J Clin Pathol, 2001. 54(5): p. 391-5.
57. Perl, A.K., et al., *A causal role for E-cadherin in the transition from adenoma to carcinoma*. Nature, 1998. 392(6672): p. 190-3.
58. Sato, M., D.S. Shames, and Y. Hasegawa, *Emerging evidence of epithelial-to-mesenchymal transition in lung carcinogenesis*. Respirology, 2012. 17(7): p. 1048-59.
59. Hanahan, D. and R.A. Weinberg, *Hallmarks of cancer: the next generation*. Cell, 2011. 144(5): p. 646-74.
60. Fischer, K.R., et al., *Epithelial-to-mesenchymal transition is not required for lung metastasis but contributes to chemoresistance*. Nature, 2015. 527(7579): p. 472-6.
61. Bukholm, I.K., J.M. Nesland, and A.L. Borresen-Dale, *Re-expression of E-cadherin, alpha-catenin and beta-catenin, but not of gamma-catenin, in metastatic tissue from breast cancer patients [see comments]*. J Pathol, 2000. 190(1): p. 15-9.
62. Kowalski, P.J., M.A. Rubin, and C.G. Kleer, *E-cadherin expression in primary carcinomas of the breast and its distant metastases*. Breast Cancer Res, 2003. 5(6): p. R217-22.
63. Zheng, X., et al., *Epithelial-to-mesenchymal transition is dispensable for metastasis but induces chemoresistance in pancreatic cancer*. Nature, 2015. 527(7579): p. 525-530.
64. Bornes, L., et al., *Fsp1-Mediated Lineage Tracing Fails to Detect the Majority of Disseminating Cells Undergoing EMT*. Cell Rep, 2019. 29(9): p. 2565-2569 e3.
65. Aiello, N.M., et al., *Upholding a role for EMT in pancreatic cancer metastasis*. Nature, 2017. 547(7661): p. E7-E8.
66. Kroger, C., et al., *Acquisition of a hybrid E/M state is essential for tumorigenicity of basal breast cancer cells*. Proc Natl Acad Sci U S A, 2019. 116(15): p. 7353-7362.
67. Patchell, R.A., et al., *Postoperative radiotherapy in the treatment of single metastases to the brain: a randomized trial*. JAMA, 1998. 280(17): p. 1485-9.
68. Mahajan, A., et al., *Post-operative stereotactic radiosurgery versus observation for completely resected brain metastases: a single-centre, randomised, controlled, phase 3 trial*. Lancet Oncol, 2017. 18(8): p. 1040-1048.
69. Dudas, J., et al., *Epithelial to Mesenchymal Transition: A Mechanism that Fuels Cancer Radio/Chemoresistance*. Cells, 2020. 9(2).
70. Marie-Egyptienne, D.T., I. Lohse, and R.P. Hill, *Cancer stem cells, the epithelial to mesenchymal transition (EMT) and radioresistance: potential role of hypoxia*. Cancer Lett, 2013. 341(1): p. 63-72.
71. Qiao, L., et al., *Targeting Epithelial-to-Mesenchymal Transition in Radioresistance: Crosslinked Mechanisms and Strategies*. Front Oncol, 2022. 12: p. 775238.
72. Connolly, E.C., J. Freimuth, and R.J. Akhurst, *Complexities of TGF-beta targeted cancer therapy*. Int J Biol Sci, 2012. 8(7): p. 964-78.

73. Gok Yavuz, B., et al., *Cancer associated fibroblasts sculpt tumour microenvironment by recruiting monocytes and inducing immunosuppressive PD-1(+) TAMs*. *Sci Rep*, 2019. 9(1): p. 3172.
74. Karagiannis, G.S., et al., *Cancer-associated fibroblasts drive the progression of metastasis through both paracrine and mechanical pressure on cancer tissue*. *Mol Cancer Res*, 2012. 10(11): p. 1403-18.
75. Fiori, M.E., et al., *Cancer-associated fibroblasts as abettors of tumor progression at the crossroads of EMT and therapy resistance*. *Mol Cancer*, 2019. 18(1): p. 70.
76. Hodi, F.S., et al., *Improved survival with ipilimumab in patients with metastatic melanoma*. *N Engl J Med*, 2010. 363(8): p. 711-23.
77. Deeks, E.D., *Nivolumab: a review of its use in patients with malignant melanoma*. *Drugs*, 2014. 74(11): p. 1233-9.
78. Borghaei, H., et al., *Nivolumab versus Docetaxel in Advanced Nonsquamous Non-Small-Cell Lung Cancer*. *N Engl J Med*, 2015. 373(17): p. 1627-39.
79. Ventola, C.L., *Cancer Immunotherapy, Part 3: Challenges and Future Trends*. *P T*, 2017. 42(8): p. 514-521.
80. Galea, I., I. Bechmann, and V.H. Perry, *What is immune privilege (not)?* *Trends Immunol*, 2007. 28(1): p. 12-8.
81. Ransohoff, R.M., P. Kivisakk, and G. Kidd, *Three or more routes for leukocyte migration into the central nervous system*. *Nat Rev Immunol*, 2003. 3(7): p. 569-81.
82. Harter, P.N., et al., *Distribution and prognostic relevance of tumor-infiltrating lymphocytes (TILs) and PD-1/PD-L1 immune checkpoints in human brain metastases*. *Oncotarget*, 2015. 6(38): p. 40836-49.
83. Berghoff, A.S., et al., *Density of tumor-infiltrating lymphocytes correlates with extent of brain edema and overall survival time in patients with brain metastases*. *Oncoimmunology*, 2016. 5(1): p. e1057388.
84. Brastianos, P.K., et al., *Genomic Characterization of Brain Metastases Reveals Branched Evolution and Potential Therapeutic Targets*. *Cancer Discov*, 2015. 5(11): p. 1164-1177.
85. Wolchok, J.D., et al., *Ipilimumab monotherapy in patients with pretreated advanced melanoma: a randomised, double-blind, multicentre, phase 2, dose-ranging study*. *Lancet Oncol*, 2010. 11(2): p. 155-64.
86. Reardon, D.A., et al., *Effect of Nivolumab vs Bevacizumab in Patients With Recurrent Glioblastoma: The CheckMate 143 Phase 3 Randomized Clinical Trial*. *JAMA Oncol*, 2020. 6(7): p. 1003-1010.
87. Simoni, Y., et al., *Bystander CD8(+) T cells are abundant and phenotypically distinct in human tumour infiltrates*. *Nature*, 2018. 557(7706): p. 575-579.
88. Messmer, M.N., A.G. Snyder, and A. Oberst, *Comparing the effects of different cell death programs in tumor progression and immunotherapy*. *Cell Death Differ*, 2019. 26(1): p. 115-129.
89. Chacon, J.A., K. Schutsky, and D.J. Powell, *The Impact of Chemotherapy, Radiation and Epigenetic Modifiers in Cancer Cell Expression of Immune Inhibitory and Stimulatory Molecules and Anti-Tumor Efficacy*. *Vaccines (Basel)*, 2016. 4(4).
90. Wang, M., et al., *Therapeutic strategies to remodel immunologically cold tumors*. *Clin Transl Immunology*, 2020. 9(12): p. e1226.
91. Nio, Y., et al., *Induction of tumor-specific antitumor immunity after chemotherapy with cisplatin in mice bearing MOPC-104E plasmacytoma by modulation of MHC expression on tumor surface*. *Anticancer Res*, 2000. 20(5A): p. 3293-9.
92. Ohtsukasa, S., et al., *Increased expression of CEA and MHC class I in colorectal cancer cell lines exposed to chemotherapy drugs*. *J Cancer Res Clin Oncol*, 2003. 129(12): p. 719-26.
93. de Biasi, A.R., J. Villena-Vargas, and P.S. Adusumilli, *Cisplatin-induced antitumor immunomodulation: a review of preclinical and clinical evidence*. *Clin Cancer Res*, 2014. 20(21): p. 5384-91.
94. Wan, S., et al., *Chemotherapeutics and radiation stimulate MHC class I expression through elevated interferon-beta signaling in breast cancer cells*. *PLoS One*, 2012. 7(3): p. e32542.

95. Sapkota, B., C.E. Hill, and B.P. Pollack, *Vemurafenib enhances MHC induction in BRAF(V600E) homozygous melanoma cells*. *Oncoimmunology*, 2013. 2(1): p. e22890.
96. Alizadeh, D., et al., *Doxorubicin eliminates myeloid-derived suppressor cells and enhances the efficacy of adoptive T-cell transfer in breast cancer*. *Cancer Res*, 2014. 74(1): p. 104-18.
97. Sistigu, A., et al., *Cancer cell-autonomous contribution of type I interferon signaling to the efficacy of chemotherapy*. *Nat Med*, 2014. 20(11): p. 1301-9.
98. Casares, N., et al., *Caspase-dependent immunogenicity of doxorubicin-induced tumor cell death*. *J Exp Med*, 2005. 202(12): p. 1691-701.
99. Voorwerk, L., et al., *Publisher Correction: Immune induction strategies in metastatic triple-negative breast cancer to enhance the sensitivity to PD-1 blockade: the TONIC trial*. *Nat Med*, 2019. 25(7): p. 1175.
100. Niesel, K., et al., *The immune suppressive microenvironment affects efficacy of radio-immunotherapy in brain metastasis*. *EMBO Mol Med*, 2021. 13(5): p. e13412.
101. Demaria, S., et al., *Ionizing radiation inhibition of distant untreated tumors (abscopal effect) is immune mediated*. *Int J Radiat Oncol Biol Phys*, 2004. 58(3): p. 862-70.
102. Vanpouille-Box, C., et al., *DNA exonuclease Trex1 regulates radiotherapy-induced tumour immunogenicity*. *Nat Commun*, 2017. 8: p. 15618.
103. Sundahl, N., et al., *Phase 2 Trial of Nivolumab Combined With Stereotactic Body Radiation Therapy in Patients With Metastatic or Locally Advanced Inoperable Melanoma*. *Int J Radiat Oncol Biol Phys*, 2019. 104(4): p. 828-835.



# Appendix





## NEDERLANDSE SAMENVATTING

Hersentumoren kunnen worden ingedeeld in twee categorieën: primaire tumoren die ontstaan binnen het hersenweefsel, zoals gliomen, en secundaire tumoren die elders in het lichaam ontstaan en zich vervolgens naar de hersenen verspreiden. Onder de hersenmetastasen (BrM) zijn longkanker, melanoom en borstkanker (BCs) de meest voorkomende primaire tumoren die in verband worden gebracht met hun ontwikkeling. Ondanks de vooruitgang in tumor detectie, lokale behandelingen en de opkomst van nieuwe therapieën, blijft de prognose voor mensen gediagnosticeerd met agressieve hersenkanker ontmoedigend. De algehele overlevingskansen van 5 jaar zijn helaas laag, wat het kritische belang benadrukt van een dieper begrip van deze ziekte om effectieve behandelingsstrategieën te ontwikkelen.

In **Hoofdstuk 1** introduceer ik alle concepten die nodig zijn om dit proefschrift te kunnen volgen. **Hoofdstuk 2** richt zich op het gebruik van muismodellen voor borstkankerhersenmetastasen (BCBM) die zijn ontwikkeld in ons laboratorium om het mechanisme van chemoresistentie te bestuderen. We laten zien hoe tumorcellen de borstkankerresistentie-eiwit (BCRP) kunnen overexpresseren om zich aan te passen aan nieuwe omgevingen, wat uiteindelijk leidt tot therapieresistentie. Dit onderzoek werpt licht op de onderliggende mechanismen van chemoresistentie en biedt belangrijke inzichten in mogelijke strategieën om dit probleem te overwinnen. **Hoofdstuk 3** introduceert een nieuw combinatie van behandelingen voor het effectief beheer van hersenmetastasen, met een specifieke focus op remming van immuuncontrolepunten. We stellen een unieke strategie voor om de micro-omgeving van de hersenen te moduleren door gebruik te maken van doxorubicinebehandelingen, die tumorsenescentie veroorzaken. Deze inductie leidt tot de werving van cytotoxische T-cellen die PD1 tot expressie brengen. Vervolgens wordt remming van het immuuncontrolepunt toegepast, wat leidt tot een opmerkelijke toename van de overlevingskans van muizen. Deze bevindingen bieden inzicht in de mogelijke implementatie van remmers van immuuncontrolepunten, specifiek voor hersenmetastasen, en verstrekken waardevolle informatie voor de ontwikkeling van verbeterde therapeutische strategieën. In de volgende twee hoofdstukken zal ik me richten op een belangrijk probleem dat gepaard gaat met hersentumoren: hun invasieve potentieel. In **Hoofdstuk 4** benadruk ik het belang van GFAP-isoformen bij het reguleren van de invasie van gliomen en tumordynamiek door gebruik te maken van intravitale microscopie. Ik benadruk het belang van het begrijpen van de invasieve gedragingen van verschillende GFAP-positieve populaties binnen glioomtumoren, aangezien dit sterk kan bijdragen aan de ontwikkeling van effectievere therapieën tegen invasie. In **Hoofdstuk 5** verschuift de focus naar het onderzoeken van het gedrag van hersenmetastasen in de afwezigheid van behandeling met behulp van intravitale microscopie. Onze bevindingen onthullen dat het proces dat bekend staat als epitheliale-mesenchymale overgang (EMT) een cruciale rol

speelt bij het stimuleren van de lokale invasie van hersenmetastasen. Door de migratie van deze mesenchymale tumorcellen aan te pakken door middel van het uitschakelen van ARPC3, observeren we een aanzienlijke afname van de kans op tumorrecidief bij muizen. We ontdekken ook dat deze mesenchymale tumorcellen plastisch zijn en het vermogen hebben om nieuwe metastatische laesies te vormen wanneer ze opnieuw in de hersenen van muizen worden geïnjecteerd. Om de relevantie van onze bevindingen in een klinische context te valideren, analyseren we een kleine cohort van verwijderde hersenmetastasen van borstkanker bij mensen.

Al met al bieden deze hoofdstukken een uitgebreide verkenning van verschillende aspecten met betrekking tot de invasie van gliomen, hersenmetastase en chemoresistentie. Door het gebruik van geavanceerde beeldvormingstechnieken, preklinische modellen en klinische validatie dragen we bij aan ons begrip van de onderliggende mechanismen en potentiële therapeutische wegen voor hersentumoren.

## ENGLISH SUMMARY

Brain malignancies can be classified into two categories: primary tumors that originate within the brain tissue, such as gliomas, and secondary tumors known as metastases, which originate elsewhere in the body and subsequently spread to the brain. Among brain metastases (BrM), the most common primary tumors associated with their development are lung, melanoma, and breast cancers (BCs). Despite advancements in tumor detection, local treatments, and the emergence of novel therapies, the prognosis for individuals diagnosed with aggressive brain cancer remains discouraging. The 5-year overall survival rates are unfortunately low, underlining the critical need for a deeper understanding of this disease to help with the development of effective treatment strategies.

**Chapter 1**, I introduce all concepts that are important for this thesis. **Chapter 2** focuses on the use of mouse BCBM models developed in our laboratory to study the mechanism of chemoresistance. We demonstrate how tumor cells can overexpress the breast cancer resistance protein (BCRP) to adapt to new environments, ultimately leading to therapy resistance. This research sheds light on the underlying mechanisms of chemoresistance and provides important insights into potential strategies for overcoming this challenge.

**Chapter 3** introduces a novel combination of treatments for the effective management of brain metastases, with a specific focus on immune checkpoint inhibition. We propose a unique strategy to modulate the brain microenvironment by employing doxorubicin treatments, which induce tumor senescence. This induction triggers the recruitment of cytotoxic T cells expressing PD1. Subsequently, immune checkpoint blockade is applied, leading to a remarkable increase in the survival rate of mice. These findings offer insights into the potential implementation of immune checkpoint inhibitors specifically for brain metastases and provide valuable information for the development of improved therapeutic strategies. In **Chapters 4 and 5**, I will focus on a significant issue associated with brain tumors: their invasive potential. In **Chapter 4**, I highlight the significance of GFAP-isoforms in regulating glioma invasion and tumor dynamics by employing intravital microscopy. I emphasize the importance of understanding the invasive behaviors of various GFAP-positive populations within glioma tumors, as it can greatly contribute to the development of more effective therapies against invasion. Moving on to **Chapter 5**, the focus shifts to investigating the behavior of brain metastases in the absence of treatment using intravital microscopy. Our findings reveal that the process known as epithelial-to-mesenchymal transition (EMT) plays a pivotal role in driving the local invasion of brain metastases. By targeting the migration of these mesenchymal tumor cells through the knockdown of ARPC3, we observe a significant decrease in the probability of tumor recurrence in mice. We also discover that these mesenchymal tumor cells exhibit plasticity and possess the ability to form new metastatic lesions when reinjected into the brains of mice. To validate

the relevance of our findings in a clinical context, we analyze a small cohort of resected human breast cancer brain metastases.

Overall, these chapters offer a comprehensive exploration of various aspects related to glioma invasion, brain metastasis, and chemoresistance. Through the use of advanced imaging techniques, preclinical models, and clinical validation, we contribute to our understanding of the underlying mechanisms and potential therapeutic avenues for brain tumors.

## RESUMEN EN ESPAÑOL

Los tumores cerebrales malignos se dividen en dos tipos: los tumores primarios que tienen su origen en el tejido cerebral, como los gliomas, y los tumores secundarios, conocidos como metástasis, que provienen de otras partes del cuerpo y luego se propagan al cerebro. Entre las metástasis cerebrales, los tumores primarios más comunes asociados con su desarrollo son los de pulmón, melanoma y cáncer de mama. A pesar de los avances en la detección de tumores, los tratamientos y la aparición de terapias innovadoras, el pronóstico para las personas diagnosticadas con tumores cerebrales sigue siendo poco alentador. Lamentablemente, las tasas de supervivencia global a los 5 años son bajas, lo que destaca la necesidad crítica de comprender mejor esta enfermedad para contribuir al desarrollo de nuevos tratamientos eficaces.

El **Capítulo 1** introduce todos los conceptos que son importantes para esta tesis. El **Capítulo 2** se enfoca en el uso de modelos de ratones de cáncer de mama con metástasis en cerebro desarrollados en nuestro laboratorio para investigar el mecanismo de la quimiorresistencia. Mostramos cómo las células tumorales presentan mayor cantidad de la proteína de resistencia al cáncer de mama (BCRP) para adaptarse a nuevos entornos, lo que finalmente conduce a la resistencia al tratamiento. Esta investigación arroja luz sobre los mecanismos subyacentes de la quimiorresistencia y proporciona perspectivas importantes sobre posibles estrategias para superar este desafío. El **Capítulo 3** presenta una combinación novedosa de tratamientos para el manejo efectivo de las metástasis cerebrales, con un enfoque específico en la inhibición de puntos de control inmunológicos. Proponemos una estrategia única para modular el microentorno cerebral mediante tratamientos con doxorrubicina, que inducen senescencia en células tumorales. Esta inducción desencadena el reclutamiento de células T citotóxicas que expresan PD1. Posteriormente, se aplica el bloqueo de puntos de control inmunológicos, lo que conduce a un notable aumento en la tasa de supervivencia de los ratones. Estos hallazgos brindan ideas sobre la posible implementación de inhibidores de puntos de control inmunológico específicamente para las metástasis cerebrales y proporcionan información valiosa para el desarrollo de nuevas estrategias terapéuticas. En los próximos dos capítulos, me centraré en un problema significativo asociado con los tumores cerebrales: su potencial invasivo. En el **Capítulo 4**, destaco la importancia de las isoformas de GFAP en la regulación de la invasión del glioma y la dinámica tumoral mediante el uso de microscopía intravital. Hago hincapié en la importancia de comprender los comportamientos invasivos de varias poblaciones GFAP positivas dentro de los tumores de glioma, ya que esto puede contribuir en gran medida al desarrollo de terapias más efectivas contra la invasión. En el **Capítulo 5**, el enfoque se centra en investigar el comportamiento de las metástasis cerebrales en ausencia de tratamiento utilizando microscopía intravital. Nuestros hallazgos revelan que el proceso conocido como transición epitelio-mesénquima (EMT) desempeña un papel

crucial en impulsar la invasión local de las metástasis cerebrales. Al inhibir la migración de estas células tumorales mesenquimales mediante la inhibición de ARPC3, observamos una disminución significativa en la probabilidad de recurrencia del tumor en los ratones. También descubrimos que estas células tumorales mesenquimales muestran plasticidad y poseen la capacidad de formar nuevas lesiones metastásicas cuando se reinyectan en los cerebros de los ratones. Para validar la relevancia de nuestros hallazgos en un contexto clínico, analizamos un pequeño grupo de metástasis cerebrales de cáncer de mama humano resecaadas.

En resumen, estos capítulos ofrecen una exploración exhaustiva de varios aspectos relacionados con la invasión de gliomas, la metástasis cerebral y la quimiorresistencia. Mediante el uso de técnicas avanzadas de imagen, modelos preclínicos y validación clínica, contribuimos a la comprensión de los mecanismos subyacentes y las posibles vías terapéuticas para los tumores cerebrales.

## **CURRICULUM VITAE**

Rebeca Uceda Castro was born on October 4th, 1994, in Madrid, Spain, where she grew up. In September 2012 after completing High school, she started her Bachelor in Biology at the Faculty of Biology at Autonomia University of Madrid. In her fourth year, she participated in the Erasmus program, embarking on a year-long academic journey at the University of Tor Vergata in Rome. She continued her studies by enrolling in a Master Program of Biochemistry, Molecular Biology and Biomedicine at the Complutense University in Madrid. During the last year of the Bachelor and the Master she pursued her internship at the Centro de Investigaciones Biologicas (Cib), Madrid, in the laboratory of Dr. Maria Angeles Garcia Pardo. Over the course of her internships, she focused on the “Role of MMP9 in chronic lymphocytic leukemia migration”. While characterizing the role of MMP in the migration of leukemia cells, she discovered CD99 as an MMP-9 target and a novel partner in malignant cell migration/arrest. After finishing her Master’s, an inspiring talk by Jacco van Rheenen motivated her to get in touch. In September 2018, she joined the laboratory of Prof. Dr. Jacco van Rheenen at the Netherlands Cancer Institute in Amsterdam. The results of her PhD research are described in this thesis. Since November 2023, she works at the Institute of Cancer Research (ICR) in London continuing her research in breast cancer and new potential treatment strategies.

## LIST OF PUBLICATIONS

Aguilera-Montilla, N., Bailón, E., **Uceda-Castro, R.**, Ugarte-Berzal, E., Santos, A., Gutiérrez-González, A., Pérez-Sánchez, C., Van den Steen, P. E., Opdenakker, G., García-Marco, J. A., & García-Pardo, A#. (2019). MMP-9 affects gene expression in chronic lymphocytic leukemia revealing CD99 as an MMP-9 target and a novel partner in malignant cell migration/arrest. *Oncogene*. 2019;38(23):4605-4619.

Aguilera-Montilla, N., Bailón, E., Ugarte-Berzal, E., **Uceda-Castro, R.**, Prieto-Solano, M., García-Martínez, E., Samaniego, R., Van den Steen, P. E., Opdenakker, G., García-Marco, J. A., & García-Pardo, A#. (2019). Matrix metalloproteinase-9 induces a pro-angiogenic profile in chronic lymphocytic leukemia cells. *Biochem Biophys Res Commun*. 2019;520(1):198-204.

**Uceda-Castro R\***, van Asperen JV\*, Vennin C, Sluijs JA, van Bodegraven EJ, Margarido AS, Robe PAJ, van Rheenen J#, Hol EM#. GFAP splice variants fine-tune glioma cell invasion and tumour dynamics by modulating migration persistence. *Sci Rep*. 2022;12(1):424.

Margarido AS, **Uceda-Castro R**, Hahn K, de Bruijn R, Kester L, Hofland I, Lohuis J, Seinstra D, Broeks A, Jonkers J, Broekman MLD, Wesseling P, Vennin C, Vizoso M#, van Rheenen J#. Epithelial-to-mesenchymal transition drives invasiveness of breast cancer brain metastases. *Cancers*. 2022;14(13):3115.

**Uceda-Castro R\***, Margarido AS\*, A. S., Cornet, L., Vegna S, Hahn K, Song JY, Putavet DA, van Geldorp M, Çitirikkaya CH, de Keizer PLJ, ter Beek LC, Borst GR, Akkari L, van Tellingen O, Broekman MLD, Vennin C#, van Rheenen J#. Re-purposing the pro-senescence properties of doxorubicin to introduce immunotherapy in breast cancer brain metastasis. *Cell Rep Med*. 2022;3(11):100821

Buikhuisen, J. Y., Gomez Barila, P. M., Cameron, K., Suijkerbuijk, S. J. E., Liefstink, C., di Franco, S., Krotenberg Garcia, A., **Uceda-Castro, R.**, Lenos, K. J., Nijman, L. E., Torang, A., Longobardi, C., de Jong, J. H., Dekker, D., Stassi, G., Vermeulen, L., Beijersbergen, R. L., van Rheenen, J., Huveneers, S., & Medema, J. P#. Subtype-specific kinase dependency regulates growth and metastasis of poor-prognosis mesenchymal colorectal cancer. *Journal of experimental & clinical cancer research*. *J Exp Clin Cancer Res*. 2023;42(1):56. Published 2023 Mar 3.



**Uceda-Castro R**, Margarido AS, Song JY, Ji-Ying Song, Mark C. de Gooijer, Hendrik A. Messal, Cecilia R. Chambers, Max Nobis, Ceren H. Çitirikkaya, Kerstin Hahn, Danielle Seinstra, David Herrmann, Paul Timpson, Pieter Wesseling, Olaf van Tellingen, Vennin C#, van Rheenen J#. BCRP drives intrinsic chemoresistance in chemotherapy-naïve breast cancer brain metastasis. *Science Advances*. 2023

\* Equal contribution; # Correspondence

## ACKNOWLEDGMENTS

A big thanks to everyone at NKI!! These past five years have been a wild ride, and I couldn't have done it without your support. Thanks a lot for the good vibes, great conversations, and all-around fantastic times. You've made this thesis journey way more enjoyable!

**Jacco** I would like to thank you for this big opportunity. Your passion for research has been really motivating, and your support has meant a lot to me. I'm grateful for the opportunities you've given me to learn and grow. Thanks for believing in me and helping me develop as a researcher. Finally, thank you for being so patient during my not-so-good English days, I really appreciate the effort.

I would like to thank **Jos Jonkers, Elly Hol, Marike Broekman, Madelon Maurice** and **Olaf van Tellingen** for reading and assessing my thesis, and a special big thanks to Jos, Olaf and **Gerben Borst**, part of my OOA committee, for all the scientific discussion and helpful suggestions on my PhD projects.

Just want to give a big thanks to everyone in the **van Rheenen group**. Working together has been great! The teamwork and good times have made this more than just a job. Your input has made things better, and I appreciate the support. Thanks for keeping it real and making our workspace a good place to be. Also, I don't want to forget the **former members**, especially **Colinda** for helping me out during those long days in C0 and my office mates **Evelyne, Saskia S.** and **Lotte** for creating a nice environment. **Hendrik**, you may not be the ideal office mate (some days), but I still appreciate you, and you know it! **Maria** and **Dimitris**, I want to thank you for always being there to support and listen. I will always miss those improvised borrels in our office and even our short 20 minutes workout! I am pretty sure you have a brilliant future ahead! **Guillaume**, my lovely French/Spanish friend, keep being so enthusiastic about food- it's the best thing in life! A big thank you to the **new generation** of the group and I wish you all the best as you start on this exciting journey! **Mirjam, Tom** and **Hristina**, it was amazing to share office with you! I will always miss the snack break and Spanish lesson time. **Laura**, you are one of the few people that was there during my whole PhD journey. Thank you so much for the help during this time and for introducing me to the amazing world of the mouse breeding.

**Albertito**, te tenía en mente como el stalker de LinkedIn de mi amiga Andreia y resulta que al final eres un tipo majo! muchas gracias por esos mesecillos que tanto me enseñaste y que sirvieron para añadir un traumita más a la lista cuando vi esa aorta sangrar a chorro perdido.

I want to say a big thank you to everyone at the **bioimaging** and **flow cytometry facilities**, and a special mention to the **Pathology team**. Thanks for always helping out, even when I needed stuff at the last minute, and for being quick with those last-minute experiments. Your support has meant a lot!

I would like to thank my collaborators, especially **Jessy** for all the scientific discussions and nice work done together. It was always easy to work with you, and I'm glad I could

share this experience with you. To my student **Lesley**, a big thanks for helping me with my research projects.

To all current and former members of the **intervention unit** and **T1 people** including the **IVD members**, and in particular to **Bjorn** and **Natalie**. Thank you for taking care of all my countless experiments and for always being so helpful.

I would like to thank everyone in the **C2 department** including **Ellen**, **Suzanne** and **Rosalinda** for always being so helpful and specially the people from **Jos group**. It was a great working environment and lots of fun! **Felipe**, gracias por todas esas conversaciones odiando nuestras vidas pero sobre todo por todos esos abrazos! Espero que en tu próximo destino te valoren como te mereces! Thank you also to **Xue** for all those bike rides and lovely time. I will see you soon!

All the **Spanish NKI crew**, thank you for being part of the PhD journey, and all the memorable borrels and OOA retreats! **Carmen** y **Alberto**, lo que la OOA unió, que no lo separe nadie. Gracias, amigos, por estar ahí, apoyándonos en esta movida que solitos decidimos meternos.

Next, I would like to thank my dear paranymphs that have been so special during this journey. **Ana K.** (or EEESpanish Ana). Somehow since the first day we met on those stairs, and you said “JJJello” I knew this was only the beginning of a great friendship. Thanks for being there always, when celebrating and dancing gasolina, dándolo todo, but also in not so good moments, cagándonos en todo. Your energy is inspiring! I hope our friendship lasts forever because I still need more time to understand how your time management works. Clearly, a minute in my life isn't the same as it is in yours. Einstein already spoke about the relativity of time. And, just like when you take forever to unlock your bike, some things seem to happen really slowly! **Ana M.** (or brasilian Ana) just wanted to say thanks a lot for all the good times we've had. From that colourful Brazilian meals we shared to the countless times I borrowed your bike and those nice sunny days sailing in the Amsterdam canals, each moment has been special. Even if you decide to go for the Dutch nationality, for obvious reasons, know that for me, you will always be an adopted Spaniard! **Claire**, not just my supervisor, co-promoter, and paranymph, but also a friend. I can't possibly thank you enough for all you've done. Our long hours in the animal facility were quite something. We spent a lot of time brainstorming, not necessarily about science.... While some people dreamed about becoming rich, instead our biggest dream was to do something as crazy as wearing street shoes into the super-clean facility on our last day!! Definitely my most valuable talents after these 5 years include being the quickest in the world at getting dressed and undressed, and, of course, knowing how to genotype. No matter where life takes you, everyone is lucky to have you. And a big hug for those two little Rebecos.

My lovely **brain team**, I was so lucky to be part of it with you **Andy**. I will always remember when I was so lost, and you took me to the canteen and started to draw and explain me the amazing things we could do with IVM. At that time, you did not say these

sessions could be endless, I guess to not scare me. You are so kind and sweet! Even sweeter when you speak Spanish. Thanks for everything! Not only for everything you helped me in Amsterdam but also to start my new life in London.

My 5 years in Amsterdam wouldn't have been the same without my dear **Malakitas**. Thank you for always being there and making the covid times easier and even fun! **Christinita**, I love how loud your laugh is and how free I felt every time I was talking with you. Thanks for all those deep conversations we had. Every place was a good place to talk, even in the tissue culture room. I have learnt a lot from you guapa! **Julia** de mi corazón, you gave me one of the best news ever a few days ago, I couldn't be prouder of you and what you are building! Te admiro y te envidio por muchísimas cosas y te deseo lo mejor y espero poder seguir celebrando cosas juntas forever! **Marianita**, thank you for all the great memories we made together and even though you don't know how to pronounce my name, at least I know you will always remember my birthday. **Lou**, although you joined the NKI for a short period, your positive energy makes it very easy to be around you.

Gracias a mi **familia** por todo el apoyo que me ha dado, aun estando a 1775 km de distancia, y me ha permitido llegar hasta aquí. **Abuelilla**, aunque no entiendas ni la portada de este libro, y no pueda ir a comer a tu casa los viernes, sé que te hace mucha ilusión tener una nieta Doctora. Al pesado de mi **hermano** que, aunque sea el listo de la familia ahora le gano en número de títulos. A **Ari** por cuidar del pesado de mi hermano y hacerle feliz y por ayudarme a luchar contra las injusticias y los abusones.

A mis **amigos** por seguirme y apoyarme allá donde voy. Algunos compartimos el amor por la biología y otros el vínculo por habernos conocido en el complicado momento de la adolescencia.

A mi "amiceta" **Paula**, que me aguantó en el arranque, un poco accidentado, de este viaje y que me enseñó que el valenciano tiene algo más aparte de 'tete' y 'nano'. Que las casualidades de la vida que hicieron que dos biólogas se unieran en Ámsterdam a través de Facebook y viviesen una pandemia no las separe la distancia.

Me gustaría ir finalizando, agradeciendo a las que en parte tienen gran culpa de que este libro exista y es a mis **compañeras del CIB**. En ese momento os quería matar por ir pegando la foto del que sería mi jefe durante 5 años por todos lados, pero hoy solo tengo agradecimientos.

Y por último **Pablo**, tú eres lo mejor que me ha dado la biología. Aunque la distancia entre Madrid y Ámsterdam nos haya hecho odiar las videollamadas, has hecho de esta tesis una aventura que siempre recordaré con una sonrisa. Gracias por explicarme una y mil veces como poner esas "malditas scale bars" y evitar que tirase el ordenador por la ventana otras tantas. Gracias por ser mi GPS humano integrado y llevarme de la mano en esta nueva aventura Londinense y las que nos esperan.







